Design of a Spectroscopic Ellipsometer for the Study of Planetary Surfaces

Space Engineering: MSc Thesis

Adyn Miles

TU Delft

Design of a Spectroscopic Ellipsometer for the Study of Planetary Surfaces

Space Engineering: MSc Thesis

by

Adyn Miles

to obtain the degree of Master of Science

at the Delft University of Technology,

to be defended publicly on Tuesday July 9, 2024 at 1:00 PM.

Student number:	5760658	
Project duration:	October 9, 2023 – July 9, 2024	
Thesis committee:	Prof. dr. S. Potin,	TU Delft, supervisor
	Prof. dr. A. Cervone,	TU Delft
	Prof. dr. R. Saathof,	TU Delft

Summary

The study of the surface of a planetary body can reveal information about its formation, evolution, and internal structure. When light reflects off such a surface, it undergoes a change in its orientation from which details about the surface composition and structure can be discovered. This thesis addresses the design, simulation, and calibration procedures of an instrument that will measure both spectral and polarimetric data of reflected light off of samples of planetary analogues. The combination of spectral and polarimetric data will allow researchers to investigate key targets on the surfaces of asteroids, comets, icy moons, and a wide variety of other surfaces. The instrument, called a spectroscopic ellipsometer, can also take these measurements at many different orientations through the use of two controllable arms, serving as a valuable proof of concept for future spaceborne missions.

Instrument requirements were first defined by studying literature about key targets for spectropolarimetry of planetary surfaces. As no existing instruments could meet these requirements, a custom design was instead chosen. Major design architecture decisions were then addressed to establish the main components of the system and the major design drivers. Through a subsequent detailed design process which determined specific components and their placement, the requirements that had the largest impact on the design of the instrument were the spectral range, signal-to-noise ratio, and the polarimetric accuracy.

After detailed design was complete, an end-to-end simulation was built in Python to capture the performance of the instrument from a spectral and polarimetric perspective. As instrument components were very expensive and would take a long time to manufacture and characterize, this was the most cost- and time-efficient method of verifying the instrument's performance. The performance simulations showed strong signal-to-noise ratio and spectral resolution performance, and highlighted major areas to focus on during the calibration procedure to improve polarimetric accuracy.

While not all parts of the instrument were received at the completion of this project, calibration procedures for major components of this instrument were outlined to ensure optimal spectral and polarimetric performance. Some calibration was also performed in the laboratory to ensure optimal positioning of polarization elements.

Overall, this thesis outlines the design of an instrument that will help open a new field of research involving extensive spectropolarimetric studies of planetary surfaces. While significant work needs to be done in assembly, characterization, and experimental design, the instrument shows promising performance in terms of measurement accuracy, and potential transferability to spaceborne payloads given some key developments in spectropolarimetric technologies. This work therefore serves as a stepping stone for future researchers to contribute to establishing criteria for life beyond Earth, understanding the formation and evolution of the solar system, and designing systems for human expansion.

Acknowledgments

Working on this thesis project over the past nine months has been immensely fulfilling, and an excellent way to finish my time at TU Delft.

I would first like to thank my supervisor Sandra Potin, who entrusted the design process (and budget) of an instrument important to her future research to a Master's student. Without this level of faith, my experience in this program would not have been nearly as rewarding. I am truly grateful for the opportunity to work on a project that helped me grow my skillset in so many dimensions, while having a lot of fun solving problems along the way. She gave me the support I needed to keep doing meaningful work on the project, while giving me the space I needed for creativity and learning. I am excited to see all the opportunities that this work unlocks, and I am honoured to have had the chance to contribute so early on in the process.

I would also like to extend my deepest thanks to others in the Space Instrumentation Division who have helped me along in this process and encouraged me along the way. Pierre, thank you for helping me work through some of the more difficult aspects of this thesis. Though our conversations often became long and complex, you stayed patient and supportive the entire way. Jérôme, thank you for making time to contribute to this work despite the many other projects demanding your attention, and for encouraging me to think more deeply about my decisions to develop as a researcher and engineer. Fabien, you have been a tremendous help whenever a problem arose with the project, and without you this instrument could not have become a reality.

To all my friends in Delft, thank you for helping make my time in the Master's program worthwhile. Your friendliness, enthusiasm, and support made this a period of my life I will never forget.

And lastly, to my wonderful family. It was a difficult decision to move so far away for such a long time. Despite the distance, I always felt your support as strongly as if I had never left. Thank you for absolutely everything.

Adyn Miles

Contents

List of Figures

List of Tables

Nomenclature

Abbreviations

Abbreviations are listed in alphabetical order.

Abbreviation	Definition
Al_2O_3	Sapphire
AoLP	Angle of Linear Polarization
BaF_2	Barium Fluoride
BRDF	Bidirectional Reflectance Distribution Function
CaF_2	Calcium Fluoride
CN	Cyanide
CO_2	Carbon Dioxide
dB	Decibels
DoCP	Degree of Circular Polarization
DoLP	Degree of Linear Polarization
FTS	Fourier Transform Spectrometer
He-Ne	Helium-Neon
InAsSb	Indium Arsenide Antimonide
InF_3	Fluoroindate
IR	Infrared
KBr	Potassium Bromide
KCl	Potassium Chloride
MgF_2	Magnesium Fluoride
NA	Numerical Aperture
p-polarization	Polarization oriented parallel to plane of incidence
PEM	Photoelastic Modulator
PME	Phase-Modulated Ellipsometer
QTH	Quartz-Tungsten-Halogen
RAE	Rotating Analyzer Ellipsometer
RMS	Root Mean Square
s-polarization	Polarization oriented perpendicular to plane of incidence
Si	Silicon
SNR	Signal-to-Noise Ratio
SrF_2	Strontium Fluoride
SPG	Spectro-polarimetric Goniometer
SrF_2	Strontium Fluoride
UV-VIS	Ultraviolet and Visible
ZrF_4	Fluorozirconate
$\lambda/4$	Quarter-wave

Symbols

Symbols in this section are listed in the order they appear in the text.

General Spectropolarimetry

Symbol	Definition	Units
$I_{\|\|}$	Light intensity parallel to plane of incidence	–
$I_{\perp}$	Light intensity perpendicular to plane of incidence	–
I_{+45°	Light intensity +45° from plane of incidence	–
I_{-45°	Light intensity −45° from plane of incidence	–
I_L	Intensity of left-handed circularly polarized light	–
I_R	Intensity of right-handed circularly polarized light	–
S_0	Stokes parameter 0 (total intensity)	–
S_1	Stokes parameter 1 (linear intensity)	–
S_2	Stokes parameter 2 (45° offset linear intensity)	–
S_3	Stokes parameter 3 (circular intensity)	–
θ_0	AoLP offset parameter	[rad.]
Δ	Phase difference between polarization components of light	[°]
Ψ	Amplitude ratio between polarization components of light	[°]
$\delta_{\|\|}$	Electric field phase parallel to plane of incidence	[rad.]
$\delta_{\perp}$	Electric field phase perpendicular to plane of incidence	[rad.]
δ_x	See $\delta_{\|\|}$	[rad.]
δ_y	See $\delta_{\perp}$	[rad.]
$E_{\|\|,0}$	Electric field amplitude parallel to plane of incidence	–
$E_{\perp,0}$	Electric field amplitude perpendicular to plane of incidence	–
E_x	See $E_{\|\|,0}$	–
E_y	See $E_{\perp,0}$	–

Design Geometry

Symbol	Definition	Units
w_s	Slit width	[mm]
h_s	Slit height	[mm]
w_b	Bulb width	[mm]
h_b	Bulb height	[mm]
m	Magnification	–
V	Vignetting	–
$(f/\#)_1$	f-number of condenser	–
$(f/\#)_2$	f-number of focuser	–
$I_{0.5}$	Irradiance at 0.5m from the bulb	[mWm^{-2}nm^{-1}]
F_c	Conversion factor to account for housing effects	–
$\Delta\lambda$	Spectral resolution	[nm]
w_{bf}	Width of bulb focused into monochromator entrance slit	[mm]
h_{bf}	Height of bulb focused into monochromator entrance slit	[mm]
F_{br}	Conversion factor to account for back reflector	–
w_{sf}	Width of slit focused into optical fibre input	[mm]
h_{sf}	Height of slit focused into optical fibre input	[mm]
n	Refractive index of the medium light travels through	–
θ_h	Half-angle swept by entrance cone of optical fibre	[°]
η_c	Observation collimator efficiency	–
θ_{dev}	Collimation deviation	[°]
r_{pol}	Radius of the polarizer	[mm]
r_{beam}	Radius of collimated beam at polarizer position	[mm]
T_c	Collimator transmittance	–
v_d	Abbe number, material dispersion index	–
n_c	Center wavelength for Abbe number	[nm]
n_l	Longest wavelength for Abbe number	[nm]
n_s	Shortest wavelength for Abbe number	[nm]

Signal-to-Noise Ratio

Symbol	Definition	Units
S_T	Total signal	$[e^-]$
t_{int}	Integration time	[s]
ϵ	Transmission through aperture stop, equal to vignetting	–
f_{sys}	Instrument f-number	–
h	Planck's constant	[Js]
c	Speed of light	[m/s]
I_{source}	Total irradiance from light source	[W/nm]
T_{tot}	Total instrument transmittance	–
λ	Wavelength at which signal is being measured	[nm]
R_{source}	Radiance of the light source	[Wsr^{-1}m^{-2}nm^{-1}]
k_B	Boltzmann constant	[J/K]
$I_{source,th}$	Infrared irradiance of light source from thermal emissions	[mWm^{-2}nm^{-1}]
$R_{source,th}$	Infrared radiance of light source from thermal emissions	[Wsr^{-1}m^{-2}nm^{-1}]
T	Bulb temperature	[K]
η	Detector quantum efficiency	–
R	Detector photosensitivity	[A/W]
e	Elementary charge constant	[C]
D^*	Detector specific detectivity	[cmHz$^{1/2}$W^{-1}]
i_n	Input noise current	[A]
A_d	Detector area	[m^2]
Δf	Detector frequency bandwidth	[Hz]
n_S	Shot noise	$[e^-]$
n_D	Dark noise	$[e^-]$
I_d	Dark current	[A]
n_J	Johnson (thermal) noise	$[e^-]$
T_d	Absolute detector temperature	[K]
R_{diode}	Detector shunt resistance	[Ω]
N_T	Total noise	$[e^-]$

Spectral Resolution and Spot Size Analysis

Symbol	Definition	Units
χ	Incident angle of light on the grating	[°]
k	Diffraction grating order	–
f_m	Focal length of monochromator	[mm]
N_{lines}	Grating line density	[lines/mm]
θ	Goniometer arm angle	[°]
a_0	Magnitude in x-axis	–
b_0	Magnitude in y-axis	–
c_0	Magnitude in z-axis	–
d_0	Height in xz-plane	[mm]
p	Parametrization variable	–

Polarimetric Accuracy

Symbol	Definition	Units
I	Signal intensity read at the detector	–
I_0	Initial signal intensity from the light source	–
α_0	First intensity Fourier coefficient	–
α_1	Second intensity Fourier coefficient	–
α_2	Third intensity Fourier coefficient	–
δ	Retardance	[rad.]
A	Analyzer angle	[°]
P	Polarizer angle	[°]
M	Modulator angle	[°]
F	Retardance amplitude	[°]
ω	Photoelastic modulator frequency	[kHz]
t	Timestep	[s]
J_α	Bessel function, with α as the order	–
$V_{control}$	Input control voltage to the PEM controller	[V]
ω_{ref}	Lock-in amplifier reference frequency	[Hz]
ω_{input}	Lock-in amplifier input frequency	[Hz]
X	Magnitude x-component, α_1 estimate	–
Y	Magnitude y-component, α_2 estimate	–
R	Lock-in amplifier magnitude output	–
θ_R	Lock-in amplifier phase output	[rad.]
ω_c	Lock-in amplifier cutoff frequency	[Hz]
τ	Time constant	[ms]
I_x	Algebraic intensity term from modulation at ω	–
I_y	Algebraic intensity term from modulation at 2ω	–
I_{DC}	Direct current intensity, α_0 estimate	–
I_ω	Lock-in amplifier intensity at $\omega = 42$ kHz	–
$I_{2\omega}$	Lock-in amplifier intensity at $2\omega = 84$ kHz	–
δ_0	Static retardation	[rad.]
N	Algebraic term equal to $\cos(2\Psi)$	–
S	Algebraic term equal to $\sin(2\Psi)\sin(\Delta)$	–
C	Algebraic term equal to $\sin(2\Psi)\cos(\Delta)$	–
κ	Extinction ratio	–
$\boldsymbol{L_{in}}$	Jones vector for input light polarization	–
$\boldsymbol{L_{out}}$	Jones vector for output light polarization	–
i	Imaginary number	–
$\boldsymbol{A}$	Jones matrix for analyzer	–
$\boldsymbol{R}$	Rotation matrix for polarimetric components	–
$\boldsymbol{S}$	Jones matrix for sample	–
$\boldsymbol{M}$	Jones matrix for photoelastic modulator	–
$\boldsymbol{P}$	Jones matrix for polarizer	–

Calibration

Symbol	Definition	Units
d	Diffraction grating groove spacing	[mm]
θ_k	Diffraction angle	[°]
V_{DC}	DC Voltage from lock-in amplifier	[V]
η_{AC}	Attenuation of AC relative to DC from detector	–
α	First intensity Fourier coefficient for rotating analyzer configuration	–
β	Second intensity Fourier coefficient for rotating analyzer configuration	–
ω_A	Rotation frequency for rotating analyzer design	[Hz]
α'	Experimental first Fourier coefficient	–
β'	Experimental second Fourier coefficient	–
A_s	Deviation of analyzer angle from the plane of incidence	[°]
P_s	Deviation of polarizer angle from the plane of incidence	[°]
$R(P)$	Residual function for absolute angle calibration	–

1

Introduction

1.1. Background

1.1.1. Planetary Surfaces

Gaining a deeper understanding of the Solar System is a major goal of the planetary sciences community, and studying its celestial bodies can reveal information about its largest mysteries. In particular, the surface of a planetary body can reveal key information about the formation, evolution, and internal structure of the body [1]. A planetary surface refers to the solid or liquid outer boundary of an astronomical body. The accessibility of planetary surfaces make them useful targets for missions that aim to learn more about these celestial objects as a whole, and have therefore been a target of focused research for many decades. The first planetary surface study involved the lunar surface in 1959 [2], and since then extensive studies have been carried out across the solar system involving remote sensing probes [3], robotic sample returns [4], and even human contact [5].

The celestial bodies in the Solar System vary in composition and structure, making widespread studies of planetary surfaces extremely valuable. As research continues on these surfaces, comparisons and trends can be established using known surfaces. This can help scientists draw conclusions about major questions such as the potential for life outside of Earth, the formation and evolution of the Solar System, and defining suitable candidates for potential human expansion [1].

While valuable information can be gained from all planetary surfaces, knowledge about asteroids, comets, and icy moons remains limited, and potentially contains insights about these major mysteries. Asteroids are small bodies made of rock or metal that orbit the sun. Comets are also small bodies that orbit the sun, but are primarily made of dust and ice which gives them a distinctive tail. Finally, the icy moons relevant to this work are bodies that orbit around planets in the Solar System, with a surface composed of mainly ice. Asteroids and comets remain largely unchanged since the formation of the Solar System, and thus can serve as a time capsule of the state of the universe at that time. Asteroids are also being investigated for resource extraction, and more information about their surfaces can make landing and extraction more effective [6]. Icy moons are being studied because they contain some of the ingredients necessary for harbouring life, such as water and an internal energy source. For example, Europa is thought to have a subsurface ocean which has the potential to support life [7]. Other examples of planetary surface studies include the investigation of signs of vestige water flows on Mars [8], and mapping the lunar surface for the purposes of future base development [9].

A widespread study of planetary surface composition and structure can therefore help to establish criteria for harbouring life, formulate theories about formation and evolution, and determine candidates for civilization beyond Earth.

1.1.2. Spectropolarimetry

Measuring reflected light has long been a method of determining key properties of surfaces [10–13]. It is non-destructive, and can provide details about a surface's composition, structure, and other physical properties. The composition is defined by the materials that make up a surface and their abundances, while the structure refers to the shape of a surface or any noticeable features about its texture. There are multiple ways to measure this reflected light, including spectral and polarimetric analysis, which each reveal a new dimension of information.

When light comes into contact with particles making up a surface, these particles can scatter or absorb the incident light. Scattered light is due to partial reflection and refraction of light as it hits the particle. When light is absorbed by a molecule, the molecule gets excited to a higher energy state through a charge transfer or a vibrational mode. These absorption bands would be visible when measuring the light reflected off of the surface [14]. These spectral components of light can be measured with a specific type of instrument called a spectrometer.

Spectrometry involves separating light into its composite wavelengths, in order to determine the spectral content. This can provide clues about wavelengths that may be absorbed or reflected by a surface. This is also helpful for determining the composition of surfaces or atmospheres.

There are a few ways that spectrometers can split light into its component wavelengths for measurement. Prisms can be used, which deflect light of different wavelengths at different angles due to the change in the prism's index of refraction with wavelength. The index of refraction determines how much incoming light is bent when passing through a material [15]. Gratings could also be used in order to diffract light into its composite wavelengths. Other methods can target specific spectra of light through selective filtering or optical manipulation. When light is split into these wavelengths through any of these methods, it can be directed to a detector to measure the intensity of light inside of that spectral range [14].

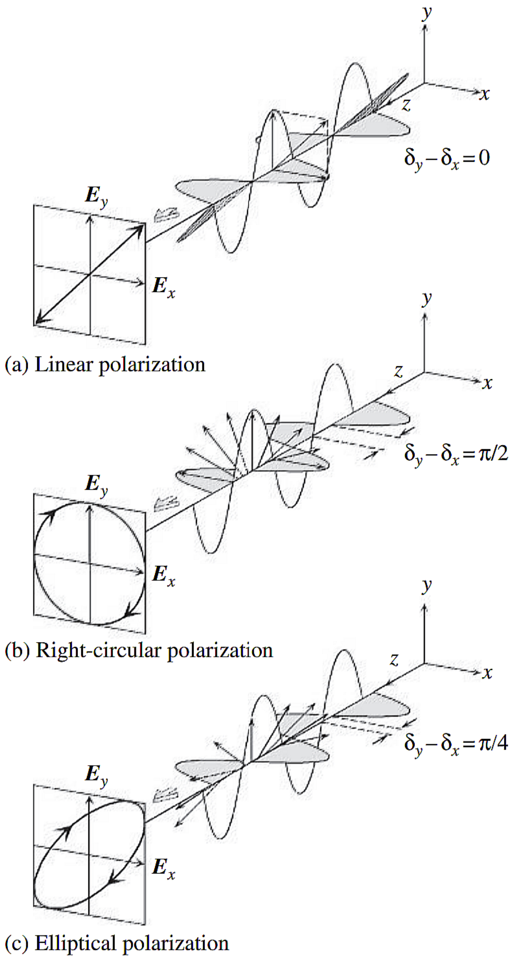

(a) Linear polarization

(b) Right-circular polarization

(c) Elliptical polarization

Figure 1.1: Typical polarization states. The terms E_x and E_y represent the density of the electric field in the defined x and y axes. Definitions for δ_x and δ_y terms are provided in Section 1.1.4. Figure from Fujiwara [16].

Aside from the spectral content of light, its polarization state can also provide important clues about the composition and physical parameters of a surface. The polarization state of light refers to the orientation of its transverse electric field vector. Light from the sun has no preferred orientation on average, and is referred to as unpolarized. When light has a preference towards a certain orientation when averaged over a time frame, that light can be considered partially or fully polarized. There are a few key orientations that are important for measurements of reflected light, as shown in Figure 1.1. Linear polarization refers to the orientation of light along a single plane. In the context of reflectance, this can be completely in a plane parallel or perpendicular to the plane of incidence, often referred to as p- and s-polarization respectively, or it can contain a combination of both planes. When some phase change is induced between the components of incoming light, this light is considered elliptically polarized. When this phase change is 90°, the light is circularly polarized. These polarization states can be created by the asymmetry of materials that the light reflects off of or refracts through. For example, if one axis of a material has a different index of refraction than the other axis due to a specific structural configuration, light will travel at different speeds in the two orientations. This is a process called phase-shifting or retardance [17].

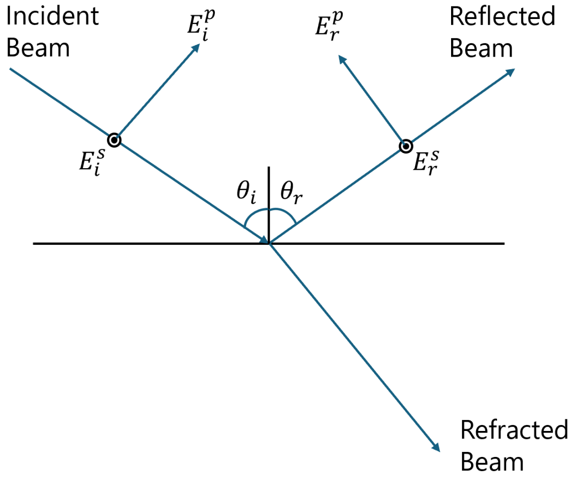

Figure 1.2: Linear polarization after reflection. The p and s superscripts correspond to p- and s-polarizations. The i and r subscripts correspond to incidence and reflectance. The s-polarized beams are pointing out of the page, which are shown by the black and white dots. Figure adapted from Fujiwara [16].

When light reflects off a planetary surface, it will generally undergo a polarization change which depends on the angle of incidence and the roughness of the surface [17]. However, some molecules, such as birefringent materials and chiral molecules, can impart circular polarization changes as well. Figure 1.2 shows how polarization can change in magnitude after reflection off of a surface. On some surfaces such as ices, part of this light gets refracted. This decreases the intensity of any reflected light being measured. Figure 1.3 shows the effects of a chiral molecule on the handedness of the circular polarization imparted on incoming light. The two chiral molecules are mirror images of each other, and thus they produce circular polarizations of the opposite handedness.

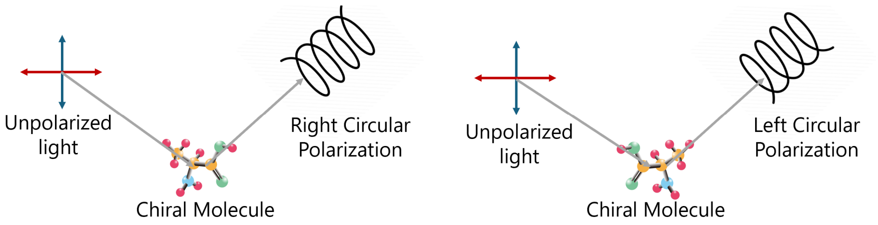

Figure 1.3: Circular polarization after reflection. Figure adapted from Sequin [18].

These polarization states can be measured using various optical elements. To measure linear polarization, a linear polarizer will only let light of a specific polarization pass through. For shifting the phase of light, a waveplate can be used. A quarter waveplate, for instance, will bring the two components of light out of phase by 90°, which can convert linear polarization into circular polarization, and vice versa. The use of these optical instruments in a clever arrangement will change the intensity incident on the detector, and allow one to deduce the polarization state of the light. Measuring the polarization of light through an assortment of polarizers, waveplates, and other components is a process known as polarimetry [17].

Combining the insights gained from polarimetric measurements and spectroscopic measurements can provide even more useful information about the material being observed. Some materials exhibit different polarization behaviours as a function of the wavelength being measured, and some materials can exhibit different spectral characteristics as a result of the polarization of incoming light [19]. This allows for more detailed descriptions of composition, which can help for identifying biosignatures, classifying asteroids, and determining planetary origins [20]. Some key species of interest for these planetary bodies include cyanide (CN), pyroxenes, olivines, water ice, carbon dioxide (CO_2) ice, hydroxides, and aromatic compounds. Each of these signatures will be fully investigated in Section 2.1.

This work seeks to combine the insights gained from polarimetric and spectroscopic measurements to study planetary surfaces, in order to gain a comprehensive overview of their composition and structure. Surface studies with resolved images have been extensively covered by other ground-based and space-based missions [21], and thus will not be considered in this work.

1.1.3. Spectropolarimetric Data

As the combination of spectral and polarimetric data is central to this work, it is important to describe how this data is represented. Starting with polarimetric data, the Stokes vector is a commonly used format for describing polarization states [16]. It is a 4-element vector defined as follows:

$$\begin{bmatrix} S_0 \\ S_1 \\ S_2 \\ S_3 \end{bmatrix} = \begin{bmatrix} I_{\parallel} + I_{\perp} \\ I_{\parallel} - I_{\perp} \\ I_{+45^\circ} - I_{-45^\circ} \\ I_R - I_L \end{bmatrix} \tag{1.1}$$

Here, $I_{\parallel}$ is the intensity of the electric field vector parallel to the plane of incidence of the beam, $I_{\perp}$ is the intensity of the electric field vector perpendicular to the plane of incidence of the beam, I_{+45° and I_{-45° are the intensities at 45° and −45°, respectively, from the plane of incidence, and I_R and I_L refer respectively to the intensity of right- and left-handed circular polarization. Figure 1.4 shows a visual representation of these Stokes parameters. The plane of incidence refers to the plane containing both the incident and reflected beams of light. Figure 1.2 shows the components of light involved in the plane of incidence, with p-polarized light oscillating in this plane and s-polarized light oscillating outside of this plane.

By dividing components by the total intensity, the polarization can be expressed as a percentage, which can be useful for representing accuracy and measurement error. For linear polarization, this is called the Degree of Linear Polarization (DoLP):

$$DoLP = \frac{\sqrt{(S_1)^2 + (S_2)^2}}{S_0} \quad (\%) \tag{1.2}$$

For circular polarization, an analogous parameter called the Degree of Circular Polarization (DoCP) can be used:

$$DoCP = \frac{S_3}{S_0} \quad (\%) \tag{1.3}$$

The Angle of Linear Polarization (AoLP) is another parameter that provides the angle of the linearly polarized

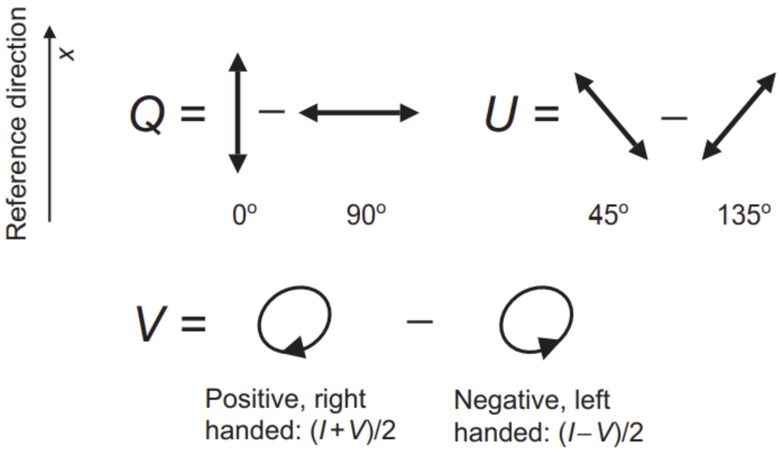

Figure 1.4: Visual representation of Stokes parameters. Figure from Bagnulo [22].

light reflecting off of the sample. This can be helpful in situations where the orientation of light may quickly change, such as near the inversion angle of an asteroid [23]:

$$AoLP = \frac{1}{2}\tan^{-1}\left(\frac{S_2}{S_1}\right) + \theta_0 \tag{1.4}$$

Here, $\theta_0 = 0$ if $S_1 > 0$ and $S_2 \geq 0$, $\theta_0 = \pi$ if $S_1 > 0$ and $S_2 \leq 0$, and $\theta_0 = \pi/2$ if $S_1 \leq 0$.

Each component of the Stokes vector therefore provides another piece of information about the orientation of light, and measuring all four Stokes parameters will provide a full description of the polarization state of light. When these parameters are measured at each wavelength within the spectral range of the instrument, they can be combined to form spectropolarimetric data.

1.1.4. Spectroscopic Ellipsometry

A spectroscopic ellipsometer is an instrument that can be used to measure spectropolarimetric data of surfaces with extremely high accuracy. Figure 1.5 shows an example of an ellipsometric setup. All ellipsometer configurations measure the change in polarization as a result of an input light source reflecting off of a sample. There are many configurations of this architecture, for purposes that will be discussed in Chapter 4. However, Figure 1.5 shows the most basic depiction that will generate useful spectropolarimetric data.

Spectroscopic ellipsometers can be very broadly broken down into an illumination arm which provides the input light to the sample, and an observation arm which collects some of the light reflected from the sample. More specifically, all ellipsometers consist of at least a light source, a detector, two polarizers, and a sample. The light source sends in either white light over a desired spectral range, or one that has already been split into a component wavelength, also referred to as monochromatic light. The first polarizer configures the polarization of light that arrives at the sample, while the second polarizer, often referred to as the analyzer, is responsible for measuring the change in polarization induced by the sample. This setup is only capable of measuring the linear polarization change induced by the sample. In some contexts, which will be discussed further in Chapter 2, the circular polarization change is also of interest. For this, an instrument called a compensator is inserted into the ellipsometer. This compensator is any retarder capable of modifying its retardance. A detector that is able to measure the intensity of the light across the desired spectral range is the final component in the spectroscopic ellipsometer system.

In order to determine the polarization change induced by the sample, it is important that one of the polarimetric components modulates the polarization state. This means that the polarization state should be changing with time. If the detector only measures a single orientation, it is difficult to reconstruct the entire polarization

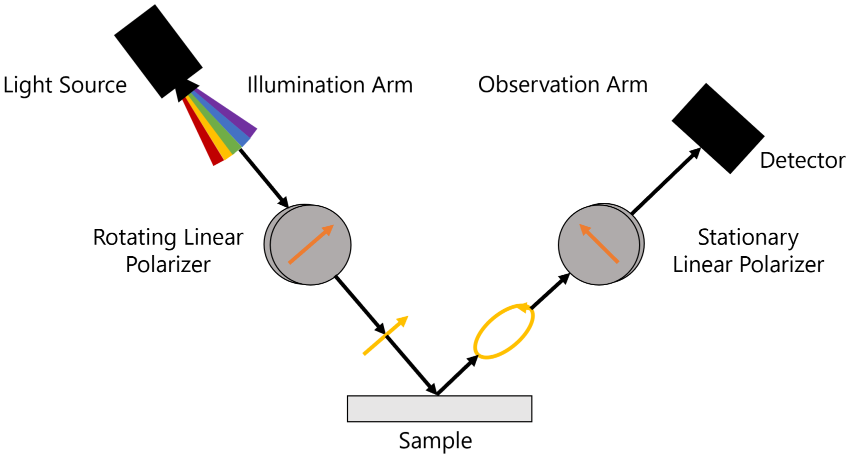

Figure 1.5: Diagram showing the components of a basic ellipsometer setup.

state as only a component of it has been transmitted. It is also possible that the components themselves have had an effect on the polarization state, and measurements at various orientations help to reduce this error considerably [16]. Modulation is typically achieved through the continuous rotation of one of the polarimetric components, but can also be performed through other methods. The specific components and their use cases will be discussed in more detail in Chapter 4.

Typically, an ellipsometer is used for characterizing thin films. It is especially useful for measuring the complex dielectric function ϵ for integrated circuit films and substrates such as silicon dioxide [16]. This provides a measure of its electrical capabilities as well as the surface roughness, which can be critical in validating the performance of an integrated circuit [24]. It is also used heavily in the analysis of glass, gold, and polymer surfaces [24].

While the Stokes vector described in Section 1.1.3 is useful for describing the full polarization state of light, ellipsometers typically output data in the form $\{\Psi, \Delta\}$. This is a convenient coordinate system for describing elliptically polarized light. Here, Ψ is an angle representing the amplitude ratio, and Δ represents the phase difference between the two components of incoming light. Figure 1.6 visually represents these two terms. Written mathematically, these coordinates can be expressed as the following:

$$\tan(\Psi) = \frac{E_{\|,0}}{E_{\perp,0}} \tag{1.5}$$

$$\Delta = \delta_{\|} - \delta_{\perp} \tag{1.6}$$

Here, $E_{\|,0}$ and $E_{\perp,0}$ (also referred to as E_x and E_y) correspond to the amplitudes of the parallel and perpendicular components of the electric field vector, while $\delta_{\|}$ and $\delta_{\perp}$ (also referred to as δ_x and δ_y) correspond to the phase of these two components.

The primary goal of a spectroscopic ellipsometer is to measure the Ψ and Δ values for incoming light with sufficient sensitivity over a desired spectral range. This polarimetric data is coupled with spectral data by measuring the Ψ and Δ values with changing wavelength inputs. An alternative method of measuring spectropolarimetric data is to generate intensity plots over a spectrum at a few desired polarization states. However, since high-sensitivity polarimetric data is less prevalent for planetary surfaces than spectroscopic data, the wavelength of light will be an independent variable, while Ψ and Δ will be corresponding dependent variables in this work.

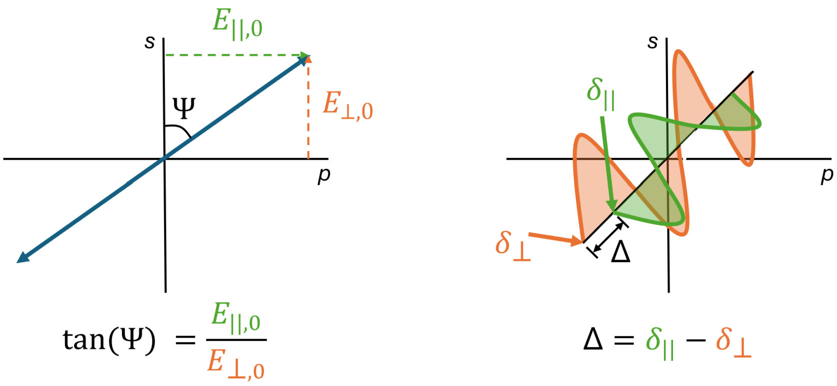

Figure 1.6: Visual representation of Ψ (left) and Δ (right).

1.1.5. Bidirectional Reflectance

Bidirectional reflectance defines how light reflects off a surface such as a planetary analogue. It is typically described by the bidirectional reflectance distribution function (BRDF), which compares the emitted power to the incident power in a given orientation of incoming and outgoing light directions.

For smooth surfaces, the most dominant form of reflection is specular reflection. This reflection is similar to that of a mirror, where the angle of reflectance is equal to the angle of incidence. However, many planetary surfaces are not smooth, and consist of powders or small rocks that can impact the reflectance properties. When light interacts with a rough surface, it gets scattered due to the random orientation of the grains. The direction and degree of this scattering depends on both the orientation and brightness of the sample surface. Darker samples will have fewer reflections of light between the grains, and shadows can also limit the amount of light reflected [23].

The reflectance of light from the surface can be split into two lobes, one in the specular direction, and one in the opposition direction. When light scatters in the specular direction, it is referred to as forward-scattering. Light scattering in the opposition direction is referred to as back-scattering. Figure 1.7 shows the geometry for bidirectional reflectance measurements.

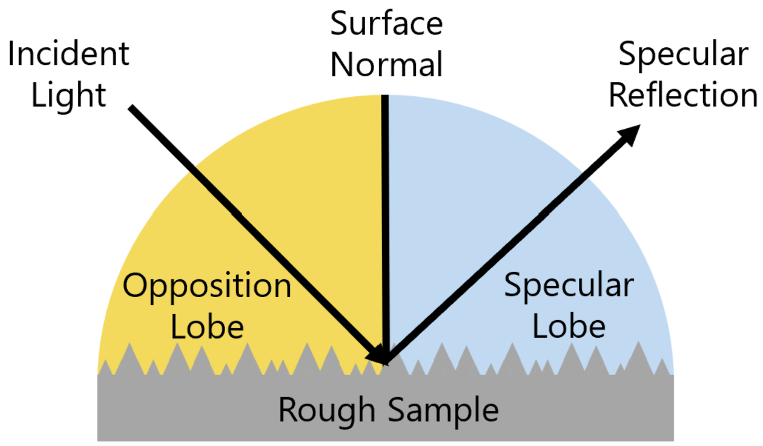

Figure 1.7: Geometry definitions for bidirectional reflectance measurements.

When there is no angle between the incidence and reflectance of light, this is referred to as opposition, and is a special case where the reflected power can increase. Measurements at these conditions can therefore provide an additional piece of information about the surface which can help in identification and classification, and should also be considered.

Measuring the bidirectional reflectance function in these four conditions (specular, forward-scattering, back-scattering, and opposition) helps to provide an overview of the surface from a structural and compositional perspective, which can also provide clues about events that could have influenced the surface structure in the past.

1.1.6. Goniometry

Ellipsometers can also have goniometric capabilities, meaning that both the arms that are visible in Figure 1.5 can be fully controlled and moved. For this reason, some spectroscopic ellipsometers can also be referred to as spectropolarimetric goniometers. This allows for a change in the angle of incidence and emergence, which can correspond to a different polarization change. The ellipsometer can therefore address some of the bidirectional reflectance studies outlined in Section 1.1.5. It also mimics a changing phase angle that is experienced when an observer, the sun, and a planetary body are moving through space. Figure 1.8 defines the typical nomenclature for reflectance studies involving a goniometer.

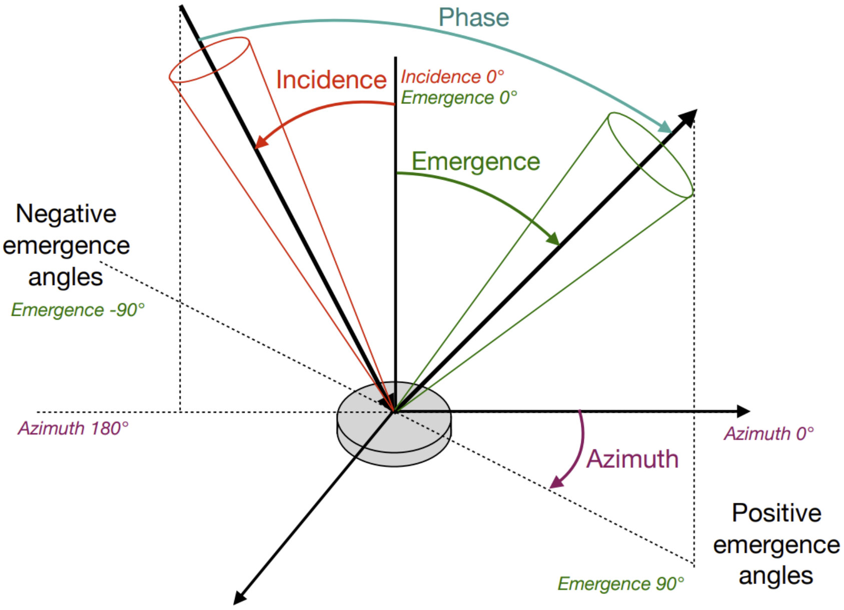

Figure 1.8: Definition of angles for the goniometric setup. Figure from [23].

Among commercially available ellipsometers, goniometry capabilities remain limited. Most are designed to operate at the Brewster angle, which maximizes the reflection of polarized light in order to achieve the best possible signal-to-noise ratio [16]. While the arms of the spectroscopic ellipsometer are designed to move for this purpose, they are often not designed to move independently. Typical ellipsometry setups only measure specular reflection properties. When the arms can move independently, the effects of scattering reflectance can also be measured, which can be useful for the study of planetary surfaces [23]. This research gap will be further explored in Section 2.3.

Ground-based polarimeters are typically only able to observe planetary bodies at small phase angles due to the relative position of Earth, the Sun, and the body of interest [25]. However, this instrument will allow measurements at a wide range of phase angles to be performed, which is particularly useful for asteroid classification due to the unique relationship between polarization and phase angle for each asteroid [25]. It can also serve as a valuable proof of concept for future space instruments that can image from similar points of view.

1.1.7. Spectroscopic Ellipsometry for Planetary Sciences

Overall a spectroscopic ellipsometer is a suitable instrument for high-accuracy spectropolarimetric measurements of planetary surfaces. However, some limitations of commercially available ellipsometers, including independently controllable arms, wide spectral range, and sample orientation, will necessitate the custom design of a spectroscopic ellipsometer. The reasoning behind this decision is further explained in Section 2.3. The design of the instrument and associated experimentation is meant to provide a valuable archive of spectropolarimetric properties that can be used to detect clues about biosignatures, as well as the origin of planetary bodies.

According to studies of the current literature, the applications of ellipsometry to planetary surfaces remain limited. Therefore, the samples in the context of this thesis will be geological or icy samples which are representative of an asteroid, comet, or icy moon. This instrument could however be used in a wide variety of applications, and is thus not limited to asteroids, comets, and icy moons.

The spectroscopic ellipsometer is meant to perform in the laboratory, as it provides its own light source and detection methods. Not only can this laboratory data be used as an archive for future space missions, but the ellipsometric principles can be extended to spacecraft in future applications, by replacing the illumination arm of the instrument with sunlight.

1.2. Research Questions

In a broad sense, this thesis seeks to contribute to some key questions regarding the characterization of planetary surfaces. Given the limits in scope for a Master's Thesis, these major scientific questions will not be answered in this work. However, the work done in this thesis will contribute towards answering these guiding questions in future work:

1. How does polarization change with the composition of a planetary surface?
2. How does polarization change as a function of the viewing geometry?
3. How does polarization change with the structure of the planetary surface?

Due to its high accuracy and reliability for laboratory-based experimentation, the spectroscopic ellipsometer was chosen as the main instrument to address these scientific research questions. However, due to the limited applications of spectroscopic ellipsometry to planetary surfaces as described further in Section 2.3, commercially available models are not suitable for these applications, necessitating the design and build of a custom spectroscopic ellipsometer.

As a result, this thesis seeks to address the main research question: ***To what extent can spectroscopic ellipsometry be used for the compositional and structural analysis of planetary surfaces?***

It does this by exploring the following sub-questions in depth through the design, simulation, and calibration of a spectroscopic ellipsometer:

1. What are the design drivers of a spectroscopic ellipsometer intended for planetary surface studies?
2. How can sufficient goniometric, spectroscopic, and polarimetric performance of the instrument be validated?
3. How can a spectroscopic ellipsometer be calibrated to take effective measurements of planetary surfaces?

While the scientific questions remain the driving motivation behind the design of the ellipsometer, this research question and sub-questions are targeted more towards the design, simulation, and calibration of the instrument. Addressing these questions will help determine whether the instrument is capable of answering the guiding scientific questions in future work.

2

Scientific Goals

2.1. Targets of Interest

Spectropolarimetry is becoming more common as scientists wish to harness the complete range of information that light offers in order to better characterize materials of interest. This section will outline some of the key targets that spectropolarimetry can help to analyze, particularly within the confines of spectroscopic ellipsometry.

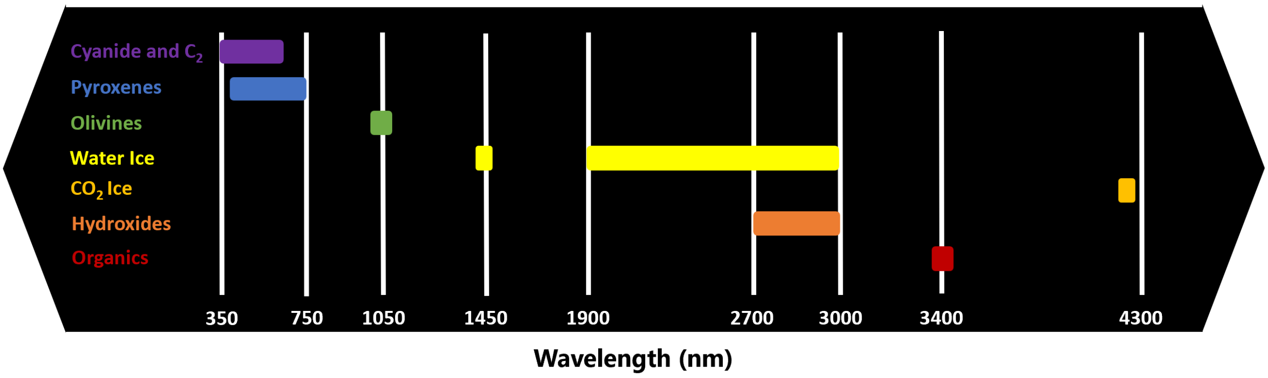

Figure 2.1: Spectral coverage of the proposed spectroscopic ellipsometer and associated targets of interest [26–31].

2.1.1. Spectropolarimetric Database

Perhaps the most immediate application of the spectroscopic ellipsometer instrument is for the general study of polarization changes around key absorption spectra shown in Figure 2.1. Measurements of planetary analogues with this instrument will allow for a deeper understanding of the effects on polarization at specific spectral points of interest, which can help better identify the components of complex features as well as overall surface composition. In order to measure all the spectral targets, the instrument will require a spectral range of 300 – 4500 nm.

For all planetary surfaces discussed in this section, spectropolarimetric data will also enable the instrument to gather details about the structure of a planetary surface, critical for understanding potential causes of surface features such as water flows and winds, or sub-surface events such as volcanism.

The polarization change, represented with $\{\Psi, \Delta\}$ and the Stokes parameters, will be recorded for each specimen at the key spectral locations highlighted in Figure 2.1. This will help facilitate future planetary sciences research, as well as highlight potential areas for future study.

2.1.2. Asteroid Classification

The linear polarization of light reflected off an asteroid can be recorded as a function of the phase angle, which is the angle between the observer, the sun, and the asteroid. This produces what is called a phase-polarization curve. The angle at which the degree of linear polarization is zero, meaning the contributions of parallel and perpendicular polarization are equal, is called the inversion angle. When the phase angle is less than the inversion angle, the polarization is more perpendicular to the surface than parallel, and vice versa when the phase angle is greater than the inversion angle. The inversion angle is a method of classifying asteroids, as asteroids with similar inversion angles can have similar compositional properties [25]. These phase angles are typically small for ground-based measurements (< 30° [25]), but larger angles can also be useful. At larger phase angles, linear polarization can change up to 1% between the two extremes of the visible spectrum [32]. In this instrument, the sun would be replaced by the illumination arm, meaning a wide range of phase angles can be achieved. More data about various phase angles and surface types will help to develop the theory behind the polarization of light scattered by rough surfaces. These polarization properties can also help to distinguish more about an asteroid's composition and texture than the spectroscopic properties alone [25]. A method of reliably classifying asteroids in the lab would be invaluable to the taxonomy process.

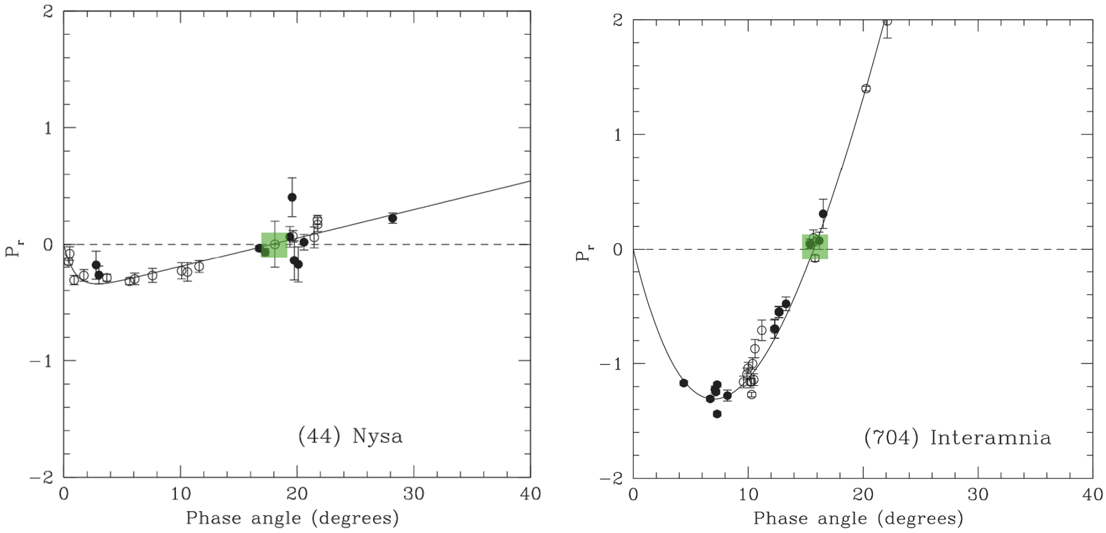

Figure 2.2: Phase-polarization curve for asteroids 44 Nysa and 704 Interamnia. The inversion angles are highlighted in green. Figure from Cellino [33].

Figure 2.2 shows the phase-polarization curve for two asteroids which have different surface properties [33]. The respective inversion angles are highlighted in green. Negative values of P_r in the figure refer to polarizations that are more perpendicular to the surface than parallel, with positive values representing the opposite. These asteroids have slightly different inversion angles, but the shape of their phase-polarization curves are very different, as the asteroid 704 Interamnia (shown on the right) has a much lower minimum. This comparison shows that both the shape of the phase-polarization curve and the inversion angle location can be important for identifying and classifying asteroids, necessitating polarimetric measurements over a wide range of phase angles.

Figure 2.3 shows a typical spectrum for an asteroid. The relevant spectral bands for asteroid classification include the pyroxene band between 375 − 750 nm [26], olivines at 1050 nm [27], hydroxides between 2700 − 3000 nm [28], and organics at 3400 nm [29]. Pyroxenes are a group of silicate materials found in igneous rocks. Measuring the spectral content of pyroxenes, such as those with Fe^{2+} and Fe^{3+}, can reveal the genesis and history of meteorites and upper planetary crusts [26], which polarimetry can enhance by highlighting details about composition and structure [32]. Olivines are rock-forming minerals found on Earth and in asteroids. They are often indicative of a low-silica environment which can help in the classification of asteroids [27]. Hydroxides often indicate asteroidal water, which is an excellent identifying feature for asteroids [28], and can also be a useful indicator of potential resource mining activities. They can also be found in hydrated minerals, called phyllosilicates, which result from the interaction between olivines and water [34]. An example of this is the magnesium hydroxide band, a sharp feature that can be found at 2700 nm [35]. Water ice, which can be found on asteroids, can often be found with organic compounds such as aromatics [29], which blur the line between comets and asteroids and require a deeper investigation. There are also carbonates and ammonium salts with complex spectra between 3200 and 3600 nm [36]. Measuring spectropolarimetric data around these spectral targets could help to better characterize these complicated bands.

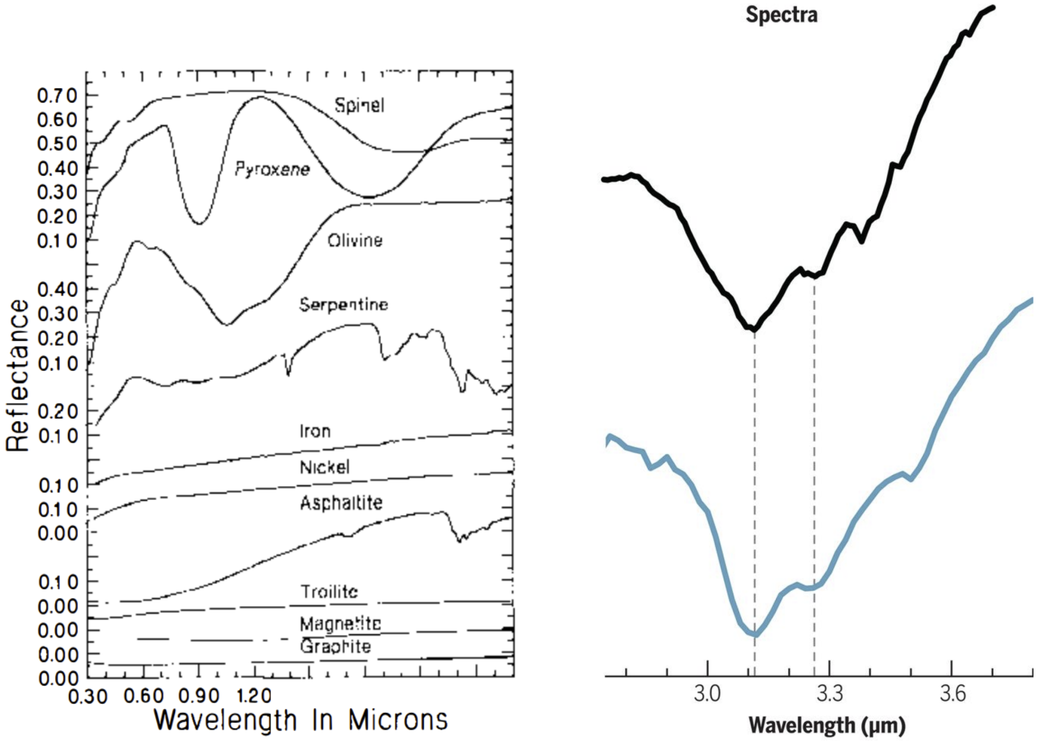

(a) Spectrum from 300 – 2700 nm. Figure from [37].

(b) Spectrum from 2700 – 3800 nm. Figure from [36].

Figure 2.3: Typical asteroid bidirectional reflectance spectrum.

2.1.3. Comet Spectropolarimetry

Comets are small, icy and dusty bodies inside the solar system that warm and begin to outgas as they pass close to the Sun. This outgassing creates an unstable tail of gas and dust, forming a coma. These bodies are of general interest due to their potential for uncovering mysteries about the Solar System's origin, as they remain relatively unchanged in structure and composition since their inception [38].

The main advantage of spectropolarimetry for observing comets is the evaluation of intrinsic polarization of the comet without molecular line contamination of the tail. For comets, the phase-polarization curves at small phase angles are of particular interest. The molecular emission lines from the gases surrounding the comet can influence broadband polarization measurements. When these polarization measurements are combined with spectroscopy, regions of the spectrum can be identified where there are no emission lines, in order to pinpoint the polarization effects of the comet's body itself [39]. Both linear and circular polarization measurements are useful for learning more about comet structures. Similarly to asteroids, comets also display different polarization behaviour as a function of wavelength [40]. Circular polarization is particularly understudied, and could have a noticeable role in the polarization characteristics of the comet [40].

A lot of the spectral bands of interest for comets are similar to those of asteroids [41, 42], however there are a few key additions that help from a spectropolarimetry perspective. For example, C_2 and CN bands produced by gas emissions at the comet tail can contaminate spectropolarimetric data [40], and exist between 350 nm and 620 nm [31]. Comets can also hold macro-organic molecules due to their water content, which can be detectable in the infrared range as well [43].

2.1.4. Icy Surfaces

Water ice visible between 1900 nm and 3000 nm [30] is another interesting potential target for the spectroscopic ellipsometer. Figure 2.4 shows some specific bands of interest for water ice. The presence of water ice on icy moons such as Europa and Enceladus is a strong indicator of the potential presence of life on these moons, and thus a more thorough study into the composition of these water ices can help to more easily identify other planetary bodies that may also have potential biosignatures. Polarimetry can also help to distinguish between degrees of crystallinity within icy structures. This ice structure can change with temperature, meaning this can have an effect on polarization as well [19].

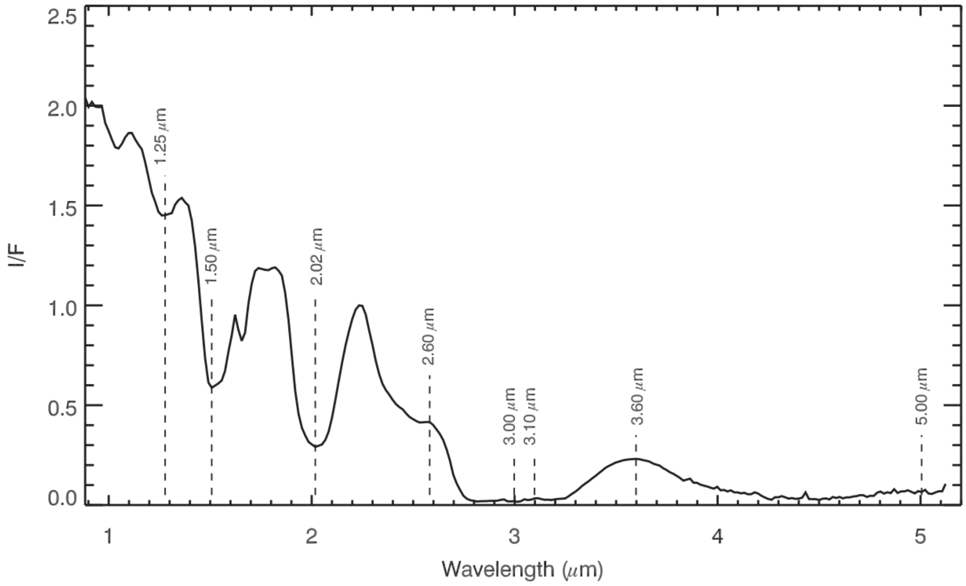

Figure 2.4: Spectrum for water ice, with relevant bands labelled. Figure from [30].

The major difficulty in studying ice composition using the proposed ellipsometry setup is the fidelity of the samples. The roughness of icy surfaces can provide clues about areas where subsurface oceans may be welling up, while the composition of the ice can indicate biosignatures [44]. However, the samples are meant to be small, which reduces their effectiveness at recognizing rough areas. Additionally, as temperature can have an effect on the polarization behaviour of icy moon surfaces, maintaining constant sample temperature will be another challenge for this instrument.

Carbon dioxide (CO_2) ice is also a potential target, with a primary absorption band at 4.26 μm [45]. There is evidence of an interesting polarimetric-spectral interdependence for CO_2 ice in this region from a study involving a changing concentration of CO_2 in an accreted icy surface [19]. By sending light at parallel and perpendicular polarizations and recording the absorption profiles at different temperatures, the authors were able to determine a change in the spectral peaks as a result of the incoming polarization. The proposed ellipsometry setup in this work is designed to measure the polarization as a function of the wavelength, while this study did the inverse by measuring the spectrum at two known polarization states. It could be valuable to see how polarization changes as a function of wavelength for CO_2 ice in order to supplement this research.

2.1.5. Viewing Geometry

The goniometric arms can also be used to measure the effects of viewing geometry on the polarization state of reflected light. Figure 2.5 shows a changing reflectance slope as a function of the incidence angle for the

Mukundpura meteorite [46]. Following from this research, there could be strong variations in polarization with incidence angle as well. This is separate from generating the polarization-phase curves as described in Section 2.1.2. The same phase angle can be measured at different incidence angles by controlling the position of the emergence angle. While there is extensive research on phase-polarization curves, there is limited research showing the specific effect of incidence angle on the polarization.

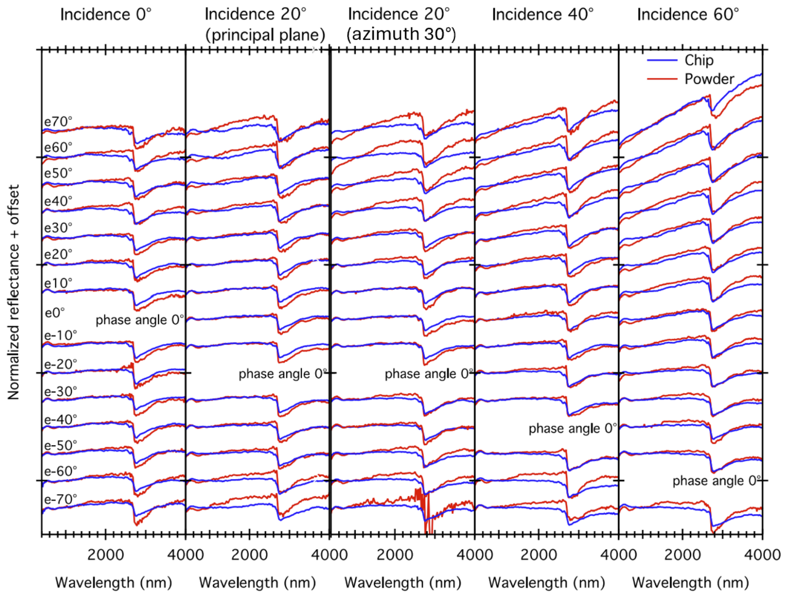

Figure 2.5: Reflectance spectra as a function of changing incidence angle. Figure from [46].

Interesting phenomena can also be observed as the phase angle approaches 0°. At low phase angles, a non-linear increase in reflectance and polarization intensity can be observed, called the opposition effect [47]. This effect includes the cancelling of shadows at small phase angles, as well as the constructive interference of light that backscatters off a surface [48]. This has been studied on planetary analogues at phase angles as small as 0.05° [48, 49], but this was not an extensive study over a wide range of wavelengths or materials. Building on this study can help give more context to phase-polarization curves, allowing for more accurate surface classification. With minimum phase angles of 4 or 5°, some shadowing opposition effects can potentially be detected [23]. While tailored instruments are typically built for more thorough opposition studies, being able to take some opposition measurements would greatly improve the versatility of a spectroscopic ellipsometer for planetary surface studies.

Having this control over the viewing geometry of planetary surface analogues also makes this instrument a strong proof of concept for future spaceborne spectropolarimeters. These instruments will be able to observe planetary bodies at a variety of incidence and phase angles. Ground-based studies are therefore useful for validating that these measurements can be valuable in future applications.

2.1.6. General Materials

The spectroscopic ellipsometer can also be applied to the same terrestrial materials that are commonly studied by this instrument. This includes silicon and polymer films, as well as oxides. Ellipsometers can measure properties such as film thickness and optical constants, which could be useful in verifying the performance of integrated circuits, for example.

Additionally, there are many applications on Earth for spectropolarimetry, including the study of vegetation [50], biomedical tissue diagnostics, and general surface composition identification [20]. While not the primary purpose of this instrument, this does highlight that the versatility of the design makes it applicable to potentially unforeseen research areas.

2.2. Instrument Performance

2.2.1. Polarimetric Accuracy

In order for the instrument to take useful measurements of smaller features on a planetary surface, a minimum accuracy and sensitivity must be defined. Applications of ellipsometry to planetary sciences remain limited, meaning the requirements of ellipsometer performance are largely undefined. However, requirements for polarimetric accuracy are critical at this stage to ensure the instrument is able to make valuable contributions to compositional and structural analysis. There are two potential starting points for reaching polarimetric performance requirements for this instrument.

The first is using typical performance values for ellipsometers. This instrument is meant to be used on a wide variety of surfaces, and therefore should be competitive with commercial ellipsometers. Typical uncertainty values of $\{\Psi, \Delta\}$ for spectroscopic ellipsometers have been reported as $\{0.01°, 0.02°\}$ over the entire spectral range of the instrument [16, 51].

Another method of reaching performance requirements for the instrument is to make the sensitivity better than the minimum linear and circular polarization intensities expected on planetary surfaces. These intensities are typically reported using Stokes parameters, as defined in Section 1.1.3. Linear intensities of polarization for asteroids and comets typically range from 0.2% – 2% [52]. Instruments with potential applications to icy moons, such as SPEX, have linear polarization sensitivities around 0.5% [44]. Circular intensities for some planetary surfaces can be much smaller at around 0.05% [53]. This comes close to reaching the limits of some polarimetric instrumentation [53].

Both sets of requirements could be valuable to guide the ellipsometer design, however the first two regarding typical ellipsometer performance will be adhered to during the design process. The ellipsometer's $\{\Psi, \Delta\}$ performance, when converted to Stokes vectors, results in a possible sensitivity of 0.003% [16], which far exceeds the expected intensities. This makes the typical ellipsometer requirements the more stringent set of requirements, and makes the ellipsometer useful in a wider range of applications. Further refinement to this critical requirement will be considered if signal-to-noise ratio or measurement error prevent the ellipsometer from reaching this level of performance.

2.2.2. Spectral Resolution

The spectroscopic data also requires a minimum resolution to distinguish the features outlined in Section 2.1. This will allow the ellipsometer to perform a more detailed compositional analysis of planetary surfaces. Each of the planetary surface analogues being measured have relatively wide spectral features, meaning an extremely high spectral resolution (for example, < 1 nm) is not required.

As the eventual goal for this instrument is a spacecraft payload, the target spectral resolution should also be competitive with spacecraft that currently investigate asteroids, comets, and icy moons. An example of such a spacecraft is Hayabusa2, housing a near-infrared spectrometer payload with an average spectral resolution of 18 nm in the infrared (1.8 – 3.2 μm) [54]. At a minimum, the spectroscopic ellipsometer will therefore be required to achieve a spectral resolution of at least 20 nm across the entire spectral range. However, light at lower wavelengths has higher energy, meaning a similar signal can be achieved for a smaller resolution. This smaller resolution can help distinguish bands in the visible regime, which is why an additional requirement of at least 5 nm spectral resolution in the ultraviolet and visible regime will also be set. This requirement is comparable to the spectral resolution of the OSIRIS-REx asteroid study mission, which is less than 7.5 nm in the visible region [55]. Similarly to the polarimetric accuracy requirements, signal-to-noise ratio constraints could also impact future revisions of these requirements.

This spectral resolution also gives it similar performance to the SHADOWS instrument [13], making this spectroscopic ellipsometer a direct evolution of that instrument with the addition of polarimetric capabilities.

2.2.3. Goniometric Requirements

The goal of the goniometry function of this instrument is to mimic the orientations that a spacecraft could reach. However, an instrument with arms for illumination and observation will have greater limitations than a spacecraft. The arms of the instrument cannot cross each other, because the components would collide or obscure each other. Therefore, it will be necessary to use samples that are flat and isotropic, meaning they are symmetrical in all directions.

Typical goniometers measure the bidirectional reflectance distribution function (BRDF), as defined in Section 1.1.5. A flat and isotropic sample will result in a symmetric BRDF, meaning the instrument only needs to measure half of the angular range. For this reason, the illumination arm will only be required to move between 0° and 90° in the incidence plane, as defined in Figure 1.8. Note that the incidence angle is positive when in the regime of negative emergence angles. Actual measurements will likely not be possible up to 90° due to the light missing the sample, but this range is reserved for pass-through configurations which could be helpful for calibration of the instrument. The observation arm will be required to capture both negative and positive emergence angles in order to measure both forward-scattering and back-scattering of light from the sample. In order to not collide with the illumination arm, the observation arm should be restricted to a range between -75° and 90°, as defined in Figure 1.8. Due to the symmetrical reflectance of flat, isotropic samples, as well as space restrictions in the laboratory, measurement in the azimuthal plane is not required for this instrument.

A certain degree of goniometric precision is also required to ensure the accuracy of the BRDF. As it is not the primary measurement output of the instrument, a precision of 0.1° was chosen as a similar performance metric to existing goniometers [12].

2.2.4. Signal-to-Noise Ratio

The signal-to-noise ratio is another important metric that describes the quality of a measurement. A minimum signal-to-noise ratio should be established for each spectral target of interest to ensure that the data is sufficiently accurate.

The instruments from Hayabusa2 and OSIRIS-REx both had SNR requirements of greater than 50 [54, 56]. Since they measure surfaces with similar properties to the proposed instrument, a similar SNR requirement was derived for this instrument.

The proposed instrument does not need to consider taking images with spatial resolution, which means it can collect all the signal into a single pixel. However, it also needs to perform polarimetry measurements, which can limit signal-to-noise ratio as the polarizing elements transmit only a single orientation of incoming light. Considering these competing factors in the design of the proposed instrument, the SNR requirement may be updated if design work reveals it cannot be met.

2.3. Existing Instruments

Multiple missions have combined polarimetric and spectroscopic data, however there is still a large niche for the type of measurements that are required to make necessary conclusions about planetary surfaces. Table 2.1 shows a summary of various related instruments, including those with goniometric, ellipsometric, and spectropolarimetric capabilities. This is not an exhaustive list of all instruments with these capabilities, but it displays a sample of the current available capabilities for these types of instruments.

As can be seen in Table 2.1, the traditional ellipsometer setup has largely been used to characterize thin films, and has not yet been used for planetary surface applications. The development of spectroscopic ellipsometry is quite a mature field, with the majority of these breakthroughs taking place before the start of the 21st century. More recently, commercial spectroscopic ellipsometers have also been released with goniometric capabilities. However, their intended applications largely remain the same, and applications to planetary surfaces remain underexplored. These instruments exist in all spectral ranges with both linear and circular

Table 2.1: A summary of past goniometers, ellipsometers, and spectropolarimeters. Green: spectroscopic ellipsometers with goniometric capability. Lavender: spectroscopic ellipsometers without goniometric capability. Orange: space-based spectropolarimeter instruments. Blue: goniometers without spectropolarimetric capability.

Instrument	Year	Spectral Range [nm]	Goniometric Incidence Range [°]	Linear Polarization	Circular Polarization	Primary Target
SenTech [57]	2022	190 – 3500	20 – 100	●	●	Characterization of thin films
Sopra GES 5E [58]	2022	190 – 1700	20 – 90	●	●	Characterization of thin films
Woollam [59]	2022	240 – 4000	15 – 90	●	●	Characterization of thin films
Horiba [60]	2020	450 – 1000	45 – 90	●	●	Characterization of thin films
Hokkaido University [50]	2019	400 – 800	4 – 68	●		Bidirectional reflectance of leaves
DRDC [61]	2017	350 – 2500	−75 – 75	●	●	Characterization of general materials
Bruker FilmTek 6000 [62]	2023	190 – 1700	N/A	●	●	Characterization of thin films
Lee RCE [63]	1998	400 – 700	N/A	●	●	Characterization of thin films
Kim RPE [64]	1990	375 – 830	N/A	●		In-situ gold oxide characterization
Infrared FTIR PME [65]	1986	2800 – 14300	N/A	●	●	Infrared characterization of thin polymer films
Aspnes RAE [66]	1975	225 – 720	N/A	●		Characterization of films and dielectrics
SPEXOne [67]	2019	385 – 770	N/A	●		Atmospheric aerosols
POLDER [68]	1994	443 – 910	N/A	●		Aerosols, clouds, and surface vegetation
SHADOWS [13]	2018	400 – 4700	−85 – 75			Bidirectional reflectance of asteroid and meteorite samples
SHINE [12]	2004	400 – 4800	−85 – 80			Bidirectional reflectance of ice and shiny surfaces
FIGOS [11]	1999	300 – 2450	0 – 180			Bidirectional reflectance of vegetation and soil
RELAB [10]	1993	320 – 2550	−70 – 70			Bidirectional reflectance of Earth and planetary materials

polarization capabilities, and thus transferring this technology to planetary surfaces is a logical next step.

The main limitations of the commercial ellipsometer include the limited spectral range and goniometric capabilities. Only two of the ellipsometers span from the ultravolet to the infrared [57, 59], and they still do not cover the desired spectral range from 300 – 4500 nm. None of the ellipsometers allow for independent arm control, meaning that the illumination and observation arms only move symmetrically in order to maintain a specular configuration. This makes it impossible to take forward- and back-scattering measurements. Some commercial ellipsometers also place the sample in a vertical configuration, or have a very small maximum sample size or thickness [59, 60, 62]. For example, the Woollam spectroscopic ellipsometer [59] cannot be directly used for this experiment because it measures samples vertically. The planetary analogue samples must be kept in a horizontal configuration to preserve the integrity of the sample, as powdered sample grains could not be held in place in a vertical configuration.

The spectroscopic goniometer setup sees more use on planetary surfaces, but has yet to include the additional information that polarimetry provides. It is commonly restricted to measuring the BRDF, without providing any linear or circular polarization information. The spectroscopic goniometer setup is valuable for the design of this spectroscopic ellipsometer because both the incidence and emergence angles are controllable over a wide range, such as 0° – 75° incidence and 0° – ±85° emergence [13], which allows for specific scatterometry measurements that traditional ellipsometers cannot provide.

Finally, space-based spectropolarimeters that measure planetary surfaces and atmospheres have historically had spectral ranges limited to the visible region, preventing them from gaining the insights that infrared analysis can provide. Their polarization sensitivity is also much lower when compared to that of an ellipsometer system [16, 44, 68]. However, they provide an excellent reference for determining the transferability of this proposed instrument to space payload platforms. There is a clear gap in using spectropolarimetric technology for broadband analysis of planetary surfaces. Leveraging the ellipsometry setup allows for a strong proof of concept in the laboratory for this type of analysis, which can be further developed into a spaceborne platform in future work.

In order to meet the requirements of thorough planetary surface investigation, it is necessary to design a custom spectroscopic ellipsometer. The following chapters will discuss this design process, as well as the performance and calibration of the instrument to address the main research questions of this work.

3

Instrument Requirements

This chapter defines the general requirements and design drivers for the spectroscopic ellipsometer instrument. These will guide the design decisions made in the following chapters of this work. In each requirement table, a requirement ID is included for easier verification that these instrument requirements are being met. These requirements will be frequently referred to in later sections of this work by these requirement IDs. Each requirement ID begins with SPG, a label meaning spectropolarimetric goniometer. It is followed by a type identifier, either *F*, *P*, or *C*, corresponding to functional, performance, and constraint requirements. The ID also includes a number for easier reference. Next, the identifier and description columns provide the necessary information about the requirement. Finally, the verification method categorizes requirements based on how they get verified. *T* means the requirement needs to be verified through testing in the lab with the real instrument components. *A* means the requirement can be verified through a simulation or analysis that does not involve any assembly. Finally, *R* is a requirement that can be confirmed through a review of the design, meaning datasheets for selected components, drawings, or other given information about the design.

3.1. Instrument Functions

Table 3.1 lists the functional requirements for the instrument.

The majority of these requirements are put in place so that the instrument is capable of achieving the goals outlined in Chapters 1 and 2, and thus specific definitions of most terms used in the functional requirements can be found in those sections. However, some terms are not fully addressed, and will be addressed here:

- **Static measurements** [SPG-F-04]: This refers to measurements where the properties of the sample are not changing with time, unlike samples with film growth or ice melt. There must be some effort to keep the sample in a constant condition throughout the measurement cycle.
- **Known polarization input** [SPG-F-09]: In order for the ellipsometer to be able to accurately measure the change in polarization, the initial polarization state must also be known. Therefore, unpolarized light cannot be hitting the sample. Only a linear polarization state is required, as circular polarization can be set before the sample or measured after the sample [16].
- **Stray light** [SPG-F-13]: Stray light refers to any unwanted light in the system, such as from other light sources in the lab. This can be limited through methods such as an enclosure or blackout curtains which would go around the entire instrument to keep the surroundings dark.
- **Alignment accessibility** [SPG-F-14]: Some components will require access in order to be slightly tilted or shifted. While some alignment equipment is hand actuated, others require screwdrivers or other tools to manipulate. There needs to be enough room between components for tools such as screwdrivers to be applied to the integrated instrument.
- **Manual realignment of the optical system** [SPG-F-15]: Moving components around to optimize for a certain part of the spectral range will make measurement repeatability very difficult to achieve. It will also add significant time to the experiment. Component movement should be kept to a minimum in general, and should be automated. The minimum requirement here is that a manual readjustment should not be necessary after each measurement.

Table 3.1: High level functional requirements for the ellipsometer design. The verification methods for each requirement are also listed, with R: Review of design, T: Testing, and A: Analysis.

Req ID	Title	Description	Verification method
SPG-F-01	Polarimetry	The instrument shall take polarimetric measurements of light reflected off of a sample.	R
SPG-F-02	Spectroscopy	The instrument shall take spectral measurements of light reflected off of a sample.	R
SPG-F-03	Spectropolarimeter functionality	The instrument shall take simultaneous polarimetric and spectral measurements of light reflected off of a sample to produce spectropolarimetric data.	R
SPG-F-04	Type of measurements	The instrument shall take static measurements with the sample located inside of the instrument.	R
SPG-F-05	Output format	The instrument shall output the four components of the traditional Stokes vector and $\{\Psi, \Delta\}$ for polarimetric measurements.	R, T
SPG-F-06	Light source	The instrument shall have an illumination arm that can be repositioned automatically.	R
SPG-F-07	Observation	The instrument shall have an observation arm that can be repositioned automatically.	R
SPG-F-08	Sample types	The instrument shall analyze rock, powder, and ice samples.	R, T
SPG-F-09	Source polarization (linear)	The instrument shall produce a known linear polarization source as an input to the sample.	A, T
SPG-F-10	Source spectrum	The instrument shall produce a known wavelength or spectrum as an input to the sample.	A, T
SPG-F-11	Load bearing	The instrument shall support the weight of all optical components in the illumination and observation arms.	A
SPG-F-12	Mounting	The instrument shall have mounts for all optical components on both the illumination and observation arms.	R
SPG-F-13	Stray light	The instrument shall have a method of stray light mitigation.	R
SPG-F-14	Alignment	Each optical component of the instrument shall be accessible for alignment.	R
SPG-F-15	Polarimetric considerations	The instrument shall allow for multiple polarimetric configurations without repeated manual realignment of the optical system.	R, T
SPG-F-16	Safety	The instrument shall have mechanisms to limit movement and prevent damage.	R

3.2. Instrument Constraints

Table 3.2 lists constraint-based requirements for the instrument. These are external limitations based on the funds available for the project, and the conditions in the lab where this instrument will be built.

Table 3.2: High-level constraints for the instrument design. The verification methods for each requirement are also listed, with R: Review of design, T: Testing, and A: Analysis.

Req ID	Title	Description	Verification method
SPG-C-01	Instrument cost	The instrument shall cost less than €180,000 to design and build.	R
SPG-C-02	Instrument volume	The instrument shall fit in a volume envelope of $2 \times 2 \times 2$ m.	R
SPG-C-03	Temperature range	The instrument shall operate between temperatures of 15 °C and 25 °C (room temperature).	R

3.3. Instrument Performance

Table 3.3 lists the performance requirements for the instrument. Some additional context behind specific requirements is also provided in this section:

- **Minimum sample reflection** [SPG-P-07]: A minimum sample reflection is necessary as some dark samples will not provide enough signal to be accurately measured. This focuses sample procurement efforts on sample types that are worth measuring.
- **Sample grain size** [SPG-P-09]: The sample grain size is largely a result of the observation spot size, which is the size of the image of the detector when projected onto the sample. In each observation, there needs to be enough grains to result in a statistically relevant measurement. Typically, this is on the order of 100 [23]. The grains therefore need to be small enough such that at least 100 grains are visible, but large enough such that features can be detected.
- **Phase angles** [SPG-P-10]: A minimum phase angle requirement is necessary because the components on the illumination and observation arms can collide with or obscure eachother. If both the illumination and observation arms are at normal incidence, it also becomes impossible to distinguish between p- and s-polarizations [16]. A maximum phase angle requirement exists due to the geometry of the system, ensuring light reflects off the sample with sufficient signal in every orientation.
- **Source collimation** [SPG-P-12]: The degree of collimation refers to how close to parallel incoming beams are when entering an optical component. The accuracy and sensitivity of components such as linear polarizers and photoelastic modulators decreases with an increasing incidence angle [69, 70].
- **Tip/tilt adjustment** [SPG-P-17]: The sample position needs to be adjustable such that both arms point at the sample in all orientations. Additionally, the sample can be flattened so that symmetrical reflectance measurements can be completed.
- **Clock angle, decenter, despace adjustment** [SPG-P-18, SPG-P-19, SPG-P-20]: Fine precision capabilities are necessary for reducing aberrations (decenter, despace) and the accuracy of the polarimetric system (clock angle). The concepts of despace, decenter, and clock (or azimuth) angle are shown in Figure 3.1. The values of these requirements are established through simulations discussed in Chapter 6.
- **Angular resolution** [SPG-P-21]: In the context of goniometers, angular resolution refers to the angle swept out by the cone of light accepted by the observation arm of the ellipsometer. This is shown visually in Figure 1.8, with the green emergence cone corresponding to the angular resolution.
- **Observation spot diameter** [SPG-P-22]: The observation spot size needs to be large enough to cover a sufficient portion of the sample, but not large enough to capture some features from the sample holder, which would contaminate the measurement results.
- **Illumination spot diameter** [SPG-P-23]: The observation spot diameter must always be smaller than or equal to the illumination spot diameter. If the observation arm measures from a point on the sample at which there is no illumination, there will not be sufficient signal at the detector.

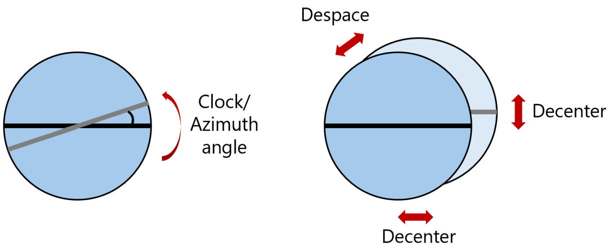

Figure 3.1: Visual depiction of clock angle, decenter, and despace concepts for a polarizer, with the black line corresponding to the transmission axis.

Table 3.3: High-level performance requirements for the instrument. The verification methods for each requirement are also listed, with R: Review of design, T: Testing, and A: Analysis.

Req ID	Title	Description	Verification method
SPG-P-01	Intensity polarimetric accuracy	The instrument shall measure polarimetric intensity changes (Ψ) to within 0.01°.	T
SPG-P-02	Phase polarimetric accuracy	The instrument shall measure polarimetric phase changes (Δ) to within 0.02°.	T
SPG-P-03	Spectral range linear data	The instrument shall be capable of measuring linear polarimetric data with the minimal sensitivity described in [SPG-P-01] over a spectral range of 300 – 4500 nm.	T
SPG-P-04	Spectral range circular data	The instrument shall be capable of measuring circular polarimetric data with the minimal sensitivity described in [SPG-P-02] over a spectral range of 300 – 4500 nm.	T
SPG-P-05	Infrared spectral sampling	The instrument shall be capable of measuring polarimetric data with a spectral sampling of at least 20 nm in the infrared region.	T
SPG-P-06	Visible spectral sampling	The instrument shall be capable of measuring polarimetric data with a spectral sampling of at least 5 nm in the visible region.	T
SPG-P-07	Minimum sample reflection	The instrument shall be capable of measuring sample compositions for samples reflecting at least 10% of incoming light.	T
SPG-P-08	Sample width/length	The instrument shall be capable of accepting samples between 1 and 5 cm in width and between 1 and 5 cm in length.	T
SPG-P-09	Sample grain diameter	The instrument shall be able to analyze samples with grain diameters of at least 10 μm.	T
SPG-P-10	Phase angles	The instrument shall be capable of measuring sample compositions at phase angles between 5° and 160°.	R
SPG-P-11	Signal-to-noise ratio	The instrument shall have a signal to noise ratio of at least 17 dB (50) at the spectral targets defined in Section 2.1.	T
SPG-P-12	Source collimation	The instrument source shall be collimated to within 2°.	A, T
SPG-P-13	Achromatization	The polarizer elements shall be achromatized to within 1 % over the spectral range of the instrument.	R
SPG-P-14	Illumination arm range	The illumination arm shall be capable of rotating between 0° and 90° with respect to the sample normal.	R, T
SPG-P-15	Observation arm range	The observation arm shall be capable of rotating between -75° and 90° with respect to the sample normal.	R, T
SPG-P-16	Goniometric accuracy	The illumination and observation arms shall be capable of being positioned to within 0.1°.	T
SPG-P-17	Tip/Tilt adjustment	The instrument's sample shall be capable of tip/tilt adjustment to 0.1° precision.	T
SPG-P-18	Clock angle adjustment	The instrument's polarizer elements shall be capable of azimuth angle adjustment of 0.01° precision.	R
SPG-P-19	Decenter adjustment	The instrument's optical elements shall be capable of decenter adjustment to within 100 μm precision.	R
SPG-P-20	Despace adjustment	The instrument's optical elements shall be capable of despace adjustment to within 100 μm precision.	R
SPG-P-21	Angular resolution	The instrument shall have an angular resolution of at least 10°.	T
SPG-P-22	Observation spot diameter	The observation spot diameter shall be between 1 mm and 5 cm at all observation arm orientations.	T
SPG-P-23	Illumination spot diameter	The illumination spot size shall be large enough such that the observation spot size is completely inscribed at all orientations.	T

3.4. Design Drivers

Some instrument requirements are more critical than others, as they align better with the primary research questions of this work and with the overall goals of the instrument. These are the guiding principles used for making high-level design decisions. This list of drivers will be revisited at the end of this work to provide a complete answer to the first research sub-question: *What are the design drivers of a spectroscopic ellipsometer intended for planetary surface studies?*

3.4.1. Spectral Range

The targets of interest defined in Section 2.1 range from the ultraviolet to the infrared, with 300 – 4500 nm being the ideal instrument spectral range. The spectral range capabilities of chosen components will be a critical factor in the high-level design process.

Many polarimetric components are sensitive to the incoming wavelength, suffering from polarimetric errors and poor transmission. Additionally, lens components for redirecting light are sensitive to chromatic aberration, which is a change in the focal point of a lens based on the incoming wavelength, due to a spectral variation in the refractive index of the lens.

It will be critical to select components that maximize the spectral range so that these species can all be measured with sufficient accuracy.

3.4.2. Signal-to-Noise Ratio

The precision of an instrument is often limited by the amount of signal it receives. If the signal input is too low, it will be hard to distinguish characteristics at high spectral or angular resolution, and the polarimetric sensitivity will also suffer. In order to meet these requirements, it is necessary to ensure signal-to-noise ratio is maximized.

This metric is so critical because the instrument can only detect a small fraction of the light input. The white light input must be divided over each spectral band being measured when spectroscopic measurements are required. Each time light passes through a polarizer, at least half of the light intensity will be lost as well due to its blocking properties. Furthermore, when light reflects off of the sample surface, it produces a half-sphere. Only a small portion of that half-sphere can be collected by the observation arm of the instrument, meaning the majority of the reflected light is lost.

This is a complicated instrument with many optical components to fulfill the scientific requirements. Adding more components can result in losses to the input light, so minimizing the number of components will be a design consideration for improving the signal-to-noise ratio. Prioritizing high-transmission components will also be an important criteria in high-level decision making.

3.4.3. Polarimetric Coverage and Sensitivity

Different ellipsometer configurations measure different parts of the Stokes vector. Design decisions will be made to prioritize options that cover the entire Stokes vector, preferably simultaneously.

Polarimetry measurements are also a main focus of the instrument, meaning design decisions have to be made to prioritize meeting the sensitivity requirements. This can come through decisions that increase signal-to-noise ratio, but also through selecting polarimetric components with high accuracy. This will require a strong focus on metrics such as extinction ratio and retardance accuracy.

4

High-Level Instrument Design

This chapter outlines the key design decisions that influenced the major component selection of the ellipsometer. This includes all major elements of the design, comprising polarimetric and spectral measurements, the light source, and the detection elements. The chapter follows the instrument in the order that light travels through the system, and makes reference to high-level requirements listed in Chapter 3 to inform design decisions.

4.1. Light Source

The instrument needs a method of producing light to input into the system to meet instrument requirements [SPG-F-10]. The long-term goal of this instrument is to serve as a proof of concept for space missions, where the light source would be the sun. This means that a light source that has some characteristics of sunlight would be preferred. The light source for this instrument should therefore be of sufficient power to measure the polarimetric and spectral information with the required accuracy. This emission also needs to span across the entire required spectral range of the instrument, at least $300 - 4500$ nm [SPG-P-03, SPG-P-04]. It should also be an unpolarized light source such that the effect of the sample on the reflected light is clear. For these reasons, light sources such as lasers are disqualified. They are limited to a narrow wavelength band, and are typically polarized light sources.

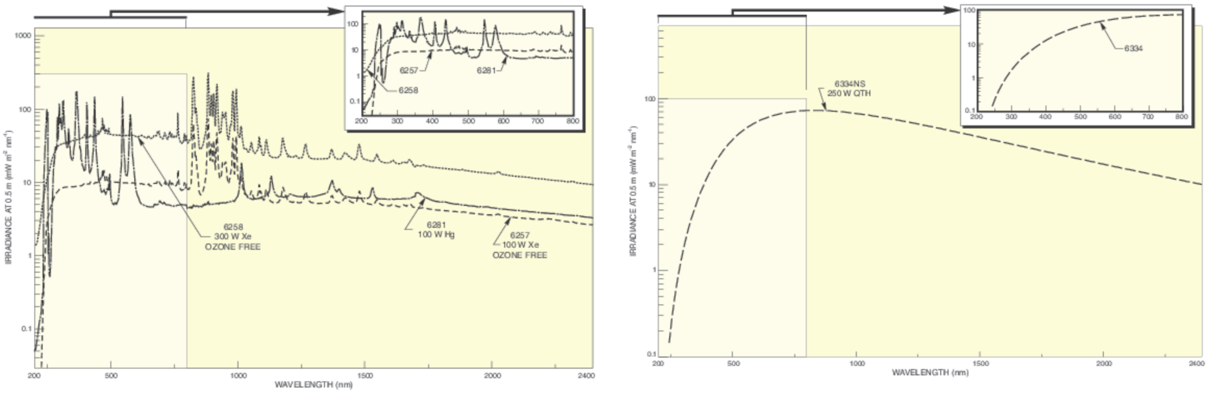

(a) Arc lamp emission spectrum [71].

(b) QTH lamp emission spectrum [72].

Figure 4.1: Emission curves for lamp options.

This limits the light source to a lamp. The most common lamp types for this application are arc lamps [71] and quartz-tungsten-halogen (QTH) lamps [72]. The arc lamp is valuable because it has a long lifetime, and a smaller divergence angle which makes light collection from the bulb more efficient. However, they do have high power emission in the ultraviolet range which can make them dangerous to handle. QTH lamps are useful for applications where high light source stability is required. Since measurements are expected to last several hours or days for this instrument, a high degree of stability is important. They also have reduced power in the ultraviolet range making them a safer option for prolonged usage. Table 4.1 shows a summary of the tradeoff criteria for the lamp type, while Figure 4.1 shows typical emission curves for an arc lamp and a QTH lamp. These emission curves only extend up to 2400 nm, but the thermal emission of the bulb will provide light in the infrared region as well. Figure 4.1a shows that the arc lamp has some emission peaks between 750 – 1000 nm, whereas the QTH lamp curve shown in Figure 4.1b is much smoother.

Table 4.1: Trade study criteria for lamp options. Green text corresponds to an option that meets requirements and is the best option in its category. Yellow text corresponds to an option that meets requirements but is not the best in its category. Red text corresponds to an option that does not meet requirements.

Criteria	Arc Lamps [71]	QTH Lamps [72]
Spectral Range	UV - IR	UV - IR
Stability	Medium	High
Lifetime	1500 hr/bulb	200 hr/bulb
Safety	Medium	High
Cost	~ €7000	~ €7000

The smooth output curve, reduced power in the ultraviolet range, and improved stability make the QTH lamp the ideal choice for this instrument.

4.2. Spectral Considerations

There are multiple ways to get the required spectral data for spectropolarimetric measurements. Figure 4.2 shows the major options that allow the instrument to take spectral measurements [SPG-F-02, SPG-F-03].

Typical grating spectrometers or prism spectrometers are commonly used in spectral measurements. Unfortunately, the dispersion characteristics of the grating and prism-based spectrometers do not match the configuration of the rest of the system. These spectrometer systems typically disperse light spatially, such that light of different wavelengths lands on different pixels on the detector face. However, this instrument will not have imaging capabilities, and thus would not be able to interpret the spectral differences produced by the grating. These types of spectrometers will therefore not be considered for this instrument.

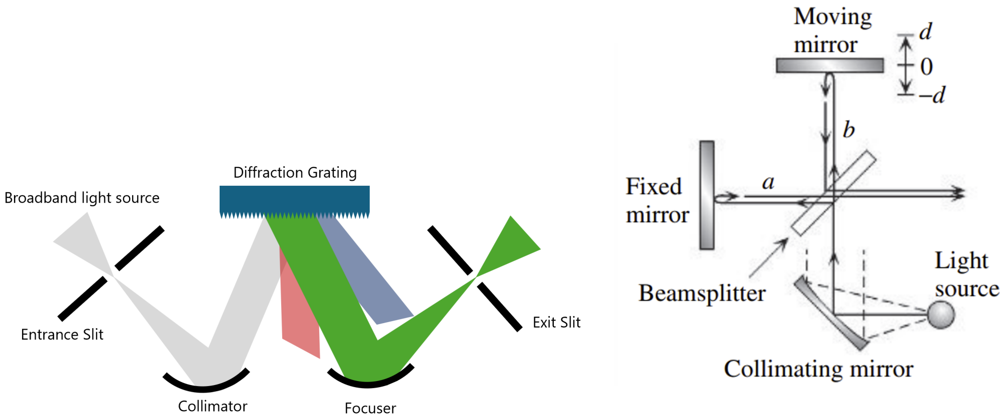

(a) Simplified monochromator diagram. Figure adapted from [73].

(b) Fourier transform spectrometer (FTS). Figure adapted from [16].

Figure 4.2: Spectrometry options.

A monochromator is a device that uses a grating to let a selected narrow band of light through. This band can be configured and allows for a single wavelength to be transmitted at a time, while all other wavelengths are blocked. The basic operating principle is shown in Figure 4.2a. These devices have large spectral ranges and adjustable resolution, which is important for ensuring the correct bands are being measured. Additionally, since only one wavelength is being sent in at a time, the rest of the optical track does not need to be optimized for performance over a wide range of wavelengths. Components can be switched out or modified to work better with the input wavelength. While this can improve performance at specific wavelengths, this does make measurements over broadband spectrums take significantly longer. The monochromator typically uses a grating or prism for dispersion [74], which can be quite sensitive to polarization effects [75]. However, using it at the source of the ellipsometer, before light has reached the polarimetric elements, should result in minimal polarization effects.

A Fourier transform spectrometer (FTS) is another method of creating this spectrum. As shown in Figure 4.2b, this spectrometer is operated by an interferometer containing a movable mirror that can modify the interference pattern of light to produce an interferogram. Moving this mirror and recording these interferograms in a synchronized manner can allow for the inference of intensity as a function of wavelength using the Fourier transform. The FTS is a valuable option because it allows for broadband measurements to be performed simultaneously, only limited by the spectral range of the detector, which can save time. This may be important for certain samples such as ices which need to stay in constant conditions throughout testing. Interferometers also have less of an effect on polarization than grating-based spectrometers, which can help with reducing measurement error [16]. However, they are more complicated to use, and require precise synchronization with the detector in order to take useful measurements.

Table 4.2: Trade study criteria for spectrometry options. Green text corresponds to an option that meets requirements and is the best option in its category. Yellow text corresponds to an option that meets requirements but is not the best in its category. Red text corresponds to an option that does not meet requirements.

Criteria	Monochromator [76]	Fourier Transform Spectrometer [77]
Spectral Range	0.2 – 6 μm	0.3 – 700 μm
Ease of Integration	Easy	Difficult
Flexibility	High	Low
Experiment time	Minutes	Seconds
Cost	~ €30000	~ €30000

Table 4.2 shows the main considerations for choosing the best spectrometer system for the instrument. Due to the flexibility in adjusting components to fit a monochromatic band of light, and the relative simplicity of operation, the monochromator is the preferred option over the Fourier transform spectrometer.

4.3. Optical Fibres

The instrument's light source now consists of a QTH lamp and monochromator combination. These are typically large and heavy components that would not fit on an illumination arm of the size required for this experiment.

Based on the illumination arm requirement [SPG-F-06], it is therefore necessary to find a way to transfer light from this light source to the illumination arm, and to do so accurately even when the arm is in motion. The standard way of accomplishing this is through the use of an optical fibre.

An optical fibre typically consists of a core of glass or plastic, surrounded by a cladding of lower refractive index. A basic functional diagram is shown in Figure 4.3. Light is guided through the fibre through total internal reflection in the core. An optical fibre can bend to accommodate the moving illumination arm of the instrument, though it is important to ensure the fibre does not bend or stretch too much due to transmission losses and potential fractures in the core. If the fibre bends too much, the critical angle for total internal reflection may be exceeded, and light will instead be lost to the cladding through refraction. While these are important considerations to address during the detailed design process, the optical fibre is the preferred method of transmitting light from the light source to the illumination arm of the instrument.

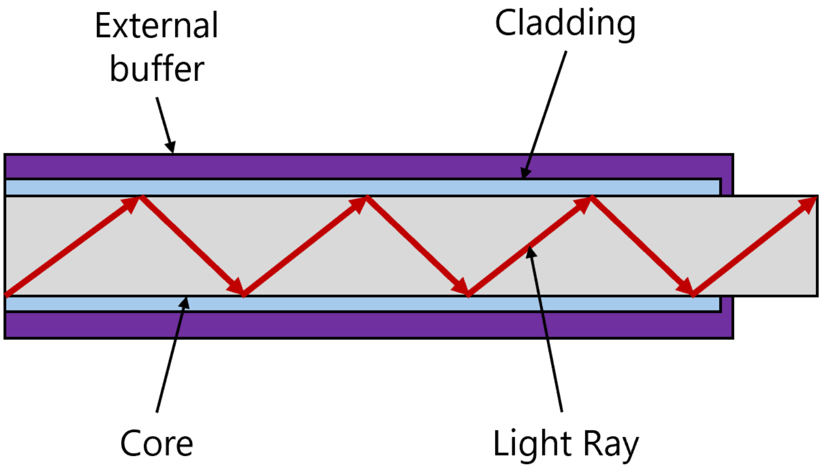

Figure 4.3: Optical fibre functional diagram.

4.4. Ellipsometer Architecture

Specific configurations of polarization elements allow for measurements of certain subsets of the complete Stokes vector description of the polarization state. The complete Stokes vector description implies that Ψ and Δ can also be measured. Each of these standard ellipsometer architectures have typical use cases, which will be compared in this section to determine the best possible configuration for the instrument requirements.

4.4.1. Linear Polarimetry

In order to measure linear polarimetry [SPG-F-01, SPG-F-05, SPG-F-09], the ellipsometer needs linear polarizers. The most basic ellipsometer design is a rotating polarizer or analyzer design, as shown in Figure 1.5. This design is only able to capture changes in linear polarization using a polarizer with a controllable orientation. This will form the basis for the ellipsometer architecture, to which circular polarimetry capabilities will be added as discussed in Section 4.4.2.

There are some main candidates for these linear polarizers, which are summarized in Table 4.3.

Table 4.3: Trade study criteria for linear polarimetry options. Green text corresponds to an option that meets requirements and is the best option in its category. Yellow text corresponds to an option that meets requirements but is not the best in its category. Red text corresponds to an option that does not meet requirements.

Criteria	Crystalline Polarizers [78]	Wire-grid Polarizers [69]
Angular Separation	1° – 15°	N/A
Spectral Range	130 – 7000 nm	250 – 4000 nm
Extinction Ratio	[10, 000 – 200, 000] : 1	[100 – 10, 000] : 1
Cost	~ €1000	~ €1000

The first type of linear polarizer can be broadly categorized as a crystalline polarizer. These consist of two prisms cemented together and made from birefringent materials. At the interface between the prisms, two orthogonally polarized beams are produced that exit the prism with some relative divergence angle [79]. Some types of crystalline polarizers, such as the Rochon prism (pictured in Figure 4.4a), also have a very wide spectral range (130 – 7000 nm) [78]. The main disadvantage of using these prisms is their low angular separation. The majority of detectors are not designed to measure polarization, only intensity, meaning only one polarization component should be transmitted to a detector at a time. The detector can then determine the polarization through modulation of the intensity of that polarization component. Since the p- and s-polarizations of the output light are only separated by a maximum of a few degrees, a very long optical track is required to only capture one of these components. This makes the illumination arm of the spectroscopic ellipsometer at least a few metres long, which makes it difficult to safely achieve the full range of motion [SPG-P-14, SPG-P-15] inside the restricted lab space, and does not meet volume requirements for the instrument [SPG-C-02].

(a) Rochon prism. Figure from Edmund Optics [78]. **(b)** Wire-grid polarizer. Figure from Thorlabs [69].

Figure 4.4: Linear polarimetry options.

Another polarizer type is the wire-grid polarizer, which are a series of fine metallic wires arranged very close together in a single plane. Their orientation reflects parallel polarized light, while perpendicularly polarized light passes through [15]. This means that a wire-grid polarizer will not suffer from the same angular separation problems as a crystalline polarizer. A major drawback of the wire-grid polarizer is an inconsistent extinction ratio over the spectral range of the instrument. This can make it difficult to guarantee sufficient polarimetric accuracy for all of the target species and meet spectral range requirements [SPG-P-03]. Furthermore, even polarizers classified as ultra-broadband are rated for a maximum of 4 μm [69], meaning the 4.3 μm carbon dioxide ice band would likely have much higher measurement error.

While the spectral range limitation of the wire-grid polarizer is a significant drawback, the mechanical limitations that the crystalline polarizers impose are much more restrictive as they prevent the arms of the instrument from moving almost entirely. The wire-grid polarizers are therefore the best option for the ellipsometer.

4.4.2. Circular Polarimetry

In order to measure the change in circular polarization from reflected light, a rotating compensator is typically applied. While a stationary compensator could also be used, it requires a rotating analyzer and two compensator configurations to cover all the Stokes parameters, and thus a single rotating compensator is often more convenient [16]. This typically comes in the form of a quarter waveplate with an adjustable orientation, an example of which is shown in Figure 4.5a. While this allows all components of the Stokes vector to be measured, the major drawback of this technology is the limited passband for waveplates. Even superachromatic waveplate technologies from Thorlabs [80] are not able to cover the entire spectral range required by the targets of interest, thus not meeting achromaticity requirements [SPG-P-04, SPG-P-13].

The waveplate can be replaced with another retarder element such as a Fresnel rhomb, as shown in Figure 4.5b. Fresnel rhombs are often used in situations where a static half-wave or quarter-wave modulation is needed over a broader spectral range. They apply a phase difference to incoming light using the principle of total internal reflection. Though they are meant to have broader achromatic ranges than waveplates, available selections of standard and custom waveplates still do not cover the required $300-4500$ nm wavelength range [82, 83]. Fresnel rhombs can also be prone to error in calibration and alignment. They require four discrete angular positions in order to calculate the full Stokes vector [84]. Additionally, due to their size and material, holding the Fresnel rhomb in place and rotating it to these discrete positions can induce strain on the rhomb, causing residual birefringence that can impact the accuracy of the retardation significantly [85].

A third alternative that allows for the measurement of all four Stokes parameters is the photoelastic modulator (PEM), as shown in Figure 4.5c. This is a more recent technology with use in many ellipsometer designs,

(a) Thorlabs achromatic waveplate. Figure from Thorlabs [80]. **(b)** Fresnel rhomb. Figure from Laser 2000 [81]. **(c)** Photoelastic modulator. Figure from HINDS [70].

Figure 4.5: Circular polarimetry options.

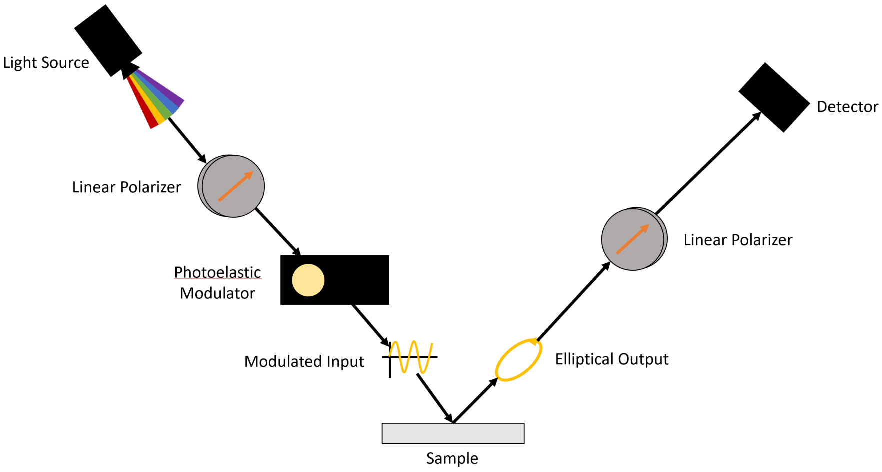

Figure 4.6: Diagram showing the components of a photoelastic modulator ellipsometer setup.

referred to as phase-modulated ellipsometers (PME). It works by applying stress to a quartz crystal in order to modify its structure, and thus its birefringence properties. This can be done by changing the voltage applied to the crystal, which eliminates the need for continuously rotating parts. The PEM modulates the retardance induced by the crystal at a very high frequency, and the Stokes parameters can be later extracted using a lock-in amplifier. PEMs also have a larger spectral transmission range, with models reaching 300 – 3500 nm [70]. They have an extremely fast modulation time, often on the order of microseconds, allowing for a similarly fast acquisition time [16]. These devices do have some drawbacks, including cost, increased sensitivity to temperature, and potential residual strain birefringence errors [70]. One photoelastic modulator cannot be used to measure the complete Stokes vector at one time, and must be rotated and measured in two configurations in order to capture both S_1 and S_2 [16]. Figure 4.6 shows the architecture of the standard photoelastic modulator ellipsometer.

All three options have associated benefits and drawbacks, which are summarized in Table 4.4. Since the spectral range would be severely limited by the capabilities of both the waveplate and the Fresnel rhomb, the photoelastic modulator was chosen to allow the ellipsometer to take circular polarimetry measurements of infrared targets. Its spectral range is still limited relative to the other optical components in the instrument, so if measurements are desired for samples beyond 3.5 μm, it is recommended to remove the PEM from the system for those measurements and apply a rotating analyzer ellipsometry configuration.

Typically, the photoelastic modulator can be placed before or after the sample, and it would work very similarly [16]. However, the photoelastic modulator needs to be aligned with the polarizer on the illumination arm, and these components need to rotate together to capture the full Stokes vector [16, 70]. To ease the alignment process, the photoelastic modulator should therefore be placed on the illumination arm.

Table 4.4: Tradeoff criteria for circular polarimetry options. Green text corresponds to an option that meets requirements and is the best option in its category. Yellow text corresponds to an option that meets requirements but is not the best in its category. Red text corresponds to an option that does not meet requirements.

Criteria	Achromatic Waveplates [80]	Fresnel Rhombs [83]	Photoelastic Modulators [70]
Retardance Accuracy	1%	1%	1%
Achromatic Range	600 – 2700 nm	215 – 1700 nm	300 – 3500 nm
Usage Difficulty	Easy	Medium	Hard
Cost	~ €3000	~ €750	~ €20,000

4.4.3. Depolarization Effects

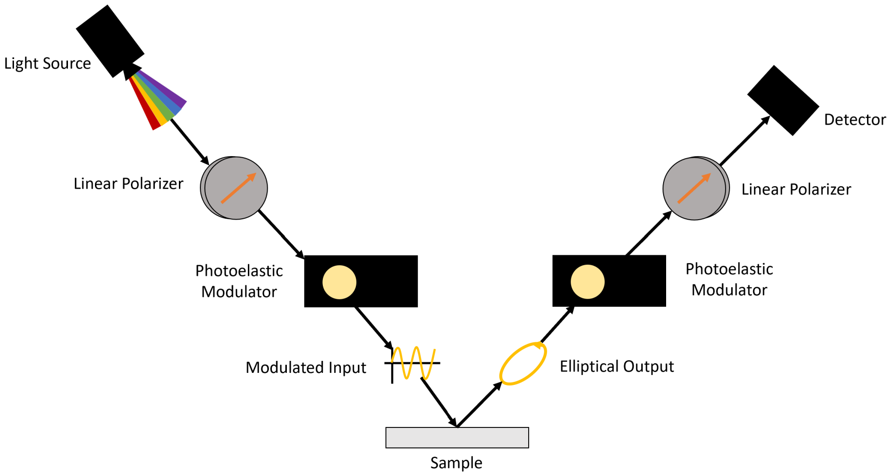

Figure 4.7: Diagram showing the components of a Mueller matrix ellipsometer setup.

The choice of instrument also depends on the samples used. If anisotropic samples, referring to samples that are not symmetric in all directions, with a high degree of surface roughness are expected to be used, then a Mueller matrix ellipsometer may be appropriate to capture the change in polarization with higher accuracy. The Mueller matrix is a representation of polarimetric states that can also include varying degrees of unpolarized and partially polarized light. Rougher samples can cause some depolarization of the incident light, which can be measured to better determine the sample's structure. The Mueller matrix ellipsometer employs an additional compensator after the sample, which in this case would be another photoelastic modulator. When two photoelastic modulators are used, the full Stokes vector can be measured simultaneously as well, without the need for multiple configurations. However, this adds significant complexity and cost. The PEM unit price is approximately €20,000, and extra lock-in amplifiers would also be required. Furthermore, calibration between the modulators is quite complex [16]. Figure 4.7 shows an example of a Mueller matrix ellipsometer.

As this instrument is a proof of concept for ellipsometry applied to planetary surfaces, anisotropic and rough surface samples are not a main focus. Due to the high price of the photoelastic modulator and the complicated alignment procedure, adding full Mueller matrix functionality is not necessary for this instrument.

4.5. Detection

The final component in the ellipsometer setup is the detector. Considering the wide spectral range required for spectropolarimetric measurements, it could be difficult to cover the entire spectral range of the system with a single detector. Figure 4.8 shows the sensitive regions for a Silicon (Si) detector and an Indium Arsenide

Antimonide (InAsSb) detector, as an example of the limitations of typical detectors.

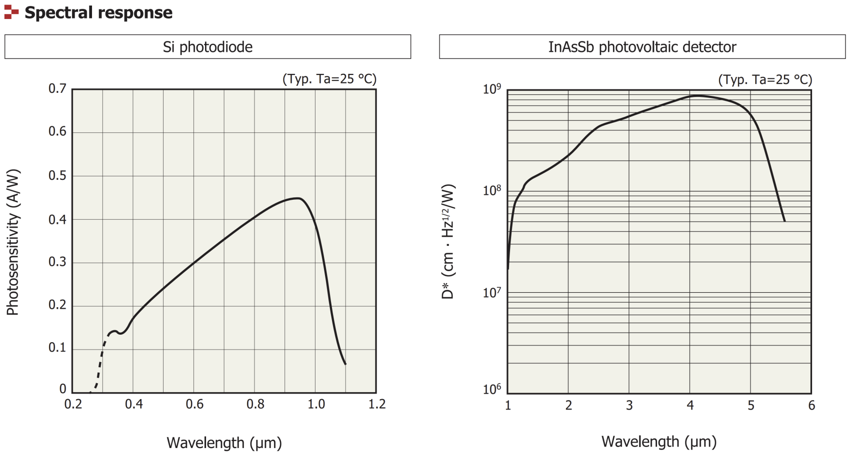

Figure 4.8: Typical spectral ranges for visible and infrared detectors. Figure from [86].

Most detectors are not sensitive to polarization and only measure intensity. Polarization-sensitive detectors are a modern development, but they are still restricted in terms of spectral range and availability [87]. Polarimetric data will therefore be measured through traditional methods, using the modulation of other polarizing components.

In order to successfully measure polarization states over the entire spectral range, there are a few options.The first is a beam splitter design, that splits the light path towards two specialized detectors. The first detector can capture infrared data, and the second can capture visible spectrum data. While this is a simple solution, and possible due to relaxed constraints on volume, it could pose problems for the intensity of light received on the detector face. If the signal-to-noise ratio is too low, it may not be a feasible design. It is not an ideal solution for the monochromator design where the input wavelength is known because half of the signal is being wasted. It also complicates the design as it would be difficult to have two split light paths mounted on the observation arm.

The second is called a two-color detector face, such as the ones offered by Hamamatsu [86]. The two-color detector is depicted in Figure 4.9, with an example from Hamamatsu in Figure 4.9b. These detectors have infrared and visible detectors integrated onto the same detector face, negating the need for a beam splitter and conserving some of the signal. The main concern with this option is the effect that the transparent visible detector face can have on both the focus quality and intensity of light on the infrared detector face. It may also be difficult to get light to fill both the silicon and infrared detector, which limits the signal at the detector face. This issue is shown in Figure 4.9a, as the cone of light does not fill the visible detector face, only the infrared.

The final possibility, if signal-to-noise ratio proves to be a very challenging concern, is changing out the detector to correspond to the signal coming in. This works well when coupled with the monochromator, as the detector could be configured for one wavelength at a time. This, however, does make the experiment take much longer, and could be prone to calibration inconsistencies between the two detectors leading to measurement error.

Table 4.5 summarizes the considerations involved in choosing the best detector configuration for the design. Due to its integration with the observation arm of the ellipsometer, and its simplification of the optical path, the two-color detector was the superior choice for this instrument.

4.6. Goniometric Capabilities

Aside from the optical components in the ellipsometer instrument, the movement of the arms themselves needs to be optimized to observe the full range of goniometric measurements. This section outlines the key considerations in determining how the illumination and observation arms can meet the movement

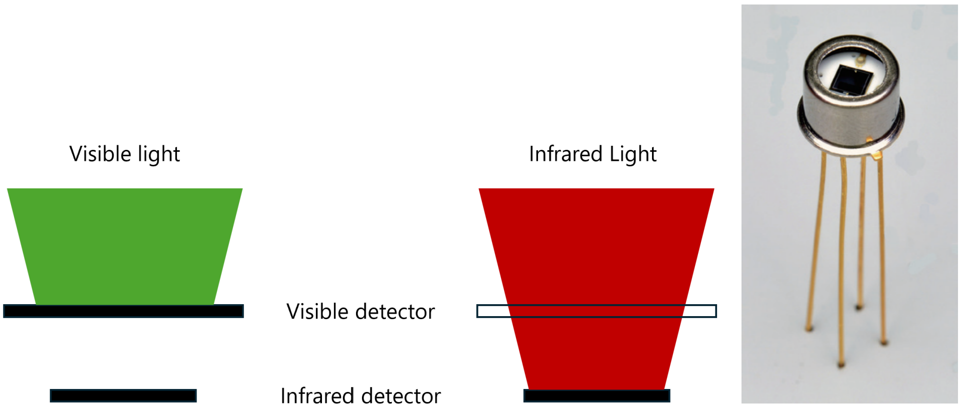

(a) Diagram of two-color detector operation. Note that the visible detector is transparent to infrared light.

(b) Example of two-color detector. Figure from Hamamatsu [86].

Figure 4.9: Two-color detectors.

Table 4.5: Tradeoff criteria for detector options. Green text corresponds to an option that meets requirements and is the best option in its category. Yellow text corresponds to an option that meets requirements but is not the best in its category. Red text corresponds to an option that does not meet requirements.

Criteria	Beam Splitters	Two-Color Detectors [86]	Switch Detectors
Signal-to-Noise Ratio	Low	Medium	High
Experiment Automation	Easy	Easy	Difficult
Complexity	High	Low	High
Calibration Accuracy	High	Medium	Low

requirements [SPG-F-06, SPG-F-07].

4.6.1. Specular

Specular reflection is when the angle of incidence is equal to the angle of reflection. This is the configuration that is commonly used for the majority of ellipsometers [16]. It requires some degree of accuracy and repeatability to ensure that the arms are at the same angles. Figure 4.10 shows the specular reflection configuration of the instrument. For this configuration, the illumination arm can be placed at angles up to 80°. At 0° in the specular configuration, also called opposition, the p- and s-polarizations of light cannot be distinguished, and thus ellipsometry cannot be performed [16]. At angles less than 5° between the arms, collisions or obscuration between components of the illumination and observation arms are possible, and thus the minimum angle will be investigated in Section 5.5.2. If the angle is above 80°, the spot sizes of illumination and observation would become quite large, meaning that some features of the sample holder may appear in the ellipsometry measurements. This contaminates the features of the sample and must be avoided.

For this, the most logical option is to use a heavy duty rotation stage for each arm, with enough torque and precision to drive both the arm and the optical components mounted to it.

4.6.2. Forward and Back-Scattering

Scattered light can reveal a lot more about surface structure and composition than specular reflection, as surface roughness features and other irregularities can be observed. Figure 4.11 shows the scattering configurations

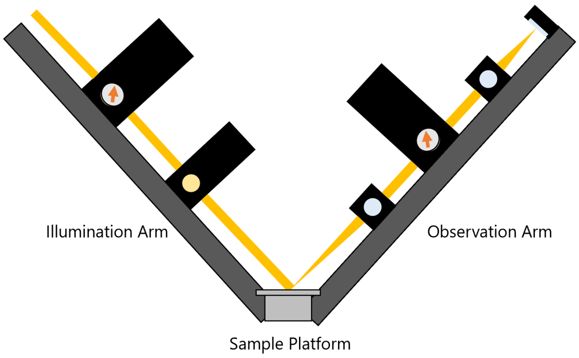

Figure 4.10: Specular configuration for the ellipsometer. The light source is omitted for simplicity.

for the goniometer.

The illumination arm and observation arm can be moved independently such that they are on opposite sides of the sample with respect to the normal, but the angle of incidence does not equal the angle of emergence. This allows the instrument to achieve the forward-scattering orientation as defined in Section 1.1.5. In these situations, it is possible to have the illumination or observation arm be positioned directly at 0°, as long as the angle between the two arms is large enough to prevent obscurations in the image or collisions between optical components. Figure 4.11a shows the forward-scattering orientation.

Back-scattering is a feature of this instrument that separates it from the capabilities of typical ellipsometers. This refers to configurations in which the illumination and observation arms are on the same side of the sample relative to the normal. Figure 4.11b shows an example of this configuration.

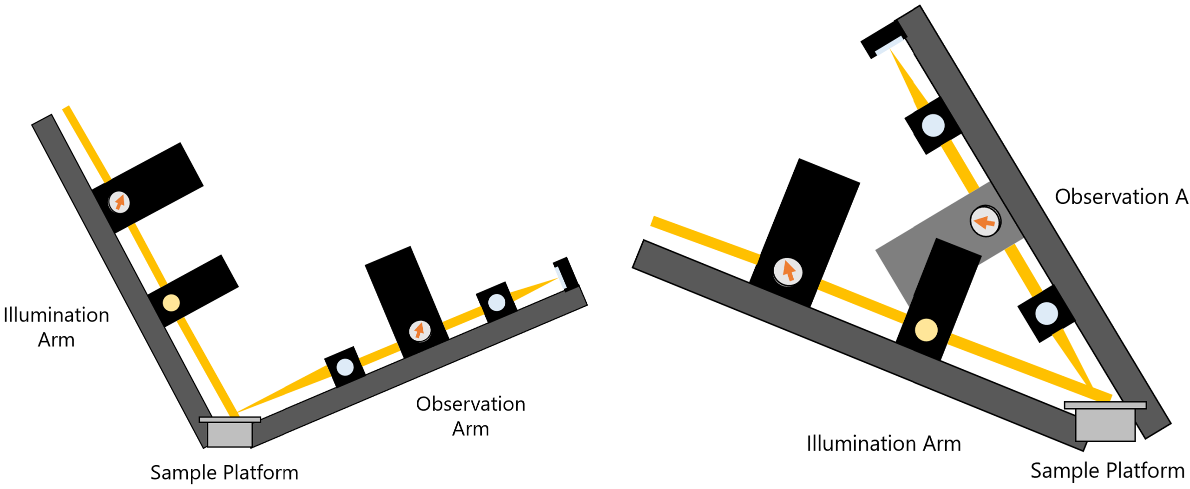

(a) Forward-scattering configuration.

(b) Backscattering configuration.

Figure 4.11: Scattering configurations for the ellipsometer. The light source is omitted for simplicity.

The heavy duty rotation stages should therefore support bi-directional 180° rotation for the observation arm, and bi-directional 90° rotation for the illumination arm. This will exceed the movement requirements [SPG-P-14, SPG-P-15] and would thus need some limits to ensure that the arms do not collide with anything. The design should limit the amount of non-transmissive material in the goniometer path, including mounts and electrical components. It is likely however that the arms will not be able to cross over each other, based on some large optical components on each arm. This will require design work involving sample selection and placement to ensure that this does not further restrict the data the instrument can measure. This reduces the phase angles at which there would be obscuration or collision. Detailed considerations in regards to component placement will be made in Section 5.5.

4.6.3. Calibration and Characterization

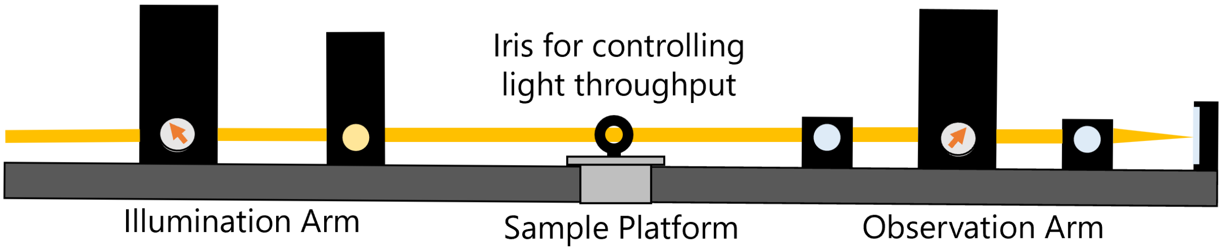

Figure 4.12: Calibration and characterization configuration for the ellipsometer. The light source is omitted from the figure for simplicity.

The final notable mode for the instrument is calibration and characterization. This configuration removes the sample from the optical track, passing the collimated light output from the illumination arm into the collimator input of the observation arm. This is useful for polarizer angle alignment, spectrometer calibration, and chacterization of the system. Figure 4.12 shows the positioning of the arms in this configuration. It can also be helpful to add an iris around where the sample would be in an ellipsometric configuration, in order to control the light throughput to the observation arm. This helps measure signals that are more representative of the throughput expected when a sample is included.

From a mechanical standpoint, this could add some challenges with making sure there is ample clearance between the arm rotation and any surface the instrument is mounted to. Components striking these surfaces should also be avoided, which will require some limits to be put in place for safety.

4.7. Operating Modes

In order to meet the majority of polarimetry and spectroscopy requirements, the instrument requires three configurations. These configurations refer to the polarimetric components involved and their angular positioning. These will be referred to in future sections as configuration 1, configuration 2, and configuration 3. The three configurations are shown in Figure 4.13.

- **Configuration 1** involves the polarizer at +45°, the PEM at 0°, and the analyzer at −45°. This configuration will allow the ellipsometer to measure S_0, S_2, and S_3. A mathematical explanation of why that is the case can be found in Section 6.4.1.
- **Configuration 2** involves the polarizer at 0°, the PEM at −45°, and the analyzer at −45°. The polarizer and PEM will rotate simultaneously to reach this configuration from configuration 1. In this configuration, the ellipsometer can measure S_0, S_1, and S_3.
- **Configuration 3** involves the polarizer at +45°, the PEM optical head removed from the instrument, and the analyzer rotating through a 360° range at 10 – 100 Hz [16]. In this configuration, the ellipsometer can measure S_0, S_1, and S_2, as it is unable to distinguish left and right circular polarization. However, it does extend the spectral range of the instrument to at least 4.0 μm.

To take a single polarimetric measurement of the full Stokes vector of a sample between 300 – 3500 nm, a measurement in both configurations 1 and 2 needs to be taken at each wavelength. The switch between these configurations should therefore be automated, which can be done using precision rotation mounts. To take polarimetric measurements of samples between 3500 – 4500 nm, configuration 3 is required, which does not include the PEM. It is therefore likely that manual intervention is necessary to remove the PEM and replace it when going back to full polarimetric measurements. This may make the manual realignment requirement [SPG-F-15] difficult to achieve. Automated designs should be considered, and the advantages of additional spectral range for linear polarization measurements should be weighed against the repeatability of all instrument measurements.

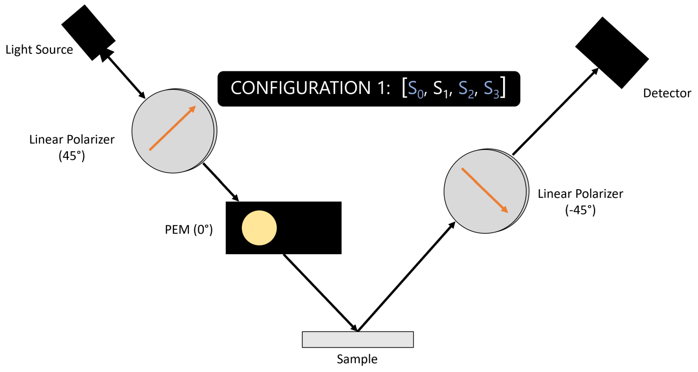

(a) Configuration 1.

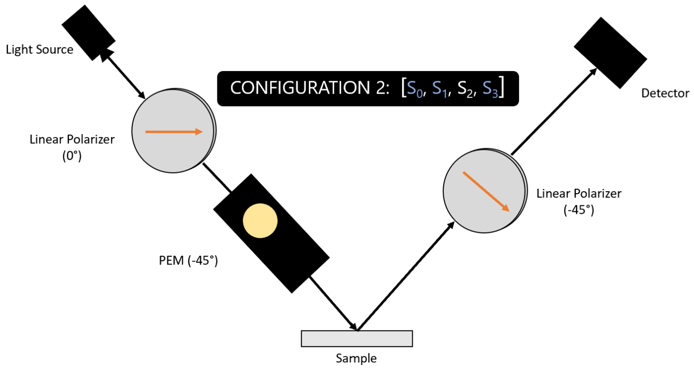

(b) Configuration 2.

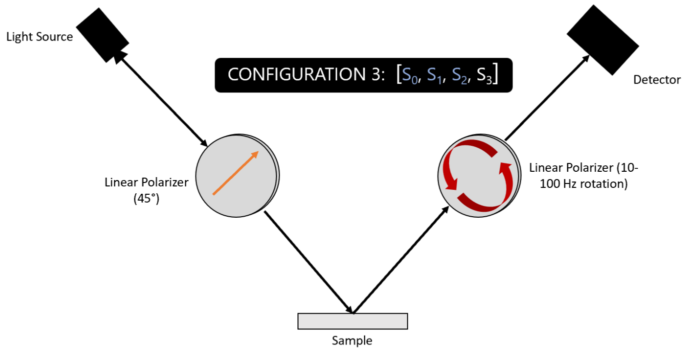

(c) Configuration 3.

Figure 4.13: Polarimetric operating modes for the ellipsometer.

4.8. Architecture Summary

Based on the high-level design decisions made in this section, the overall architecture of the ellipsometer is shown in Figure 4.14. The instrument can be broadly split into three sections. The light source includes the lamp, monochromator, and optical fibre, as well as mirrors and lenses for guiding light through these components. The illumination arm contains the collimating mirror, the polarizer and photoelastic modulator. The observation arm is the final section, and includes the analyzer as well as the detector.

The following section will outline the detailed design decisions, which seek to identify specific components, as well as their sizing and placement.

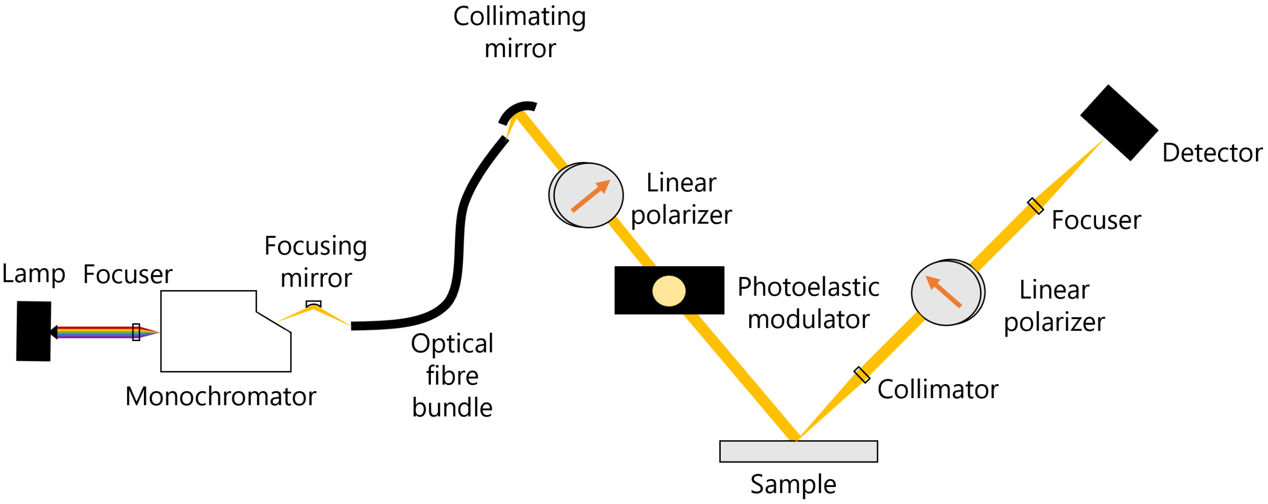

Figure 4.14: Full architecture for the spectroscopic ellipsometer.

5

Detailed Instrument Design

This section outlines the detailed design of each component. Given the high-level design decisions from the previous section, the characteristics and geometry of each component is analyzed at a deeper level. The selection of these components is also verified using the requirements outlined in Chapter 3. Each component of the instrument will be described in an order following the light path through the system, starting with the lamp and ending with the detector. A mechanical analysis of the system is also discussed to address the instrument's goniometric performance, as well as the physical instrument layout in the lab. Additional details such as the instrument budget can be found in Appendix A.

5.1. Light Source

5.1.1. Lamp

Throughput Considerations

In Section 4.1, it was determined that a QTH lamp would be the best option for the ellipsometer as opposed to an arc lamp, as it has high stability and has a safer bulb.

Newport has a wide variety of QTH lamps, which come with a housing that mounts, cools, and condenses the output of the bulb. They also have a separate power supply and controller unit that can be used to adjust the light output. The detailed design of the lamp involves comparing the light throughput of each lamp, as well as thermal, transmission, and stability considerations. The main requirements involved in lamp selection are signal-to-noise ratio [SPG-P-11] and spectral range [SPG-P-03, SPG-P-04]. The main lamp candidates are shown in Figure 5.1.

(a) 1000 W QTH lamp. Figure from Newport [88]. **(b)** 250 W QTH lamp. Figure from Newport [89]. **(c)** 100 W QTH IR lamp. Figure from Newport [90].

Figure 5.1: Lamp and housing options.

The 1000 W option shown in Figure 5.1a was a candidate due to it being the highest power option that Newport provided, which could help meet the signal-to-noise ratio requirements. The 250 W option shown in Figure 5.1b was another candidate, in case the 1000 W option was too powerful or wasteful. It also has a condenser with a lower f-number, meaning more light can be collected from the bulb. Light throughput is typically a critical consideration involved in determining the best lamp for the instrument. The highest power option does not necessarily mean the best light throughput through the rest of the system. Finally, the 100 W infrared option shown in Figure 5.1c was considered as it was the highest power option that used mirrors instead of lenses, ensuring transmission across the entire spectral range.

Each lamp has a thin bulb with a defined height and width. These bulbs emit light in all directions. The lamp housing contains a condenser lens, the job of which is to collect as much light as possible, and collimate the exit beam. This exit beam then needs to be focused onto the input slit of the monochromator. Figure 5.2 shows how light gets focused onto the input slit of the monochromator.

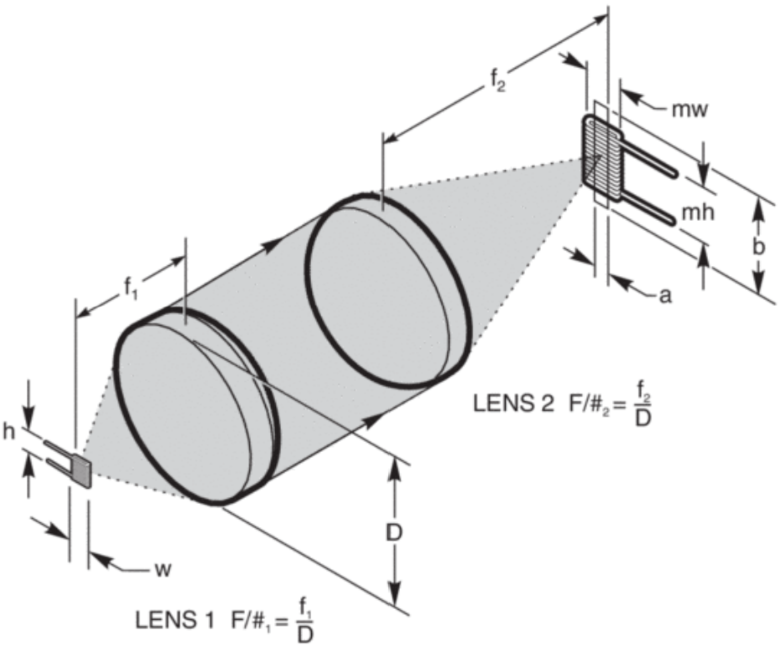

Figure 5.2: Light from QTH bulb being condensed and focused onto monochromator slit. Figure from Newport [91].

The efficiency of light injection into the monochromator can be defined by a term called the vignetting, or V:

$$V = \frac{w_s \times h_s}{mw_b \times mh_b} \tag{5.1}$$

Here, w_s is the slit width, h_s is the slit height, w_b is the bulb width, h_b is the bulb height, and m is the magnification. The magnification refers to how much larger the bulb appears when imaged onto the input slit. It can be calculated as follows:

$$m = \frac{(f/\#)_2}{(f/\#)_1} \tag{5.2}$$

The f-number of the focuser, $(f/\#)_2$, needs to match the f-number of the monochromator for the most efficient light collection [91]. The f-number of the chosen monochromator is $f/3.9$. The f-number of the lamp housing condenser, $(f/\#)_1$, is an option that Newport provides.

While efficiency is important to ensure that stray light is being limited and a lamp is being chosen that is appropriate for the instrument, the main metric is the power throughput into the monochromator input slit. That can be calculated as follows:

$$P = \frac{m^2}{(f/\#)_1^2} \times V \times I_{0.5} \times F_c \times \Delta\lambda \tag{5.3}$$

This power throughput depends on the spectral resolution $\Delta\lambda$ at a given wavelength, but it was chosen to use the infrared region, as that is likely a region with limited signal, as well as important scientific consequences. Other terms in this equation include $I_{0.5}$, the irradiance at 0.5 m from the bulb, a metric commonly provided by Newport for its bulbs, and F_c which is the conversion factor provided by Newport which accounts for the effects of the housing.

Table 5.1 shows a comparison of the vignetting V and power throughput P of each lamp. Since the power throughput is proportional to $1/(f/\#)_1^2$, only the condenser option with the lowest f-number was considered for each lamp type.

Table 5.1: Efficiency and throughput metrics for each of the lamp options. For all calculations, the focuser f-number $(f/\#)_2$ is $f/3.9$, the slit height is 5.5 mm, the slit width is 694 μm, and the spectral resolution is 20 nm.

Lamp Properties	1000 W Lamp [88]	250 W Lamp [89]	100 W lamp [90]
Condenser $f/\#$	$f/1$	$f/0.85$	$f/2$
Bulb Temperature [K]	3200	3400	3300
Irradiance at 0.5 m [mWm^{-2}nm^{-1}]	100	25	15
Bulb Dimensions [mm × mm]	5.0 x 18.0	3.5 x 7.0	2.3 x 4.2
Vignetting Efficiency [%]	0.28	0.74	10.4
Power Throughput [mW]	11.07	14.02	1.78

The 250 W lamp has the most efficient power throughput of any of the systems, despite its lower power. This lower power also means less thermal damage to the housing, and a longer lifetime for the system, as high power light can wear down components over time.

The bulb's thermal emission will be used to generate signal in the infrared. The thermal emission is based on the temperature of the bulb, where a higher bulb temperature results in a higher radiance. Table 5.1 shows the temperatures for each bulb, and the 250 W lamp also has the highest temperature. The full calculations for the lamp emission can be found in Section 6.1.

Transmission Considerations

While the 250 W lamp has the highest throughput and highest emission in the infrared, the housing is not rated for the required spectral range of the instrument. Newport uses a condenser made from fused silica, meaning the transmittance falls off sharply above 2700 nm. In order to reach the targets of interest in the infrared and fulfill spectral range requirements [SPG-P-03, SPG-P-04], a different solution is required.

The IR housing from Newport (shown in Figure 5.1c) uses a protected aluminum off-axis parabolic mirror to condense the light from the bulb, which means it can transmit over the entire wavelength range, and does not suffer from chromatic aberration. However, this IR housing is quite limited from a power throughput perspective. It has a condenser with an f-number of $f/2.0$, and the lack of cooling inside the housing means it can only support up to a 100 W lamp. This makes the 250 W lamp much better from a throughput perspective.

In order to work around this issue, the 250 W lamp condenser will be replaced with a custom condenser. This condenser will use glass materials that transmit over the entire spectral range, to keep the design as similar as possible to the standard condenser. The concept for such a condenser is shown in Figure 5.3. One important consideration is the thermal effects of having the 250 W bulb so close to a mounted lens. Under thermal stress, the lens can stretch and compress, producing unwanted aberrations and potentially damaging the lens. This custom condenser design will require a more concentrated design effort, and will only be addressed at a high level in this work.

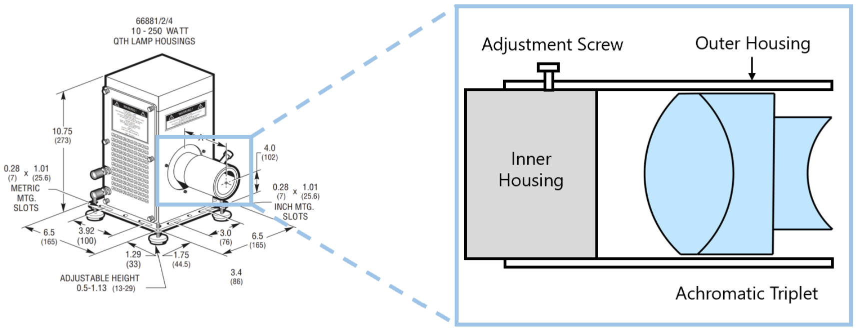

Figure 5.3: Custom condenser design concept. Figure adapted from Newport [92].

5.1.2. Condenser and Focuser

Sequential Analysis

Focusing light into the monochromator is where the highest percentage of light losses occur, due to the small size of the monochromator entrance slit when compared to the magnified image of the bulb, and the fact that the bulb emits in all directions. Table 5.1 shows the magnitude of these losses. The focuser's primary job is to mitigate these losses by catching and focusing light as efficiently as possible into the monochromator, in order to better achieve signal-to-noise ratio requirements [SPG-P-11].

The collimator and focuser for the observation arm were designed before this condenser and focuser combination, and an achromatic triplet of MgF_2 - CaF_2 - MgF_2 worked well for those applications, so it was used again for this condenser and focuser design. Significant light losses were expected between the lamp and monochromator, and thus a triplet would help to maximize the performance here as well. A full description of the material selection and manufacturability considerations is provided in Section 5.4.3. Singlet and doublet designs were also attempted as discussed in the non-sequential analysis part of this section, but the throughput was significantly worse.

The first iteration of this design was completed in sequential mode in Zemax, meaning that light begins at the first surface, the lamp bulb, then enters through each optical surface sequentially. This was later verified and optimized using a non-sequential analysis, where light can collide with surfaces out of order or miss surfaces entirely. This mode also provides more customizability for the light source and the image shape, which in this case is the monochromator entrance slit. The sequential simulation is still useful as a first-pass design to settle on the optical geometry at a high level.

The bulb dimensions are 3.5 mm × 7.0 mm. Light is assumed to radiate in all directions from the bulb, however the light is radiated the strongest in the forward-facing direction due to the bulb design [91]. For this first iteration analysis, light exiting the bulb is given a high angular spread. If the angular spread was too high, Zemax would be unable to complete ray tracing analysis as key surfaces would be missed. However, this high spread is meant to represent the fact that the majority of the bulb's radiation will not be caught by the condenser. Another important attribute of the housing is the back reflector, which is a mirror on the back inside wall of the housing that redirects light out of the condenser, boosting the exit radiance by 60% [93]. This cannot be accurately simulated in sequential mode, so it is simply added as a factor in throughput calculations.

For all Zemax simulations, components were analyzed at the following wavelengths: 300 nm, 600 nm, 900 nm, 1200 nm, 1500 nm, 2000 nm, 3000 nm, 3500 nm, 4000 nm, and 4500 nm. This ensures that the effects of wavelength are being considered in the optimization of each component. The first triplet was optimized using Zemax's angular RMS merit function. This seeks to minimize the root mean square angular deviation of each analyzed beam, with the end result being a beam that is close to being collimated. After a collimated exit beam was achieved for the condenser, a focuser was added in order to inject light into the monochromator. In order to most efficiently inject light into the monochromator, the f-number of the focuser should match the f-number of the monochromator entrance, meaning the lens should have an f-number of $f/3.9$ [94]. Since the exit beam from the collimator is 38.1 mm in diameter, a distance of 148.6 mm will produce the desired entrance cone for the focuser triplet. The triplet's radii of curvature and thicknesses were set as free variables in the optimization, as the diameter and focal length remained fixed. The focuser was then optimized for spot size, which involves minimizing the root mean square (RMS) radius of the spot produced by rays that hit the target image. Figure 5.4 shows the condenser and focuser as optimized in Zemax. Once the focuser was added, both the spot size and the collimation were optimized again at the same time using Zemax's multi-objective optimization for intermediate surfaces. The beam was optimized to be collimated at the entrance of the focuser, while the spot size of the focused beam was designed to be minimized at the slit.

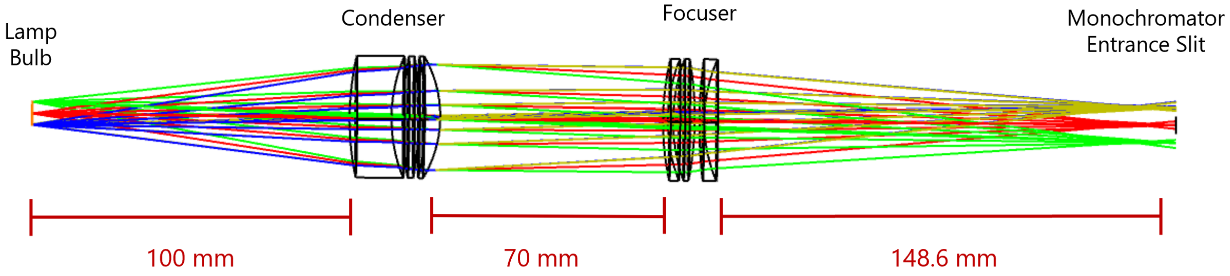

Figure 5.4: Condenser and focuser optimized design in Zemax at 600 nm. Different ray colours correspond to different starting fields on the bulb. Performance across wavelengths is quite similar for this lens configuration and has been omitted for clarity.

Table 5.2 shows a summary of the lens specifications for the condenser and the focuser. Manufacturability was taken into account, using air gaps and constrained radii of curvature and thicknesses. However, in order to maximize performance, slightly larger radii of curvature were used than the constraints that apply to the observation arm collimator and focuser designs. Consultation with custom lens manufacturers will determine if these lenses are still manufacturable with these parameters. A full description of manufacturability constraints is given in Section 5.4.3.

Table 5.2: Lens specifications for the condenser and focuser. The diameter of all lenses is 38.1 mm.

Lens	Material	Front Radius [mm]	Back Radius [mm]	Thickness [mm]	Air Gap After Lens [mm]
Condenser Front	MgF_2	88.340	48.612	13.192	3.505
Condenser Center	CaF_2	101.989	−119.132	5.075	2.062
Condenser Back	MgF_2	−89.314	−37.143	4.699	N/A
Focuser Front	MgF_2	86.127	51.054	1.498	1.689
Focuser Center	CaF_2	53.583	−103.115	6.779	1.499
Focuser Back	MgF_2	148.360	46.693	1.508	N/A

In order to better estimate the light losses from the lamp to the monochromator, the percentage of radiance leaving the bulb that reaches the monochromator slit can be estimated using ray tracing. By adjusting the field and seeing which rays land on the detector with the optimized design, the parts of the bulb that miss the monochromator entrance slit can be determined. For this design, only 0.2 mm of the bulb's 3.5 mm width reaches the slit, and this is only from the front side of the bulb. Similarly, only 2.8 mm of the bulb's 7.0 mm height reaches the entrance slit. This percentage can be multiplied by 1.6 to account for extra reflected light from the back reflector, which cannot be modelled effectively in sequential mode. With w_{bf} and h_{bf} being the respective height and width of the bulb that gets successfully focused into the monochromator, w_b and h_b as the original bulb width and height, and F_{br} as the factor due to the back reflector, the percentage of light that enters the monochromator with this optimized design is therefore:

$$\text{Focusing Efficiency} = \frac{w_{bf} \times h_{bf}}{w_b \times h_b} \times F_{br} = \frac{0.2 \times 2.8}{7.0 \times 14.0} \times 1.6 = 1.4\% \qquad (5.4)$$

This is an improvement over the original estimate of 0.74% due to the optimization of the triplets themselves and the inclusion of the back reflector, however this is a significant loss in intensity that will make prioritization of signal-to-noise ratio critical in other design decisions along the optical track.

Non-Sequential Analysis

The condenser-focuser design was re-modelled in non-sequential mode to get a better estimate of the expected system throughput. In non-sequential mode, a light bulb can be modelled that emits light in all directions, as well as the back reflector. This back reflector cannot be modelled precisely as the specifications are not provided by Newport, but its behaviour can be approximated. Lastly, slits can be modelled in non-sequential mode using non-circular detectors to track light throughput.

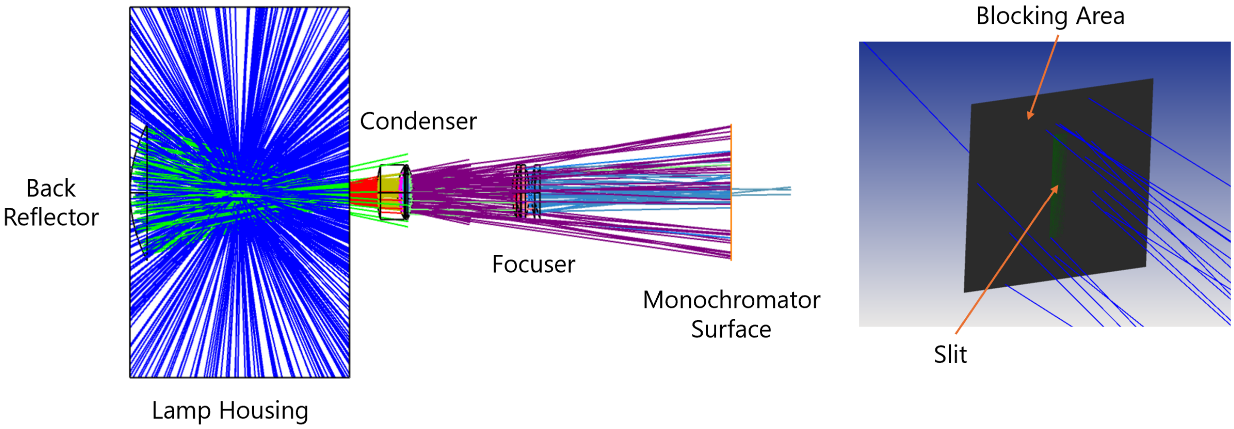

Figure 5.5: Zemax non-sequential visualization of optical track from lamp to monochromator input. The rays are coloured according to the segment of the optical track they are derived from. Dark blue rays are directly from the bulb, green rays have reflected off the back reflector, red rays have left the housing aperture, purple rays have passed through the condenser, and lighter blue rays have passed through the focuser. If rays of a different colour are shown in an incorrect segment, it means that the ray did not reach one of these components of the optical track.

Figure 5.5 shows the non-sequential design, complete with a model of the housing dimensions, back-reflector, and slit. Surfaces such as the housing interior and the blocking area of the slit were given absorbent material properties to show wasted light rays in the process. It is clear that relative to the amount of light emitted by the bulb at the centre of the housing, the amount of light that passes through the monochromator entrance slit is extremely small.

In the visualization, 1000 rays are drawn, while only 2 rays pass through the monochromator. While more rays cannot feasibly be shown due to processing limits, ray tracing can be computed for millions of rays to get a more accurate picture of the losses from the light bulb to the monochromator. Setting the number of analyzed rays to 1×10^6, and the test wavelengths to the same set used for the sequential analysis, a more complete throughput study can be performed using the detector analysis tools in Zemax. These will provide a calculation of the total amount of power that enters the detector. Since the detector has the same dimensions as the entrance slit of the monochromator (0.694 mm × 5.5 mm) and is positioned where the entrance slit would be, it is also providing metrics about the light throughput through the monochromator entrance slit.

The lightbulb power was set to 1 W such that any throughput metrics would be calculated as a fraction of the initial power. This will be compared with the throughput efficiency calculation from Equation 5.4 to confirm its accuracy in calculating the light losses in the system. The detector tool in Zemax reported a total throughput through the monochromator slit entrance of 2.0×10^{-3} W, meaning a 0.2% light throughput. This is lower than the original estimates from the sequential system, likely due to the divergence of light arriving from the bulb. As that divergence is an extended source with extensive error, the condenser is likely collimating light with some deviation. The back-reflector also requires the condenser to accept a wide variety of entrance incidence angles. Based on this deviation from a collimated beam, the focuser would then be unable to focus light as effectively into the slit, resulting in many beams missing the slit.

Optimization of the non-sequential system did not provide superior results over the theoretical throughput from the optimized design of the sequential system (1.4%). As each radius of curvature and lens thickness required optimization, the optimization process had 18 variables. The RMS spot radius was first minimized in the optimization process, however this was not very useful as the monochromator entrance slit was only modelled as a single pixel. It would not matter where the rays land on the entrance slit for this merit function, thus complicating the function for minimal benefit. Instead, it was decided to maximize the total incoherent flux through the slit. This would optimize the design to direct more light into the slit regardless of location in the slit.

One issue could be that the optimizer was required to optimize too many variables at once, and was getting caught in local minima due to the complex merit function. The condenser-focuser combination was therefore redesigned to focus light using singlets and doublets. However, with a similar optimization process, the light throughput decreased by a factor of 10. As the light throughput is already low, further losses of that magnitude would not be acceptable. Therefore, it was decided to return to the triplet design. Overall, the condenser-focuser design could likely benefit from an improved optimization process. A deeper analysis of which parameters are most critical to maximizing throughput would be useful, so as to simplify the optimization. It would also help define more useful constraints for the problem. Another feature that could improve the design is installing a baffle around the condenser and focuser to limit stray light and increase throughput. However, further optimization of the condenser-focuser pairing was deemed non-critical for the purposes of this work.

5.1.3. Monochromator

Focused light then enters the monochromator. The function of the monochromator is to accept polychromatic light and output monochromatic light with a specified spectral resolution, adhering with spectrometry requirements for the instrument [SPG-F-02, SPG-F-03, SPG-F-10]. Newport is a reliable and established monochromator developer, and they were again consulted for the design of the monochromator. Figure 5.6 shows the selected monochromator for this instrument. The monochromator will be programmed for automatic control with a computer and handheld controller. The monochromator also comes with accessories to improve its performance, shown in Figure 5.8. The monochromator can either be a single-output or a dual-output version. However, a single-output version was chosen as the instrument only has one detector and this option limits stray light [94].

Figure 5.6: Monochromator purchased from Newport. Figure from Newport [76].

Custom Grating Design

A monochromator must be selected such that it meets the spectral range [SPG-P-03, SPG-P-04] and spectral resolution [SPG-P-05, SPG-P-06] requirements, and the most critical design aspect is the grating selection. None of the standard monochromators from Newport could meet the spectral range requirement, meaning a custom design was required. To cover the entire spectral range, the monochromator contains a grating turret, which has 4 gratings attached that can be rotated depending on the desired output wavelength. A schematic of the monochromator with the grating turret is shown in Figure 5.7.

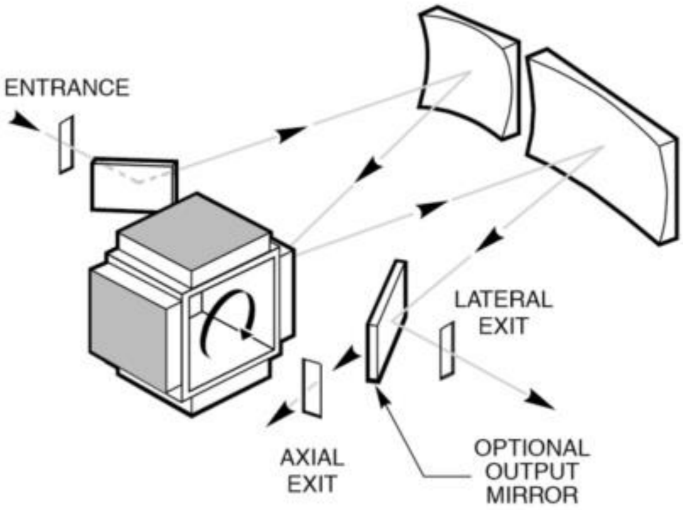

Figure 5.7: Diagram of internal components and grating turret function for Newport monochromators. Figure from Newport [95].

The spectral coverage of the selected gratings are summarized in Table 5.3, along with their groove density, important for calculating the spectral resolution of the instrument. These gratings were chosen through consultation with the optical engineers at Newport, based on a combination of diffraction efficiency and spectral range coverage. There is significant overlap between the gratings. The choice of which grating gets used at which wavelength when overlap occurs will require characterization of the monochromator. Some gratings may have a higher throughput or spectral resolution, or could be more sensitive to polarization in certain wavelength ranges.

Table 5.3: Monochromator grating spectral range and line density specifications [76].

Grating	Spectral Range [nm]	Line Density [lines/mm]
330R [96]	250 – 900	1200
560R [97]	800 – 2300	600
636R [98]	1600 – 3000	200
690R [99]	2400 – 6000	150

Slit Dimensions

Another important factor in the spectral resolution is the slit height and width. The slit width needs to be small enough to adhere to the spectral resolution requirements [SPG-P-05, SPG-P-06], but large enough to allow for sufficient throughput and signal-to-noise ratio [SPG-P-11]. The slit height and width at the entrance and exit of the monochromator should be the same to maximize throughput [95].

In order to reach the necessary spectral resolution of 5 nm in the ultraviolet and visible (UV-VIS) range and 20 nm in the infrared (IR) range, a slit width of 694 μm was selected. Full spectral resolution calculations can be found in Section 6.2. This will be adjustable using micrometer driven slits, shown in Figure 5.8a, which were deemed more reliable than automatic slits. They do however have a repeatability of 10 μm and an accuracy of ±5%, which means this exact slit width may not be precisely achieved. The slit height is also adjustable between 3 and 12 mm [100]. Maximizing the slit height will increase the light throughput, as the magnified bulb size is larger than the slit. However, the total system throughput is limited by components such as the optical fibre entrance. In order to match the dimensions of the optical fibre, a monochromator exit slit height of 5.5 mm was selected.

The slit height and width are both nominal values that can potentially be adjusted based on the wavelength and other experimental parameters. If better resolution is desired to focus on a specific feature, the slit width can be decreased as long as the signal-to-noise ratio remains sufficient for measurement. If better throughput is desired for a certain measurement at the expense of spectral resolution, increasing the slit width can be a challenge. This is because the fibre dimensions will still limit the spectral resolution, and they remain fixed for the chosen slit width and mirror. A method of decreasing the spectral resolution for certain experiments could be through the use of a separate grating that can be added to the turret for specific experiments. Though the fibre dimensions remain the same, the dispersion of light can be modified by changing the grating, thus changing the resolution. However, this use case was not considered further in this design, and should be analyzed in future work if lower resolution measurements are desired.

Filter Wheel

The monochromator uses a diffraction grating to disperse light. Gratings can diffract at higher orders, which will output light of a wavelength of some integer divisor of the target wavelength. For example, an input wavelength of 600 nm will produce higher order diffractions at 600/2 nm, 600/3 nm, 600/4 nm, and further higher orders. This can produce unwanted stray light and affect the quality of results.

(a) Micrometer-driven slits. Figure from Newport [100].

(b) Filter wheel for the monochromator. Figure from Newport [101].

Figure 5.8: Accessories for the monochromator.

To mitigate this, a filter wheel is placed at the exit slit of the monochromator to block these higher order diffractions. This is shown in Figure 5.8b. The filter wheel consists of a series of long-pass filters, which can be adjusted based on the target wavelength. The largest higher order diffraction will occur at half of the target wavelength, with additional diffraction at each successive integer divisor.

Table 5.4 shows a breakdown of the pass bands for each filter in the wheel. One of the filter wheel slots will be left empty as the majority of the optical components, including the detector, do not transmit or accept light below 300 nm, meaning a filter is unnecessary. Another one will be left empty as the entire spectral range can be covered using only five of the six slots.

Table 5.4: Filter wheel passband specifications.

Slot	Model	Passband [nm]	Band where higher orders are filtered [nm]
1	No Filter	>300	300 – 599
2	10CGA-590 [102]	>590	590 – 1079
3	10CGA-1000 [103]	>1000	1000 – 1999
4	EO-68652 [104]	>1650	1730 – 3300
5	EO-68653 [105]	>2400	2520 – 4800

5.1.4. Focusing Mirror

In order to redirect light from the monochromator exit slit to the input of the optical fibre, a mirror is the preferred option because the focal point of the mirror does not depend on the wavelength of light. This means that across the entire spectral range, the mirror will exhibit similar focusing behaviour into the optical fibre. This mirror design is mainly meant to help the instrument reach the signal-to-noise ratio requirement [SPG-P-11].

Mirror Selection

The SHADOWS instrument used a similar layout with a single spherical mirror to focus light into the optical fibre [13]. However, due to the dimensions of the exit slit and the fibre for this instrument, alternatives will be re-examined for this component. The three alternatives are shown in Figure 5.9.

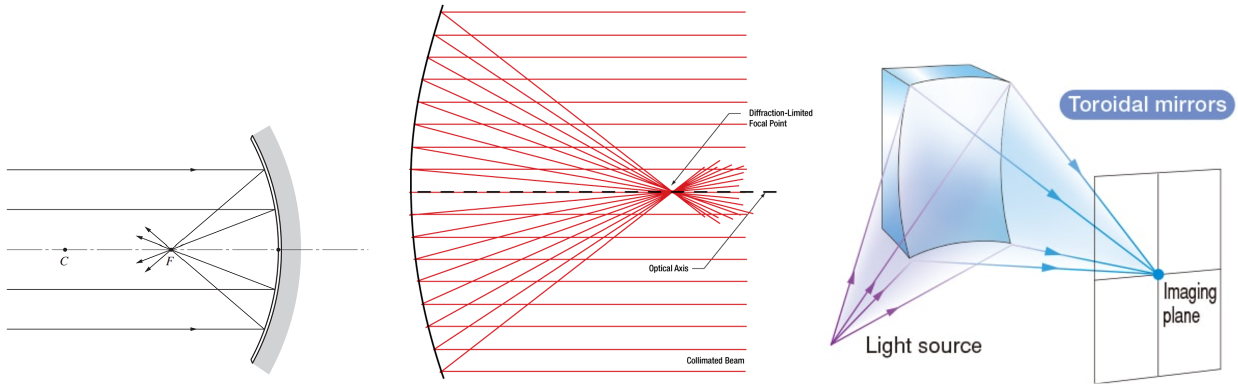

(a) Spherical mirror. Figure from Hecht [15]. **(b)** Parabolic mirror. Figure from Thorlabs [106]. **(c)** Toroidal mirror. Figure from Shimadzu [107].

Figure 5.9: Focusing mirror comparison.

Parabolic mirrors are commonly used for focusing or collimating light and redirecting it in a different direction than that of the incident light. They can also be made off-axis, consisting of a section of a parabolic mirror that is angled to redirect light in the intended direction. Parabolic mirrors are valuable because, unlike spherical mirrors, they do not exhibit spherical aberration [15]. A depiction of spherical aberration for lenses is shown in Figure 5.26b, with the concept being the same for mirrors. However, the parabolic mirror does suffer from astigmatism as shown in Figure 5.10, which is a difference in focus between light entering from two perpendicular planes. Parabolic mirror types were not strongly considered for this application because two would be necessary to effectively focus light into the fibre. If a single parabolic mirror is used, a focused beam input would result in a collimated beam output, and vice versa. They can be used for refocusing off-axis input and output beams, but the focal points would be very distorted and cause significant aberration [106]. This means that an extra surface is necessary to refocus the beam, which can add to signal losses and alignment errors. As reducing the number of components was a key design driver outlined in Section 3.4, the off-axis parabolic design would only be considered if the aberrations for the other two mirror types were too large.

A spherical mirror is another option because only one would be required to sufficiently focus the light from the exit of the monochromator slit to the entrance of the optical fibre. However, spherical mirrors can exhibit higher spherical aberration and astigmatism, making it difficult to focus light into the fibre near the edges of the slit [15]. While these aberrations are not desired, the mirror's heritage on SHADOWS as part of a working design create a compelling case for its inclusion in this instrument.

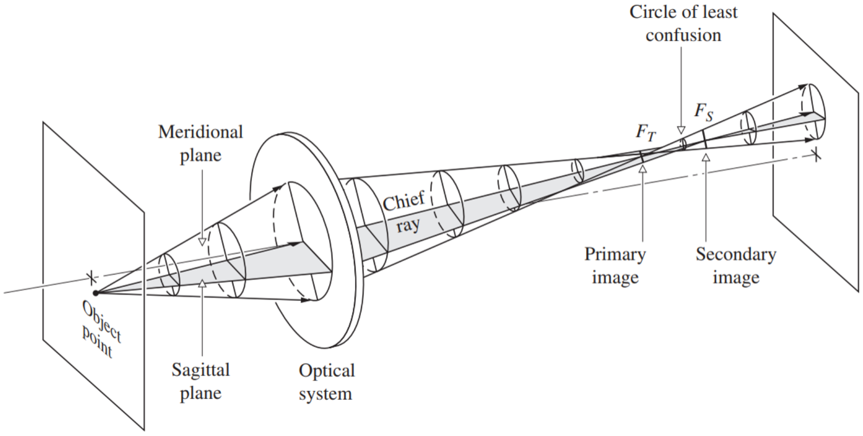

Figure 5.10: Diagram showing astigmatism aberration. Figure from Hecht [15].

The final option is a toroidal mirror, which has a different radius of curvature in the horizontal and vertical axes. This can produce separate focusing behaviour in these axes, and eliminate astigmatism aberrations while reducing other aberrations as well [107]. However, these mirrors have more limited availability and can be more expensive to integrate with the instrument as a result.

The dimensions of the optical fibre input are 0.6 mm × 4.8 mm. The slit width at the monochromator exit is 0.694 mm, and the height is adjustable between 3 and 12 mm. Maximizing the height of the slit could be beneficial for increasing light throughput, but if it cannot be focused into the fibre it is not useful, and could actually be detrimental due to increased stray light in the system. It would be more valuable to match the height of the slit to maintain the same proportion with the slit width as the optical fibre dimensions. This results in a slit height of 5.5 mm. Using this proportion, light can be more efficiently redirected into the optical fibre, even using a spherical mirror with astigmatism.

While the size of the slit and fibre are important, the solid angle of light exiting the monochromator and entering the fibre also need to be optimized to maximize the optical throughput. The monochromator has an f-number of $f/3.9$ at the exit slit, while the optical fibre accepts an angle up to 11.5°. The f-number of the mirror reflection can therefore not exceed $f/2.5$.

There are additional constraints due to the placement of components at the exit of the monochromator. The filter wheel shown in Figure 5.8b is placed after the exit slit of the monochromator, and is 172.5 mm wide and 54 mm thick. The mirror needs to be placed sufficiently far from the monochromator exit to avoid contact with the filter wheel. Additional separation between the optical fibre input and the filter wheel should be kept as heat from the monochromator and filter wheel can influence the optical fibre bundle properties and reduce performance.

Overall, the toroidal mirror performed best given the constraints of the instrument geometry, as the spherical mirror needed to be closer to the fibre input to focus as much light as the toroidal mirror. A toroidal mirror was therefore chosen to focus light into the optical fibre.

Focuser Optimization

With a toroidal mirror, two radii of curvature can be optimized, as well as the distance between the mirror and the fibre input. Optimizing the angle of reflection in Zemax was attempted, but the optimal angle would require the mirror to reflect light back along the axis of incidence. As this is not feasible geometrically, it was instead decided to fix the off-axis angle to be the smallest angle that would comply with the constraints of the filter wheel and monochromator. This results in an angle of 25° between the axis of incidence and the axis of reflection for the mirror.

The rest of the mirror parameters were kept variable for the optimization in Zemax. The merit function was designed to minimize the RMS spot size on the optical fibre surface, and maximize the coupling efficiency of the fibre. Zemax has coupling efficiency metrics for single-mode fibres, however these were not used as multi-mode fibres are used in this instrument design. Instead, the coupling efficiency was maximized geometrically by matching the waist of the Gaussian beam to the optical fibre input. The waist of the Gaussian beam refers to its width at its narrowest point, which can indicate that the beam of incoming light is filling the fibre based on the fibre's acceptance cone and diameter.

Figure 5.11 shows the toroidal mirror configuration used to focus light from the monochromator exit slit to the optical fibre input. Additional surfaces are placed in Zemax to show the clearance necessary for the filter wheel.

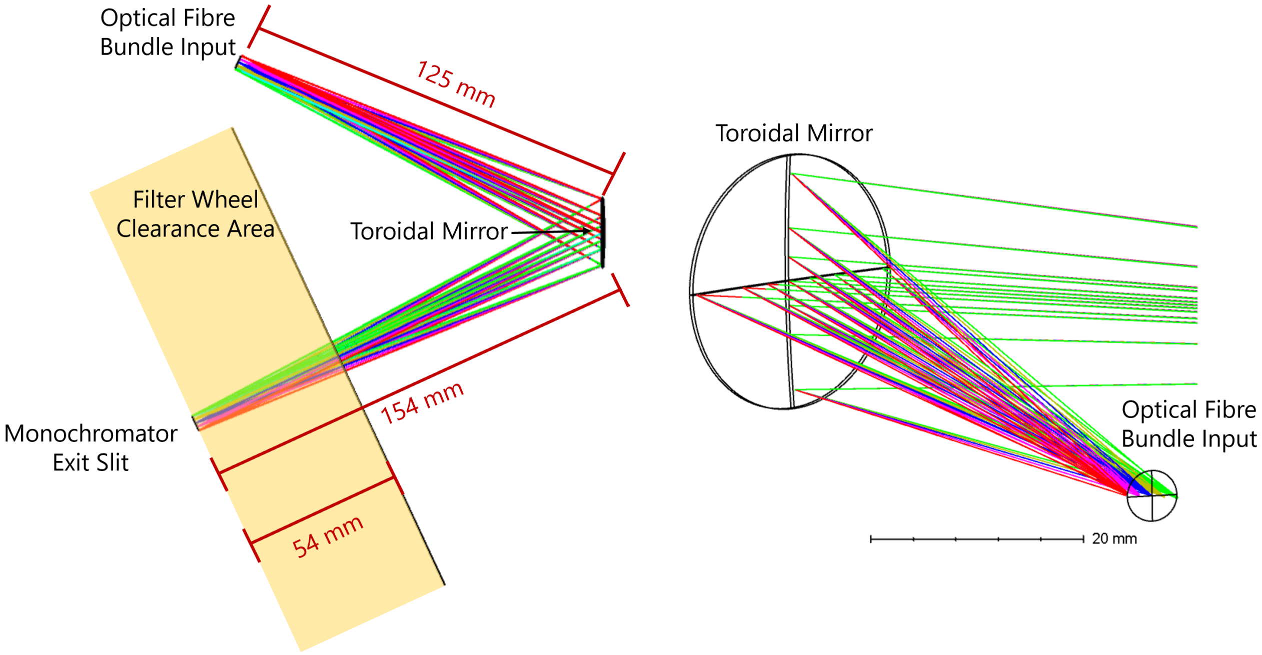

Figure 5.11: Toroidal mirror focuser design in Zemax, including a close-up version and full model. Different ray colours correspond to light starting at five locations spread out diagonally across the monochromator exit slit.

Zemax's coupling efficiency metrics were not very accurate for a multi-mode fibre, as those types of fibres can accept multiple modes at once, and thus are more lenient in terms of acceptance angle. More information on multi-mode fibres can be found in section 5.1.5. Instead, the focusing efficiency of the mirror was calculated by estimating the percentage of beams from the exit slit of the monochromator that land within the fibre bundle input. This was done by adjusting the input field for an optimized mirror until light beams fell outside of the fibre input image, using visual and geometric image analysis tools in Zemax. This is a similar method to the focusing efficiency calculation done in Section 5.1.2. Beams from across the entire width of the exit slit can be focused into the fibre, but the mirror is not able to focus light from the edges of the slit along its height, with only 5.1mm of the slit height focusing into the fibre. The efficiency can then be calculated as the slit area that is successfully focused onto the fibre (focused width multiplied by focused height $w_{sf} \times h_{sf}$) divided by the total slit area (slit width multiplied by slit height $w_s \times h_s$):

$$\text{Focusing Efficiency} = \frac{w_{sf} \times h_{sf}}{w_s \times h_s} = \frac{0.694 \times 5.1}{0.694 \times 5.5} = 92.7\% \tag{5.5}$$

The mirror can therefore successfully focus 92.7% of the light into the fibre, and similar performance can be expected across the spectral range of the instrument due to the use of a mirror. The final dimensions of the toroidal mirror were a primary radius of curvature of −160.37 mm, a diameter of 24 mm, and a secondary radius of −131.89 mm. The mirror is located 154 mm from the monochromator exit slit, and 125 mm from the optical fibre input. Based on these dimensions, light enters the fibre at a half-angle of 4.5°, well below the maximum accepted half-angle of 11.5°. Conversations with Shimadzu [107] or other prominent toroidal mirror providers would be necessary to verify the manufacturability of a mirror with these dimensions.

Due to the small size of each of the fibres in the bundle, it is worthwhile to check the diffraction limit for this system. The diffraction limit refers to the theoretical resolution limit due to the size of the Airy disk, produced when light diffracts through a finite aperture. The diffraction limited resolution d is given by the following:

$$d = \frac{\lambda}{2n \sin \theta_h} \tag{5.6}$$

Here, n is the refractive index of air (1.00), and θ_h is the acceptance half-angle of the optical fibre (11.5°). These terms are defined more clearly in Section 5.1.5. The maximum diffraction limit is at $\lambda = 4.5$ μm, and is equal to 11.3 μm. This is much smaller than the optical fibre diameter 600 μm, and thus is not a limiting factor for the design. All other surfaces in this design are larger than this fibre diameter, and thus the diffraction limit will not be further considered in this work.

5.1.5. Optical Fibre Bundle

The optical fibre bundle is responsible for flexibly transmitting light from the light source to the illumination arm of the optical track. This helps meet requirement [SPG-F-06], as the light source could otherwise not be repositioned relative to the sample. For this, optical fibre manufacturer Le Verre Fluoré was consulted for design and assembly, due to their wide variety of custom fibres and expertise. Table 5.5 shows a summary of the selected optical fibre's performance characteristics.

Table 5.5: Optical fibre specifications summary.

Parameter	Specification
Type	Multi-mode
Material	Fluorozirconate
Sheath Material	Stainless Steel
Numerical Aperture	0.2
Length	2 m
Core Diameter	600 μm
Number of Fibres	8
Minimum Bending Radius	180 mm

The first consideration was whether the fibre would be single mode or multi-mode. Multi-mode fibres can accept multiple modes of light transmission through the fibre, meaning they have a much larger diameter and can accept a higher light throughput. A disadvantage of the multi-mode fibre is that the signal gets attenuated much more quickly with an increasing fibre length, making it unsuitable for long-distance applications [15]. Figure 5.13 shows the attenuation of the signal per kilometre of fibre, resulting in minimal attenuation over the 2 m length of the fibres. The multi-mode fibre is therefore preferred for its high throughput.

The diameter and cladding size was the next major selection. As maximizing throughput was a major goal, the largest standard core/cladding size were chosen for the fibre, 600/680 μm. This comes with a standard numerical aperture of 0.2. The numerical aperture (NA) is a measure of the range of angles over which light can be accepted or emitted by an optical system [15], and is a function of the refractive index n of the medium the lens is in and the maximum angle of incoming/exiting light θ_h:

$$NA = n \sin \theta_h \tag{5.7}$$

Figure 5.12 shows a diagram of numerical apertures for different systems. The throughput into an optical fibre can be increased by a micro-lens array. These arrays can be placed over the input of the optical fibre, refracting light into the fibre and effectively increasing its acceptance numerical aperture. However, for infrared applications, micro-lens array technology is not yet as developed. Building arrays out of materials that transmit in the infrared such as Calcium Fluoride would result in a very brittle and imprecise lens array due to the properties of the material and the procedures needed to manufacture these lenses [108]. A micro-lens array made out of a standard material such as fused silica would result in more losses due to low transmission in infrared than the throughput benefits from using the micro-lens array. Therefore, the fibre input will be unmodified, with a NA of 0.2.

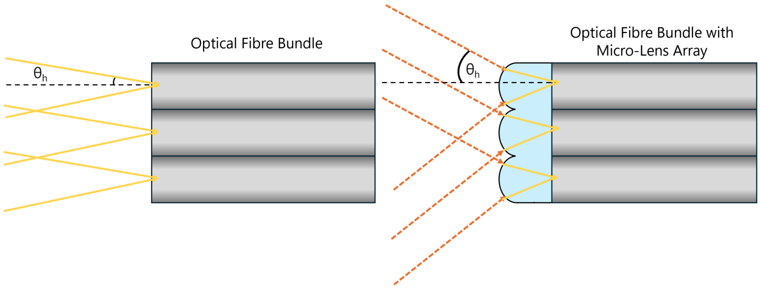

Figure 5.12: The effect of adding a micro-lens array to an optical fibre system.

Optical fibres for transmission in ultraviolet, visible, and infrared are largely manufactured from two materials, fluorozirconate (ZrF_4), and fluoroindate (InF_3). The transmission spectra of both these materials, as well as their attenuation per kilometre, are shown in Figure 5.13. Fluoroindate's transmission spectrum stays above 90% until 4.5 μm, as shown in Figure 5.13b. However, there is a large dip in transmission performance between 0.6 and 1.5 μm, with transmission dropping below 70%. As shown in Figure 5.13a, fluorozirconate cuts below 90% transmission at 3.6 μm, but maintains some transmission throughout the rest of the spectral range, where fewer measurements will be taking place. Additionally, fluorozirconate is half the price of fluoroindate for the same fibre length and diameter. Due to these advantages, fluorozirconate was selected as the optical fibre material.

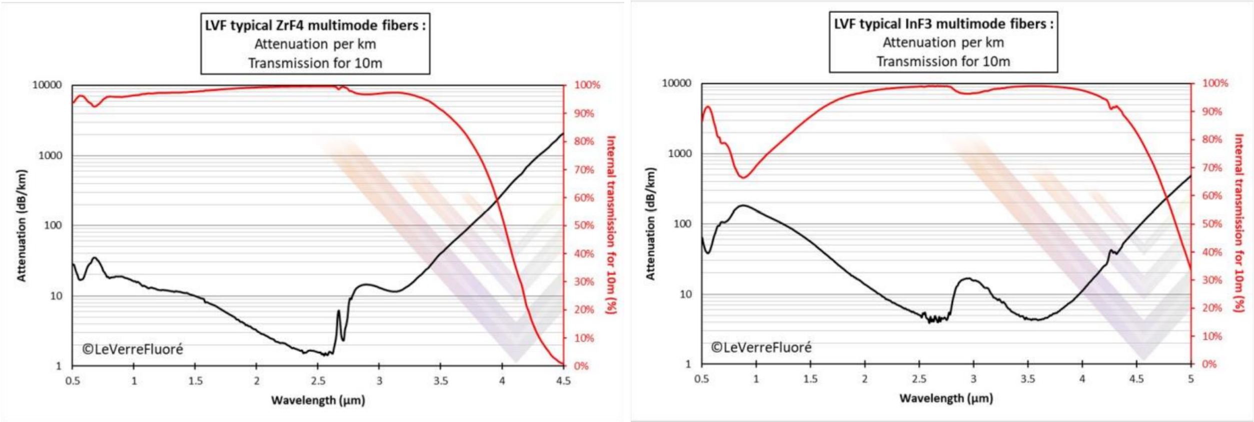

(a) Fluorozirconate transmission plot. Figure from Le Verre Fluoré [109].

(b) Fluoroindate transmission plot. Figure from Le Verre Fluoré [110].

Figure 5.13: Optical fibre transmission comparison.

A fibre bundle is typically used to further increase the throughput or adjust the shape of the input or output of the fibre. The bundle is sheathed in stainless steel to provide extra resistance against damage due to bending or striking. The bundle does limit the minimum bending radius to 180 mm, which limits its maneuverability. This fibre bundle interfaces between the exit slit of the monochromator and a linear polarizer in the illumination arm of the instrument. The exit slit is a thin rectangle with dimensions 0.694 mm × 5.5 mm, so the input to the optical fibre was also arranged linearly to come close to these dimensions. Using 8 fibres as part of the bundle, the dimensions of the linear fibre input are approximately 0.6 mm × 4.8 mm. The linear polarizer is a circular component, and thus the output of the fibre bundle is arranged in a circle. Figure 5.14 shows an image of the optical fibre bundle.

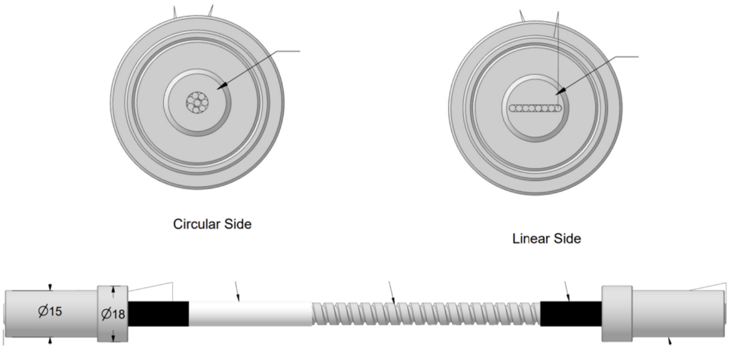

Figure 5.14: Optical fibre bundle orientation drawing, provided by Le Verre Fluoré. The full drawing with dimensions is included in Appendix A.2.

The fibre bundle needs to be long enough to reach the illumination arm in all orientations. Figure 5.15 shows the mechanical considerations for the optical fibre. As the arm will be moving, there needs to be enough slack in the fibre to support some rotation and bending, but not too much slack such that excessive folding or tangling become likely. A length of 2 m was chosen for the fibre, based on the 825 mm arm length. As shown in Figure 5.15a, this gives the fibre twice as much length as strictly necessary, which gives it room for maneuverability without becoming excessive. Adding length also costs €3840 per metre for a bundle of 8 fibres, and causes 0.01 – 0.05 dB per metre of losses due to attenuation, depending on the wavelength [109]. Figure 5.15b shows how the fibre will be attached to the goniometer, such that the attachment point on the illumination arm is always approximately the same distance from the mount. Justification for the attachment point to the goniometer arms is provided in Section 5.2.1.

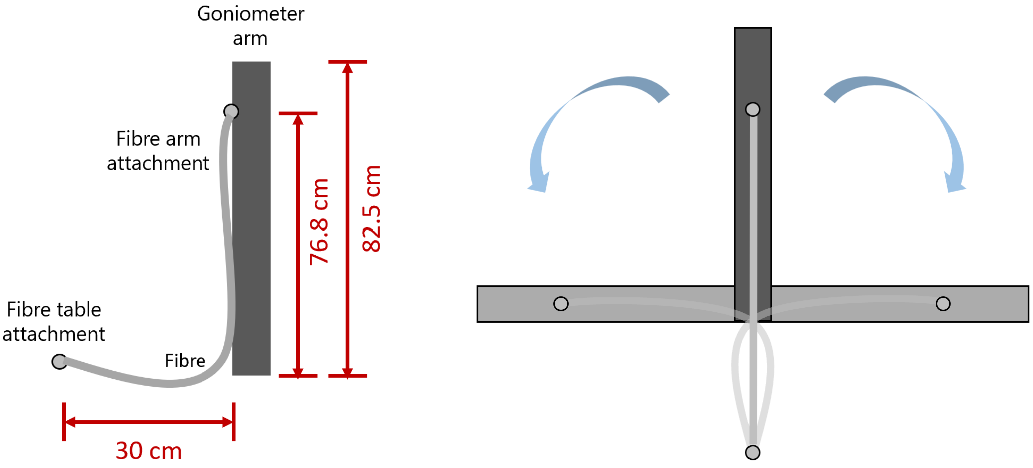

(a) Fibre length with attachment points.

(b) Fibre connection to moving goniometer.

Figure 5.15: Optical fibre mechanical considerations.

5.2. Illumination Arm

5.2.1. Off-Axis Parabolic Mirror

Light will exit the optical fibre in a cone according to its numerical aperture of 0.2. The polarizer and photoelastic modulator on the illumination arm are sensitive to the incidence angle of light. This can change their polarization characteristics, and angles that are too large can cause severe measurement error. It is therefore important that light entering the illumination arm is collimated across the entire spectral range, particularly to meet polarization sensitivity requirements [SPG-P-01, SPG-P-02]. Since light has not yet been polarized, a mirror is an effective choice for this collimator, as its focal point does not change with wavelength.

An off-axis parabolic mirror can effectively collimate light from a focal point and redirect it to a different axis. This configuration is ideal for the illumination arm, as the optical fibre bundle and mounting would otherwise obscure some of the collimated light.

The size of the optical fibre exit bundle will dictate the necessary off-axis angle for the collimator. From the mechanical drawing shown in Figure 5.14, the diameter of the end connector is 15 mm. Typical optical fibre mounts from Thorlabs add $3 - 5$ mm to the fibre bundle diameter [111], bringing the total clearance diameter to 20 mm. As a result, the off-axis angle was set to 25°.

Another constraint for the design of this collimator is the aperture size. The linear polarizer has a clear aperture of 25.4 mm, while the photoelastic modulator has a clear aperture of 27 mm. This means that the beam of light should have a maximum diameter of 25.4 mm to ensure that no light is being blocked in the system. It is also ideal, in accordance with the design drivers outlined in Section 3.4, to have a single component responsible for the collimation, meaning additional refocusing mirrors would be strongly discouraged in the design. This places a limit on how big the collimator can be. Ideally, the collimator would be able to catch all of the light coming out of the optical fibre, which has a fixed exit cone. Since the collimated beam diameter is fixed, there is also a limit on how far the mirror can be from the fibre, while still catching all of the light.

Using these constraints, the collimator was optimized by minimizing the RMS angular deviation of the light rays exiting the mirror. Figure 5.16 shows the results of the optimization in Zemax, with additional surfaces shown to represent the geometric clearance requirements of the optical fibre mount. This merit function will optimize the mirror such that it achieves the best possible collimation across all input locations from the fibre bundle and all wavelengths. However, as there is some deviation in the collimation of the beam, some light is wasted and not transmitted through the polarizer and PEM. At the polarizer entrance, the collimated beam radius is 14.6 mm, and it is 15.5 mm at the PEM entrance. From these diameters, the beam collimation deviation was calculated as 1.05°. What is important to recognize is that this collimation deviation is not because the mirror is out of focus. The fibre exit is an extended source, meaning that it is not a point source. Light coming from the edges of the fibre exit will leave the collimating mirror collimated relative to the other rays of light from the edge of the fibre exit, but relative to the chief ray at the center of the mirror they will have a slight tilt. The degree of this tilt is what is referred to when discussing collimation deviation. This deviation cannot be eliminated, only improved through decreasing the size of the extended source, or increasing the focal length between the fibre exit and the collimating mirror. As the size and numerical aperture of the fibre have been decided, some collimation deviation will need to be accepted in the design. A more detailed explanation of collimation deviation is provided in Section 5.4.1.

There will therefore be some small angle of incidence for most of the collimated light. However, wire-grid polarizers are rated for use at up to 20° angle of incidence [69], and PEM retardation efficiency remains above 98% at angles below 20° as well [112]. Thus, this collimator design should be more than sufficient for this requirement. The dimensions of the off-axis parabolic mirror are a diameter of 25.4 mm, a focal length of 63.5 mm, and a radius of curvature of -126.49 mm.

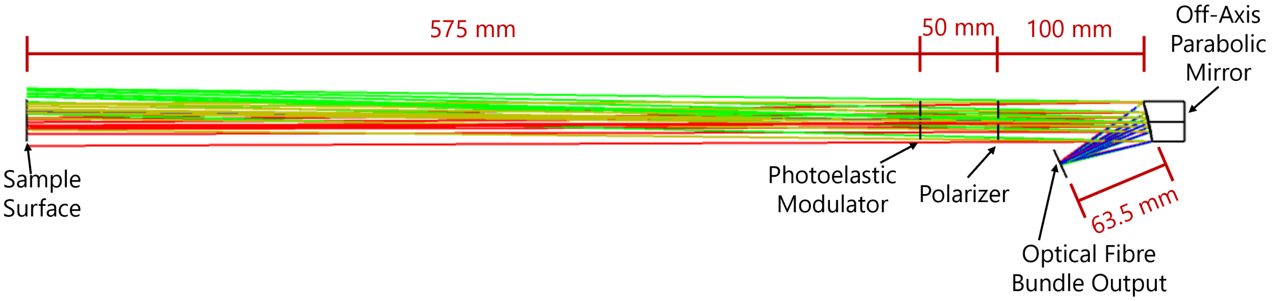

Figure 5.16: Off-axis parabolic mirror collimator design in Zemax. Different ray colours correspond to light starting at four locations along the diameter of the fibre bundle.

5.2.2. Polarizer

The linear polarizers are responsible both for polarizing the light incident on the sample [SPG-F-09], and the light exiting from the sample [SPG-F-01, SPG-F-03]. Two identical wire-grid polarizers will be used in the instrument, one on the illumination arm, and one on the observation arm. They were chosen to be identical for simplicity, as they both have the same polarimetry requirements.

Table 5.6: Polarizer extinction ratio performance [69].

Spectral Range	Extinction Ratio
250 nm – 4000 nm	>10:1
300 nm – 4000 nm	>100:1
600 nm – 4000 nm	>1000:1
2250 nm – 4000 nm	>10000:1

The Thorlabs wire-grid polarizer with ultra-broadband performance, shown in Figure 4.4b, was chosen because it has a relatively wide spectral range and good extinction ratio characteristics [69]. The extinction ratio is a measure of how well the polarizer can block light that is oriented perpendicularly to the polarizer's transmission axis. A higher extinction ratio means that more light is transmitted parallel to the transmission axis relative to perpendicular transmission. The extinction ratio can therefore have an effect on both the linear and circular polarization sensitivity of the instrument [SPG-P-01, SPG-P-02]. The extinction ratio performance of the selected polarizer is shown in Table 5.6.

Figure 5.17: Rotation mount with mounted wire-grid polarizer.

Both polarizers need to be able to be rotated with high precision to a defined azimuth/clock angle. This is important for ensuring the desired performance from the polarizer. Angular errors can have harsh penalties on the polarimetric sensitivity of the instrument. To mitigate these effects, both wire-grid polarizers will be mounted in precision stepper-motor rotation mounts from Thorlabs. These mounts have high accuracy (0.14°) and repeatability (50 μrad) that will be valuable for initial alignment of the instrument and for further adjustments [113]. These rotation mounts allow the system to adhere to alignment requirements [SPG-F-12, SPG-F-14, SPG-F-15]. However, further calibration may be required to allow the system to reach the azimuth angle positioning requirement [SPG-P-18], as this requirement is tighter than the accuracy of the mount. This rotation mount is shown in Figure 5.17.

5.2.3. Photoelastic Modulator

The photoelastic modulator (PEM), when combined with the two linear polarizers, will allow the system to measure both linear and circular polarization. This helps the system achieve all of the polarimetric requirements [SPG-F-05, SPG-P-01, SPG-P-02].

PEM Specification

HINDS Instruments is a company that specializes in the development of PEMs, and were consulted for the design of this instrument. The chosen photoelastic modulator is a PEM-CSC with a 42 kHz Infrasil optical head, shown in Figure 4.5c. This component did not require any customization, and was purchased as a standard model from HINDS. This unit contains a controller, an electrical head, and an optical head. A complete diagram of the photoelastic modulator's electrical setup is shown in Figure 5.18. The controller is the interface with the computer, and can be used to modify the retardance of the PEM. The electrical head is responsible for driving the PEM at the system frequency and the desired retardance. The optical head contains a vibrating crystal which transmits light and modulates its polarization state. Two lock-in amplifiers were purchased separately from HINDS to extract the modulated signal such that it can be converted to polarimetric parameters. The need for two lock-in amplifiers is explained further in Section 6.4.1.

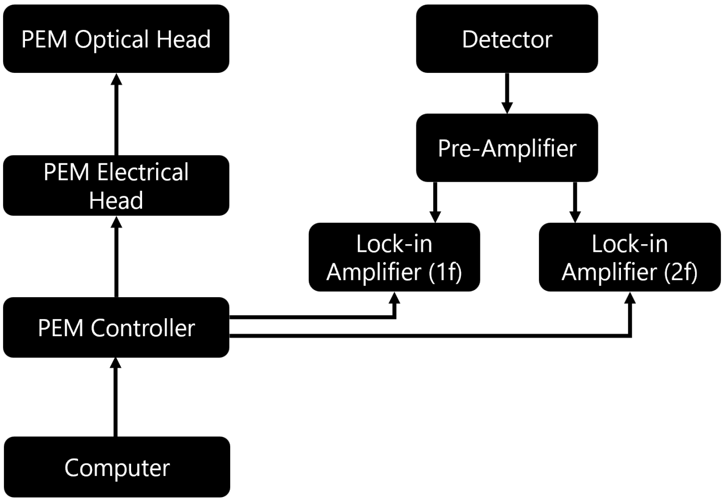

Figure 5.18: Connection layout of PEM and its accessory components.

Infrasil was the chosen crystal material due to its spectral range characteristics [70]. It is able to transmit from 300 – 3500 nm. There were anti-reflective coating options, but none of them improve performance over the entire spectral range. Some coatings improved performance over a certain part of the spectral range, but worsened performance in another, and therefore a PEM without coatings was selected. Figure 5.19 shows the transmission spectrum for the selected PEM.

The clear aperture of the PEM is based on the size of the crystal, which comes standard at 27 mm. This is slightly larger than the 25.4 mm diameter of the polarizer, meaning the edges of the clear aperture may not receive significant light throughput. This is acceptable, as the retardation accuracy decreases with distance from the center of the PEM optical head [112].

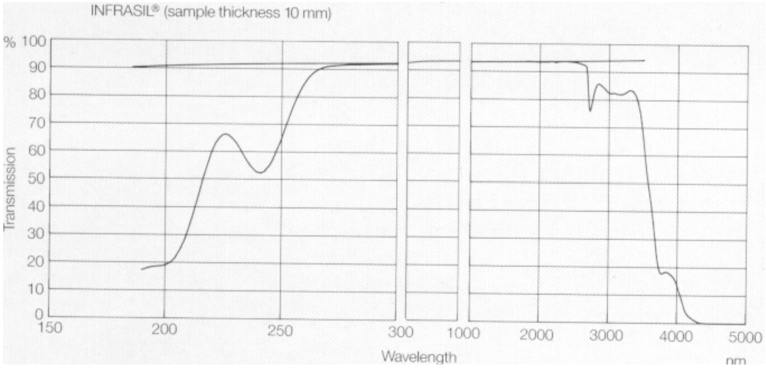

Figure 5.19: Transmission spectrum of PEM optical head. Figure provided by HINDS.

PEM Operation

Generating useful signals from the PEM is more complicated than a standard rotating analyzer or compensator method due to the high-frequency light modulation.

In order to capture both Ψ and Δ, as well as the full Stokes vector, it is necessary to have the PEM in two separate configurations. The first is with the polarizer at 45°, the PEM at 0°, and the analyzer at −45°. The second is with the polarizer at 0°, the PEM at −45°, and the analyzer at −45°. Mathematical explanation of these two configurations is given in Section 6.4.1.

In order to ensure precise rotation between the polarizer and the PEM, and that the PEM maintains a constant angle relative to the polarizer, the PEM will be attached to the same rotation mount as the polarizer using an optical cage system. This system will have an adapter to account for the change in interface size between the rotation mount and the PEM optical head. Figure 5.20 shows how this mount is designed. Since the aperture of the optical head is off-axis relative to the mounting points, compensation was necessary such that the optical head is rotating around a constant point located at the centre of the aperture. Otherwise, the aperture would move as it was rotated, stopping transmission through the system. Thorlabs recommends limiting the torque acting on the rotation mount as much as possible to reduce the risk of damage to the motor or gears. A moment analysis will be performed before this cage mount is installed, and will be made shorter or designed to relieve torque from the rotation mount if necessary. As a collimated beam is passing through the polarizer and PEM, the two components could also be placed right next to eachother, with only the adapter plate between them. This does somewhat hinder accessibility if cleaning or further alignment is needed, but may be required due to torque constraints. The adapter and cage mount design should also be easily removable and replaceable with minimal recalibration, so that the instrument can be used in all configurations with minimal downtime. However, full design of the adapter was deemed out of the scope of this work.

The PEM will modulate the light at a specific frequency, which for the selected PEM is 42 kHz. This means that at this frequency, the light exiting the PEM will cycle between linearly and circularly polarized states, as well as elliptically polarized states in between. Figure 5.21 shows a visualization of this modulation cycle. A lock-in amplifier needs to be connected to the detector and supplied with a 42 kHz reference signal from the PEM controller. In order to capture simultaneous measurements of the frequencies, a second lock-in amplifier needs to be connected to the detector and supplied with an 84 kHz reference signal, which is two times the modulation frequency. The mathematical reasoning behind this setup is explained in Section 6.4.1.

As the detector integrates the signal passed through the instrument, the lock-in amplifier will capture the signal at the modulation frequency. The magnitude of the signal from the lock-in amplifier can then be used to algebraically calculate Ψ, Δ, and the four Stokes parameters.

The PEM can then be readjusted using the controller such that its retardance is $\lambda/4$ regardless of the input wavelength. This is done simply by changing the voltage supplied to the crystal in HINDS' PEM software.

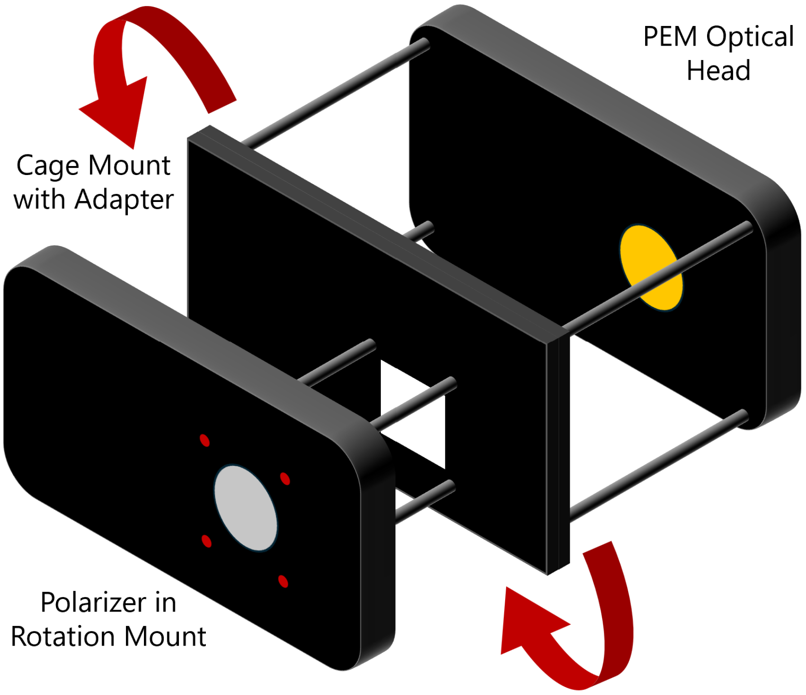

Figure 5.20: Cage mounting concept for polarizer and PEM. Red circles indicate attachment points for the cage mounting on the rotation mount. Red arrows show the directions of rotation for the assembly.

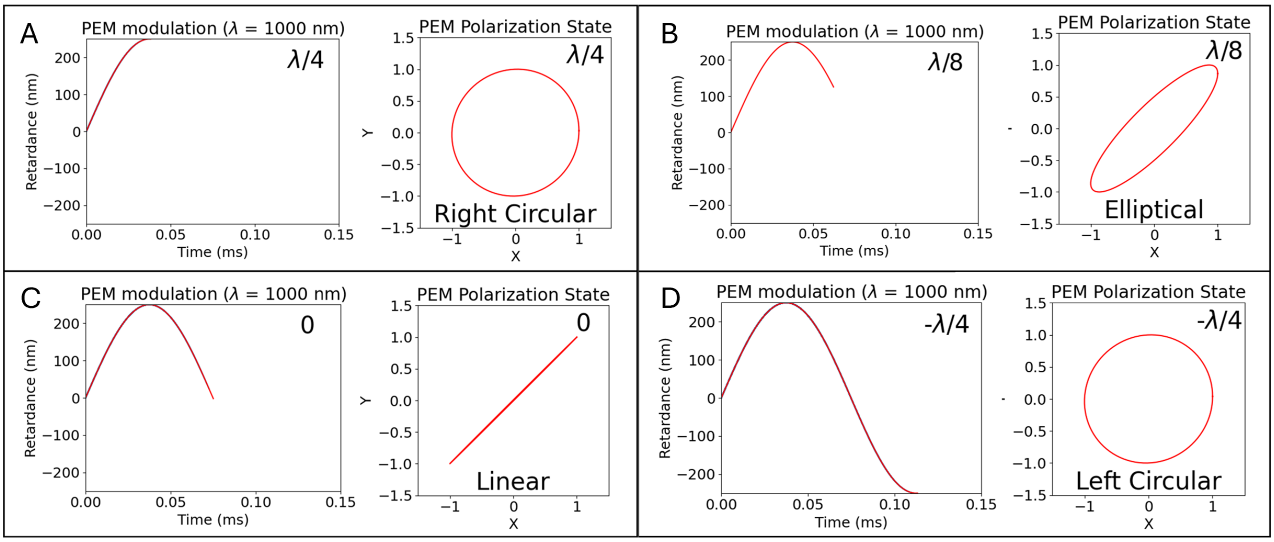

Figure 5.21: Visualization of PEM modulation cycle at 1000 nm. Section **A** of the grid shows a quarter-wave retardance, **B** shows an eighth-wave retardance, **C** shows no retardance, and **D** shows a negative quarter-wave retardance.

5.3. Sample

After light has been modulated by the PEM, it falls onto the sample. The sample will typically be a planetary analogue, made from powder or ice. These planetary analogues will resemble surfaces found on asteroids, comets, and icy moons from a compositional and structural standpoint. As the main focus of this thesis was not the application of this instrument to experiments, future work will address the selection and procurement of accurate sample analogues.

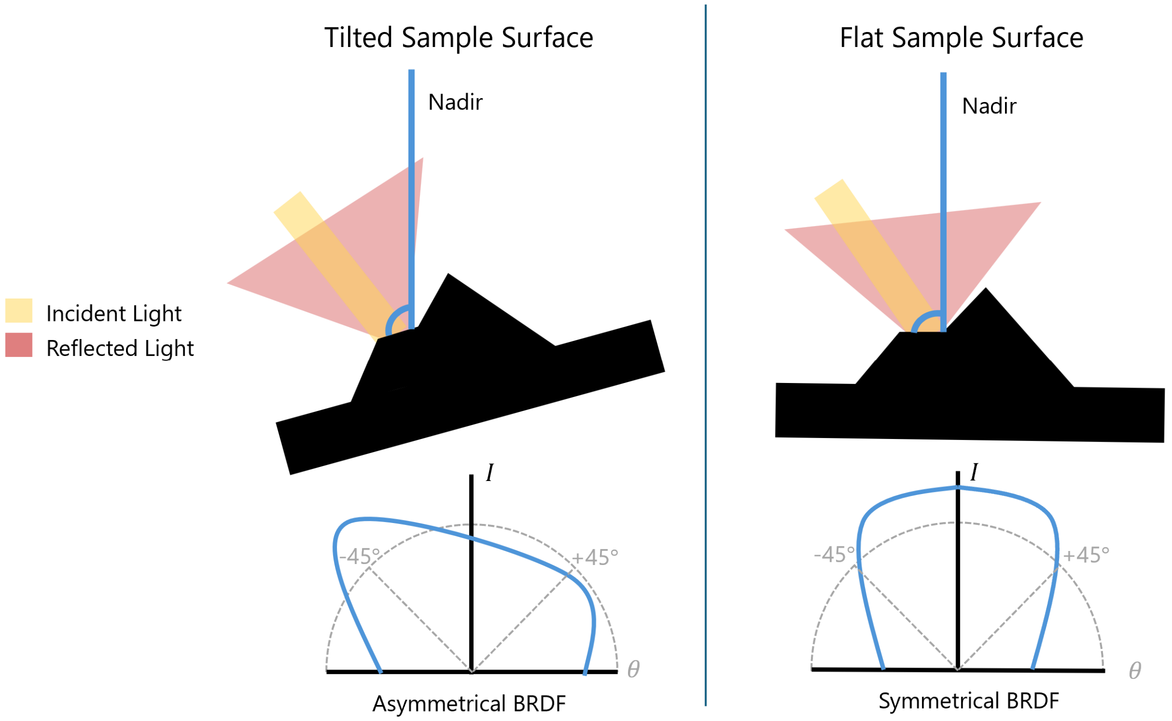

Figure 5.22: An example of how the tip/tilt stage can improve the quality of the reflectance result. The BRDF plots at the bottom of the figure are bidirectional reflectance plots in polar emergence angle coordinates.

The sample will be placed on a tip/tilt stage for manipulation of its position relative to the illumination and observation arms. This becomes especially important when considering the limitations of the goniometric arms of the instrument. For sufficiently flat, isotropic samples, bidirectional reflectance symmetry rules can be applied to limit the required elevation angle range for the illumination arm, as explained in Section 1.1.5. The same can be applied to limit the required azimuth angle range as well. Figure 5.22 shows an example of how moving the sample can help take advantage of reflection symmetry, as the bidirectional reflectance function is more symmetric for a flat sample. If the sample was not flat during measurement, the BRDF would not be symmetric, meaning the illumination and observation arms would need to cross in order to measure the complete BRDF of the sample. This is not possible for the current instrument due to mechanical constraints.

(a) Tip/tilt/rotation stage. Figure from Thorlabs [114]. **(b)** Translation stage. Figure from Thorlabs [115].

Figure 5.23: Components used for sample mounting.

To ensure the sample is horizontal, a tip/tilt/rotation stage from Thorlabs will be used [114], which will be attached to a single-axis translation stage [115] in order to move the sample up and down. These adjustments are also useful for ensuring that the illumination and observation spots both land on the sample in all orientations. Figure 5.23 shows the components used for sample mounting, with Figure 5.23a showing the tip/tilt stage and Figure 5.23b showing the translation stage.

5.4. Observation Arm

5.4.1. Collimator

Light will arrive at the sample in a collimated beam. However, when reflected off the sample, it is assumed that light will exit in a half-sphere of approximately uniform intensity. This is the bidirectional distribution function for diffuse surfaces [15]. It cannot be expected that light will also exit the sample in a collimated beam. Therefore, it is necessary to include a collimator in the observation arm to collect light that has reflected off of the sample. This is again to maximize the performance of the polarizer in the observation arm [SPG-P-01, SPG-P-02], as it can accept a maximum incidence angle of 20°. Since light has now reflected off the sample, it is important to limit the number of reflections before light hits the detector so as not to contaminate the results of the sample reflection. A lens is therefore preferred for collimation, rather than a mirror.

The collimator needs to accept light according to a defined incidence cone. This cone was determined based on a tradeoff simulation between the signal-to-noise ratio of the instrument and the angular resolution of the instrument, as described in Section 6.1.4. The placement of the collimator after the observation arm would have a large effect on these parameters because it dictates the cone of light entering the observation arm. The diameter of the collimator is fixed, due to the diameter of the polarizer being 25.4 mm. In order to not waste any of the light beam, and to limit the number of refocusing surfaces, the collimator should be capable of producing a collimated exit beam with a diameter of 25.4 mm. The cone of light that can be collected by the lens is therefore largely dictated by the distance between the lens and the sample. The distance between the focuser and the detector also depends on this distance between the sample and the collimator on the observation arm. If this collimator distance decreases, more light enters the observation arm, making it more difficult for the focusing triplet to direct it towards the detector face, as the observation arm would have a greater magnification. Based on these considerations and the simulation results, the best compromise between signal-to-noise ratio and angular resolution was achieved at a collimator distance of 180 mm.

The observation spot size was determined through an analysis of the largest spot that would still fit entirely within the illuminated area of the sample at all angular configurations of the instrument. This analysis is described in Section 6.3. The observation area is a circular spot with a diameter of 4.4 mm.

While achromatic triplets are the simplest lens design that can eliminate the most typical optical aberrations, they do not need to be the default option for all scenarios in this instrument. Triplets are more costly, and have more surfaces where signal can be lost due to reflection and absorption. The performance of a singlet lens and a doublet lens was also verified, to confirm if similar performance could be achieved for a simpler lens design. Performance was measured by using the beam diameter at the polarizer. As a large rotation mount is located around the polarizer, light will not be able to pass through the system if it is larger than the clear aperture of the polarizer. It is therefore not worth making the focuser diameter larger in order to focus more light into the detector. The collimated beam diameter should therefore be as close to 25.4 mm as possible. The total losses for a singlet, doublet, and triplet lens will be compared by taking into account their transmittance and the losses due to collimation divergence. Figure 5.24 shows how the collimator can cause these losses. Light enters from three different fields, one in the center and two on the edges of the observation spot. The rays in each field are collimated relative to each other as they exit the collimator, but they are tilted relative to the other fields. This causes the collimation deviation θ_{dev}. Rays that are in the shaded red areas as they approach the polarizer will instead be absorbed or reflected off the mount, and will not reach the detector. It is important to limit the amount of light that falls into this area so that signal-to-noise ratio can be maximized.

These losses can be combined into a single figure of merit used to capture the efficiency of the collimator. The total efficiency of the collimator η_c can be calculated using the following equation:

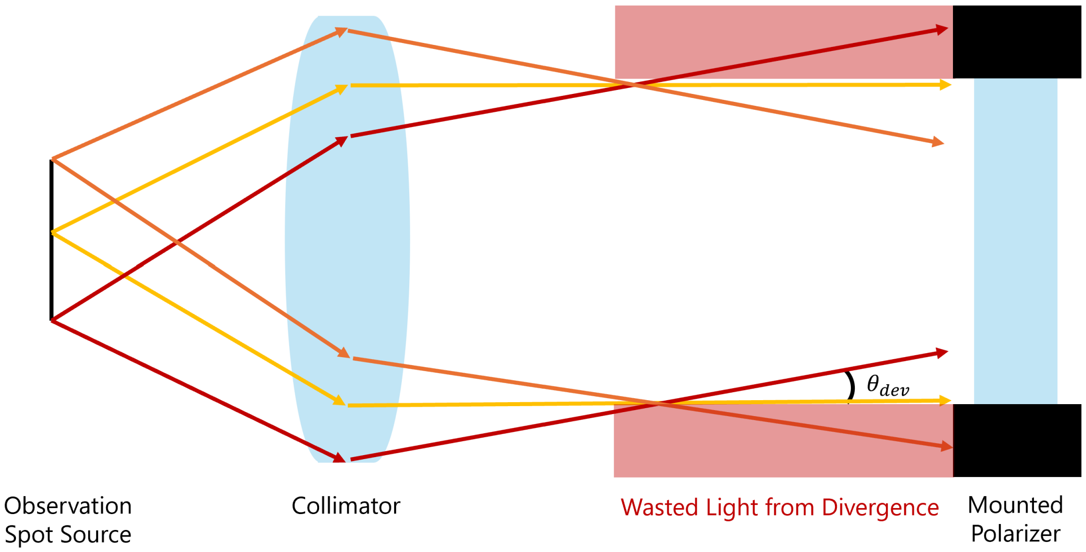

Figure 5.24: Collimator divergence causing signal losses in the observation arm.

$$\eta_c = \frac{r_{pol}^2}{r_{beam}^2} T_c \tag{5.8}$$

Here, r_{pol} is the radius of the polarizer, constant at 12.7 mm. The radius of the collimated light beam at the location of the polarizer is denoted by r_{beam}, while T_c represents the transmittance of the collimator at a given wavelength. For these calculations, the average transmittance across the spectral range is sufficient. Through designing and optimizing these lenses in Zemax, Table 5.7 shows a comparison of the results. Appendix A.3 shows the singlet and doublet collimation performance from Zemax.

Table 5.7: Lens type efficiency study for observation arm collimator.

Lens Type	Beam Radius r_{beam} [mm]	Transmittance T_c	Collimator Efficiency η_c
Singlet	20.56	0.955	0.364
Doublet	16.50	0.899	0.533
Triplet	13.30	0.859	0.783

Overall, a triplet design still has the highest efficiency for collimating the beam from the observation spot, and will be used for the observation collimator as well.

Figure 5.25 shows the collimator on the observation arm, optimized to minimize angular RMS error, similarly to the off-axis parabolic mirror collimator described in Section 5.2.1. The radii of curvature and thicknesses of each lens in the triplet were set as variable inputs to the optimization. The collimator diameter was set to 28.4 mm, as having a collimator that was a little larger than the intended output beam produced a collimated output beam of the desired diameter. The figure shows that the triplet produces a collimated beam across the spectral range of the instrument, and also that the beam fills the 25.4 mm diameter as intended. The collimation deviation on the observation arm is 0.52°.

Table 5.8 shows the specifications for this collimator triplet. The radii of curvature and thicknesses are quite similar to the Hastings standard model from Thorlabs [116], and air gaps are included for manufacturability considerations as well. A full explanation of manufacturability requirements is provided in Section 5.4.3.

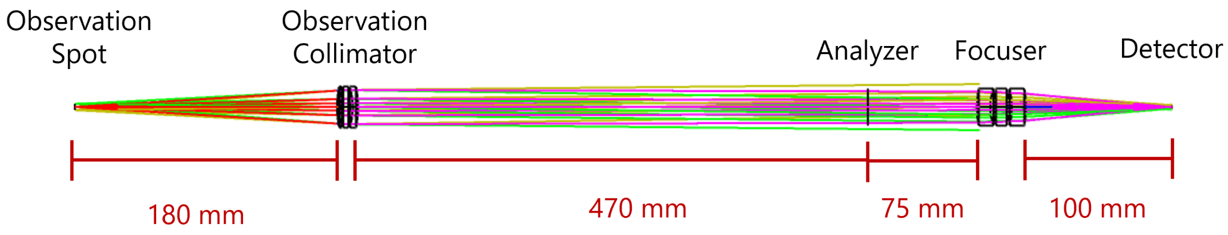

Figure 5.25: Observation arm collimator in Zemax, with the rest of the observation arm also shown. Rays of different colours represent different starting points of light, all placed around the circumference of the observation spot.

Table 5.8: Observation arm collimator specifications. The diameter of all lenses in this triplet is 28.4 mm.

Lens	Material	Front Radius [mm]	Back Radius [mm]	Thickness [mm]	Air Gap After Lens [mm]
Front	MgF_2	76.551	49.551	1.000	1.749
Center	CaF_2	75.652	−76.850	6.126	1.771
Back	MgF_2	−49.137	−78.361	3.953	N/A

5.4.2. Analyzer

The analyzer is the exact same wire-grid polarizer model as described in Section 5.2.2. It will also be placed on a precision rotation mount such that it can be rotated to −45° accurately and continuously rotated between 10 – 100 Hz in configuration 3. A more detailed analysis of the necessary measurement precision for linear polarimetry between 3.5 μm and 4.5 μm is required to determine the rotation frequency of the analyzer in configuration 3, which can be performed in future work.

5.4.3. Focuser

As the detector faces are quite small surfaces, it is necessary to focus the collimated beam exiting the analyzer so that the amount of light hitting the detector is maximized. This helps the instrument meet the signal-to-noise ratio requirement [SPG-P-11].

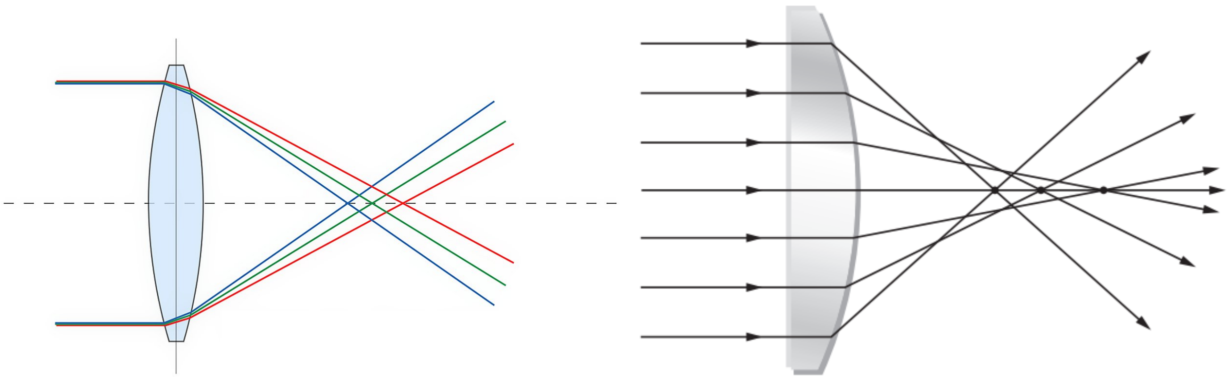

(a) Chromatic aberration, a dependence of the focal point on wavelength. Figure from ESO [117].

(b) Spherical aberration, a dependence of the focal point on aperture. Figure from Hecht [15].

Figure 5.26: Major aberrations for the design of the observation arm focuser.

For this purpose, a lens is preferred, as mirrors can impact the polarization of light in the observation arm, causing measurement errors. While lenses have a reduced effect on the polarization, it will still be important to study how they impact and are impacted by different polarization states during the characterization phase of the instrument.

A major challenge with this lens design is correcting for chromatic aberration, since the detector face is such a small surface. This is also a challenge for the other lens designs described in Sections 5.1.2 and 5.4.1. However, since the focuser has the tightest constraints of these lenses and was designed prior to the other lenses in the instrument, the detailed design process will be explained in this section.

Chromatic aberration refers to a shift in the focal point of a lens as the wavelength changes. The lens will need to focus light onto the detector face at all wavelengths from $300-4500$ nm, with a focus on wavelengths between $300-3500$ nm, meaning the chromatic shift cannot be too large. Spherical aberration is also an important factor, which refers to a change in focal point as a function of distance from the centre of the optical component. Light being focused from the outside of the aperture should also hit the detector in order to maximize the signal. The lens will require a diameter of at least 25.4 mm in order to focus the beam of light exiting the analyzer. The two faces of the detector have dimensions of 2.4×2.4 mm for the UV-VIS face, and 0.7×0.7 mm for the IR face. Figure 5.26 shows the two major aberrations considered in this lens design, with chromatic aberration in Figure 5.26a and spherical aberration in Figure 5.26b. Other aberrations such as field curvature and distortion are not as important for this instrument, as this is not an imaging system.

A singlet lens was first attempted in Zemax, but could not focus light across the spectral range onto the detector face. There was too much chromatic shift, meaning the UV rays would be properly focused, but the IR rays would miss the detector, or vice versa. Another lens was added to cancel the aberration effects of the single lens. This is often referred to as an achromatic doublet. However, over the wide spectral range of the instrument, the chromatic aberration was still too large, causing significant losses in the UV and IR. Figure 5.27a and Figure 5.27b show the chromatic aberration problems for singlet and doublet lens designs. The UV rays at 300 nm can focus effectively on the detector, but the 1200 nm and 3000 nm rays cannot also be focused onto the detector. When the infrared wavelengths are prioritized in optimizing the focuser, the IR rays can focus effectively, but the UV and visible rays will miss even the larger UV-VIS detector face. As will be shown in Section 6.1, the UV and visible regions of the spectrum have relatively low signal-to-noise ratio, meaning neither of these scenarios are acceptable for the focuser.

The simplest lens design that can correct for all of the most critical aberrations is an achromatic triplet [15]. An achromatic triplet consists of three lenses, which are either cemented together or spaced with air gaps. Achromatic triplets combine a positive power (converging) lens and a negative power (diverging) lens which serve to cancel out some of the aberration produced by the other lens. In a typical triplet focuser design, the positive power lens is split in two and makes up the ends of the triplet, while the negative power lens is placed in between. This combination of negative and positive lenses is able to produce enough symmetry to balance longitudinal and lateral aberrations [118].

It was decided to have this triplet prioritizing light being focused onto the IR detector face, rather than the UV-VIS detector face. As the IR detector face is smaller and farther, light that is focused onto it will also pass through the UV-VIS detector face. Since imaging is not a concern, light does not need to be focused onto the UV-VIS detector face, it simply needs to hit some part of the surface.

Material Options

Off-the-shelf triplet designs do not meet the spectral range requirements of the instrument, necessitating a custom design. The first decision involved in this triplet design is the material of each of the lenses. Each lens does not have to be the same material, and sometimes this is more effective as the effects of each material can cancel out some aberrations. The material options were limited to ones in Zemax that could transmit between 0.3 μm and 4.5 μm, the spectral range of the instrument. The list of material options is shown in Table 5.9. Along with a few comments about the suitability of the material for this application, the spectral range of the material and the Abbe number are provided. The Abbe number v_d is a measure of the material's dispersion characteristics, or how much the refractive index changes with increasing wavelength. The Abbe number is therefore a key parameter in selecting materials for the achromatic triplet. It is calculated using the following equation:

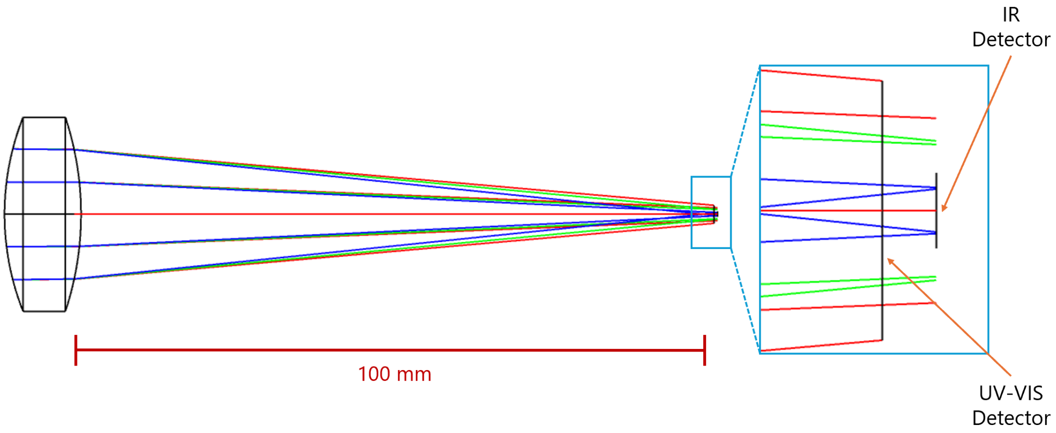

(a) Singlet focuser performance, with a magnified view of the detector shown in the blue window.

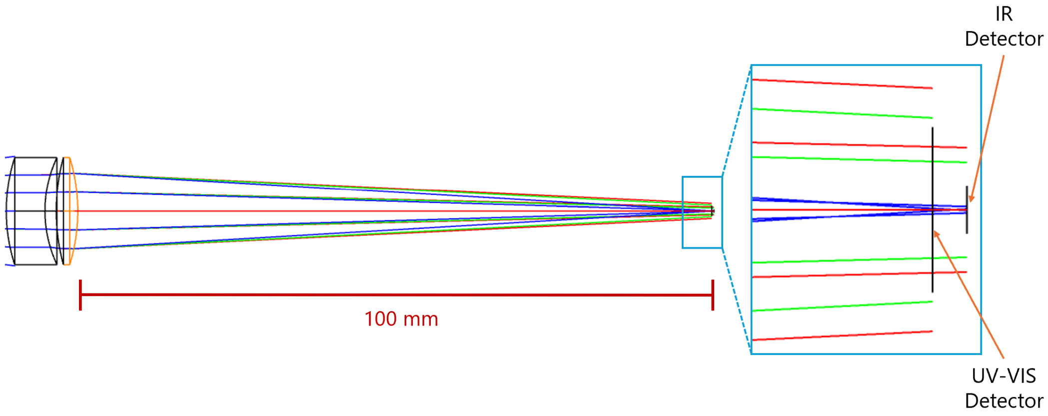

(b) Doublet focuser performance, with a magnified view of the detector shown in the blue window.

Figure 5.27: Chromatic aberration for the singlet and doublet focuser configurations. Blue rays represent light at 300 nm, green rays are at 1200 nm, and red rays are at 3000 nm.

$$v_d = \frac{n_c - 1}{n_l - n_s} \tag{5.9}$$

Here, n_c represents the center wavelength in the spectral range of interest, while n_l and n_s are the longest and shortest wavelengths, respectively. A higher Abbe number is better as it means the material has lower dispersion characteristics.

Based on the available options, the material will be limited to CaF_2, MgF_2, BaF_2, or any combinations of these materials. These materials can be put together in various combinations to examine their chromatic focal shift. However, it is important to be careful with using the chromatic shift as the sole determining factor of the best performing lens. This is because there is actually a desired focal shift due to the two-color design of the detector. A focal shift in the ultraviolet and visible regime may not be a concern, as the detector face for UV-VIS light is much larger. Therefore, chromatic shift will need to be further investigated to understand where this shift is happening and if it is acceptable based on the dimensions of the detector.

Table 5.9: Material options for the achromatic triplet. Feasible options are coloured in green, those that are immediately not feasible are coloured in red, and those with concerns are coloured in yellow. Values are retrieved from the infrared catalog in Zemax.

Material	Transmittance Range [μm]	Abbe Number	Comments
Calcium Fluoride (CaF_2)	0.2 – 9.7	95.0	Common for UV-IR lens applications [119].
Magnesium Fluoride (MgF_2)	0.2 – 7.0	106.2	Common for UV-IR lens applications [119].
Potassium Bromide (KBr)	0.2 – 30.0	32.0	Common for windows but not easily manufacturable into lens shapes. Low Abbe number [119].
Potassium Chloride (KCl)	0.2 – 30.0	43.3	Common for windows but not easily manufacturable into lens shapes. Low Abbe number [119].
Barium Fluoride (BaF_2)	0.27 – 10.3	81.6	Common for UV-IR lens applications [119].
Sapphire (Al_2O_3)	0.2 – 5.5	72.2	Common for windows expensive for lens applications. Somewhat low Abbe number [119].
Strontium Fluoride (SrF_2)	0.21 – 11.5	91.6	Similar properties to other fluoride lenses, but availability is low [119].

Optimization

The optimization and material selection should be done together, as comparisons can only be made between lenses that can focus light onto the detector. Optimization will be focused on minimizing the RMS spot size on the infrared detector face, as well as the RMS wavefront error to reduce aberrations. A standard Hastings achromatic triplet lens was used as the baseline for this design, as it is designed for focusing infinite conjugates, or collimated light [116]. Thicknesses and radii of curvature were kept as free variables in the optimization. An important note about the Hastings triplet is that it is cemented together, so there are only four independent surfaces. Many triplets can instead be air-spaced if optical cement does not exist that transmits the required wavelengths. This will change the performance of the triplet, but was also considered in later iterations to prioritize manufacturability. The distance between the focuser and the detector was also limited between 100 – 300 mm to ensure enough room for assembly and alignment, while keeping the observation arm at a reasonable length based on volume constraints [SPG-C-02].

The CaF_2 triplet was first considered for its relatively low chromatic shift of 3.1 mm compared to other material options. However, the majority of this shift is happening in the infrared region, meaning some rays of light miss the infrared detector face at certain wavelengths. Figure 5.28a shows the focusing capabilities of the lens onto the detector in the UV-VIS (300 nm) and infrared (1200 nm and 3000 nm). These wavelengths are chosen as the visualization wavelengths due to their importance for measuring target species and their spread across the spectral range of the instrument. Light at 4000 nm and 4500 nm was also considered in aberration analysis but are not visualized as the instrument will not have full polarimetric capabilities at those wavelengths. Figure 5.29a shows the transverse focus aberrations, with different colours denoting different wavelengths. It is clear that despite having the lowest overall chromatic shift, the CaF_2 triplet does not have the best performance in the infrared.

A MgF_2 - CaF_2 - MgF_2 triplet was also attempted, and has much better performance in the infrared. Other combinations including BaF_2 and CaF_2 were attempted, but did not perform as well as this combination, and are thus discussed in Appendix A.4 for brevity. Figures 5.28 and 5.29 compare the MgF_2 - CaF_2 - MgF_2 and CaF_2 triplets. It can be seen in Figure 5.28b that the MgF_2 - CaF_2 - MgF_2 triplet has much better focusing performance than the CaF_2 triplet across the entire spectral range. Some UV rays miss the IR detector face, but

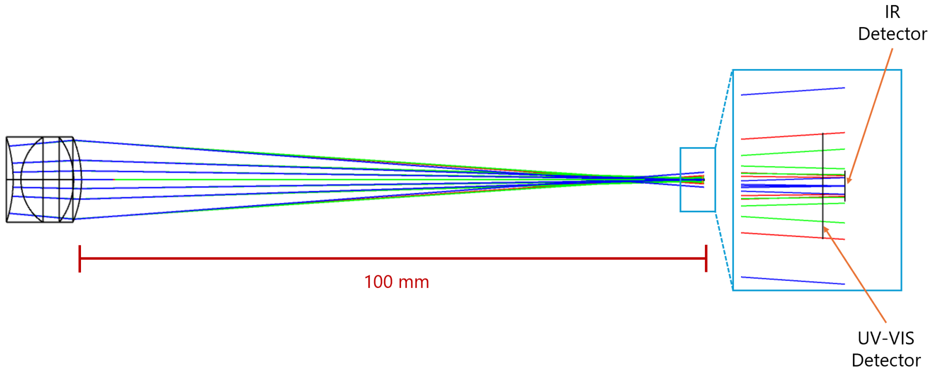

(a) CaF_2 triplet, with a magnified view of the detector shown in the blue window.

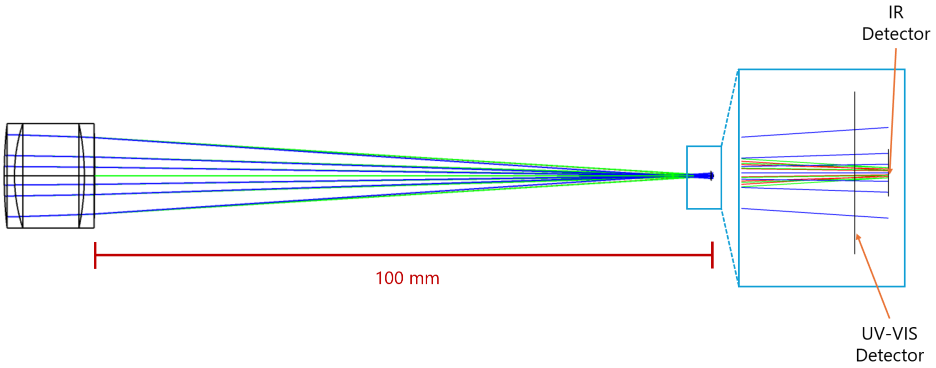

(b) MgF_2 - CaF_2 - MgF_2 triplet, with a magnified view of the detector shown in the blue window.

Figure 5.28: Focuser comparison. Blue rays are light at 300 nm, red rays are light at 1200 nm, and green rays are light at 3000 nm.

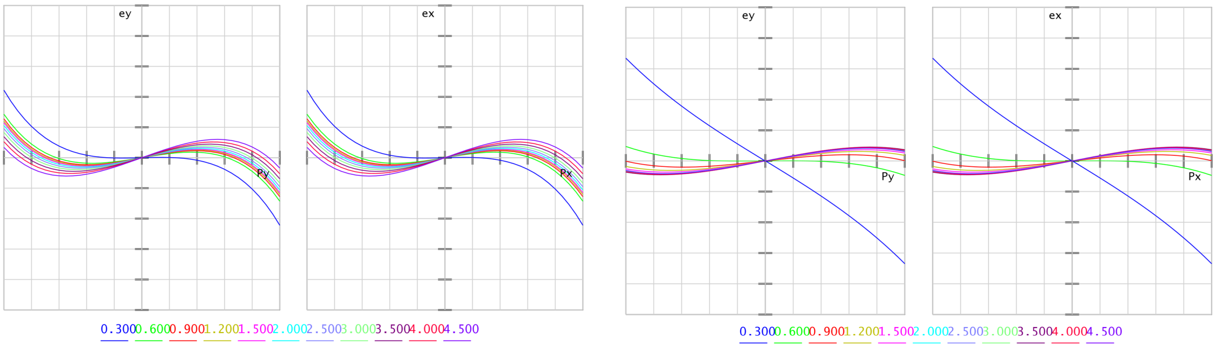

(a) CaF_2 triplet transverse ray aberration.

(b) MgF_2 - CaF_2 - MgF_2 triplet transverse ray aberration.

Figure 5.29: Comparison of transverse ray aberrations. Curves with larger deviations from a horizontal line have a larger transverse aberration.

no rays miss the UV-VIS detector face, while some do for the CaF_2 triplet shown in Figure 5.28a. In the infrared, the focus is much better, with no light missing the detector face at any wavelength. Figure 5.29b shows the aberrations of this triplet, which are much lower than the CaF_2 triplet, save for the single wavelength in the UV. Despite the MgF_2 - CaF_2 - MgF_2 triplet's much higher overall chromatic shift (15.2 mm), the direction of the shift makes this triplet a better option than the CaF_2 triplet.

Manufacturability

As for the manufacturability of this triplet, there are a few considerations to keep in mind. If the lenses are to be cemented together, it will be necessary to find an optical cement with a similar refractive index to the glass being used, that is transmissive over the entire spectral range. Such cement could negatively effect the focus quality of the triplet.

Another consideration is the radius of curvature and thickness of each lens. These parameters must be restricted such that they are manufacturable. With this in mind, radius of curvature constraints and thickness constraints were included in the optimization. The radius of curvature was limited between 30 and 100 mm in order to approximate the radius of curvature of the Thorlabs triplet, which is known to be manufacturable. The triplet is also converted into one with air gaps, such that no optical cement is necessary. While the air gaps can also affect the focus quality of the triplet, optical cement with the appropriate transmittance and refractive index could not be sourced. The thicknesses of each lens and air gap were also controlled via the optimization constraints, as a minimum thickness of about 1 mm is required to ensure manufacturability [120].

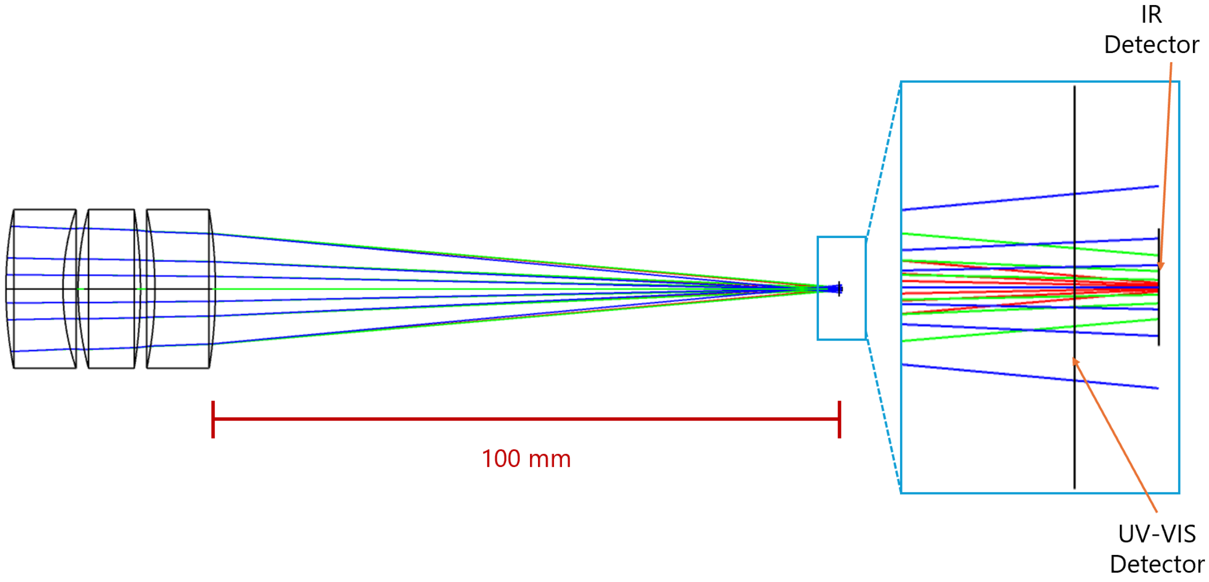

Figure 5.30: Focuser with air gaps for manufacturability. Blue rays indicate light at 300 nm, green at 1200 nm, and red at 3000 nm.

With these new constraints, an improved triplet was designed, as shown in Figure 5.30. The focuser and collimator for the observation arm were also optimized together in Zemax using multi-objective optimization, combining the goals of the collimator and focuser in a single optical system. While the aberration profile shown in Figure 5.31 is worse than that of the previous cemented design, all light still reaches the intended detector face, meaning the primary role of the focuser has been accomplished. The specifications of this achromatic triplet are also included in Table 5.10, as a product of the optimization process.

Table 5.10: Observation arm focuser specifications. The diameter of all lenses in this triplet is 25.4 mm.

Lens	Material	Front Radius [mm]	Back Radius [mm]	Thickness [mm]	Air Gap After Lens [mm]
Front	MgF_2	65.624	39.498	9.142	2.420
Center	CaF_2	48.909	−79.649	10.000	2.305
Back	MgF_2	−62.034	−80.329	9.696	N/A

One important component that has yet to be modelled is the effect that transmission through the UV-VIS detector could have on focus quality on the IR detector. The UV-VIS detector allows IR light to pass through to reach the IR detector. This detector face is made of Silicon, which has a large refractive index of approximately 3.4 in the IR region. This can impact how light is focused onto the rear detector, particularly if light arrives at the detector face off-axis. A potential way to mitigate this is to have 3-axis translation control of the detector position, though the design of this detector mount falls outside the scope of this work.

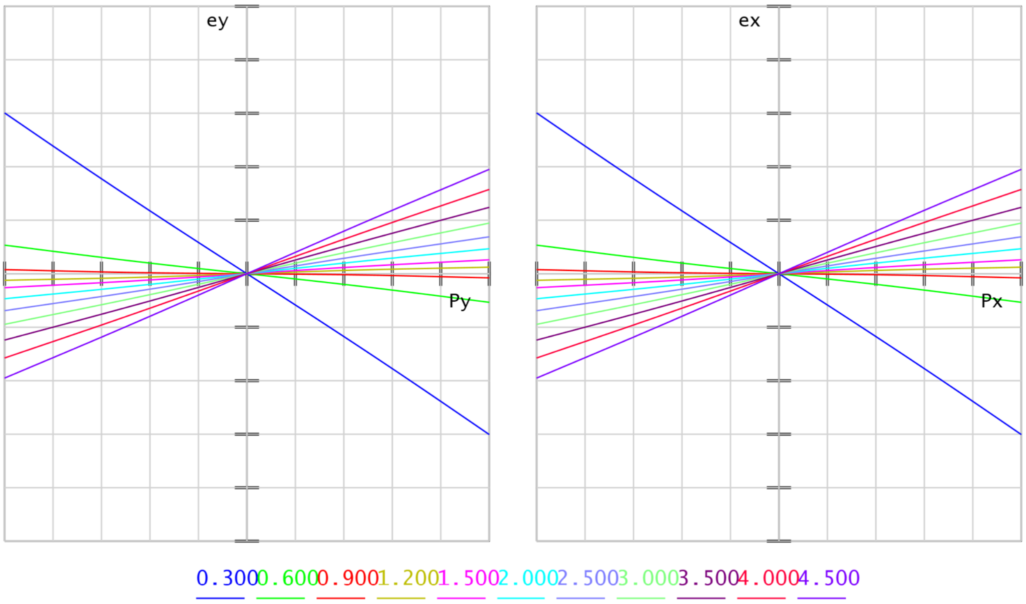

Figure 5.31: Transverse ray aberrations for focuser design with air gaps. Curves with larger deviations from a horizontal line have a larger transverse aberration.

5.4.4. Detector

The detector is required for taking all system measurements, and thus helps the instrument achieve its main spectropolarimetric requirements [SPG-F-01, SPG-F-02, SPG-F-03]. The selected detector is the Hamamatsu K1713-003 two-color detector [86], as shown in Figure 4.9b. It has a spectral range from 0.3 – 5.3 μm, with spectral response curves shown in Figure 4.8. It has a silicon detector face for capturing ultraviolet and visible light with an area of 2.4 mm × 2.4 mm, and a separate indium arsenide antimonide (InAsSb) detector face for capturing infrared light with an area of 0.7 mm × 0.7 mm.

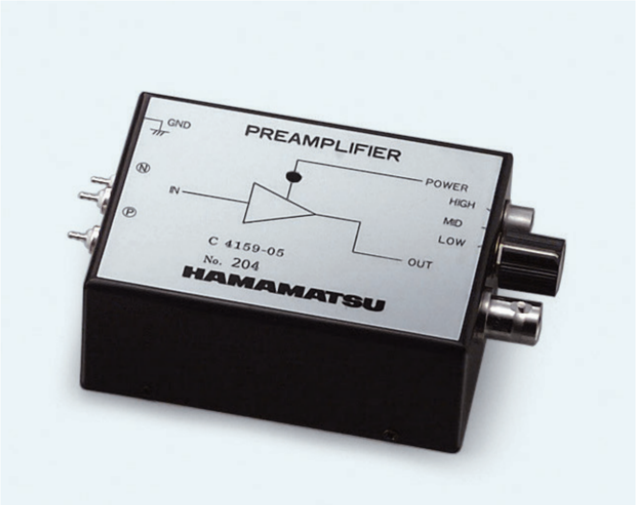

Figure 5.32: C4159 series pre-amplifier used to boost detector signal. Figure from Hamamatsu [121].

The detector also comes with a pre-amplifier, shown in Figure 5.32, to boost the signal and send this signal to the lock-in amplifiers. The C4159 series pre-amplifier has a frequency response from DC −100 kHz, though this could be limited to 60 kHz when connected to the detector [121]. It is required that the maximum frequency response is higher than the modulation frequency of the PEM (42 kHz). However, HINDS suggests that the best performance can be obtained when the maximum frequency response is higher than twice the modulation frequency (84 kHz). This aligns with Nyquist-Shannon sampling theorem, which requires a sampling frequency of twice the signal frequency in order to properly capture a signal [122]. These pre-amplifier limitations may lead to some measurement error, which will be discussed in Section 6.4.5. However, the spectral range capabilities of the detector were deemed valuable enough to accept a non-ideal frequency response performance.

5.5. Mechanical Analysis

In order to meet the movement requirements of the instrument [SPG-F-06, SPG-F-07, SPG-P-14, SPG-P-15, SPG-P-16], as well as the mechanical requirements [SPG-F-12, SPG-F-16], precision rotation stages are required. These will be attached to movable arms to manipulate the instrument into different phase and incidence angle configurations.

5.5.1. Arm Layout and Moment Analysis

The optical components on the illumination and observation arms will be mounted to optical railings. Each railing is 825 mm in length [123]. This length was chosen because it gives each component in the instrument enough room for assembly and alignment, and is a standard size offered by Thorlabs. It also is the longest standard size that meets volume constraints for the instrument [SPG-C-02].

The rotation stages used for the goniometer need to be more powerful than the mounts used for polarizer rotation due to the weight of the arms. Based on the combination of component mass and distance from the rotation stage, the total torque the rotation stage will have to impart can be calculated. The weight of the arms themselves was also taken into account, by taking the total weight of the arm and having it act at half of the arm's length from the rotation stage. Table 5.11 shows these calculations, resulting in a maximum moment of 10.1 Nm. As a result, the RV120BPP high torque rotation stages from Newport were selected, which can impart a torque up to 15 Nm [124]. Figure 5.33 shows the goniometric setup for the instrument, with the rotation stage pictured in Figure 5.33a and the railings pictured in Figure 5.33b.

(a) Rotation stage for arm manipulation. Figure from Newport [124]. **(b)** Optical mounting railings. Figure from Thorlabs [123].

Figure 5.33: Goniometer mechanical components.

5.5.2. Minimum Phase Angle

As described in Section 2.1.5, measurements at different phase angles are valuable for generating phase-polarization curves of asteroid surfaces. However, as the phase angle approaches 0°, it becomes more difficult

Table 5.11: Moment calculations for goniometric arms, with illumination arm components on the left, and observation arm components on the right.

Component	Mass [g]	Distance [mm]	Moment [Nm]
Optical Fibre Mount	30	761.5	0.22
Mirror Collimator	30	825	0.24
Collimator Mount	70	825	0.57
Polarizer	20	725	0.14
Polarizer Rotation Mount	410	725	2.91
Photoelastic Modulator	500	675	3.31
Cage Mount	160	700	1.10
Arm	400	412.5	1.62
TOTAL (ILLUMINATION)			**10.11 Nm**

Component	Mass [g]	Distance [mm]	Moment [Nm]
Collimator Mount	70	180	0.12
Collimator	50	180	0.09
Polarizer	20	650	0.13
Polarizer Rotation Mount	410	650	2.61
Focuser	50	725	0.36
Focuser Mount	70	725	0.50
Detector	10	825	0.08
Detector Mount	100	825	0.81
Arm	400	412.5	1.62
TOTAL (OBSERVATION)			**6.31 Nm**

to get high-quality spectropolarimetric data. There is a geometric concern, as optical components from the illumination arm can block the optical components from the observation arm and vice versa, reducing the signal considerably. Low phase angles also increase the measurement error for ellipsometry setups in the specular configuration significantly, as the p- and s-polarizations become difficult to distinguish [16].

Due to the size of the optical components, the geometric concern is likely the largest factor in limiting the minimum phase angle. This will not be accurately known until the exact mounting geometry for each component with the railing is known. However, estimates can be made using the dimensions of major components on the illumination arm. The largest components are the rotation mount and the photoelastic modulator optical head. The rotation mount has a width of 107.0 mm, while the PEM optical head has a width of 144.0 mm. Assuming the components can be mounted such that the aperture is the only protruding component, this width decreases to approximately 50 mm for the rotation mount, and 56.5 mm for the optical head. A 25.4 mm collimated beam diameter is assumed.

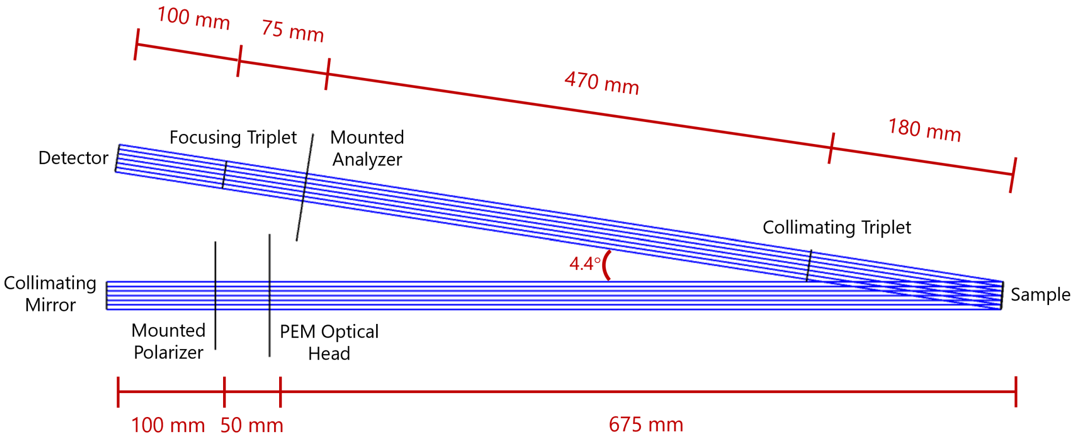

Figure 5.34: Minimum phase angle for the instrument without obscuration.

The goal is to find the smallest separation in phase angle such that none of the components of the illumination arm are blocking the collimated light beam of the observation arm, and vice versa. Modelling these surfaces in Zemax and adjusting the reflective angle was the simplest way to accomplish this. One method of decreasing the minimum phase angle is to move large components further away from the sample. However, this is limited, as it also increases the moment acting on the rotation stage. Especially with large components such as the rotation mount and optical head, they need to stay close enough to the sample to ensure the rotation stage is able to move the arm. As length continues to increase, collimation deviations could start to become a limiting factor, as well as the placement of components such as collimators and focusers, where spacing is critical. Figure 5.34 shows the Zemax depiction of the minimum phase angle achievable when each component is at the distances listed in Table 5.11.

The minimum phase angle with the current instrument configuration is 4.4°, which could be small enough to cover some opposition effects. This phase angle is currently limited by the placement of the observation collimator at 180 mm from the sample. This could also be further limited depending on the placement of the sample relative to the rotation stages.

5.5.3. Instrument Layout

As the lab has limited space for a large instrument, it is important to lay out how the instrument should be set up and operated. The instrument consists of two major sections from a volume perspective, the light source and the goniometric arms. Both the light source and the goniometric arms will be set up on an optical table, because the table can limit vibrations. This will be important for keeping powders in place for accurate measurements, but also to avoid potential interference with the PEM. The goniometric arms only need to rotate in a single axis, as there is no azimuthal control. This means the goniometer can be set up against one of the walls of the laboratory. This saves space in the lab and is safer for other people working in the lab as well.

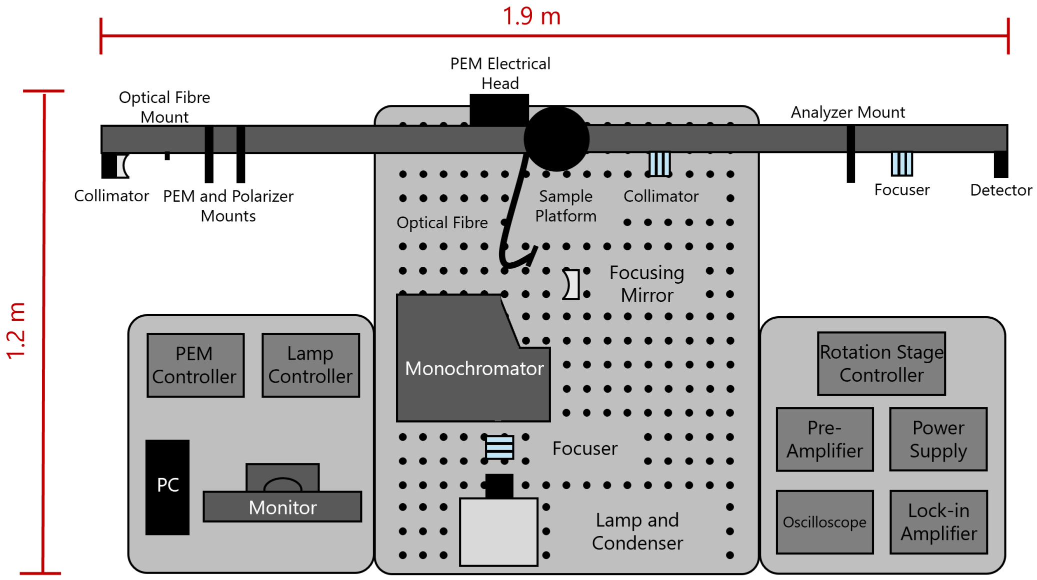

Figure 5.35: Instrument layout, including supporting components. Precise spacing of components is not to scale and is simply intended for illustration.

Figure 5.35 shows the layout of the instrument in the lab. Based on the dimensions of the goniometer and the optical table, the overall volume of the instrument is 1.2 m [depth] × 1.9 m [width] × 2 m [height], which fits within the volume constraints for the instrument [SPG-C-02]. A detailed layout designed in CAD modelling software with accurate component sizing is shown in Appendix A.5.

6

Simulation Results

This section outlines the major instrument simulations, the logic and assumptions behind them, and their results. These simulations are helpful for verifying that the instrument's performance meets the requirements, or for highlighting issues with the design that should be improved.

The simulations discussed in this section include signal-to-noise ratio performance, spectral resolution, illumination and observation spot size analysis, and polarimetric accuracy. When combined, these analyses produce what is typically called an end-to-end simulation, which provides insight into instrument performance from the light source to the detector.

6.1. Signal-to-Noise Ratio Performance

The signal-to-noise ratio (SNR) is a metric related to the quality of the instrument's measurements. The signal represents the total number of photons derived from the light source that reflect off the sample and reach the detector. The signal is the desired part of the measurement that provides useful information. The noise includes the sum of photons received from other sources such as light present in the lab, as well as imperfections in the detector that impact the measurement. A measurement with too much noise or not enough signal can make it difficult to achieve high accuracy. This section will outline the steps involved in calculating the SNR for this instrument.

It is first important to note that this program calculates the SNR incident on the detector. This will be worse than the actual SNR of the system due to the use of a lock-in amplifier. Noise generally enters at different frequencies than the signal, meaning the lock-in amplifier would be able to filter out most sources of noise. The calculations in this program therefore represent a worst-case scenario for the SNR.

6.1.1. Signal

The SNR calculation is split into two major components, the signal and the noise. Both of these terms will be expressed in electrons, e^-. The signal is calculated using the following equation [125]:

$$S_T = \frac{t_{int}\epsilon}{f_{sys}^2 hc} I_{source} T_{tot} \lambda(\Delta\lambda) \tag{6.1}$$

Here, t_{int} is the integration time of the detector, meaning how much time the detector is collecting light during a single capture. ϵ is the throughput efficiency at the aperture stop, which for this system is the monochromator entrance slit. The system f-number, f_{sys}, is the ratio of the effective focal length f of the lamp condenser to its diameter D. I_{source} represents the total irradiance of light incident from the lamp, while T_{tot} is the total transmittance of the entire system. As this system can take spectral measurements, λ and $\Delta\lambda$ represent the incoming wavelength and the spectral resolution of the system at that wavelength, respectively. The equation also includes Planck's constant h (6.63×10^{-34} Js) and the speed of light c (3.00×10^8 m/s).

Table 6.1 shows the input parameters for the signal calculation. The source radiance, system transmittance,

Table 6.1: Constant input parameters for the SNR program. Other parameters such as transmittance, radiance, and spectral resolution depend on the input wavelength and are omitted for brevity.

Parameter	Value
Integration Time (t_{int})	1 s
Aperture Throughput Efficiency (ϵ)	0.74%
System f-number ($f/\#$)	$f/0.85$ [89]
Housing Factor (F_c)	0.13 [93]
Back Reflector Factor (F_{br})	1.6 [93]
Bulb Temperature (T)	3400 K [89]
Detector Areas (A_d)	**UV-VIS**: 2.4 × 2.4 mm [86] **IR**: 0.7 × 0.7 mm [86]
Dark Current (I_d)	**UV-VIS**: 100 nA [86] **IR**: 83 nA [86]
Absolute Detector Temperature (T_d)	298 K [86]
Shunt Resistance (R_{diode})	300 Ω [86]
Bulb Dimensions ($w_b \times h_b$)	3.5 mm × 7.0 mm [89]

and spectral resolution are dependent on wavelength and have more involved calculations, and therefore will be addressed in their own subsections.

Source Irradiance

Newport provides data for the irradiance of its light sources at a distance of 0.5 m from the bulb. Examples of this data are shown in Figure 4.1. This does not take into account the effects of the housing or the back reflector. It also needs to be corrected for the measured distance from the bulb to better fit the application to this instrument. The irradiance of the source I_{source} refers to the radiant flux that is actually experienced by an object located on the surface of the bulb, with units of mW m^{-2} nm^{-1}. These corrections can be made using the following equation:

$$I_{source} = I_{0.5m} \times F_c \times F_{br} \times \frac{(w_b/2)^2}{(0.5)^2} \tag{6.2}$$

Here, F_c and F_{br} are the respective conversion factors for the housing and the back reflector, while $w_b/2$ refers to half of the width of the bulb, or the approximate distance from the bulb filament to the surface of the bulb.

Newport only provides data for the QTH lamp source emission up to 2400 nm, as the fused silica condensers can only transmit up to that limit. Beyond 2400 nm, it was necessary to use the thermal emission of the lamp to calculate the source irradiance. The source radiance of the lamp can be calculated using Planck's law [126]:

$$R_{source}(\lambda, T) = \frac{2hc^2}{\lambda^5} \frac{1}{e^{hc/k_B T} - 1} \tag{6.3}$$

Here, λ refers to the incoming wavelength, and T is the temperature of the bulb. The rest of the terms are constants, including the Planck's constant h, the speed of light c, and the Boltzmann constant k_B (1.38×10^{-23} J/K). The source radiance R_{source} refers to the flux emitted by the light source per unit of solid angle, per unit of projected area, and as a function of wavelength. The units are therefore W sr^{-1} m^{-2} nm^{-1}. It is necessary to convert these radiance units into the same units as the Newport lamp irradiance, by first integrating over the spherical solid angle around the bulb, then applying the housing conversion factor F_c and back reflector factor F_{br}.

$$I_{source,th} = R_{source,th} \times F_c \times F_{br} \times 4\pi^2 \tag{6.4}$$

Figure 6.1 shows the emission over the spectral range from 300 nm to 4000 nm for the 250 W Newport lamp. This was the spectral range for SNR measurements as the polarimetry components did not have available data above 4000 nm. The performance beyond 4000 nm, including the CO_2 ice band at 4.27 μm, is therefore unclear from this analysis and would require characterization of the assembled design.

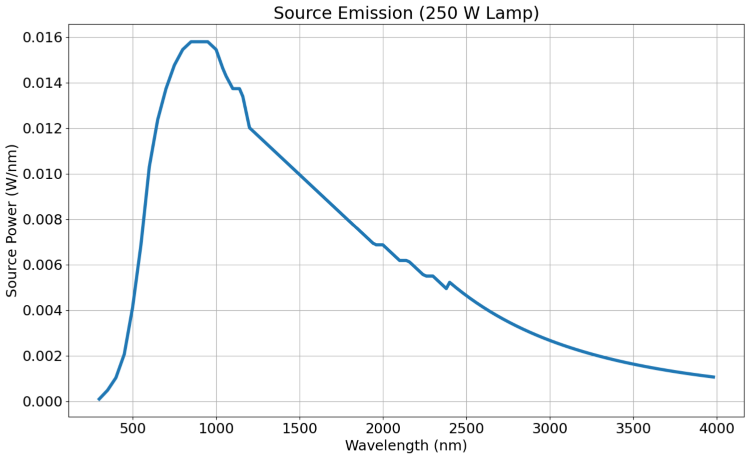

Figure 6.1: Source emission in W/nm from the 250 W lamp.

Total Transmittance

As light travels through the instrument, some signal is lost due to unwanted reflection or absorption by the components of the optical track. Each component has a transmission or reflection spectrum over the spectral range, and the transmittance or reflectance of each component needs to be multiplied together to get the total system transmission. Lenses and polarimetric elements have transmittance spectra, while mirrors have reflectance spectra. For some custom components such as triplets, the transmission spectrum was broken down based on the material of each lens in the triplet. Figure 6.2 shows a general breakdown of the transmission of light through the system. Some major contributors to light losses include the monochromator input, the sample reflection, and the detector. As described in Section 5.1.2, most of the light from the lamp's QTH bulb is lost before entering the monochromator due to the small relative slit size. The effects of inputting white light and outputting monochromatic light are also included in the analysis, as most of the light is also lost inside the monochromator. The sample itself also limits transmission because it has a minimum reflectivity of 10% from requirement [SPG-P-07], and reflects light in a hemisphere, only a small fraction of which can be captured by the observation arm.

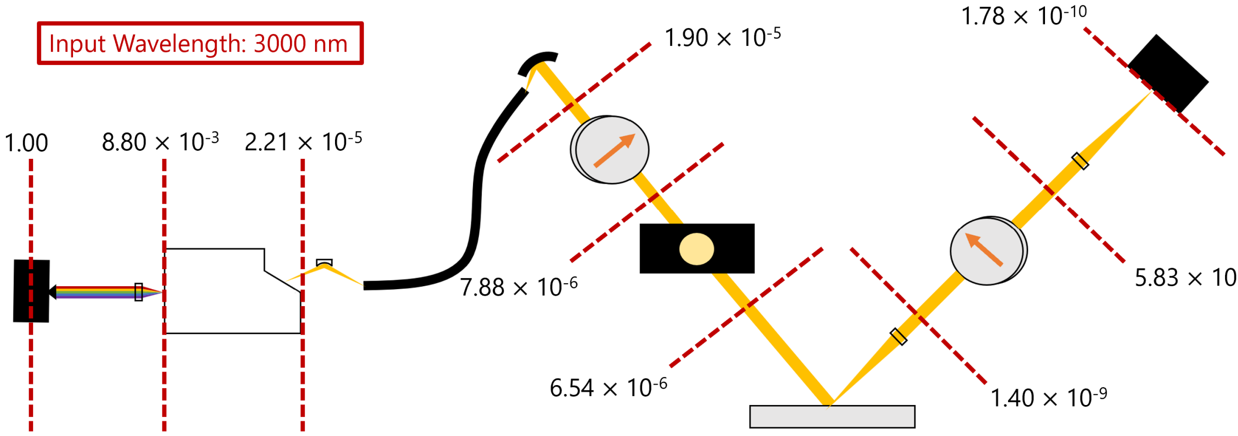

Figure 6.2: Diagram showing light losses through the system from the light source to the detector.

The final significant component of the transmission of the instrument is called the quantum efficiency of the detector. This refers to the detector's efficiency at converting incident photons into electrons that can be interpreted as signal. Hamamatsu does not provide this information, as it can vary from detector to detector. As the detector was not yet received when this analysis was performed, approximations were made to capture the performance. Hamamatsu provides the photosensitivity for the UV-VIS detector, and the specific detectivity for the IR detector [86]. The quantum efficiency η can be calculated using the photosensitivity R with the following equation, with e as the elementary charge constant (1.60×10^{-19} C):

$$\eta = R\frac{hc}{\lambda e} \tag{6.5}$$

The specific detectivity can also be converted to quantum efficiency using the following equation:

$$\eta = D^* \frac{hci_n}{\lambda e\sqrt{A_d \Delta f}} \tag{6.6}$$

Here, D^* is the specific detectivity in cm Hz$^{1/2}$ W^{-1}, i_n is the input noise current (using dark current as an estimate), A_d is the detector area, and Δf is the measurement bandwidth, in this case equal to the spectral range expressed in frequency. Quantum efficiency must be scaled to some value between 0 and 1, and the quantum efficiency of the same detector in the visible range was limited between 0 and 0.45, as calculated from Equation 6.5. The values derived from using the specific detectivity were therefore normalized to these boundaries as a conservative estimate of the quantum efficiency. Further characterization of the detector would provide a more accurate quantum efficiency measurement, which can improve the SNR estimate overall.

The remaining components used transmittance spectra given from manufacturers. Based on the detailed design of the instrument, there are eight MgF_2 lenses, four CaF_2 lenses, and five mirrors (including three inside the monochromator) to consider, as well as the efficiency of the grating, the optical fibre, and each polarimetry element.

Figure 6.3 shows the transmission spectrum for the entire instrument as a function of wavelength. Transmission is very limited in the region from 300 nm to 1250 nm, largely due to the reduced transmission from the detector and polarimetric elements in this regions. Specifically, the band between 1100 nm and 1250 nm has a transmittance of 5.3×10^{-11}, an order of magnitude less than the maximum transmittance. This is the region of spectral range overlap between the UV-VIS detector and the IR detector. Both detectors have reduced quantum efficiency in this region, causing total transmittance to hit a minimum.

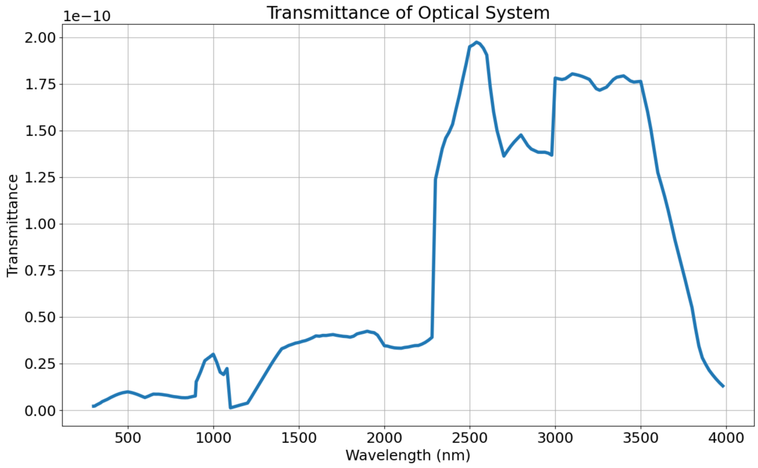

Figure 6.3: Transmittance of the entire instrument, expressed as a fraction of the original light input.

6.1.2. Noise

The other critical element of the SNR calculation is the total detector noise. This does not include factors such as stray light, which are difficult to characterize due to unknown ambient conditions in the laboratory. It instead focuses on typical noise sources involved with detectors used for measuring intensity.

The first type of noise is shot noise, n_S. This refers to random fluctuations in the input beam signal, and is equal to the square root of the input signal, $\sqrt{S}$ [15]. Dark current is also a significant noise contributor for detector systems. This refers to any current that flows inside of a detector when there is no light incident on the detector. The dark noise n_D can similarly be defined as the shot noise of this dark current over the integration period, $\sqrt{I_d t_{int}}$. The final significant contributor to detector noise is Johnson noise n_J. This is defined as thermal noise inside the electronics of the detector. The Johnson noise is expressed using the following equation:

$$n_J = \frac{1}{e}\sqrt{\frac{2k_B T_d t_{int}}{R_{diode}}} \tag{6.7}$$

Here, T_d is the absolute detector temperature, set to 298 K based on expected ambient conditions in the lab, and R_{diode} is the shunt resistance of the detector, which is 300 Ω for the Hamamatsu two-color detector [86].

Other noise sources exist, such as the quantization noise, readout noise, and reset noise, however their contributions were calculated to be negligible for this instrument. The total noise can then be calculated by adding the significant noise constituents in quadrature:

$$N_T = \sqrt{(n_S)^2 + (n_D)^2 + (n_J)^2} \tag{6.8}$$

6.1.3. SNR Calculation

Having calculated the signal and noise, the SNR can then be calculated as the ratio of the two. For systems that can have a large variance in the SNR over the spectral range, it is common to logarithmically scale the SNR using the decibel (dB) system. The SNR is therefore calculated in dB using the following expression:

$$\text{SNR [dB]} = 10\log_{10}\left(\frac{S_T}{N_T}\right) \tag{6.9}$$

6.1.4. Tradeoff with Angular Resolution

The SNR program is also quite valuable for determining how much light should be captured by the observation arm. The placement of the collimator described in Section 5.4.1 is important because it directly determines the cone of light that is captured by the observation arm. Changing the position of this triplet directly impacts the SNR, as well as the angular resolution of the system. The angular resolution of the system is defined in Section 3.3. Figure 6.4 shows the effect of moving the collimator triplet on these system properties.

If the collimator is very close to the sample, a larger cone of light will be collected by the observation arm, increasing the signal incident on the detector. However, the angular resolution would then decrease. This would make it more difficult to differentiate between bidirectional reflectance distribution functions produced by different surfaces, particularly between surfaces with small grain sizes. A collimator placed farther from the sample will improve the angular resolution, but may not guarantee enough signal at the detector for high quality measurements. The collimator should therefore be placed at a position which balances both of these requirements.

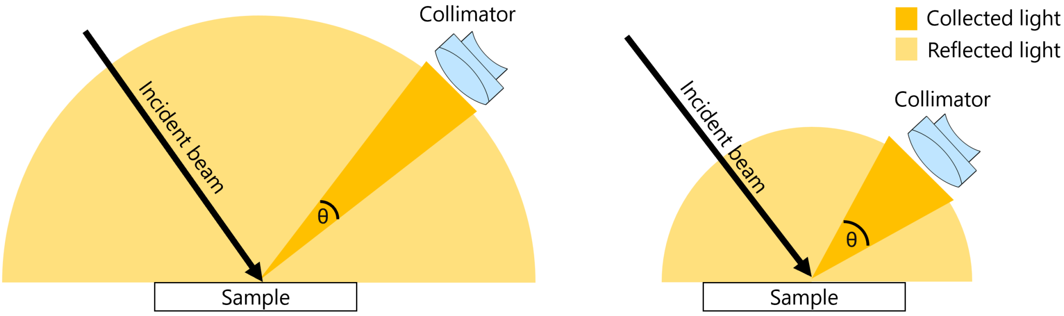

Figure 6.4: The effect of collimator placement on the angular resolution and SNR of the instrument.

Figure 6.5 shows this tradeoff graphically depicted. Based on the angular resolution and SNR behaviour, 180 mm spacing was chosen as an appropriate compromise. This results in an angular resolution of 8.0°, and an average SNR of 35.3 dB. Considerations during the assembly phase, especially those involving the minimum phase angle of the instrument, may require this placement to be reevaluated.

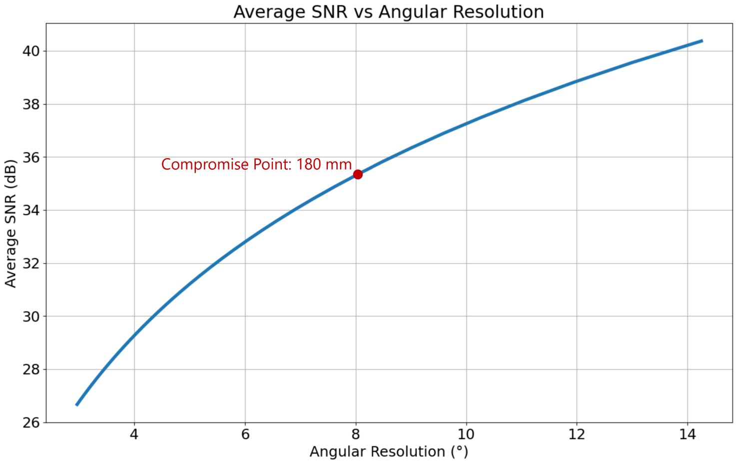

Figure 6.5: SNR plotted against angular resolution.

6.1.5. Lamp Detailed Design Tradeoff

The SNR code was also used to evaluate the performance of each lamp option outlined in Section 5.1.1. Figure 6.6 shows the SNR of each lamp option over the spectral range.

The small discontinuities at 2400 nm are due to the estimation of the IR emission of the lamp using Planck's law. The 100 W and 1000 W lamps have a lower SNR in the visible range because the condensers collect less light than the 250 W option. The 250 W lamp also has a higher SNR in the infrared region because the bulb burns at a higher temperature. Overall, the 250 W lamp is the most efficient option for the system, and provides the highest SNR over the entire spectral range. Therefore, the SNR analysis further confirmed the decision to use the 250 W lamp for the instrument.

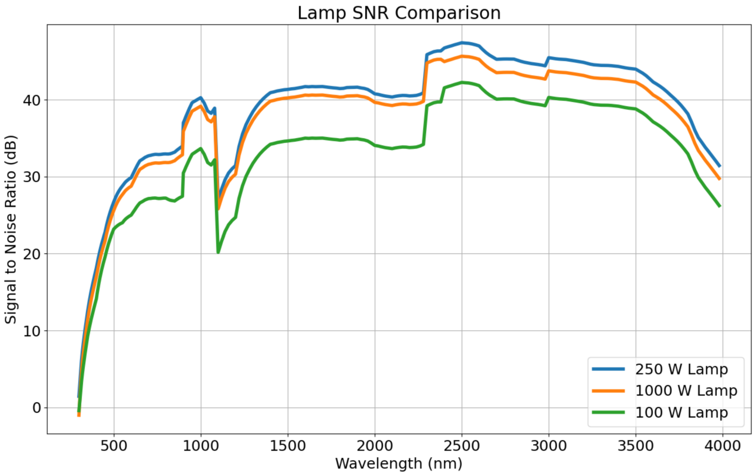

Figure 6.6: SNR comparison for the lamp options.

6.1.6. SNR Final Results

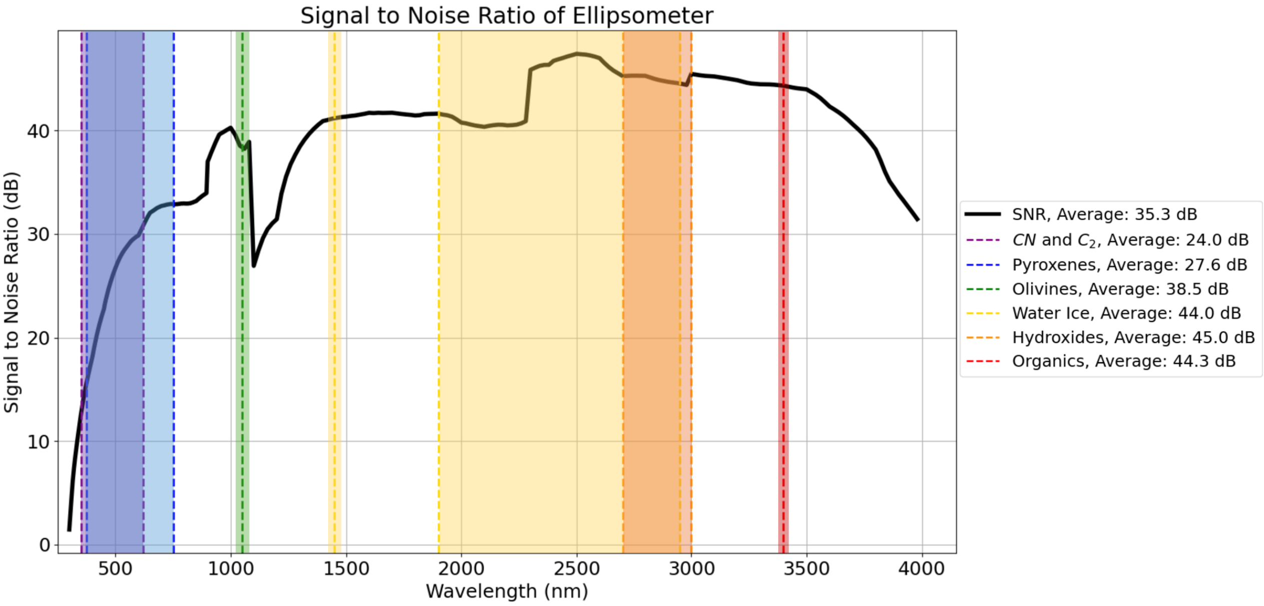

Figure 6.7: SNR over the spectral range, with spectral targets labelled.

With the chosen lamp and collimator distance, the SNR is shown as a function of wavelength in Figure 6.7. The target species for the ellipsometer are included in the plot to show the SNR at wavelengths of interest. The average SNR over the entire spectral range is 35.3 dB, and the instrument is able to achieve an SNR of at least 17 dB for all spectral targets of interest, meeting SNR requirements [SPG-P-11].

6.2. Spectral Resolution Performance

The spectral resolution of the instrument is a function of the monochromator specifications. It can be calculated using the following equation [23]:

$$\Delta\lambda = w_s \left[\cos\chi \sqrt{\left(\frac{1}{k f_m N_{lines}}\right)^2 - \left(\frac{\lambda}{2 f_m \cos\chi}\right)^2} + \tan\left(\chi \frac{\lambda}{f_m}\right) \right] \tag{6.10}$$

Here, $\Delta\lambda$ is the spectral resolution in nanometres, w_s is the slit width (0.694 mm), χ is the incident angle of light on the grating (14.74° [91]), k is the order of the diffraction grating (only 1st order is considered as all other orders are blocked by the filter wheel), f_m is the monochromator focal length (260 mm [95]), and N_{lines} is the line density of the grating, listed in Table 5.3.

Table 6.2: Spectral resolution for each grating in the monochromator.

Grating Spectral Range [nm]	Required Spectral Resolution [nm]	Calculated Spectral Resolution [nm]
250 – 900	5	2.32 – 2.42
900 – 2300	20	4.59 – 4.84
2300 – 3000	20	14.12 – 14.33
3000 – 4500	20	18.80 – 19.22

Table 6.2 shows the spectral resolution for each grating, as well as the spectral resolution requirement in that part of the spectral range. With the chosen slit width, the monochromator has a spectral resolution of less than 5 nm in the ultraviolet and visible ranges, and a resolution of less than 20 nm in the infrared range. This means the monochromator is able to meet the spectral resolution requirements for the instrument [SPG-P-05, SPG-P-06].

6.3. Spot Size Analysis

If the sample is not effectively illuminated, there may not be enough signal reaching the detector for high quality measurements. In order to achieve the maximum illumination, the spot imaged by the observation arm should fall completely within the spot imaged by the illumination arm. Additionally, the observation spot should fall on the sample completely, in order to ensure that the instrument is not measuring features from the sample holder.

As some samples will be rock or powder-based analogues, they will be composed of smaller grains. In order for a measurement to be statistically relevant in planetary sciences, it must measure a minimum of 100 grains [23]. Therefore, the size of the observation spot has a direct impact on the grain size and total size of the sample [SPG-P-08, SPG-P-09].

The angle of each of the goniometric arms will also influence the size of the spot on the sample. It is important that the instrument meets the requirements at all combinations of angles to meet the range of motion requirements [SPG-P-14, SPG-P-15].

6.3.1. Illumination Spot Size

The illumination spot size can be represented approximately as the intersection of a cylinder with a plane. The cylinder represents the illumination beam, while the plane represents the sample. As the angle of the goniometric arm changes, so would the angle of the cylinder relative to the sample plane. When the illumination arm is at 0°, the arm is said to be at nadir. In this configuration, the projection of the illumination spot onto the sample is a circle, as the collimated beam from the off-axis parabolic mirror is circular. When the illumination arm is not at nadir, this intersection becomes an ellipse. Figure 6.8 shows how the shape of the spot changes with the angle of the illumination beam relative to a flat sample.

The simplest way to represent this intersection mathematically is to rotate the sample plane relative to a stationary illumination cylinder. In reality, the cylinder moves relative to the sample, but the two representations

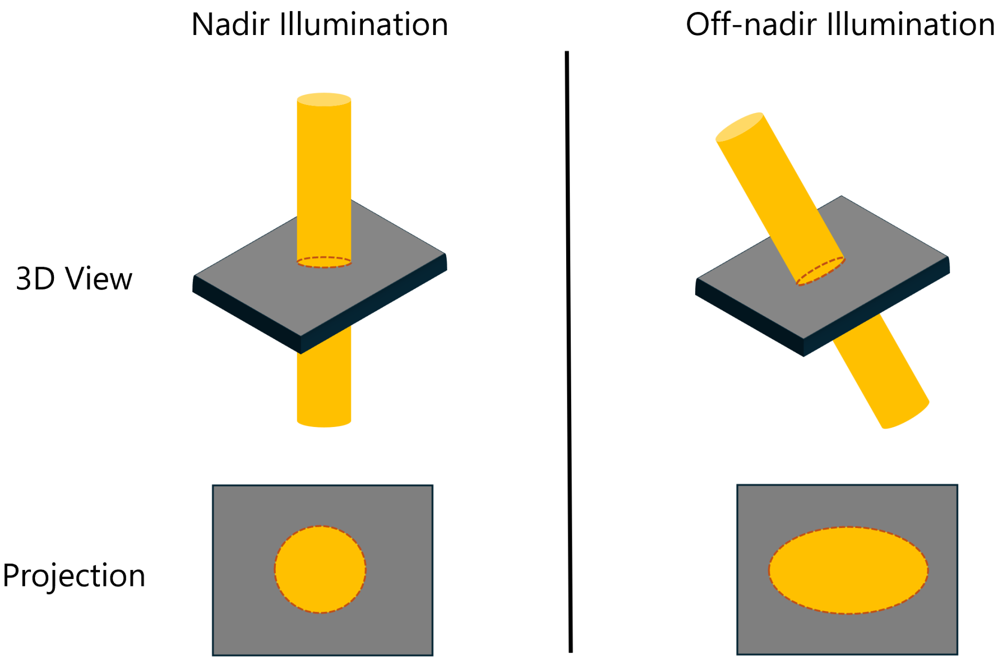

Figure 6.8: Visualization of intersection between collimated beam and sample at different goniometer arm angles.

are identical. The equation for the sample can be represented with the following general equation of a plane in three-dimensional space:

$$a_0x + b_0y + c_0z + d_0 = 0 \tag{6.11}$$

The coefficients a_0, b_0, and c_0 can be used to represent rotations in 3D space. This is done using a rotation matrix which defines the rotations of the goniometer in the principal plane. The rotation matrix is applied to a column vector representing the position of the illumination arm at nadir, with θ equal to the angle of the goniometer arm from the nadir. There is no rotation for the coefficient b_0 because there is no azimuth rotation for the goniometer. The centre of the sample is assumed to be at origin, meaning d_0 is equal to zero.

$$\begin{bmatrix} a_0 \\ b_0 \\ c_0 \end{bmatrix} = \begin{bmatrix} \cos\theta & 0 & \sin\theta \\ 0 & 1 & 0 \\ -\sin\theta & 0 & \cos\theta \end{bmatrix} \begin{bmatrix} 0 \\ 0 \\ 1 \end{bmatrix} \tag{6.12}$$

In order to model the intersection, the sample plane equation is equated to the equation for the illumination beam, represented as a cylinder in 3D space:

$$x^2 + y^2 - r^2 = x\sin\theta + z\cos\theta \tag{6.13}$$

Here, r is the radius of the collimated illumination beam. In order to produce an system of equations that can be solved, x and y can be parametrized in terms of p, then used to solve for z from Equation 6.13.

$$\vec{r}(t) = \langle x(p), y(p), z(p) \rangle = \langle r\cos p, r\sin p, -r\tan\theta\cos p \rangle \tag{6.14}$$

These parametrizations can then be used to trace out the shape of the intersection, where the radius and diameter of the spot size can then be calculated. The collimated beam diameter is designed to be 25.4 mm. Due

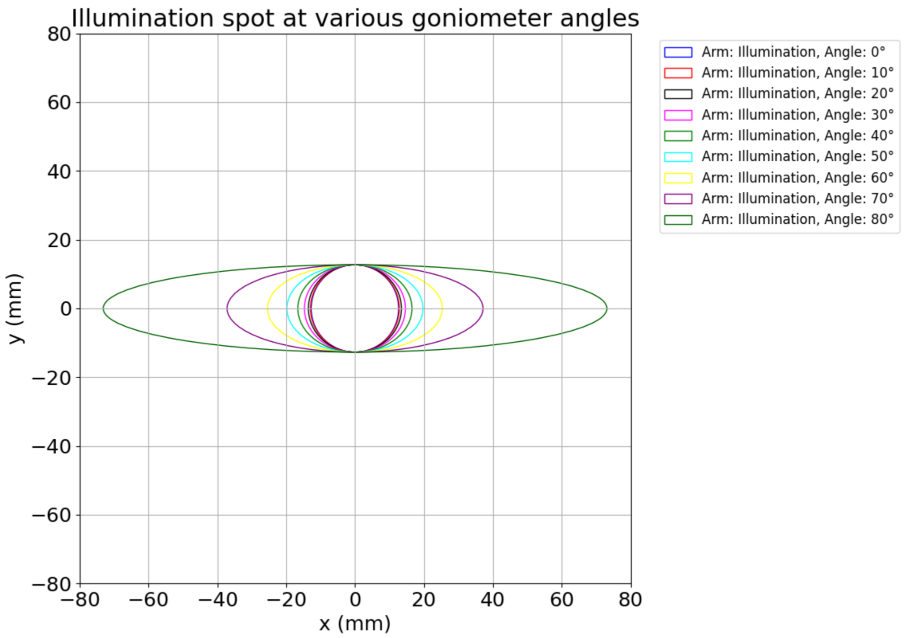

Figure 6.9: Illumination spot size projections as a function of the goniometer angle.

to a 1.05° deviation from perfect collimation, the actual beam diameter at the sample surface is 55.0 mm. Some of the illumination will therefore not fall on the sample, however the highest-intensity illumination will still be confined to this 25.4 mm diameter region. Figure 6.9 shows the illumination spot as a function of the angle of the goniometer arm from nadir. The sample should be a similar size to the illumination spot, such that a large fraction of the sample can be observed without too much stray light. It is therefore recommended to size the sample between 3 and 5 cm for sufficient illumination at all goniometer angles. As the goniometer angle approaches 80°, the spot size starts to significantly increase, meaning a lot more light will be lost as the angle approaches 90°. This could cause a significant drop in SNR as well as additional stray light consequences, meaning it was necessary to set a limit to the maximum goniometer angle at 80°. If image quality still suffers at angles approaching 80° during the characterization and calibration phase of this instrument, then this maximum goniometer angle could be further limited.

6.3.2. Observation Spot Size

The size of the observation spot is more critical to control than the size of the illumination spot, because any light within the observation spot will be measured by the detector. This spot size defines the specifications of the observation arm collimator described in Section 5.4.1. The observation spot size was calculated in the same way as the illumination spot size, however the radius of the spot at nadir was not initially defined.

As the observation spot size needs to be inscribed within the illumination spot at all times, the configuration in which the observation spot size is the largest while the illumination spot size is the smallest can be used to determine the maximum observation spot size at nadir.

The most limiting configuration is when the observation arm is at 80°, and the illumination arm is at nadir. This means that the major axis of the observation spot cannot be larger than 25.4 mm at 80°, which translates to a maximum diameter of 4.4 mm at nadir. Figure 6.10 shows the observation spots inscribed within the illumination spot at all angles between 0° and 80°. Additional plots showing how the spot diameter and area increase with the goniometer angle can be found in Appendix B.1.

Based on the observation spot diameter of 4.4 mm, the maximum grain diameter must be approximately 40 μm in order to achieve statistically relevant measurements, meeting the sample grain size requirement [SPG-P-09]

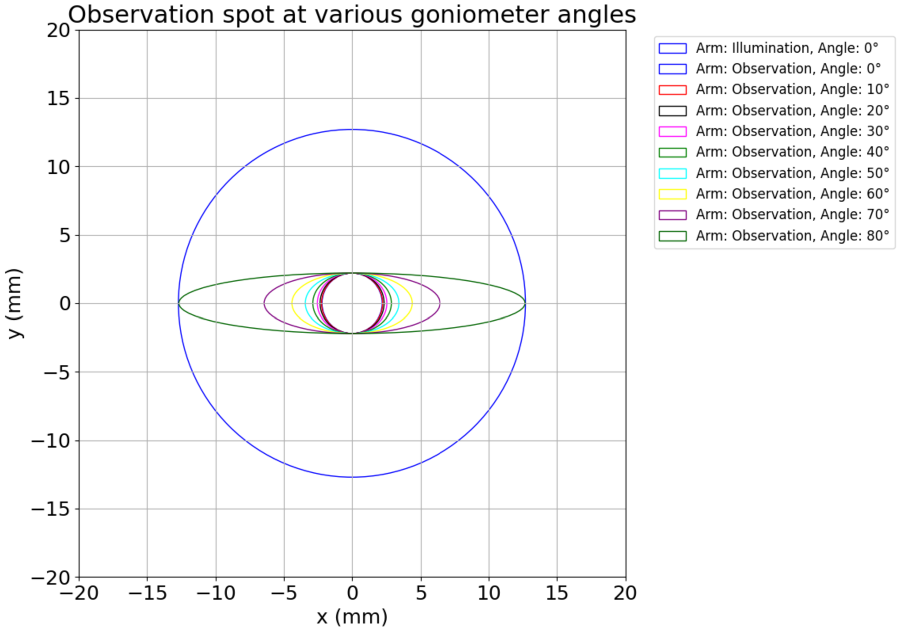

Figure 6.10: Observation spot sizes inscribed within the minimum illumination spot size as a function of goniometer angle.

6.4. Polarimetric Accuracy and Sensitivity Analysis

A polarimetric accuracy and sensitivity analysis involves simulating how close the instrument can get to achieving the desired results, and how much small changes in system inputs can affect these results. As the system has some small intrinsic error due to angular positioning of the mounts, imperfect retardance of the PEM, and the extinction ratio of the polarizers, this will also provide a good measure of the instrument's accuracy and precision. This is relevant to ensure the system meets all polarimetry requirements [SPG-P-01, SPG-P-02].

In order to simulate the polarimetric sensitivity, an end-to-end simulation of the instrument that captures the behaviour of the polarizers, PEM, and sample was necessary. First, the equations and logic used in the simulator are defined. The effects of input errors for each parameter are then investigated, first in isolation to determine relative impact, and then in combination to determine the most likely performance scenarios. The combination analysis is done using a Monte Carlo simulation, which randomizes the values of the inputs within a defined range over the course of many trials. Aside from the analysis of the extinction ratio and signal-to-noise ratio, these simulations are done independently of wavelength. After successful calibration of the instrument, angular error and retardance error are not impacted by wavelength significantly [70], and thus should have similar effects over the entire spectral range. However, this assumption will still need validation through characterization of the instrument in future work.

6.4.1. Simulation Theory

An ellipsometer that uses a photoelastic modulator can be described by the following set of equations [16]:

$$I = I_0\{\alpha_0 + \alpha_1 \sin\delta + \alpha_2 \cos\delta\} \tag{6.15a}$$

$$\begin{aligned}\alpha_0 = {} & [1 - \cos(2\Psi)\cos(2A) + \cos(2(P-M))\cos(2M)(\cos(2A) - \cos(2\Psi))] \\ & + \sin(2A)\cos(\Delta)\cos(2(P-M))\sin(2\Psi)\sin(2M)\end{aligned} \tag{6.15b}$$

$$\alpha_1 = \sin(2(P-M))\sin(2A)\sin(2\Psi)\sin(\Delta) \tag{6.15c}$$

$$\begin{aligned}\alpha_2 = {} & \sin(2(P-M))[(\cos(2\Psi) - \cos(2A))\sin(2M) \\ & + \sin(2A)\cos(2M)\sin(2\Psi)\cos(\Delta)]\end{aligned} \tag{6.15d}$$

Here, I refers to the intensity of light incident on the detector, while I_0 is the intensity of light from the source. δ refers to the retardance induced by the PEM, while Ψ and Δ are the input ellipsometer magnitude and phase as defined in Section 1.1.4. For the physical instrument, the incoming intensity is measured at the detector, and would not be known in terms of Ψ and Δ. For this simulation, Ψ and Δ inputs need to be provided in order to produce an intensity input that is representative of the real instrument. This makes the code easier to validate, as the output Ψ and Δ values should match the known inputs closely. Finally, P, M, and A refer to the angles of the polarizer, photoelastic modulator, and analyzer defined relative to the plane of incidence. The derivation of this intensity equation is addressed in Appendix B.2.1.

The photoelastic modulator modulates the polarization as a function of its input retardance setting and the set frequency of the PEM. This retardance δ can be expressed as the following:

$$\sin\delta = \sin(F\sin\omega t) = 2J_1(F)\sin\omega t \tag{6.16a}$$

$$\cos\delta = \cos(F\sin\omega t) = J_0(F) + 2J_2(F)\cos(2\omega t) \tag{6.16b}$$

J_0, J_1, and J_2 are Bessel functions with respect to F, where F is the retardance amplitude, proportional to the input voltage $V_{control}$ divided by the input wavelength λ. Based on these relationships, the input voltage can be adjusted in order to keep the retardance constant regardless of the input wavelength, as the modulation frequency ω remains constant based on the choice of PEM. F is nominally set to 138° in the simulation, as this simplifies the terms of the Bessel function. This makes $J_0(F) = 0$, $2J_1(F) = 1.04$, and $2J_2(F) = 0.86$.

These formulations can be used together to produce the signal incident on the detector. Figure 6.11 shows the measured signal from the detector over a period of 500 μs. This is a sinusoidal signal which can have two oscillation frequencies for some Δ and Ψ inputs due to the dependence on ωt and $2\omega t$ in Equations 6.16a and 6.16b. The time step is chosen to be much smaller than the period of the modulation of the PEM, such that the signal is clearly inputted into the detector. For this simulation, the signal is sampled at 200 kHz.

The initial intensity I_0 also needs to be defined. The intensity equation I was derived by applying Jones matrices to an initial light input with some p- and s-polarization. Further information on the Jones matrix representation can be found in Appendix B.2.1. The input light is unpolarized in this instrument, however the Jones formulation is unable to represent unpolarized light. An approximation of unpolarized behaviour was achieved in the program by recognizing that an unpolarized light source is a source in which light does not keep a preferred orientation state when averaged over a period of time. The polarization state of light must therefore change constantly over the course of a detector integration. If the intensity is defined to scale between 0 and 1, this means both the p- and s-polarization would vary randomly between 0 and 1. The average polarization intensity is therefore 0.5, so this was used as the input intensity I_0.

The next step is to pass this input signal through a lock-in amplifier. A lock-in amplifier works because it has knowledge of the time-variant behaviour of the expected signal. It knows the expected signal frequency because it is given a reference at the desired signal frequency, allowing it to lock on to the input signal and

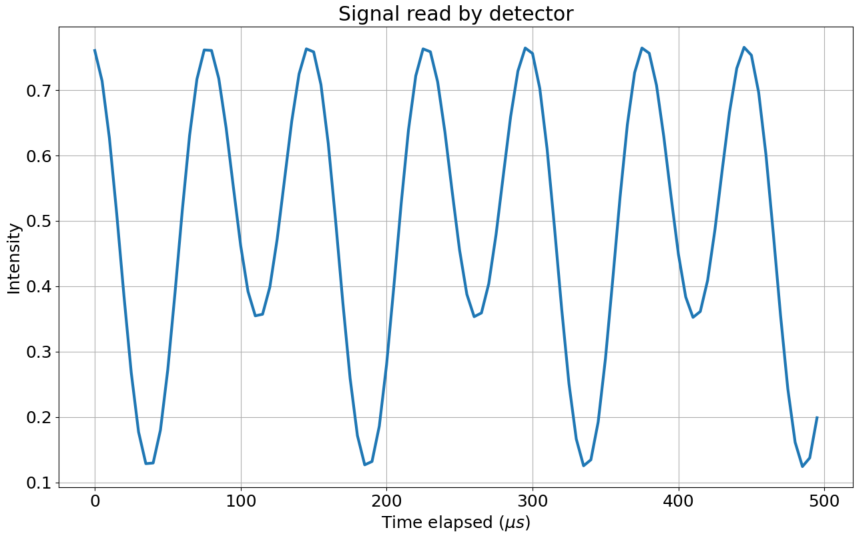

Figure 6.11: Example of a signal that would be read by the detector.

reject signals at other frequencies. This will reject most noise in the system and allow even relatively small signals to be measured [127]. Two lock-in amplifiers are necessary to detect the signals at $\omega = 42$ kHz and $2\omega = 84$ kHz. Both of these frequencies are necessary to capture the full signal as there are $\sin \omega t$, $\cos \omega t$, and $\cos 2\omega t$ terms in Equations 6.16a and 6.16b.

A lock-in amplifier consists of a multiplication of the reference signal with the input signal, followed by a low-pass filter. The multiplication of these signals produces an output according to the following trigonometric relationship:

$$\cos(\omega_{ref} t)\cos(\omega_{input} t) = \frac{1}{2}\cos[(\omega_{ref} - \omega_{input})t] + \frac{1}{2}\cos[(\omega_{ref} + \omega_{input})t] \tag{6.17}$$

As the reference frequency ω_{ref} and the input frequency ω_{input} are identical, the first term would be a term that is constant in time. The low-pass filter is then used to filter out the addition term. This relationship also applies to the sine terms. Most digital lock-in amplifiers apply a dual-phase modulation scheme, which will also be applied in this simulation. This involves multiplying the input signal by the reference signal and a 90° phase-shifted version of the reference signal. In this case, this would be a multiplication by $\cos \omega t$ and $\sin \omega t$ for the first lock-in amplifier, and by $\cos 2\omega t$ and $\sin 2\omega t$ for the second. The dual-phase modulation scheme can then be used to find the components of the signal X and Y, which in turn can be used to find the magnitude R and phase θ_R of the signal according to the following equations [127]:

$$R = \sqrt{X^2 + Y^2} \tag{6.18a}$$

$$\theta_R = \tan^{-1}\left(\frac{Y}{X}\right) \tag{6.18b}$$

The low-pass filter needs to be appropriately tuned to get an accurate signal. The main parameter that needs to be tuned is the cutoff frequency, ω_c. Any frequency above this cutoff value will then be filtered by the low-pass filter. The cutoff frequency for the filter was chosen in accordance with the specifications of the actual lock-in amplifier planned for use with the PEM, the Signaloc 2100 [128]. A time constant τ of 4 ms was selected as it would track a high-frequency signal accurately. This corresponds to a cutoff frequency of $\omega_c = 1/(2\pi\tau) = 39.8$ Hz.

Figure 6.12 shows the X and Y outputs of both lock-in amplifiers, with $\omega = 42$ kHz shown in Figure 6.12a and $2\omega = 84$ kHz shown in Figure 6.12b. The lock-in amplifiers are therefore able to settle on a stable magnitude at the two separate frequencies. These magnitudes should be equal to the coefficients of the input signal equation if the lock-in amplifier is working correctly.

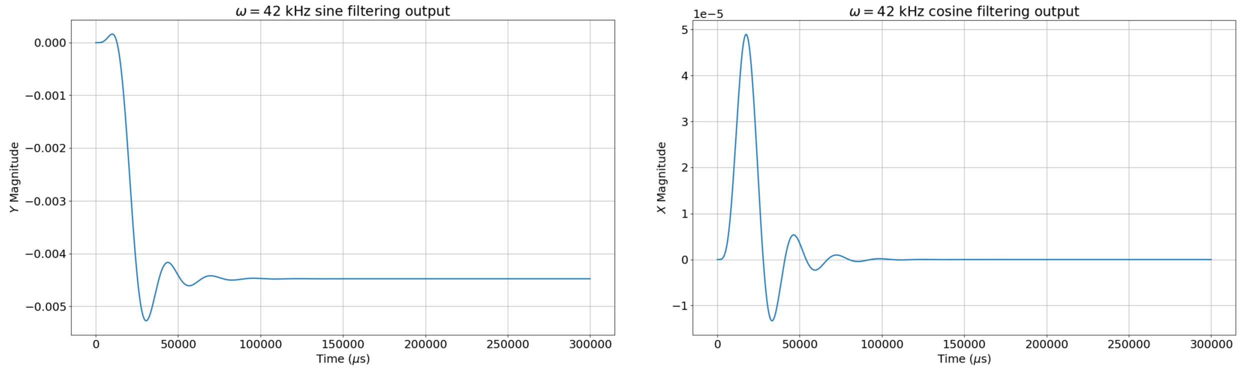

(a) Lock-in amplifier outputs at ω = 42 kHz.

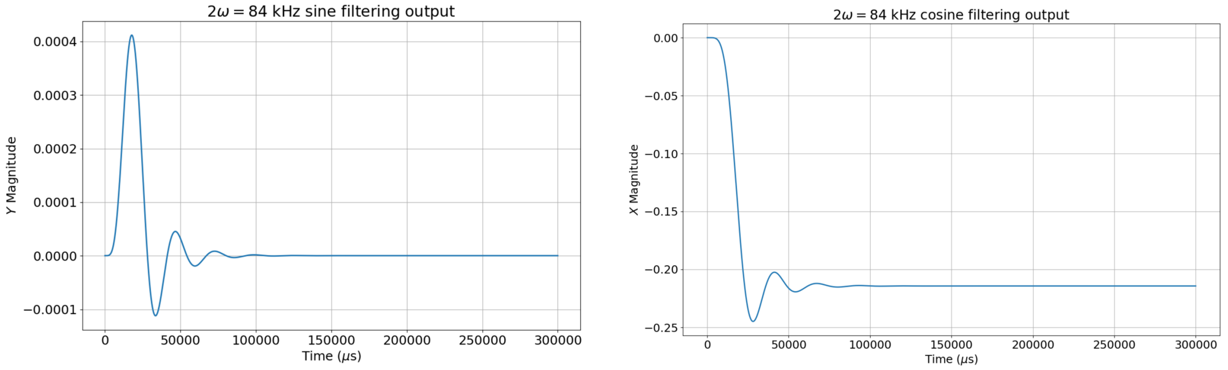

(b) Lock-in amplifier outputs at 2ω = 84 kHz.

Figure 6.12: Lock-in amplifier outputs.

These lock-in amplifier outputs can then be used to calculate Ψ and Δ algebraically. Once R is calculated for the ω and 2ω lock-in amplifiers, the two intensity components can first be calculated [129]:

$$I_x = \frac{1}{2J_1(F)}\frac{I_\omega}{I_{DC}} + \frac{\delta_0}{J_0(F)+2J_2(F)}\frac{I_{2\omega}}{I_{DC}} \tag{6.19a}$$

$$I_y = \frac{1}{J_0(F)+2J_2(F)}\frac{I_{2\omega}}{I_{DC}} + \frac{\delta_0}{2J_1(F)}\frac{I_\omega}{I_{DC}} \tag{6.19b}$$

I_x and I_y are simply algebraic terms that aid in the calculation of Ψ and Δ. Here, I_{DC} is the DC intensity, and δ_0 is the static retardation. I_ω and $I_{2\omega}$ are the R magnitude values from the lock-in amplifier at both the measured frequencies, with the phase θ_R used to determine the sign of these intensity values. The DC intensity is inputted as 1 for this simulation, but this would change based on the actual performance of the lock-in amplifier and would need to be characterized. HINDS claims that the static retardation δ_0 of the PEM is very small [129], and is therefore set at 1×10^{-5} rad. [129, 130] in simulations where static retardation error is applied. When simulating the system with no error, the δ_0 term is also set to 0 rad. These components can then be used to calculate three coefficients N, S, and C which are trigonometric expressions of Ψ and Δ [131]:

$$I_{DC} = 1 - N\cos(2A) \tag{6.20a}$$

$$I_x = S\sin(2A) \tag{6.20b}$$

$$I_y = \sin(2P)(\cos(2A) - N) - C\cos(2P)\sin(2A) \tag{6.20c}$$

The analyzer angle can be set to $A = -45°$ to further simplify these equations. However, as discussed in Section 4.7, the PEM needs to be oriented in two configurations to measure all four Stokes parameters. This is because I_y can only be used to calculate N when $P = 45°$, as the $\cos(2P)$ term vanishes. When $P = 0°$, the opposite condition is true, and the C term can be calculated. As discussed in Section 5.2.3, the PEM is mounted to the polarizer, and rotates with it. The PEM starts at 0° in configuration 1, and is rotated to −45° in configuration 2.

The N, S, and C terms are related to Ψ and Δ through trigonometric relations:

$$\Psi = \frac{1}{2}\cos^{-1}(N) \tag{6.21a}$$

$$\Delta = \tan^{-1}\left(\frac{S}{C}\right) \tag{6.21b}$$

The Stokes parameters can be calculated from Ψ and Δ using trigonometric relations as well:

$$S_1 = -\cos(2\Psi) \tag{6.22a}$$

$$S_2 = \sin(2\Psi)\cos(\Delta) \tag{6.22b}$$

$$S_3 = -\sin(2\Psi)\sin(\Delta) \tag{6.22c}$$

Once the Stokes parameters are calculated, the other parameters such as DoLP, AoLP, and DoCP can be calculated using the relationships given in Section 1.1.3. As the focus of the ellipsometer performance is Δ and Ψ performance, the Stokes and other parameters are discussed in Appendix B.2.4 and B.2.5. These sections also provide some insight about how the ellipsometer performance compares to the typical intensities of polarization features on planetary surfaces.

With no errors introduced to the system, the system outputs should match the inputs for Ψ and Δ to within some small error value. This error value accounts for any compounding precision error from the program calculations, as well as the use of the software-based lock-in amplifier to extract the signal magnitude. Figure 6.13a shows the system outputs plotted against each system input over a range of Ψ and Δ values when the other variable is held constant, while Figure 6.13b shows the error between the inputs and outputs over this range. It was decided to keep Ψ constant at 45° while Δ varies because 45° is the point of maximum error for Ψ measurements due to numerical error associated with the calculation of $\sin(2\Psi)$ [16]. The same reasoning applies for choosing a stationary Δ at 180° when Ψ is the independent variable. The error is on the order of 10^{-10}, which can be attributed to numerical error in the lock-in amplifier magnitude calculation and subsequent trigonometric operations to get Ψ and Δ.

6.4.2. Angular Error

The equations outlined in Section 6.4.1 have terms A, M and P representing the angles of the analyzer, photoelastic modulator, and polarizer, respectively. The nominal values used in the simulation in order to simplify calculations were $A = -45°$, $M = 0°$, $P = 45°$ in configuration 1, and $A = -45°$, $M = -45°$, and $P = 0°$ in configuration 2. These values can be perturbed slightly to see how the output changes.

Analyzer Angle

First, the analyzer was adjusted while all other potential sources of error were assumed perfect. This includes the polarizer angle P, the PEM angle M, and the relative angle between those components $P - M$. The minimum uncalibrated angular error for the polarimetric elements is 0.14°, as this is the accuracy of the rotation mount [113]. However, prior to calibration, the angular error would be expected to be significantly larger, as there is also error involved in mounting the polarizer inside of the rotation mount. Calibration techniques exist

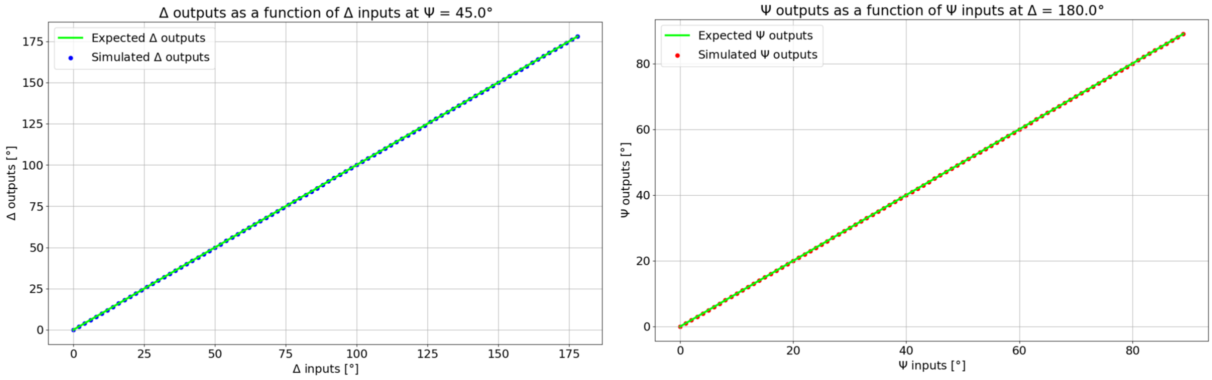

(a) Ψ and Δ outputs plotted against known inputs with no measurement error.

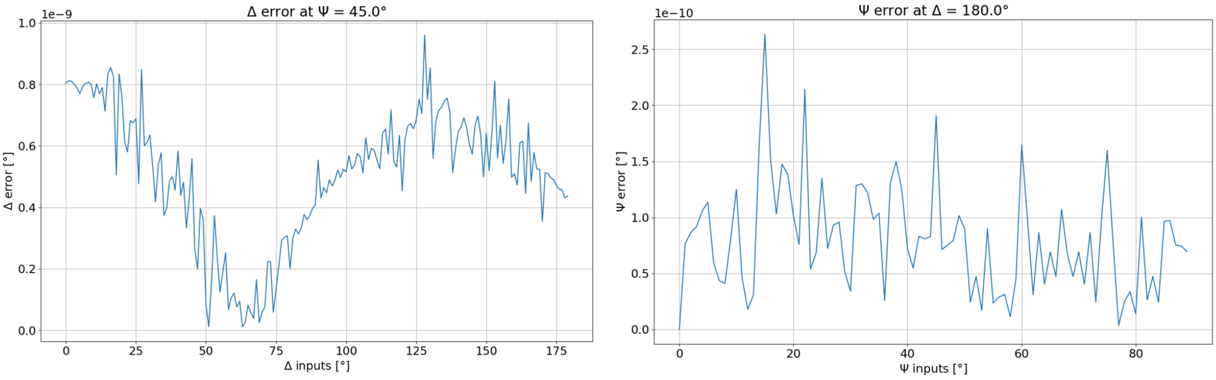

(b) Error between input and output Ψ and Δ values with no measurement error.

Figure 6.13: Polarimetric accuracy simulation performance with no input error.

for minimizing the angular error, as are discussed in Section 7.2. However, a more realistic error range was set at 1°. Figure 6.14 shows the Ψ and Δ error with a 1° analyzer error.

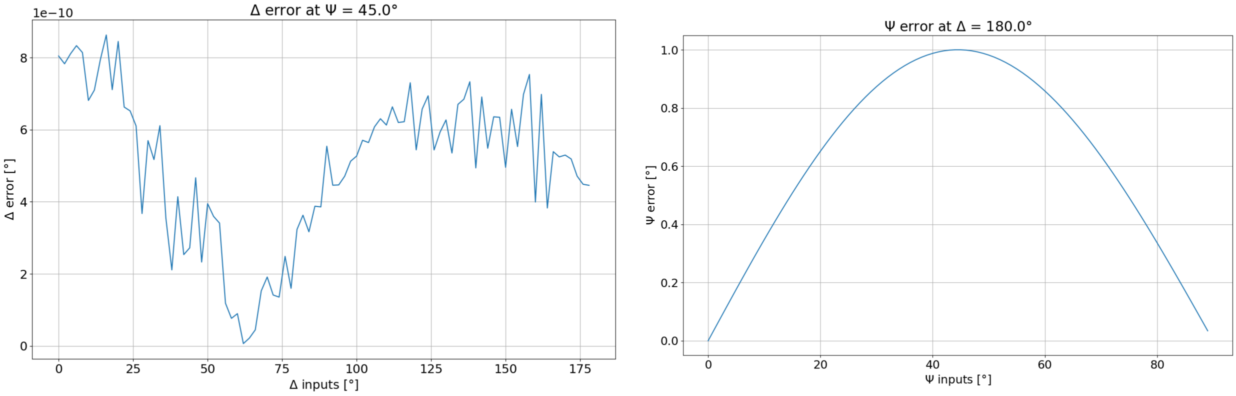

(a) Error in Δ for a 1° analyzer angular error.

(b) Error in Ψ for a 1° analyzer angular error.

Figure 6.14: Polarimetric accuracy performance with 1° analyzer angular error.

Figure 6.14a shows that the analyzer position does not have an effect on the Δ error. This can be shown mathematically in Equations 6.20b and 6.20c by recognizing that the angular error of the analyzer cancels out in the S and C terms. The analyzer position changes with $\sin(2\Psi)$, which lines up well with the results in Figure 6.14b. Therefore, to keep Ψ error below 0.01° in accordance with polarimetric requirements [SPG-P-01], it is necessary to limit analyzer error to below 0.01°.

Polarizer and PEM Absolute Angle

The polarizer and PEM angle are coupled as they must rotate together to take measurements. Mathematically, it can be difficult to model the effects of polarizer and PEM angular error, because the system of equations can only be solved for exact values of $P = 45°$ and $P = 0°$. Therefore, it was attempted to solve for Ψ and Δ parameters with angular error inputs while using the equations that assume perfect P and M placements to give an estimate of the error.

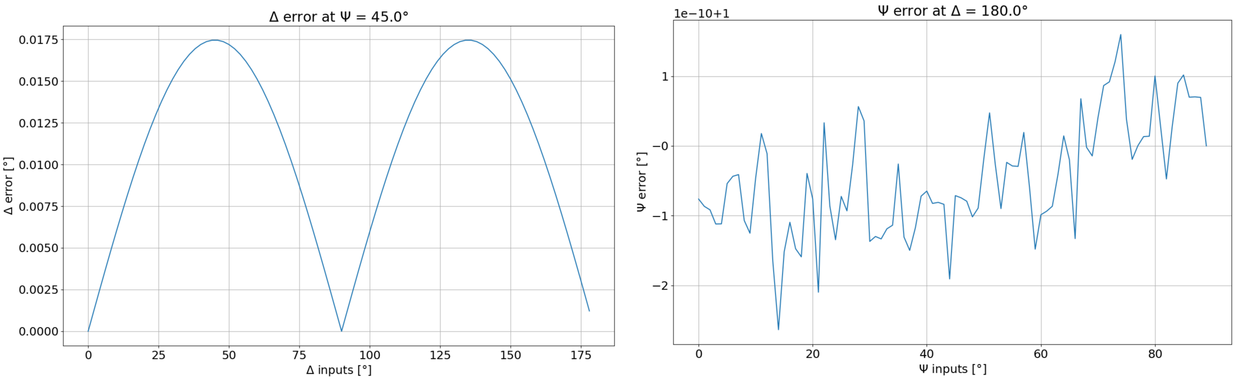

(a) Error in Δ for a 1° polarizer angular error.

(b) Error in Ψ for a 1° polarizer angular error.

Figure 6.15: Polarimetric accuracy performance with 1° polarizer angular error.

Figure 6.15 shows the Ψ and Δ error when the polarizer/PEM combination has a 1° angular error. The analyzer angle A is assumed to be exactly $-45°$, and the angle between the polarizer and PEM is assumed to be exactly 45° as well. As shown in Figure 6.15a, the polarizer error has a small effect on the Δ error. Figure 6.15b shows there is also an effect on the Ψ error, however it is just an offset of 1° with some small numerical fluctuation. This offset can be compensated for, meaning the only error for polarizer and modulator angle placement is in the Δ output. The polarizer error therefore needs to be kept below 1° at most to maintain Δ error requirements [SPG-P-02], which establishes requirement [SPG-P-18]. The same calibration methods applied to reduce analyzer angular error can be applied to the polarizer, which can further reduce this error.

Polarizer and PEM Relative Angle

Unfortunately, the Ψ and Δ error produced by relative angular error between the polarizer and PEM cannot be accurately measured in the simulation. It is required that $P - M = 45°$ in order for the system of equations to be solved. However, it can be assumed that the relative angle between the polarizer and PEM can have a similar effect as analyzer and polarizer error, and should be reduced to an error of approximately 0.01° through calibration methods, if possible.

6.4.3. Retardance Error

Static Retardation

Static retardation refers to any residual birefringence present in the crystal when it is not being driven at the resonance frequency. This can cause some small drift in the retardance value. Some ellipsometer studies report values of up to 1×10^{-3} rad. for the static retardation using other PEMs [130], and while HINDS does not provide values themselves, they do claim that the retardation is extremely small, and thus a value of 1×10^{-5} rad. was used instead. This value can be updated during the characterization procedure for the instrument. Figure 6.16 shows the errors in Ψ and Δ as a result of static retardation.

Both the Ψ and Δ errors are very small with the effects of static retardation included. The constant values for Ψ and Δ were changed for retardation analysis, as $\Delta = 180°$ would result in linear polarization. An elliptically polarized input would provide a better overview of the system performance when discussing retardance effects, thus Δ was changed to 160°.

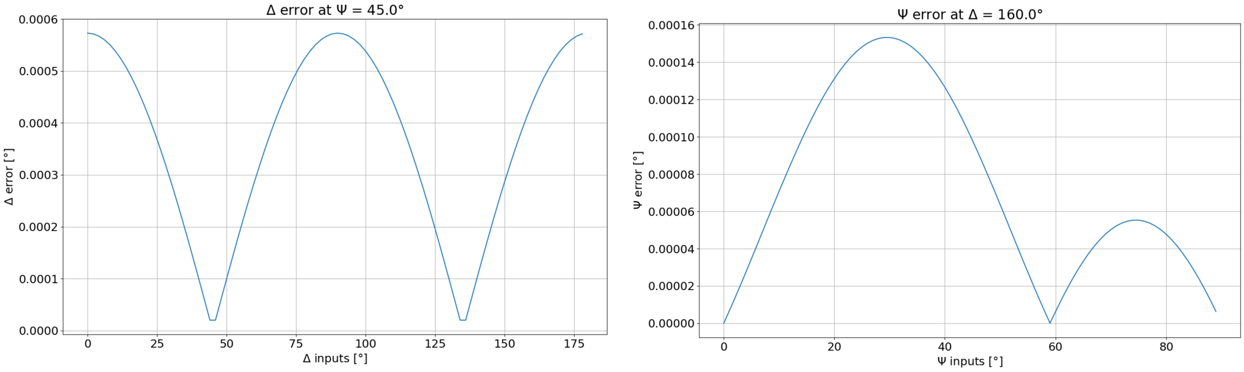

(a) Error in Δ with 1×10^{-5} rad. static retardation error.

(b) Error in Ψ with 1×10^{-5} rad. static retardation error.

Figure 6.16: Polarimetric accuracy performance with 1×10^{-5} rad. static retardation error.

Interestingly, Figure 6.16b shows that the Ψ error reaches a minimum at $\Psi = 0°$, $\Psi = 60°$ and again at $\Psi = 90°$. All other investigated errors show symmetric behaviour in Ψ and Δ. When Δ is set to a constant 20° value, which would be the symmetrically opposite angle in the Δ range, the static retardation error is the exact opposite, with a minimum at $\Psi = 0°$, $\Psi = 30°$, and $\Psi = 90°$. It is currently unclear why the static retardation is not symmetric in Ψ, however the relatively small error magnitude should not affect the total error significantly.

Modulation Error

Another source of error is the retardance of the PEM when modulating the polarization. The retardance amplitude of the PEM should be nominally set to $F = 138°$, however there can still be up to 1% error due to uncertainty in the input voltage and the PEM's retardance itself. This means that the Bessel functions introduced in Equations 6.16a and 6.16b need to be manually calculated with an input F that fluctuates within 1% of 138°.

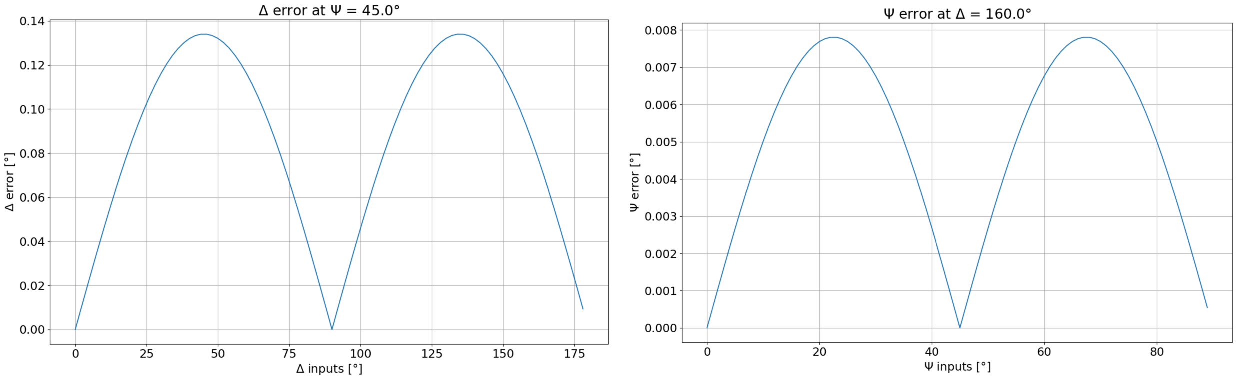

(a) Error in Δ for a 1% retardance error.

(b) Error in Ψ for a 1% retardance error.

Figure 6.17: Polarimetric accuracy performance with 1% retardance error.

Figure 6.17 shows the Ψ and Δ error when the retardance has a 1% error. A constant Δ value of 160° was used for the Ψ analysis in order to see the effects of elliptical polarization. The same error profile is seen in both Ψ and Δ, with a minimum error at 0°, half of the total range, and the maximum of the total range for both variables. The retardance error has a larger effect on Δ than on Ψ. Since the error in Δ is much larger than the polarimetric sensitivity requirement [SPG-P-02], it will be extremely important to limit the retardance error as much as possible. This can be done by keeping the room temperature controlled, and testing modulation with an oscilloscope prior to measurement. Characterization of the instrument in the laboratory will also help confirm the dependence of retardance accuracy on wavelength, which was assumed to be negligible in these simulations. Further calibration procedures for the modulation accuracy will be discussed in Section 7.1.3.

6.4.4. Extinction Ratio

The extinction ratio of the polarizers can have an effect on the value of Ψ and Δ as the polarizers can transmit some light that is oriented perpendicularly to the transmission axis. Mathematically, this is represented as:

$$\kappa = \left| \frac{I_{\parallel}}{I_{\perp}} \right| \tag{6.23}$$

Here, $I_{\parallel}$ is the intensity parallel to the polarizer, and $I_{\perp}$ is the intensity perpendicular to the polarizer. As an example, for an extinction ratio of 10000:1, there will be a leakage of 0.0001 in the direction perpendicular to the transmission axis of the polarizer, or 0.01%. This impacts the intensity read by the detector, which in turn can impact the Ψ and Δ results.

In order to simulate this, the extinction ratios for both polarizers were added together, as a function of the wavelength. The extinction ratio values are provided in Table 5.6. These extinction ratio errors were then applied to the coefficients in the intensity equation. An extinction ratio of 100:1 for each polarizer results in an error of 0.01 per polarizer, or 0.02 for both. The intensity signal was therefore multiplied by 1.02 to apply the impact of the extinction ratio to the input. Figure 6.18 shows how the extinction ratio impacts the results. Both simulations were ran at a single value of $\Psi = 45°$ and $\Delta = 180°$, as these are the angles of highest error [16].

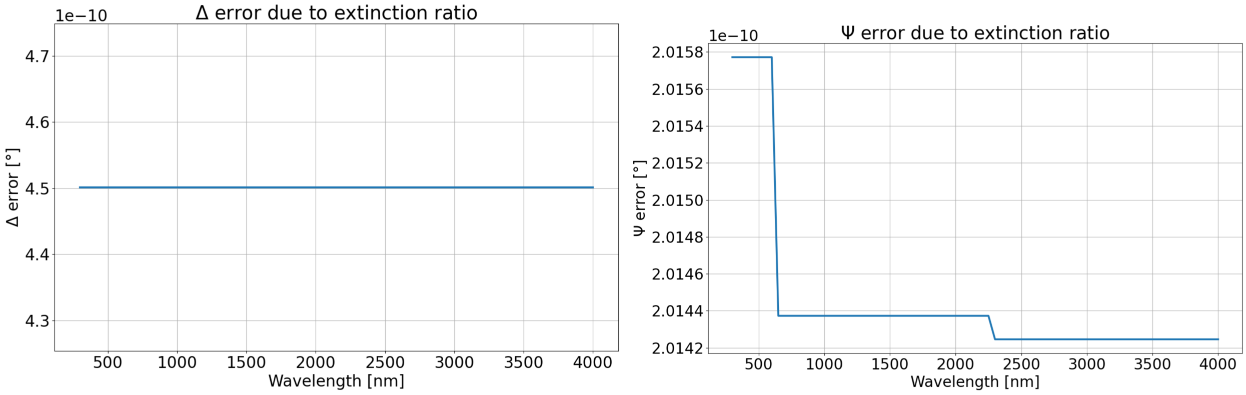

(a) Extinction ratio impacts on Δ error as a function of wavelength. **(b)** Extinction ratio impacts on Ψ error as a function of wavelength.

Figure 6.18: Extinction ratio effects on Ψ and Δ error.

Extinction ratio does not have an effect on the value of Δ based on this simulation. While there is not a clear mathematical link between the extinction ratio of the polarizer and the phase of the reflected light components, intuitively some intensity leakage through the polarizer should result in an impact on the value of Δ that the simulation cannot capture. For Ψ, the relationship is more clear, as the error decreases with improved extinction ratio in the infrared. This matches well with Equation 1.5 for Ψ. However, the error associated with extinction ratio is still extremely small when compared to angular error and retardance error, based on this simulation.

It is important to note the general trend that the instrument will have somewhat worse performance in the ultraviolet and visible region compared to the infrared region, especially when considering the lower signal in this range.

While the program predicts essentially negligible effects from the extinction ratio of the polarizers, it is necessary to verify this through chracterization in the lab. There may also be some effects on Δ that are not captured accurately by the mathematics in this simulation. Additionally, the effects on the intensity may be larger than anticipated at certain values of Δ and Ψ.

6.4.5. Detector Error

Frequency Response

Detector error can manifest in a couple of ways, with the first being the sampling rate. In Section 6.4.1 it was mentioned that the sample rate was set to 200 kHz. However, the pre-amplifier for this detector has a frequency response that only reaches 100 kHz, and can be limited to 60 kHz in some circumstances [121]. That means that the sampling rate used in the simulation likely cannot be achieved by the real pre-amplifier. This conflicts with the Nyquist-Shannon sampling theorem, stating the signal should be sampled at a minimum of twice the signal frequency in order to get an accurate measurement [122]. This means that the ideal sampling frequency would be at least 84 kHz for a 42 kHz signal. This can make it more difficult for the lock-in amplifier to properly capture the signal. Figure 6.19 shows how a change in sample rate impacts how the input signal is read.

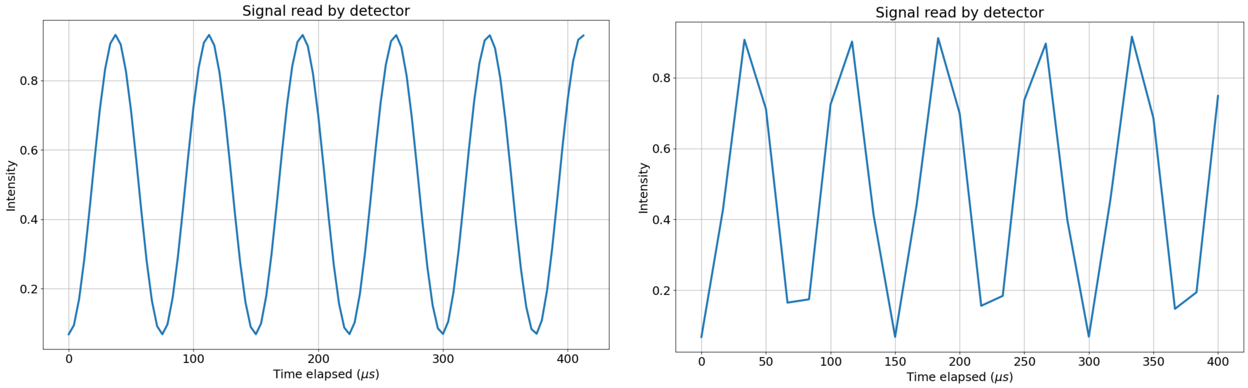

(a) Input signal with frequency response of 240 kHz.

(b) Input signal with frequency response limited to 60 kHz.

Figure 6.19: Effect of sampling rate on the input signal.

Figure 6.20 shows the effects of a lower sampling rate on the Ψ and Δ error. The error quantities are very similar to when the instrument had no error inputs. This means that despite a slower sampling rate, the lock-in amplifier is still able to extract accurate values. However, the sampling rate cannot be reduced below the photoelastic modulator modulation frequency, or else it will not be able to lock on to the signal. A 60 kHz frequency response, however, is adequate for the required measurements, as was confirmed through consultation with HINDS.

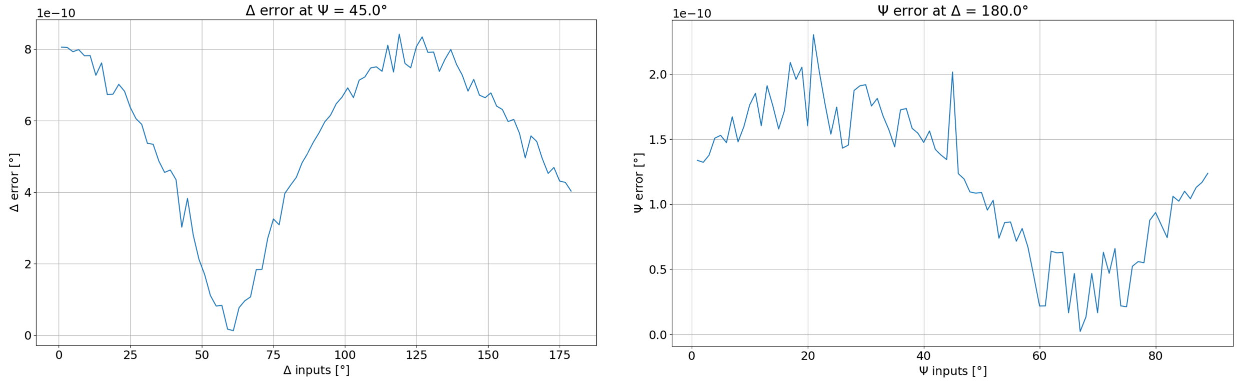

(a) Error in Δ with sampling noise.

(b) Error in Ψ with sampling noise.

Figure 6.20: Polarimetric accuracy performance with sampling noise.

Detector Noise

The second method of simulating detector noise is to add some random fluctuation to the input signal. The range of this random fluctuation is dictated by the signal-to-noise ratio at the detector. Since the average SNR of the instrument is 11786.3, the average noise fluctuation is 8.5×10^{-5}, or 0.0085% of the signal. While this noise value will have some fluctuation with wavelength, its contribution is small even relative to the extinction ratio, so the average was considered a suitable estimate. If the lock-in amplifier is correctly tuned, it should be able to filter out most noise that is not at the PEM's modulation frequency, meaning this small noise fluctuation should have a relatively minor effect on the Ψ and Δ results.

Figure 6.21 shows the Ψ and Δ errors with noise from the detector. While not negligibly small, detector noise effects are a few orders of magnitude smaller than the effects of retardance and angular error, and have a similar impact as the static retardation. Interestingly, despite having a smaller effect on the magnitude of the intensity signal, the SNR has a larger effect on the error of Ψ and Δ than the extinction ratio. This is likely due to the random behaviour of the system noise, which makes it harder for the lock-in amplifier to follow the signal when compared to a factor that increases the amplitude in a predictable manner. While achieving sufficient SNR is important for ensuring a minimum image quality, the lock-in amplifier is able to largely filter out its effect on the polarimetric accuracy and sensitivity of the instrument. To confirm this, the effects of signal-to-noise ratio were measured as a function of wavelength, and were found to have virtually no effect on the Ψ and Δ error. These results are discussed in Appendix B.2.2.

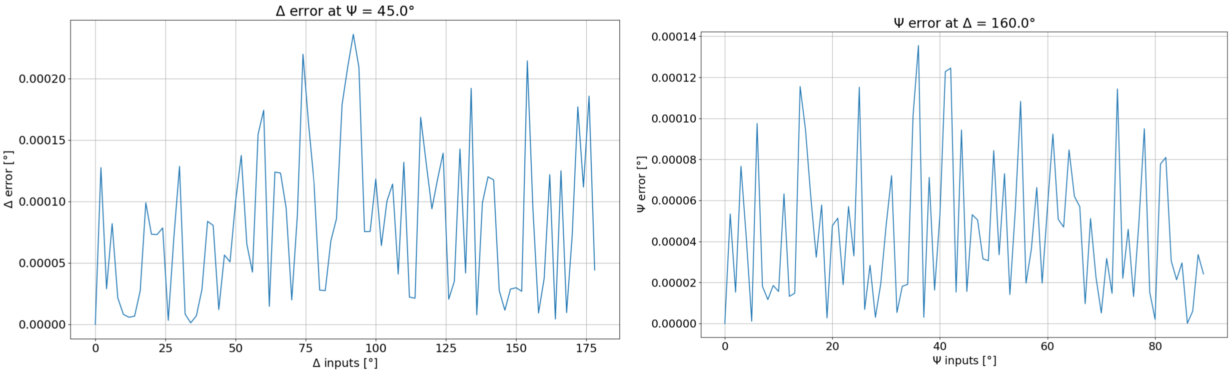

(a) Error in Δ with detector noise.

(b) Error in Ψ with detector noise.

Figure 6.21: Polarimetric accuracy performance with detector noise.

6.4.6. Monte Carlo Simulations

A Monte Carlo simulation is a method of determining the behaviour of a system given random input variables. In the case of the polarimetric accuracy simulation, when the system's inputs are all randomly perturbed, this simulation can provide the expected total error of the system in a wide variety of cases. 100 iterations of the simulation were ran at every combination of integer Ψ and Δ inputs. Δ ranges from 0° to 180°, while Ψ ranges from 0° to 90° [16]. More detailed Monte Carlo distributions at specific Δ and Ψ configurations can be found in Appendix B.2.3.

The angular errors were all perturbed with a maximum range of 1°. The retardance error had a maximum range of 1%, while the detector error had a maximum range of 0.0085%. The static retardation was set to 1×10^{-5} rad. for all levels of the error stacking simulation.

Figure 6.22 shows an error stackup for the system at $\Delta = 160°$ and $\Psi = 45°$. Only a 1° range is captured such that the spread of output results can be seen more clearly relative to the input.

For Δ, the analyzer was seen to have no effect on the error, and thus the blue profile is not visible in Figure 6.22a. Adding polarizer error increases the error profile, however the maximum error is on the order of 0.01° as shown in Figure 6.15a. Retardance error has a significant effect on the total error for Δ. When compounded with the analyzer and polarizer error, the total error in Δ grows to approximately 0.2°.

Angular and retardance errors have an even larger effect on Ψ. A 1° angular error in the analyzer produces a proportional 1° angular error in the Ψ output, while adding polarizer error nearly doubles the Ψ error.

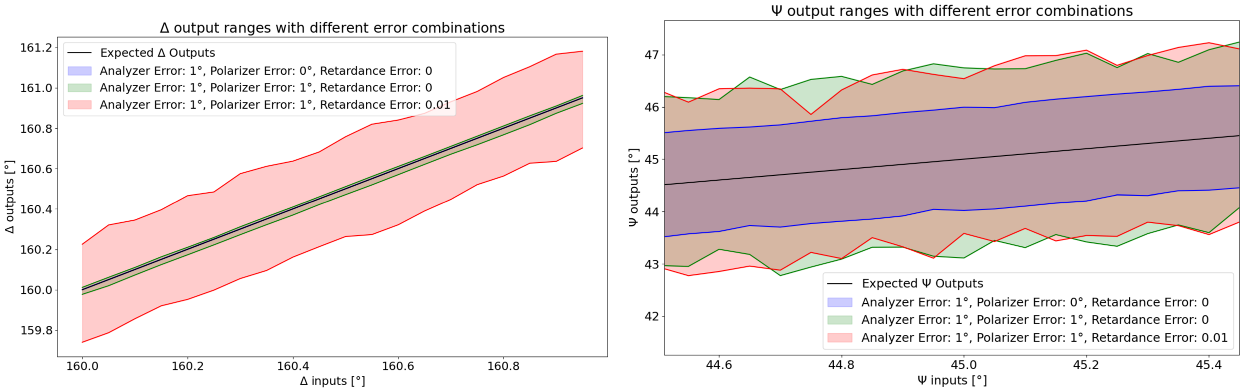

(a) Error stacking for Δ = 160°.

(b) Error stacking for Ψ = 45°.

Figure 6.22: Error stackup configurations, with just analyzer angular error, with polarizer and analyzer angular error, and both angular errors and retardance errors.

The polarizer error does however have a consistent bias which can be compensated to remove its effect as described in Figure 6.15b. Adding the retardance error makes the total error in Ψ slightly larger at some angles as shown with the green profile, however retardance error has a small effect relative to angular errors. While stacking errors can be valuable to get a more realistic view of the instrument performance, it is important to validate the individual error impact on performance before making design decisions based off the error stackup. Characterization of the instrument will be helpful in reaching this validation.

Overall, it is absolutely critical to limit both the angular error and retardance error during calibration. Methods of reducing these errors to improve polarization sensitivity will be discussed in Chapter 7. An evaluation of whether these calibration methods are sufficient to reach the required performance capabilities will also be provided.

6.5. Zemax Simulations

While Zemax was used mostly during the detailed design phase to determine component spacing and geometry, some Zemax features were also applied to verifying instrument performance. This section focuses on tolerancing for the custom components of the instrument to ensure performance can be met with standard alignment and manufacturing practices.

6.5.1. Lens Tolerancing

In Chapter 5, the optimal geometry and spacing for the refocusing elements of the instrument were determined in Zemax. In reality, manufacturing imperfections and limitations in the equipment used for aligning these elements can cause values such as the radii of curvature and spacing between components to deviate from these optimal values in the actual instrument. In order to get a better estimate of the instrument performance, it is important to gain an understanding of how these imperfections can impact the performance of the system. Simulating these effects can also help establish manufacturing tolerancing limits, which have an effect on the manufacturability and cost of the instrument as a whole. This helps inform alignment requirements as well [SPG-P-19, SPG-P-20].

The observation arm focuser has the tightest optical requirements due to the relatively small size of the IR detector. This component will therefore be used to establish tolerancing guidelines for the other lens-based components in the instrument.

All surfaces were given some uncertainty except for the spacing between the two detector faces. These uncertainties included despace and decenter as described in Section 3.3, as well as the radii of curvature of the lenses. Azimuth angle was not considered in this analysis because for lenses it would not affect the radiation hitting the detector. Azimuth angle error for polarizers is considered in Section 6.4.2. An additional consideration is the Abbe number of the lenses, accounting for any refractive index imperfections.

The tolerancing program was run at 300 nm and 3000 nm, with 20 Monte Carlo operations that randomized errors to different component parameters within the specified range. These Monte Carlo iterations were then ranked according to their RMS spot radius on the detector face. If the Monte Carlo simulation with the largest spot radius still managed to hit the UV-VIS detector face at 300 nm, and fill the IR detector face at 3000 nm, the tolerances were deemed acceptable. The goal was to find the largest tolerancing boundaries that met these requirements.

Table 6.3: Tolerances for alignment parameters. These tolerances apply to all surfaces except for the spacing between detector faces.

Alignment Parameter	Tolerance
Radius of Curvature	100 μm
Lens Thickness	100 μm
Decenter X	100 μm
Decenter Y	100 μm
Tilt X	0.1°
Tilt Y	0.1°
Abbe Number	1%

Table 6.3 shows the chosen tolerances for each alignment parameter in the system. These requirements are tighter than the Zemax default tolerances (200 μm, 0.2°), so compliance will need to be confirmed with manufacturers and with specifications for the alignment equipment. However, these tolerances still fall within reasonable ranges for standard alignment procedures and equipment [132].

Figure 6.23 shows how the focuser behaves in the worst-case Monte Carlo scenario based on these tolerances. Figure 6.23a shows the focusing performance at 300 nm, while Figure 6.23b shows the focusing performance at 3000 nm.

Based on these simulations, it is clear that the focuser performs worse when the alignment and manufacturing is not optimized. For instance, decenter causes problems in the infrared, where some of the radiation misses the target due to improper focus. However, the radiation still fills the detector face, and during assembly and calibration of the instrument, some adjustment can be made to the positioning of the detector itself to compensate for this decenter. As sufficient light reaches the detector even in the worst case Monte Carlo iteration, the tolerances in Table 6.3 were deemed acceptable for the focuser. The other lens components were given the same tolerances, as the focuser tolerances are not extremely tight compared to the industry standard [132].

6.5.2. Mirror Tolerancing

Mirrors can have different tolerancing limits than lenses, as toroidal and off-axis parabolic mirrors have different design parameters. The slit width and fibre bundle opening are on a similar order of magnitude as the detector face of the instrument, meaning that tighter tolerances than Zemax's defaults may be required.

For the mirror that focuses light exiting from the monochromator into the optical fibre, it is important to ensure that the focusing efficiency remains above 90%. This is not an official system requirement because the existence of a monochromator and optical fibre were not originally specified. However, it is important to ensure sufficient light throughput through the system. This will be calculated in the same way as in Equation 5.5. With alignment tolerances of 150 μm and 0.15°, the focusing mirror is still able to achieve a minimum focusing efficiency of 91%. Therefore, these alignment tolerances should be met for the focusing mirror.

For the off-axis collimating mirror in the illumination arm of the instrument, it is important to keep the collimation deviation below 2°. The largest alignment tolerance that still meets this collimation requirement will be applied to this collimating mirror. Using the default Zemax tolerance of 200 μm and 0.2°, the collimation

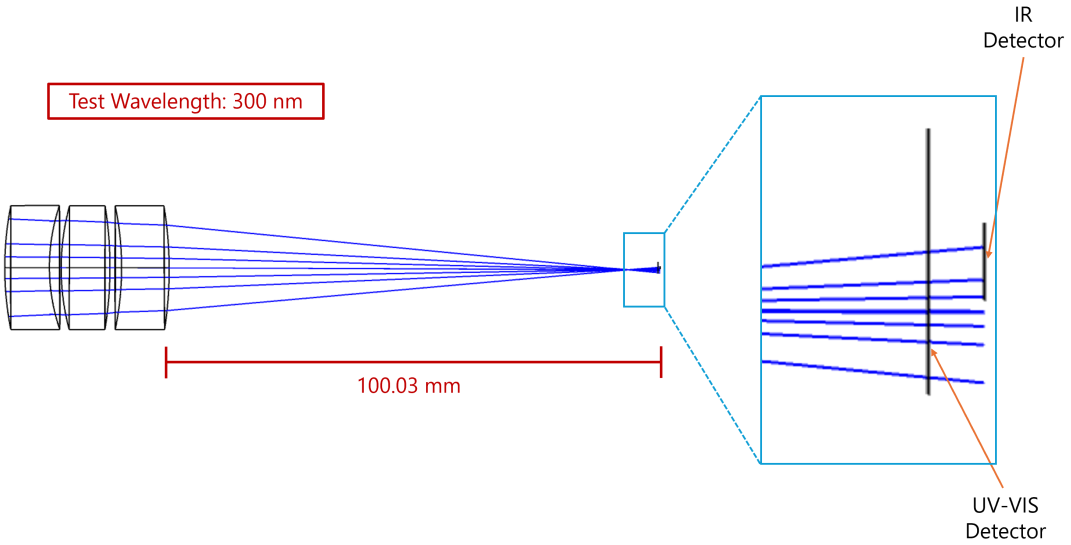

(a) Worst-case Monte Carlo simulation at test wavelength of 300 nm, with a magnified view of the detector shown in the blue window.

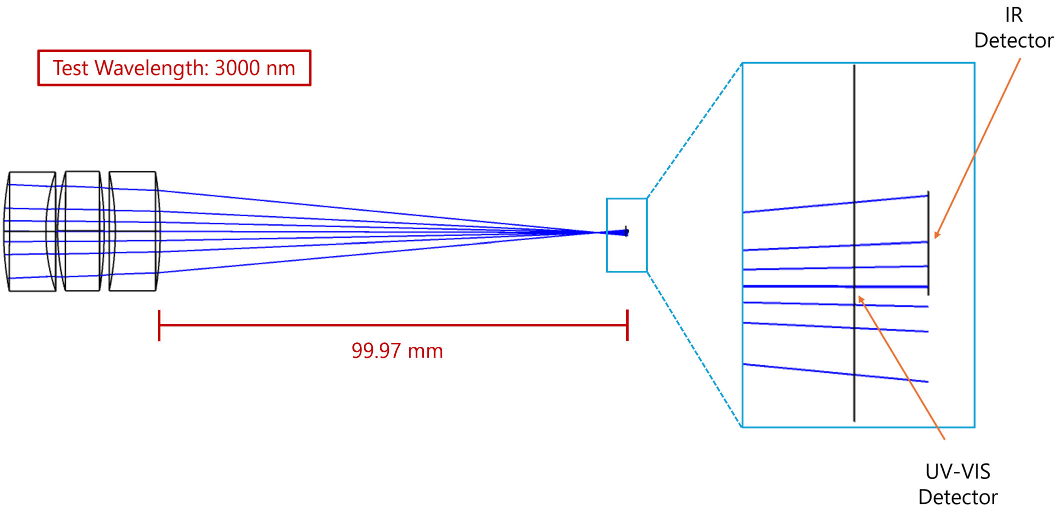

(b) Worst-case Monte Carlo simulation at test wavelength of 3000 nm, with a magnified view of the detector shown in the blue window.

Figure 6.23: Worst-case Monte Carlo simulations based on defined alignment tolerances in Table 6.3.

deviation is still well below the 2° requirement, only deviating by 1.14°. In fact, the tolerance can be increased to 1 mm while still reaching a collimation deviation of 1.92°. Off-axis parabolic mirror alignment is therefore not a critical part of system performance. However, in the interest of maximizing signal-to-noise ratio performance and instrument quality where possible, a standard 200 μm alignment tolerance will be applied.

6.6. Simulation Validation and Next Steps

The simulations discussed in this chapter provide more insight into the performance of the instrument, especially considering areas that need further design work or improvement through calibration. Literature was an important part of the validation process for the SNR [125], spectral resolution [23], and polarimetric accuracy equations [16]. Other parts of the simulation did not have similar precedence, and required validation through mathematical principles, such as the spot size analysis and polarimetric error analysis results. The polarimetric error analysis results benefitted from having inputs that can be compared to the outputs to validate some results. However, other results such as the magnitude of certain error cases, do not have similar built-in forms of validation.

As a full ellipsometer simulation does not exist publicly and had to be fully designed from scratch, full validation of the program was not feasible. The simulations do however reach some large conclusions with implications for the instrument and its scientific usefulness as a whole. For example, the polarimetric accuracy simulations suggest that some design work or a relaxation of requirements will be necessary. Since these simulations cannot be fully validated at this stage, characterization of the instrument in the lab will be necessary to evaluate the conclusions drawn from the simulations.

Further simulations can also be performed to ensure the instrument will meet the requirements. When more is known about the sample and the relative positioning of the ellipsometer arms, BRDF simulations can be performed to better assess the goniometry capabilities of the instrument. The effects of certain optical components on the polarization can also be taken into account in Zemax, to ensure lenses and other elements are not causing significant measurement error.

Simulations are still valuable at this stage to confirm decisions before spending money, but as components begin arriving it will be important to shift to a more experimental approach to the ellipsometer design. The following chapter lays the groundwork for this approach, including procedures and lab prototypes for successful calibration of the instrument.

7

Instrument Calibration and Characterization

This chapter discusses considerations for the calibration and characterization of the instrument. This includes procedures for ensuring all major components of the instrument are configured for high-quality autonomous measurements. Calibration refers to comparing and adjusting the instrument parameters based on known standards in order to improve the performance. Characterization involves taking test measurements to understand the behaviour and limitations of the instrument before applying it to experiments.

As not all components of the instrument were procured before the completion of this thesis work, some sections only outline the recommended procedure for calibration and characterization according to ellipsometer research. However, sections with real characterization and calibration work done in the lab are also included.

7.1. Characterization of Key Components

7.1.1. Lamp Characterization

Newport's lamps are spectrally calibrated to deliver the required irradiance at specific wavelengths [133]. However, when the lamps arrive they need to be characterized for stability, thermal response, and background signal. The lamp bulb also needs to be installed and its positioning adjusted to maximize the power output. The lamp housing has positioning screws for both the bulb and the back reflector to achieve this.

Stability testing can simply be achieved by having the lamp switched on constantly over a 24-hour period. This provides an estimate of how much time it takes for the lamp to warm up and reach a stable output. Secondly, it provides a measure of the lamp's peak-to-peak output ripple over a 24-hour cycle. Overall, it is important to know how much the lamp's signal is fluctuating to see how the signal received at the detector would be impacted. While characterization is the main goal, an ideal stability metric to strive towards with this setup is a 0.1% peak-to-peak output ripple over a 24-hour cycle [23]. Figure 7.1 shows the expected behaviour for the lamp when measured over a 24-hour period.

Thermal response chracteristics can also be measured during such a test, as the lamp will be on during daytime and nighttime conditions. As the temperature changes over a 24-hour cycle, measurements of the lamp output will determine if there is a strong thermal dependence. This will inform decisions such as the importance of temperature-controlled experiments for the instrument.

Background signal from the lamp will also need to be measured, in tandem with the detector used for the instrument. This will need to be done each day before measurements, as the background can change with ambient lighting conditions and the position in the room. The background signal will be reduced as much as possible using precautions such as blackout curtains, turning off laboratory lights, and covering lights of other electronics. However, it is virtually impossible to eliminate all sources of stray light in the system. Thus, measuring the background signal from the detector without any effects from a sample will still be critical for determining the effects of the sample in isolation.

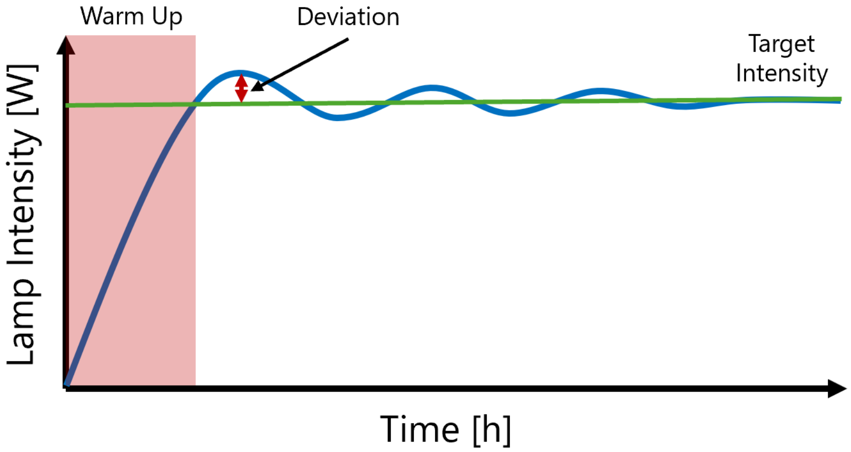

Figure 7.1: Measuring the lamp intensity over a 24-hour period.

7.1.2. Monochromator Characterization and Calibration

When the monochromator is received, it will also require some characterization and calibration in the lab before it is able to efficiently emit light at the expected wavelength. While the monochromator is calibrated at Newport's manufacturing facilities, components can shift in transit and recalibration is recommended [95]. It is also necessary to set up the monochromator for automated experiments, including automatic turret rotation and filter wheel configuration.

Grating Placement

Each grating in the turret of the monochromator must be positioned accurately such that light reflects off the grating at the correct angle and leaves the monochromator in the center of the exit slit. The geometric problem is depicted in Figure 7.2.

The grating turret sits on a rotation stage, and the position of this stage determines where light will reflect off of the final toroidal mirror before exiting the monochromator. Using a laser or other completely monochromatic light source, the monochromator first needs to be set to transmit the wavelength corresponding to that light source using the accompanying software. Figure 7.2 uses the example of a 633 nm Helium-Neon (He-Ne) laser, however other wavelengths could also be used. The entrance and exit slit widths should be configured as small as possible such that they still transmit the laser beam through the system, but at a very high spectral resolution. Once the slits and the grating are configured for operating at the test wavelength, the laser should be passed through the monochromator. It is important to first ensure that the incoming laser beam is perpendicular to the entrance slit of the monochromator for this calibration process. The rotation stage should then be rotated until the 633 nm laser can be seen at the output. It is recommended to use a detector at the output of the monochromator to detect the exiting light more accurately, rather than simply observing the exit with the eye.

It is possible to take advantage of the multiple diffraction orders of a grating in order to use the same He-Ne laser to calibrate multiple gratings. As discussed in Section 5.1.3, higher order diffractions take place at integer divisors of the diffracted wavelength. If the monochromator is used without the filter wheel, these higher order diffractions will exit the monochromator at the same angle as the first order diffraction. A grating that diffracts light at 1266 nm will also diffract at 633 nm at a higher order, due to this rule. This is proven using the grating equation, written as follows:

$$k\lambda = d(\sin\theta_k) \tag{7.1}$$

The order k is therefore an integer multiplier of the input wavelength λ, which will produce a different diffraction angle θ_k depending on the distance between the grooves of the diffraction grating d. As an example,

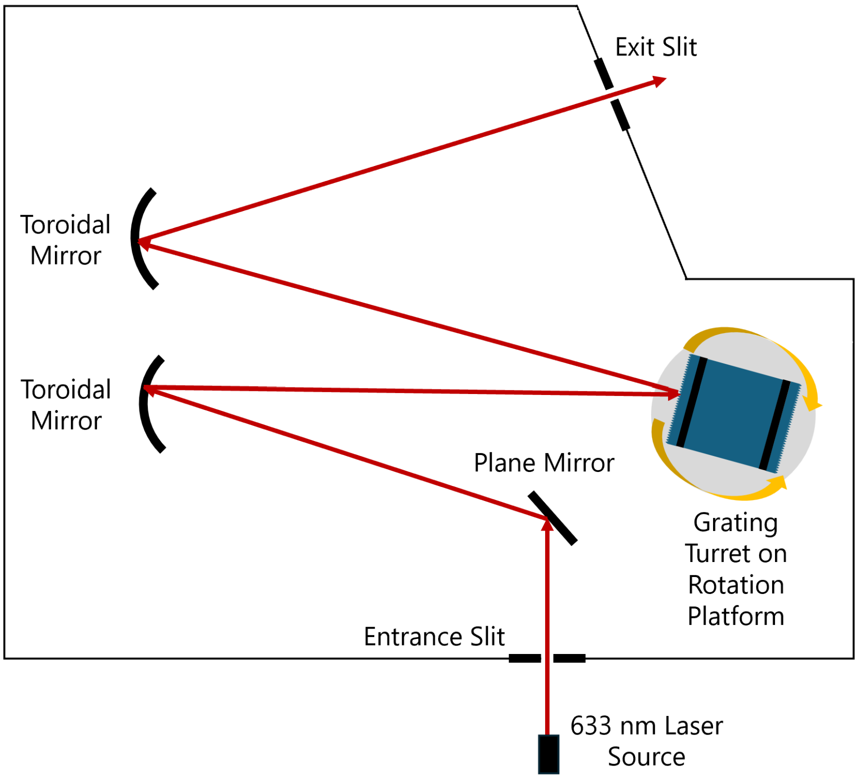

Figure 7.2: Aligning the grating turret using a 633 nm He-Ne laser.

the 4th order of the 3rd grating, with a diffraction range of 2300 – 3000 nm, can be used to calibrate that grating, as 4×633 nm is 2532 nm which falls directly in that range. Using the same laser is advantageous as it saves money spent on calibration equipment, but it also means the light source does not need to be realigned before calibrating the next grating, improving repeatability and consistency across gratings.

Once the laser is seen exiting the monochromator slit, the grating turret can then be set to that angular configuration using the CALIBRATE feature in the monochromator software [95].

Automation

The monochromator also needs to be configured so that the experiment can be run automatically over a wide spectral range. This will save time for future researchers and prevent errors in setup.

The grating turret and the filter wheel should both be configured to rotate at the required wavelengths to achieve the highest efficiency and block higher order diffraction. The exact wavelengths at which these reconfigurations happen will need to be determined based on a characterization of the monochromator. In general, the grating and filter combination that provides the highest transmittance at a given wavelength while blocking all higher-order diffractions should be used. The transmittance of the grating can depend on the polarization of light relative to the grooves of the grating, and should therefore be tested with the unpolarized light source to ensure that the efficiency matches with expectations for the instrument.

Another important part of monochromator setup is reaching accurate slit dimensions. In order to keep the system automated, the slit width and height can be verified periodically, but should not change over the course of a measurement unless required for particular high-resolution or high-signal applications. The slit width uses hand-controlled micrometers, which can be read to sufficient accuracy. The slit height uses a slider which is not marked to the same degree of accuracy. If high accuracy in the slit height is desired to better couple with the optical fibre, it is recommended to use a Vernier caliper. While motorized slits would help with the accuracy in theory, during the development of the SHADOWS instrument they often became stuck and did not reach the desired width and height [23].

7.1.3. Photoelastic Modulator Characterization and Calibration

HINDS calibrates all of its PEMs before shipping, however the rigours of travel may require the PEM to be recalibrated. There are some additional techniques that can improve the retardation accuracy of the PEM beyond what is offered by HINDS. Reaching acceptable photoelastic modulator accuracy is critical in achieving the polarimetric sensitivity and accuracy requirements for the instrument [SPG-P-01, SPG-P-02]. HINDS claims that successful calibration of the PEM while integrated with the instrument setup can improve retardation accuracy from <5% to <1% [70]. Another reason why further calibration of the PEM is necessary is that the retardation slightly changes over the aperture of the PEM by up to 4% [112]. If a laser was sent through the center of the PEM aperture at no incidence angle, this would not be a problem. However, a wide collimated beam is being used which will take up nearly the entire aperture of the PEM, and thus would not have a homogenous retardation across the beam.

Calibration with Oscilloscope

The first technique for PEM calibration uses a detector connected to an oscilloscope. In all tests using an oscilloscope, the highest possible detector frequency response is desired in order to clearly see features that indicate a calibrated PEM. If the frequency response of the detector used for this instrument is not large enough to clearly distinguish the modulation waveform, it is recommended to use a separate calibration sensor with much higher frequency response, such as the one designed by HINDS [134]. While the spectral range of these detectors is limited to $200 - 1000$ nm, being able to calibrate over that smaller region is still more valuable than no calibration at all.

HINDS recommends the use of a sharply defined monochromatic light source such as a laser or a spectral calibration lamp. White light with a monochromator can be used, however there is some uncertainty involved with the spectral resolution of the monochromator, as there may be some dependence on the emitted radiance within spectral bands. This can make it difficult to accurately coordinate the wavelength being calibrated with the wavelength exiting the monochromator.

The PEM is being used to act similarly to a rotating quarter-wave plate. As a result, the system should be calibrated to have peak retardation accuracy at a quarter-wave ($\lambda/4$). It should be connected to the electrical head and PEM controller in order to modulate at the PEM frequency and retardation. Typical calibration setups are designed for half-wave retardation, but a modification can be made to calibrate for $\lambda/4$.

The calibration setup is shown in Figure 7.3. The input light source, which can be the same laser as used for the monochromator alignment, first passes through a polarizer oriented at 45°. It then passes through the PEM's optical head, oriented at 0°, before hitting a plane mirror. After hitting this mirror, it reflects back through the same PEM optical head, before passing through an analyzer oriented at $-45°$. After transmitting through this optical system, it reaches the detector. This double-pass system converts a half-wave retardation calibration into a quarter-wave retardation calibration, as each single pass now represents quarter-wave retardation [70]. When this detector is connected to an oscilloscope, the waveform from the retardation modulation of the PEM will appear. From the figure, it appears that there is a large incidence angle for the monochromatic light source and the reflected light from the plane mirror. However, the polarizers, light source, detector, and plane mirror can all be placed far from the PEM optical head in order to decrease the incidence angle. Additionally, the retardation changes only 2% over a cone with a 20° half-angle [112], meaning this small angle of incidence will not have a large effect on the calibration result.

Figure 7.4 shows the waveforms for 90% of quarter-wave modulation, 110% of quarter-wave modulation, and precise quarter-wave modulation. A distinctive flat-topped response is achieved at the precise quarter-wave modulation, which can be confirmed by plotting Equation 6.15 with $F = \pi$ rad., equal to a half-wave retardation. By changing the modulation drive parameter $V_{control}$ in the HINDS PEM-CSC software, and analyzing the shape of the curve, the ideal calibration condition can be obtained. This flat-topped response will be more difficult to distinguish if the frequency response is not high enough, which may necessitate the calibration

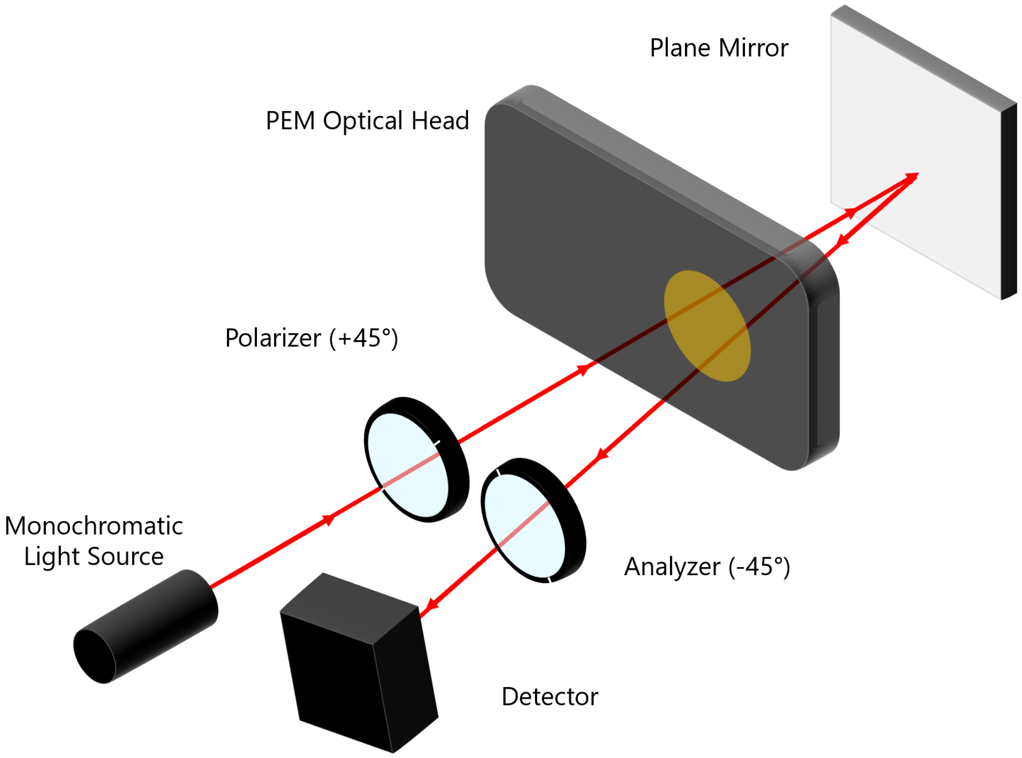

Figure 7.3: Double-pass calibration setup for minimizing uncertainty of quarter-wave modulation.

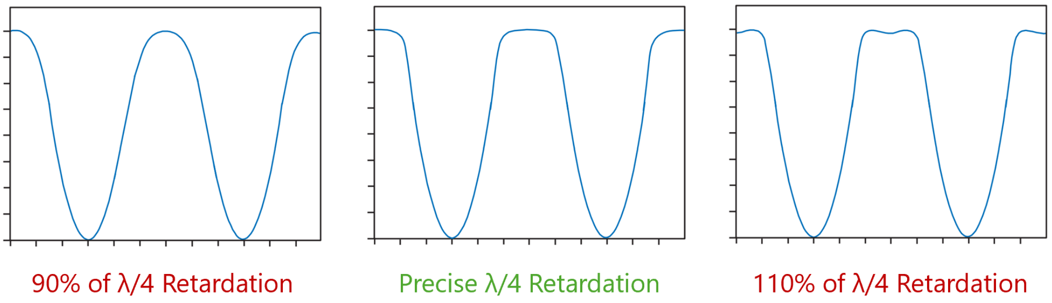

Figure 7.4: Relationship between modulation drive controller setting and waveform. Waveform figures from HINDS [70].

detector.

It is recommended to repeat this calibration with the lamp and monochromator that will be used for the ellipsometer. This is to ensure that the calibrated PEM still works for this light source, even when adding errors associated with using a beam that fills the PEM aperture. An approach that uses the laser for coarse calibration adjustments, then the monochromator and lamp for fine adjustment will likely yield the best results.

Calibration with Lock-in Amplifier

For an even more robust calibration, the lock-in amplifier can be used. In Section 6.4.1, it was stated that the retardation amplitude F is nominally set to 138° such that $J_0(F) = 0$, $2J_1(F) = 1.04$, and $2J_2(F) = 0.86$. In order to achieve this configuration accurately, the lock-in amplifier can be used to measure the DC intensity from the signal. When $J_0(F)$ vanishes, the DC intensity will be the same regardless of the orientation of the analyzer and the intensity of the light source. By changing the analyzer orientation angle and the modulation drive setting $V_{control}$ on the PEM, and recording plots of the DC voltage V_{DC}, the ideal calibration condition is achieved at the controller setting where all these curves of different analyzer orientations intersect. Figure 7.5 shows a visual representation of this calibration.

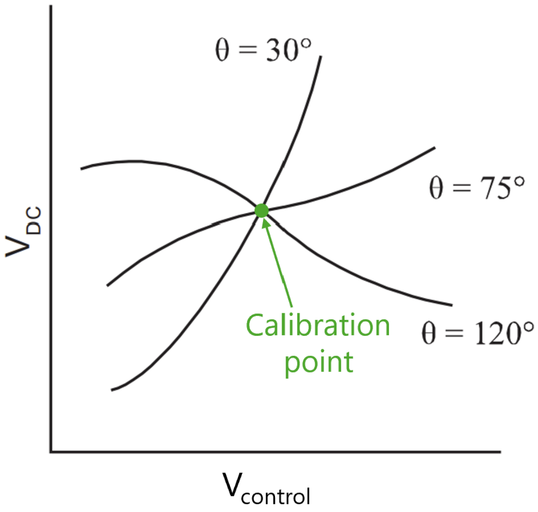

Figure 7.5: Calibration of Bessel terms using a lock-in amplifier. In this plot, θ refers to the angle of the analyzer. Figure adapted from HINDS [70].

The same is true when using a lock-in amplifier for the $J_1(F)$ and $J_2(F)$ terms, which can be made to vanish at distinct retardance amplitudes as well. Calibrating in the same way for these Bessel terms will ensure the retardation accuracy of the system is far below 1%. With the tight polarization sensitivity budget of the instrument, it is recommended to perform all of these calibrations.

Overall, calibrations should be performed at a few wavelengths spanning the entire spectral range of the instrument to ensure balanced calibration. From 300 − 3500 nm, the response of the system is quite consistent, but perfect calibration accuracy at the UV end of the spectral range could cause some imbalance at the IR end of the spectral range. A balanced calibration that minimizes the total uncertainty across all wavelengths of operation would be preferred.

7.2. Angular Error Calibration

As discussed in Section 6.4.2, reducing the angular error associated with the polarizers and the PEM is very important for ensuring sufficient polarimetric accuracy. Angular precision of approximately 0.01° is required to ensure a $\{\Psi, \Delta\}$ precision of $\{0.01°, 0.02°\}$. Such accuracy is difficult to achieve using the rotation mounts alone due to their limited precision, but there are methods of getting the best possible performance out of the available components. Additionally, the position of the polarizer inside the rotation mount is adjusted by hand, and therefore the transmission axis of the polarizer may not be precisely aligned with the 0° axis of the rotation mount. A more accurate method of positioning the polarizers is therefore required.

7.2.1. Relative Error Calibration

Relative error calibration refers to the angular error between the polarizer, the PEM, and the analyzer. The PEM had not yet arrived when this work had been completed, thus relative error calibration was only achieved between the two polarizers.

In the first measurement configuration, the two polarizers are at 90° separation from each other. The polarizer is at 45° and the analyzer is at −45°. If these polarizers were ideal and there was no stray light in the system, the intensity read by a detector placed behind these two crossed polarizers would be zero, a consequence of Malus' law stating the following [15]:

$$I = I_0 \cos^2(P - A) \tag{7.2}$$

Here, I is the intensity of light at the detector, I_0 is the intensity of light from the light source, and $P - A$ is the angle between the transmission axes of the polarizer and the analyzer.

Using this fact about ideal polarizers, the relative angle can be accurately set to 90° by adjusting the angle of one of the polarizers, and recording the intensity from the detector. The angular position with the lowest intensity corresponds to a 90° relative angle. This intensity will not be precisely zero as predicted by Malus' law due to small sources of stray light within the system, noise inherent to the detector, and imperfections in the extinction ratio of the polarizers.

A prototype for the calibration procedure was created, which includes a small QTH lamp from Thorlabs, two ultra-broadband wire-grid polarizers with rotation mounts from Thorlabs that will be used on the actual instrument, a neutral density filter with blocking level of 3.0 to ensure the detector does not become saturated, and an RGB camera from Thorlabs [135]. This camera has a pixel grid of 1440 [width] × 1080 [height] and imaging dimensions of 4.968 mm [width] × 3.726 mm [height], with three colour bands being imaged simultaneously. This is different from the detector used for the instrument, with one imaging pixel and no colour bands. The average intensity was taken across colour bands and pixels so that the data output would be comparable with the actual detector. Figure 7.6 shows the experimental setup for angular error calibration.

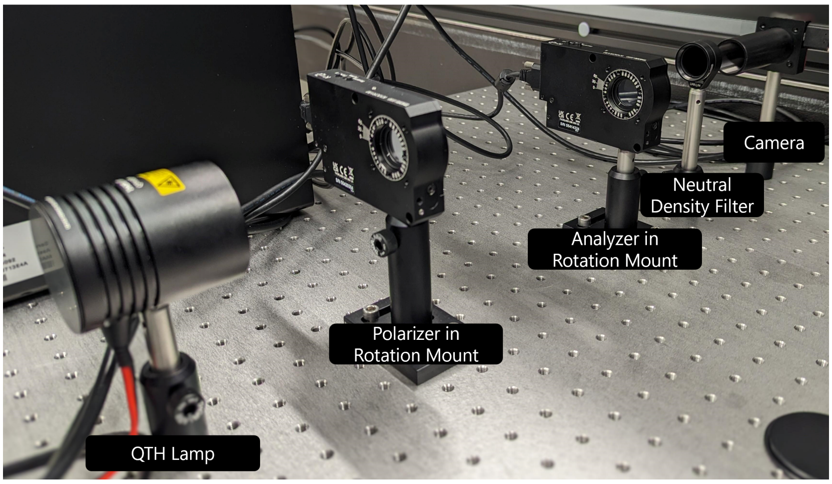

Figure 7.6: Experimental setup for angular calibration in the lab.

The rotation mounts and detector were interfaced using LabVIEW, as Thorlabs has produced software development tools for this program. Figure 7.7 shows the user interface for the program. The calibration procedure works in a loop, where the desired start position of the polarizers and the range over which to find the ideal polarizer positioning can be set. For example, if the analyzer start position is set to 315° (−45°), the calibration range to 2°, and the calibration step to 0.2°, then the analyzer will search for a minimum intensity from 313° to 317° with a step size of 0.2°.

Before setting the polarizer and analyzer to the start position, it is important to home both of the rotation mounts. The process of homing refers to defining the zero position of the mount so that the absolute position of the mount can be obtained at any point. After homing, the mounts can be set to the start position and the calibration loop can begin. At each of the angular positions within the specified range, the program will command the camera to take an image and record the mean intensity at that position. If the mean intensity of the current image is lower than the currently recorded minimum intensity, then the calibrated start position for the analyzer is updated. When the loop is complete, the program will display the calibrated position for the analyzer, as well as a plot of the mean intensity at each angle. This plot includes error bars which correspond to the standard deviation of the intensity data. Figure 7.8 shows the general outline of the calibration loop.

Using the experimental setup in Figure 7.6, the relative calibration procedure was implemented in LabVIEW.

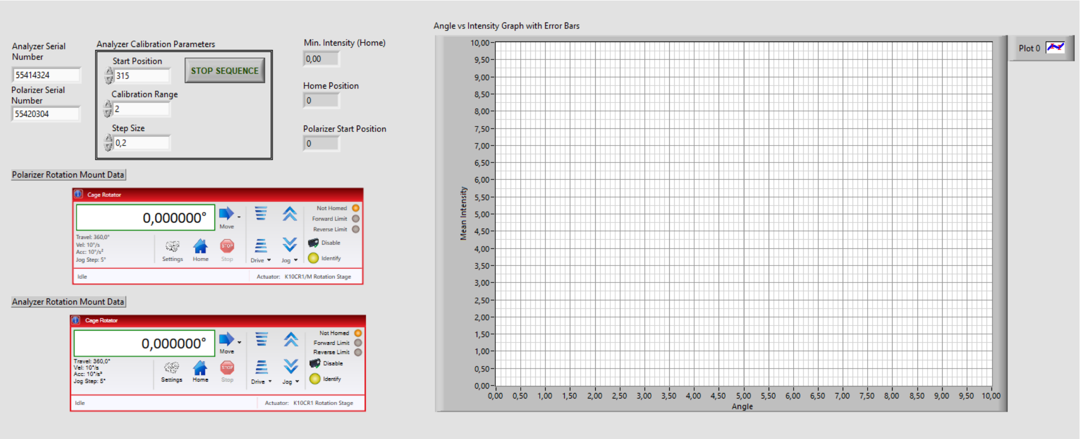

Analyzer Serial Number: 55414324
Polarizer Serial Number: 55420304
Analyzer Calibration Parameters
Start Position: 315
Calibration Range: 2
Step Size: 0,2
Min. Intensity (Home): 0,00
Home Position: 0
Polarizer Start Position: 0

Polarizer Rotation Mount Data
Cage Rotator: 0,000000°
Travel: 360,0°
Vel: 10°/s
Acc: 10°/s²
Jog Step: 5°
Idle
Actuator: K10CR1/M Rotation Stage

Analyzer Rotation Mount Data
Cage Rotator: 0,000000°
Travel: 360,0°
Vel: 10°/s
Acc: 10°/s²
Jog Step: 5°
Idle
Actuator: K10CR1 Rotation Stage

Figure 7.7: User interface for relative calibration program created in LabVIEW.

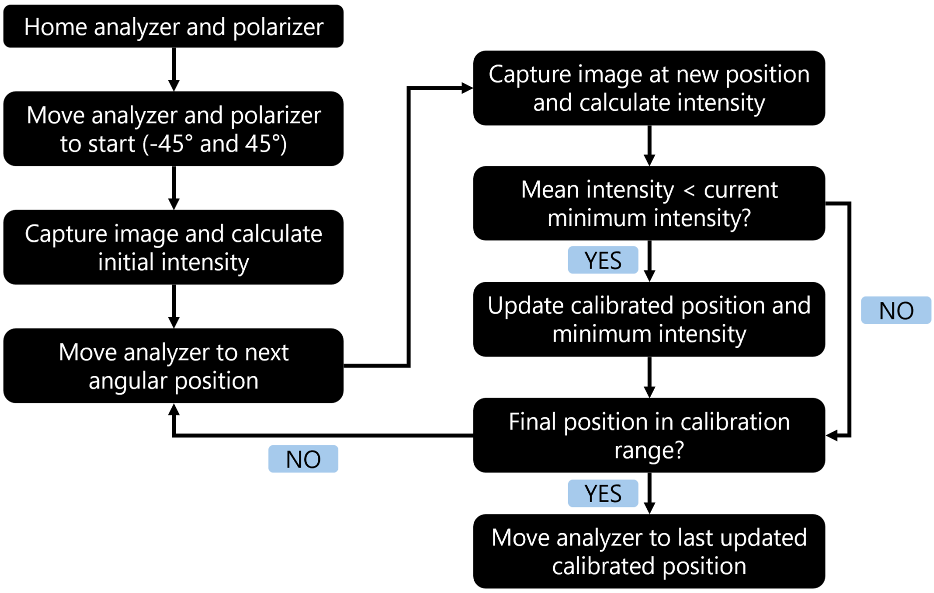

Figure 7.8: Relative calibration loop flow chart implemented in LabVIEW.

Figure 7.9 shows the mean intensity at each angular position of the analyzer for a start position of 315° (−45°), a calibration range of 2°, and a step size of 0.2°. There is some stray light in the room due to monitors, so the noise associated with each measurement is captured using the error bars. Each error bar covers the range of one standard deviation both above and below the mean. Overall, the behaviour approximates a parabola as expected from Malus' law. This is confirmed by using a parabolic curve fit over the data, which has an $R^2 = 0.953$, suggesting an excellent fit. For this setup, the calibrated analyzer position was at 315.64° (−44.36°), based on the minimum of the parabolic curve fit.

Unfortunately, one of the rotation mounts had a broken worm gear and needed to be repaired during this operation. This made it difficult to run a fully automated test as the rotation mount would often seize, making it unable to complete some rotations. When the mount was replaced, the accuracy of these results was confirmed.

A similar procedure will need to be completed with the PEM. When the PEM is not being driven, there is still residual birefringence. It is therefore recommended to calibrate the polarizer and analyzer relative to eachother with the PEM removed. The PEM can then be included, and needs to be set at −45° relative to the polarizer. The PEM will rotate with the polarizer due to the cage mount design discussed in Section 5.2.3. There will however be some angular error with the initial setup of the PEM relative to the polarizer. The angular calibration of the PEM requires connection with the lock-in amplifier and integration with a known

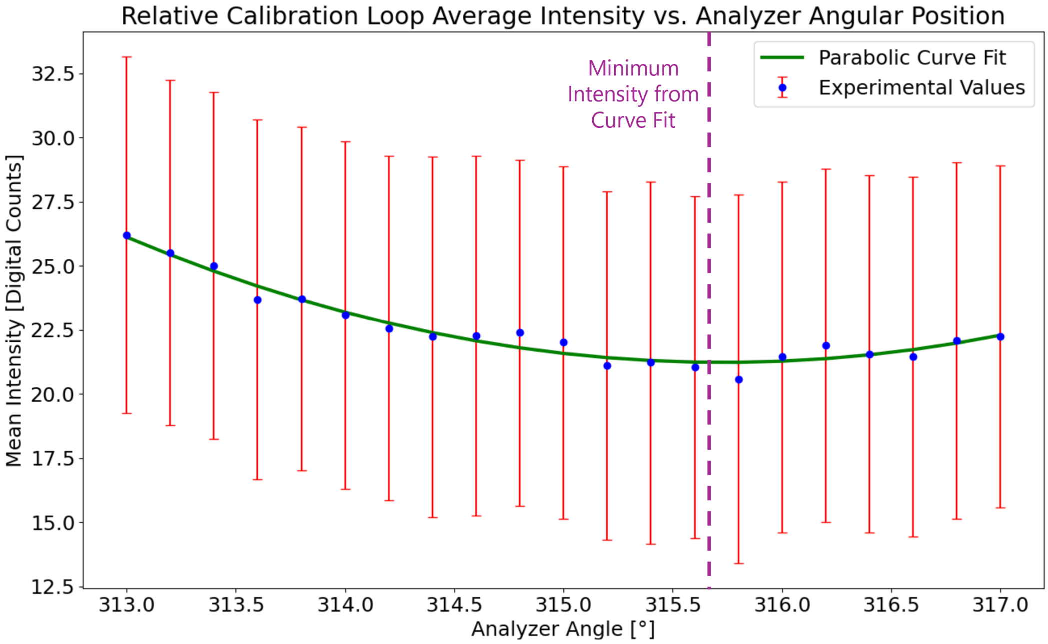

Figure 7.9: Angle vs. intensity plot for relative calibration loop, with experimental and curve fitted results shown. Error bars for mean intensity are shown in red as the standard deviation of intensity values across all pixels.

sample. The calibrated angle of the PEM will be the angle that minimizes the error between the outputted lock-in amplifier coefficients and the expected intensity coefficients from Equation 6.15. An important caveat is that this requires knowledge of the expected Ψ and Δ behaviour of the sample used for calibration. Further prototyping and development of this calibration procedure was not completed in this work, as the components were not available.

7.2.2. Absolute Error Calibration

While relative positioning between the polarizer and analyzer is important, the absolute position of the polarizer relative to the plane of incidence also needs to be calibrated. This will determine the starting point for the relative calibration of the analyzer. The plane of incidence refers to the plane containing the incident and reflected light, as well as the normal to the sample surface. It is also the plane that would contain p-polarized light.

In the calibration prototype in the lab, the plane of incidence is parallel to the optical bench, as there is no sample to determine the measurement orientation. A prototype for the absolute angular error was therefore not performed, as a more extensive setup including a sample would be required. This is because light that is entering the first polarizer is unpolarized, which would mean any planes that the light beam passes through could be defined as the p- and s-polarized planes.

For the actual instrument, absolute angular calibration is performed using the residuals method [16]. This absolute calibration is performed before the insertion of the PEM, and thus the ellipsometer at this stage can be considered a rotating analyzer ellipsometer (RAE). The intensity equation for this setup can be written as follows:

$$I_t(t) = I_0[1 + \eta\alpha \cos[2(\omega_A t - A_s)] + \eta\beta \sin[2(\omega_A t - A_s)]] \tag{7.3}$$

This expression is a better representation of the effects of angular deviation and imperfect detector efficiency on the intensity, with η_{AC} representing the attenuation of AC intensity components α and β relative to the DC component I_0, and A_s being the deviation of the analyzer from the plane of incidence. The timestep t and analyzer rotation frequency ω_A are also included as parameters in this equation. Experimental coefficients α' and β' can then be calculated using the following:

$$\begin{bmatrix} \alpha' \\ \beta' \end{bmatrix} = \eta \begin{bmatrix} \cos(2A_s) & -\sin(2A_s) \\ \sin(2A_s) & \cos(2A_s) \end{bmatrix} \begin{bmatrix} \alpha \\ \beta \end{bmatrix} \tag{7.4}$$

The residual method then focuses on minimizing a residual function which can be expressed as:

$$R(P) = 1 - (\alpha'^2 + \beta'^2) \tag{7.5a}$$

$$R(P) = (1 - \eta^2) + \eta^2 \left[\frac{\sin(2\Psi)\sin(\Delta)\sin[2(P - P_s)]}{1 - \cos(2\Psi)\cos[2(P - P_s)]} \right]^2 \tag{7.5b}$$

The residual function therefore depends on Ψ, Δ, η and the deviation of the polarizer angle $P - P_s$. When the polarizer is at exactly 0° relative to the plane of incidence, only the p-polarized component of light arriving from the lamp will illuminate the sample. Reflected light would therefore be p-polarized. Using an analyzer at 90° from the polarizer will then block light from reaching the detector. If the polarizer deviates from 0°, the reflected light would be slightly elliptically polarized, causing a larger transmission of light through the analyzer. Therefore, the polarizer position that minimizes this residual is the calibrated absolute polarizer position. Figure 7.10 shows an example of how this residual varies with the angle of the polarizer.

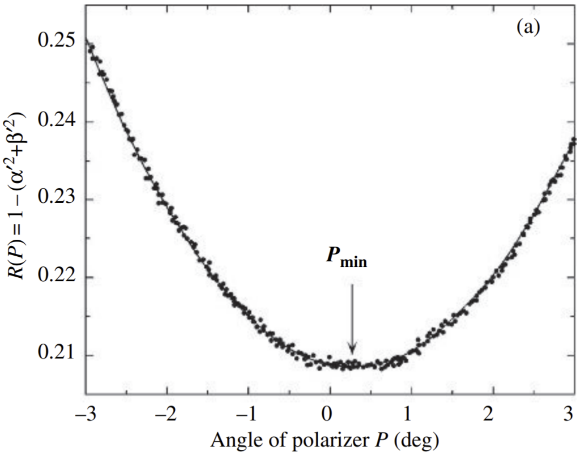

Figure 7.10: Using the residual function to calibrate the absolute position of the polarizer. Figure from [16].

The polarizer must be set at 0° in configuration 2, as defined in Section 4.7. However, in configuration 1 it must be set at 45°, which would produce an equal intensity in p and s-polarization. This is more difficult to calibrate precisely due to the elliptical polarization that will reflect from the sample at this orientation. It is therefore recommended to calibrate the polarizer at 0° relative to the incidence angle, and then set the polarizer at 45° relative to this calibration.

7.2.3. Calibration Limitations

While these calibration methods will help to get as much performance as possible from the system components, there are some physical limitations that may prevent the required angular accuracy from being reached.

The maximum accuracy of the rotation mounts used to rotate the polarizers is 0.14° [113]. While the calibration procedure can be used to help determine the calibrated angular position, some error in measurement may occur when the rotation mount is commanded to actually rotate to that calibrated position. It may be slightly off from that position by up to 0.14°. Additionally, repeatability of the measurements would also be limited by this accuracy. When the polarizer needs to rotate between configuration 1 and configuration 2, it may not be at exactly the same angle when it rotates back to configuration 1. A measurement could be taken to ensure the calibrated intensity and the experimental intensity are similar before beginning measurements. However, the intensity is also dependent on factors such as stray light that may make this verification step somewhat unreliable.

The rotation mount's accuracy is also a limiting factor when rotating between configurations. The absolute calibration procedure for configuration 2 was to set the polarizer at 45° relative to the 0° position set in configuration 1. However, this could also deviate by up to 0.14°. Angular errors of this magnitude, as shown in Section 6.4, would already cause large errors in Ψ and Δ that exceed the accuracy requirements [SPG-P-01, SPG-P-02].

Overall, it will be important to see how much this angular uncertainty affects the polarimetric accuracy during the characterization phase. However, when considering that the polarimetric accuracy will be impacted by angular error, retardance error, and other sources of error at the same time, the compounding effect of these uncertainties may make it difficult to meet the polarimetric accuracy requirements with the current design. There are also many factors that are not being captured in the simulation. Given these constraints, it may be necessary to replace the rotation mounts with more precise models, or relax the instrument requirements.

7.3. Integrated Calibration

Once optical calibration procedures are completed, the system can be assembled for an integrated characterization and calibration procedure. The main goal of characterization at this stage is to measure the performance of the instrument, including SNR and polarimetric sensitivity. This will require the entire instrument to be integrated with a sample that is representative of the planetary analogues used for real experiments.

First, the goniometric arms need to be calibrated. It is important to do this after the optical components have been attached to each of the arms. Larger loads on each of the arms cause a higher torque on the rotation stage, which could cause it to miss steps and read its position inaccurately. This risk can be reduced or eliminated by using a stronger rotation mount, but it is still worth characterizing the rotation stage to better understand the performance of the goniometer in this worst-case scenario. The rotation stages should also be calibrated to provide the angular position relative to the instrument nadir, which is normal to the optical table surface that supports the light source.

After the goniometric arms are calibrated, the end-to-end ellipsometer performance can be characterized. This can first be accomplished using a pass-through method as shown in Figure 4.12. When passing through air, the values of Ψ and Δ are 45° and 0° respectively which serve as a good calibration point, as well as a test of the instrument's polarimetric sensitivity. Other characterization points for Ψ and Δ can use common ellipsometric surfaces with known optical parameters and thicknesses. Surfaces such as silicon-oxide thin films with known thicknesses can be analyzed, with the values of Ψ and Δ being used to solve for these surface properties.

Thermal considerations are also important for the integrated system. Components such as the PEM and detector are sensitive to changes in temperature, affecting the quality of measurements. Other optical components can also deform as a result of large temperature variations. The electronic components in the monochromator can even be damaged if the temperature is too high [95]. The room should therefore be temperature controlled in order to ensure accurate measurements throughout the year.

A full characterization also requires a test of each of the operating modes. In order to get Ψ and Δ measurements, configurations 1 and 2 are required as described in Section 4.7. The main challenge is to ensure that the relative angles of the polarizer and PEM are correct and remain consistent throughout configuration changes. Configuration 3 also adds complexity, as the repeatable removal and replacement of the PEM must also be considered.

Different goniometric configurations should also be tested, including specular, back-scattering, and forward-scattering, to ensure that the illumination arm and observation arm are properly aligned with the sample, and that the SNR is sufficient in all situations.

8

Conclusions and Future Work

In this final part, the design of the instrument is first evaluated relative to the requirements defined in Chapter 3. A summarized discussion of the major research questions of the thesis is then provided. The final subsections address how this work can be improved and extended to eventually solve the overarching scientific goals of spectroscopic ellipsometry applied to planetary sciences.

8.1. Requirements Compliance

This section provides an overview of the design specifications of the spectroscopic ellipsometer, and how it performs relative to the requirements listed in Chapter 3. Table 8.1 shows the functional requirements, Table 8.2 shows the constraints, and Table 8.3 shows the performance requirements. All requirements in Chapter 3 were given a verification method of T, A, or R. Requirements with the T verification method, corresponding to testing, are not fully verified at this stage. While the green colour suggests the requirement is verified, that is only to state that the simulated design meets the requirement at this time. Requirements with the A and R verification method can be considered fully verified at this stage of the design, though testing with the actual instrument is typically still preferred.

The majority of the requirements have been verified to some extent, or needed to be modified to achieve more realistic performance. However, most performance requirements will require further verification during the assembly and characterization phase for the instrument. It is also currently unknown how much processes like angular and retardance calibration will improve measurement results, or the effects of stray light on the system. Better characterizing these effects once the instrument is assembled will help establish a more realistic performance overview of the instrument.

Table 8.1: Functional requirements compliance matrix. A red colour in the compliance column means the specification currently does not meet the requirement or has not yet been verified. A green colour in the compliance column means the specification currently meets the requirement, but may require some testing to verify. Full descriptions of associated requirements can be found in Table 3.1.

Requirement ID	Title	Description	Compliance	Comments
SPG-F-01	Polarimetry	Polarimetry of reflected light.	🟩	Verified by design.
SPG-F-02	Spectroscopy	Spectroscopy of reflected light.	🟩	Verified by design.
SPG-F-03	Spectropolarimeter functionality	Simultaneous polarimetric and spectroscopic measurements.	🟩	Verified by design.
SPG-F-04	Type of measurements	Sample located inside instrument.	🟩	Verified by design.
SPG-F-05	Output format	Stokes, Ψ, Δ.	🟩	Verified by design with 2 PEM configurations.
SPG-F-06	Light source	Repositionable illumination arm.	🟩	Verified by design.
SPG-F-07	Observation	Repositionable observation arm.	🟩	Verified by design.
SPG-F-08	Sample types	Rock, powder, and ice samples.	🟥	Must be verified using actual instrument to ensure adequate reflectance.
SPG-F-09	Source polarization (linear)	Known polarization input to the sample.	🟩	Verified by use of PEM and polarizers in design.
SPG-F-10	Source spectrum	Known wavelength input to the sample.	🟩	Verified by use of monochromator in design.
SPG-F-11	Load bearing	Support weight of components on goniometric arms.	🟩	Verified in Table 5.11.
SPG-F-12	Mounting	All components on goniometric arms need mounts.	🟩	Verified by design.
SPG-F-13	Stray light	Stray light mitigation methods.	🟥	Not yet considered in design.
SPG-F-14	Alignment	Components accessible for alignment.	🟩	Verified through design, minimum 7.5 cm spacing between components.
SPG-F-15	Polarimetric considerations	Multiple configurations without manual realignment.	🟩	Verified by use of automated rotation mounts and calibration loops. Configuration 3 realignment will require further verification.
SPG-F-16	Safety	Limiting mechanisms to prevent damage.	🟥	Not yet incorporated into design.

Table 8.2: Constraint requirements compliance matrix. A red colour in the compliance column means the specification currently does not meet the requirement or has not yet been verified. A green colour in the compliance column means the specification currently meets the requirement. Full descriptions of associated requirements can be found in Table 3.2.

Requirement ID	Title	Value	Specification	Compliance	Comments
SPG-C-01	Instrument cost	< €180,000	€122,398	🟩	Further expenses expected during development, but major expenses considered in Appendix A.1.
SPG-C-02	Instrument volume	$2 \times 2 \times 2$ m	$1.2 \times 1.9 \times 2.0$ m	🟩	Based on current component sizing.
SPG-C-03	Temperature range	15 - 25 ° C	15 - 28 ° C	🟩	Based on datasheet operating temperatures.

Table 8.3: Performance requirements compliance matrix. Red in the compliance column means the specification currently does not meet the requirement, and requires additional calibration or design to improve. Green means the specification currently meets the requirement, but requires some testing to verify. Full descriptions of associated requirements can be found in Table 3.3.

Requirement ID	Title	Value	Specification	Compliance	Comments
SPG-P-01	Intensity polarimetric accuracy	0.01	1.00	🟥	Requires calibration and design work to correct.
SPG-P-02	Phase polarimetric accuracy	0.02	0.20	🟥	Requires calibration and design work to correct.
SPG-P-03	Spectral range linear data	300 – 4500 nm	300 – 4500 nm	🟩	Requires verification of sufficient polarimetric accuracy beyond 4000 nm.
SPG-P-04	Spectral range circular data	300 – 4500 nm	300 – 3500 nm	🟥	Only linear polarization possible above 3500 nm due to PEM transmission restrictions.
SPG-P-05	Infrared spectral sampling	20 nm	4.59 – 19.22 nm	🟩	Verified in spectral resolution simulation, requires testing to verify adequate SNR at this resolution.
SPG-P-06	Visible spectral sampling	5 nm	2.32 – 2.42 nm	🟩	Verified in spectral resolution simulation, must test for adequate SNR.
SPG-P-07	Minimum sample reflection	10%	10%	🟩	Verified in SNR simulation, must test for adequate SNR.
SPG-P-08	Sample length/width	1 – 5 cm	3 – 5 cm	🟩	Verified in spot size simulation.
SPG-P-09	Sample grain diameter	>10 μm	40 μm	🟩	Verified in spot size simulation. Verify with real samples.
SPG-P-10	Phase angles	5° – 180°	4.4° – 180°	🟩	Verified using Zemax, requires physical layout or CAD modelling verification.
SPG-P-11	Signal-to-noise ratio	> 17 dB	> 24.0 dB	🟩	Includes target spectral bands. Requires testing verification for stray light effects.
SPG-P-12	Source collimation	< 2°	1.05°	🟩	Verified through Zemax simulation. Manufacturability needs verification.
SPG-P-13	Achromatization	< 1%	< 1%	🟩	Verified by HINDS.
SPG-P-14	Illumination arm range	0° – 90°	0° – 90°	🟩	Verified through design. Can be tested to ensure no mechanical limitations.
SPG-P-15	Observation arm range	−75° – 90°	−75° – 90°	🟩	Verified through design. Can be tested to ensure no mechanical limitations.
SPG-P-16	Goniometric accuracy	< 0.1°	0.008°	🟩	Verified by Newport [124].
SPG-P-17	Tip/tilt adjustment	< 0.1°	0.036°	🟩	Verified by Thorlabs [114].
SPG-P-18	Clock angle tolerance	< 0.01°	0.14°	🟥	May require rotation mounts with better accuracy.
SPG-P-19	Decenter tolerance	< 100μm	< 100μm	🟩	Falls within typical or precision tolerance ranges [132].
SPG-P-20	Despace tolerance	< 100μm	< 100μm	🟩	Falls within typical or precision tolerance ranges [132].
SPG-P-21	Angular resolution	< 10°	8.0°	🟩	Verified in SNR simulation, must test adequate SNR.
SPG-P-22	Observation spot diameter	1 – 50 mm	4.4 – 25.4 mm	🟩	Verified with spot size simulation, requires testing to verify adequate SNR.
SPG-P-23	Illumination spot diameter	Larger than observation	25.4 – 146.3 mm	🟩	Verified with spot size simulation, must test with real alignments.

8.2. Research Questions

From Chapter 1, the major research question addressed in this work is: ***To what extent can spectroscopic ellipsometry be used for the compositional and structural analysis of planetary surfaces?***

Overall, this thesis has shown that the spectroscopic ellipsometer is a promising instrument for applications to planetary sciences. While the field of spectropolarimetry for planetary sciences is still emerging, meaning requirements are not yet fully defined, the instrument shows evidence of valuable spectral and polarimetric performance after calibration and further validation through testing. This overarching research question will be fully answered once the instrument is assembled and experiments are performed, but the design shows strong potential to apply to compositional and structural analysis of planetary surfaces. This main research question was further addressed by investigating three research sub-questions which are discussed in the following subsections.

8.2.1. Design Drivers

Research sub-question 1: *What are the design drivers of a spectroscopic ellipsometer intended for planetary surface studies?*

Through a thorough design of the instrument, the major design drivers for a spectroscopic ellipsometer that is specifically applied to planetary sciences were identified:

- Spectral range is a critical component of the design, as measuring data in the UV, visible, and IR regimes is necessary to gain insights about the composition and structure of species that are common on planetary surfaces.
- Signal-to-noise ratio directly impacts all measurement data. If the SNR is not sufficiently high, the quality of measurements will not be adequate to draw scientific conclusions.
- Polarimetric sensitivity needs to be prioritized as it is the main performance metric of the instrument.

All other important aspects of the design flow from these three design drivers, including spot size analysis, angular error calibration, operational modes, and alignment tolerances. Goniometric requirements were not listed at this phase of the design as the optical design was the main focus of this work. The goniometric features were designed around the optical performance, and met requirements without significant design effort or impact on the design as a whole. Future mechanical analysis may highlight goniometric accuracy or range as another design driver.

8.2.2. Performance Validation

Research sub-question 2: *How can sufficient goniometric, spectroscopic, and polarimetric performance of the instrument be validated?*

It is often difficult to validate the performance of the instrument without a physical prototype, because real world effects such as stray light are difficult to take into account. However, as the instrument has a limited budget and assembly can take a long time, it was chosen to use simulations to validate some performance metrics for the instrument. These will need further verification and validation through physical testing, but provide an approximation of the true performance, and some insurance that the design can work as intended.

The first simulation involved the SNR design driver. The SNR simulation showed adequate performance across the entire spectral range. This simulation was validated by applying relations used in published works about other optical designs [125].

The spectral resolution simulation verified the instrument's ability to gather high-accuracy spectroscopic data. This involved a single equation, validated by the thesis work of Dr. Sandra Potin [23].

Spot-size analysis was the next simulation, which defined requirements for sample size, grain size, and the size of the cone of light collected by the observation arm. This code was based on geometry as described in Section 6.3, and thus the validation involved ensuring the visualization of the math being used in the simulation matched the real life spot size analysis orientations and relative sizes.

Finally, polarimetric sensitivity analysis completes the suite of simulations for verifying the instrument's performance relative to the requirements. This simulation has a built-in validation feature, as the inputs are required to match the outputs very closely due to the function of the lock-in amplifier. However, results such as the magnitude of polarimetric errors cannot be validated using the simulation alone.

Overall, efforts were made to verify the instrument performance and validate the simulations as much as possible using the resources available. Of course, it will be necessary to validate these simulations and the instrument's performance as a whole using physical testing on the instrument once assembled. Conditions in the lab can change some of these results, and the simulations failed to capture some effects such as stray light and thermal variations.

8.2.3. Instrument Calibration

Research sub-question 3: *How can a spectroscopic ellipsometer be calibrated to take effective measurements of planetary surfaces?*

Chapter 7 addressed the calibration of the instrument. As seen in Chapter 6, calibration is important for ensuring the instrument is minimizing error to the extent possible.

The monochromator will require calibration of the grating's position to ensure the specified wavelength is exiting the system. The PEM will also require calibration to ensure that the retardance accuracy is maximized. The instrument will also need to be calibrated for the angular position of the goniometric arms relative to the sample, and the background signature of the lamp and detector.

Work in the lab was done on an angular calibration procedure for the polarizers and PEM, which is another critical component in ensuring maximal polarization accuracy. These procedures will help to ensure that the instrument is able to get the best possible performance out of the components being used. However, it remains to be seen through actual characterization of the instrument if the calibration procedures will help the instrument meet all the requirements, or if further design work is necessary.

8.3. Immediate Next Steps

This work primarily focused on the optical design and simulation of the spectroscopic ellipsometer instrument. There is additional work to be done before assembly begins, followed by full assembly and characterization of the instrument. This section highlights some major future milestones in the project:

- **Mechanical Analysis:** The CAD model for this instrument first needs to be further developed. This is important for properly visualizing component spacing and anticipating mechanical collisions or assembly issues. It can also be used to perform deflection analysis, which can be an important factor in alignment tolerancing considerations.

- **Condenser-Focuser Design Improvements:** The custom condenser-focuser from the lamp to the monochromator still requires significant design work. From an optical perspective, additional design features such as a baffle could improve throughput into the monochromator. Thermal and mechanical mounting considerations must also be considered due to the bulb's proximity to the lenses. The custom condenser design must then be modelled in CAD to be manufactured.

- **Polarizer - PEM Mounting:** Thorlabs cautions placing high loads on the rotation mounts that hold the linear polarizers. This can cause extra resistance on the motor, making it more prone to fatigue and damage. A lightweight adapter to rotate the PEM with the polarizer mount will need to be designed. If it is still too heavy, an adapter that relieves some torque from the polarizer mount may be required.

- **Operating Mode Transitions:** The transitions between configurations 1, 2, and 3 should require minimal manual realignment of the system, and should ideally be automated. Design work will need to be done to automatically recalibrate the instrument after transitioning between operating modes.
- **Lens and Mirror Manufacturability:** Some work was done during the optimization procedure to ensure lenses and mirrors would be manufacturable. However, it is important to consult custom lens and mirror manufacturers to see if these designs can be built, or if any modifications are necessary.
- **Polarization Sensitivity of Optical Elements:** After reflection off of the sample, lenses were chosen for the collimator and focuser in order to limit further impacts on polarization. However, lenses can still affect, and be affected by, the polarization of light. These behaviours should be analyzed to ensure that errors are not too significant.
- **Sample Selection and Design:** Selecting the planetary analogues that will be used in the instrument is an important next step in using this instrument for its intended purpose. This will involve finding analogue materials that meet the reflectivity and size requirements, and purchasing them for early characterization tests. This will also lead to the development of BRDF simulations, helping to verify goniometric performance.
- **Ice Sample Experimental Setup:** Ice samples will require additional design work to ensure the temperature is kept cold and constant throughout the test. This can include using liquid nitrogen cold plates from optics equipment manufacturers.
- **Calibration of Major Components:** As major components such as the monochromator, lamp, and PEM arrive, performing the characterization and calibration steps outlined in Chapter 7 is a critical step before assembling the entire instrument. Absolute angular error calibration can also be performed using a sample as described in Section 7.2.2. This will help to confirm if any instrument redesign or requirement relaxation is necessary.
- **Prototypes:** Testing prototypes of the instrument is also important before assembling the entire setup. This can include a horizontal ellipsometer assembled on a lab bench without moving arms to test the reflection of light off of a sample. This can also be done with common ellipsometric substrates to calibrate Δ and Ψ. Early prototypes can use subsets of the instrument, such as the linear polarizers without the PEM, or spectral filters instead of the lamp and monochromator. However, it is important to build up to a full system optical prototype before introducing goniometry.
- **Goniometric Integration:** Instrument components can then be assembled on the goniometric arms to begin testing ellipsometry at different phase angles.
- **Instrument Characterization:** Once integrated, the instrument can then be characterized on real samples to verify simulated performance.
- **Applying Ψ and Δ to Planetary Surfaces:** This instrument is intended to investigate planetary surface structure and composition. However, this work has not been completed by an ellipsometer, and thus some work will be necessary to build upon the relations between $\{\Psi, \Delta\}$ and optical constants that are derived for standard ellipsometry surfaces. This also encompasses the design of any experiments where the ellipsometer can be applied.

8.4. Long-Term Evolution

The end goal of this laboratory instrument is to be adapted for a spacecraft payload, to take measurements of any surface that a spacecraft can access. The instrument designed in this thesis is not suitable for spaceflight in its current configuration. Any effort to make this instrument viable for a spacecraft payload will need to focus on a few critical spacecraft compatibility concerns once performance of the proof of concept model is verified. This is still a few years from development, but it is still worth investigating potential research avenues to realize this goal.

The instrument currently creates its own polarized light source, which will not be the case in a typical spacecraft payload configuration. The sun will be the light source for spectropolarimetric measurements, meaning unpolarized light will be reflecting off of planetary surfaces. The payload would therefore be required to measure the spectropolarimetric change from an unpolarized source. In order to do this, the photoelastic modulator could move to the observation arm with minimal impact to the instrument function [16]. The most challenging component is replacing the linear polarizer on the illumination arm, as a polarizing element cannot feasibly be placed between the sun and the planetary surface. It is otherwise quite difficult to determine the effect of the surface on the reflected light, as the input light orientation is unknown. There is very limited research on spectroscopic ellipsometry with an unpolarized source, and thus looking towards spectropolarimetric payloads such as SPEX [67] could be a useful place to start. An alternative is using retrieval methods to gather a sample from the planetary surface to use for measurements in a typical ellipsometer configuration on a spacecraft, but this would require many further developments that extend beyond instrumentation.

There is a similar issue in the spectral domain, as the monochromator limits the light input to a single wavelength, while the sun emits a spectrum. The monochromator would therefore need to be replaced by a spectrometer, either using interferometry or a dispersive element. As discussed in Section 4.2, having the spectroscopic element at the end of the optical track causes some concerns about both the sensitivity of the system to different polarizations of light, and the effect that spectroscopy can have on the polarization of light itself. These concerns will need to be addressed through the selection of components to mitigate these polarimetric effects, such as freeform mirrors [67].

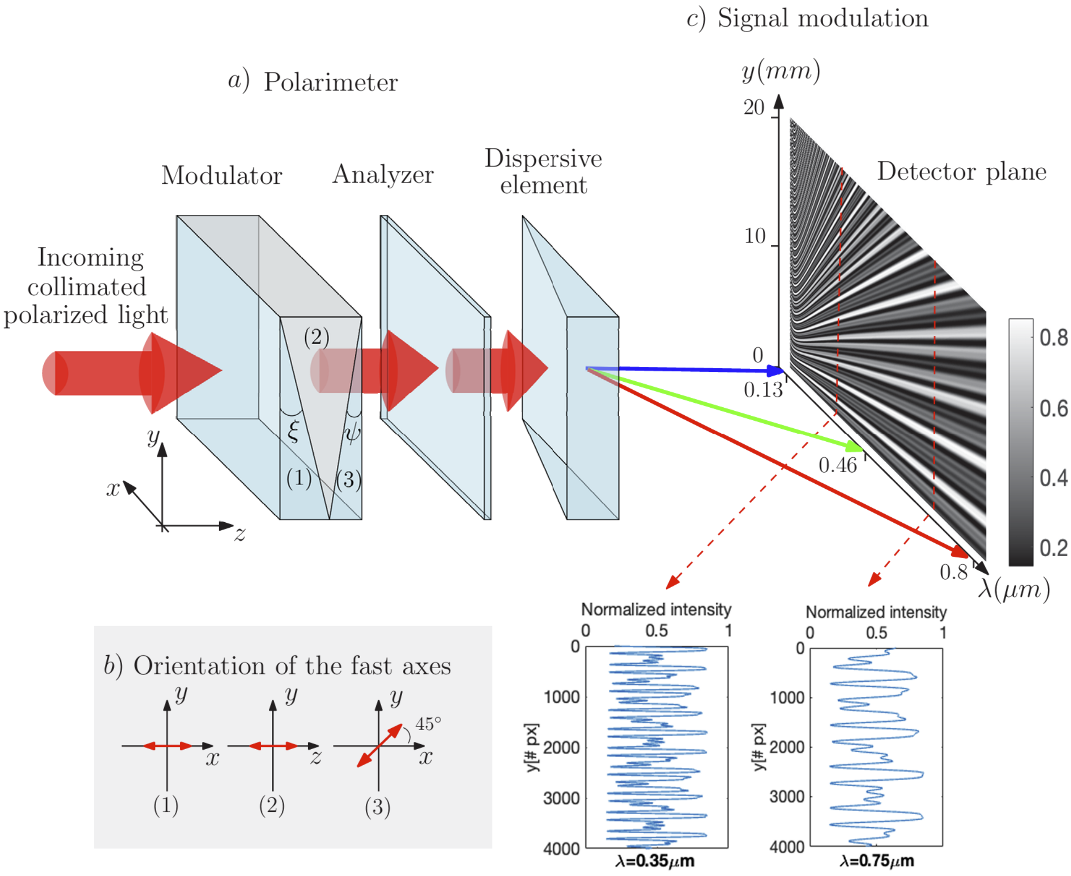

Figure 8.1: Prism-based spectropolarimetric design capable of measuring the entire Stokes vector in a single capture. Figure taken from Vasilescu [136].

Many of the components in this laboratory instrument are not rated for use in space, due to concerns about temperature or vacuum conditions. The detector may require cooling while in space to guarantee accurate measurements, which may drive up the cost significantly. The photoelastic modulator can be designed to work in a vacuum [70], but has difficulties dealing with large temperature swings and the vibrations a spacecraft undergoes while in launch and during attitude control manoeuvres in space [137]. The photoelastic modulator also requires multiple lock-in amplifiers and other electrical hardware that make it inconvenient for a compact spacecraft payload. Its achromatic modulation capabilities may need to be replaced by another component more suited to the space environment. An example of this is a prism-based spectropolarimeter design currently in development [136], which is shown in Figure 8.1. This spectropolarimeter consists of a series of prisms cemented together, each with a different fast-axis orientation. These specific orientations create a complete modulation of the polarization of light entering the system. An analyzer can then be placed after this modulator to measure an intensity variation due to this modulation. This modulation is also spectrally dependent, meaning a prism can be placed after the polarimetric elements to disperse light orthogonally to the intensity variation. Designs like these combine spectral and polarimetric measurements with materials that can be adapted to space environments. Further development of this design is required to adapt it to this instrument, such as an increased spectral range and polarimetric sensitivity, but these are the types of innovations that can make a spaceborne version of this spectroscopic ellipsometer a possibility.

The instrument discussed in this work is also limited in the spatial dimension, as it does not resolve images but rather captures intensity measurements with a single pixel. Spatially-resolved images could reveal more information than what is provided by the angular resolution of the goniometer. However, such a modification would limit the signal-to-noise ratio as light would need to be split over multiple pixels. Additionally, the PEM is not meant to take images, as the accuracy is reduced near the edges of the aperture [112]. Overall, the challenges of adding spatially-resolved measurements to the instrument would need to be weighed against the value that this added dimension provides.

As an intermediate step in this process, another goal is to have this spectropolarimeter mounted on the roof of the TU Delft Faculty of Aerospace, to gain exposure to environments with higher stray light, and to take measurements of a wide variety of targets, including vegetation, water, vehicles, and buildings. This will help expand the capabilities of the instrument for versatile use in space. It will also serve as an educational tool to expose students to spectropolarimetric data and its utility.

These developments are still multiple years away, but current developments in the field and the high potential of this proof of concept design make this evolution of the instrument worth striving towards.

8.5. Impacts and Conclusion

While there is still significant assembly and characterization work to be completed, the spectroscopic ellipsometer designed in this work is an exciting prospect for the future study of planetary surfaces. It is designed to take accurate spectroscopic and polarimetric measurements over a spectral range spanning from ultraviolet to infrared, while its goniometric arms provide complete and precise control of the viewing orientation relative to a sample.

The performance of this instrument bodes well for spectropolarimetric studies of asteroids, comets, and icy moons. The precise goniometric angle control will allow for more comprehensive phase-polarization curve studies, with limited opposition effect investigations also possible due to the small minimum phase angle. The high spectral resolution and polarimetric accuracy also make this instrument an excellent method of measuring comet surface composition in isolation from the features of the comet's tail. This instrument creates opportunities for further research into icy moon surfaces, and even applications beyond the immediate scope of this work, such as the Moon and other planets. The instrument is designed to be versatile, with multiple goniometric and polarimetric configurations for studies that have not even been conceived. These applications directly answer the scientific research questions outlined in Section 1.2, including the effects of structure, composition, and viewing geometry on the polarization of light reflected off of the sample.

While the instrument is designed for use in the lab, it also provides a valuable proof of concept for the development of spaceborne payloads for in-situ planetary surface studies. The data generated from studies of analogues can highlight areas of interest for future studies in space. Key future developments in spectropolarimetry can also better adapt this instrument to spacecraft payloads for widespread planetary studies.

Overall, this instrument will help to open an exciting new field of research in comprehensive planetary surface studies. Detailed studies on surface composition and structure can be performed, opening avenues towards discoveries about the formation and evolution of the Solar System, life outside of Earth, and expanding humanity into space.

References

[1] H Jay Melosh. *Planetary surface processes*. Vol. 13. Cambridge University Press, 2011.

[2] Evgeny Slyuta. "The Luna program". In: *Sample return missions*. Elsevier, 2021, pp. 37–78.

[3] Asif A Siddiqi and Roger Launius. *Deep space chronicle: A chronology of deep space and planetary probes 1958-2000*. Tech. rep. 2002.

[4] Yuichi Tsuda et al. "System design of the Hayabusa 2—Asteroid sample return mission to 1999 JU3". In: *Acta Astronautica* 91 (2013), pp. 356–362.

[5] Alan Shepard, Deke Slayton, and Jay Barbree. *Moon Shot: The Inside Story of America's Apollo Moon Landings*. Open Road Media, 2011.

[6] Donald Yeomans. *Why study asteroids?* URL: `https://ssd.jpl.nasa.gov/sb/why_asteroids.html`.

[7] *Exploring Icy Moons*. Feb. 2024. URL: `https://vision.esa.int/exploring-icy-moons/`.

[8] Mohammad Nazari-Sharabian et al. "Water on Mars—a literature review". In: *Galaxies* 8.2 (2020), p. 40.

[9] Junichi Haruyama et al. "Global lunar-surface mapping experiment using the Lunar Imager/Spectrometer on SELENE". In: *Earth, planets and space* 60 (2008), pp. 243–255.

[10] RELAB Web. "Reflectance Experiment Laboratory (RELAB) description and user's manual". In: (1993).

[11] Stefan R Sandmeier and Klaus I Itten. "A field goniometer system (FIGOS) for acquisition of hyperspectral BRDF data". In: *IEEE Transactions on Geoscience and Remote Sensing* 37.2 (1999), pp. 978–986.

[12] Olivier Brissaud et al. "Spectrogonio radiometer for the study of the bidirectional reflectance and polarization functions of planetary surfaces. 1. Design and tests". In: *Applied Optics* 43.9 (2004), pp. 1926–1937.

[13] Sandra Potin et al. "SHADOWS: a spectro-gonio radiometer for bidirectional reflectance studies of dark meteorites and terrestrial analogs: design, calibrations, and performances on challenging surfaces". In: *Applied optics* 57.28 (2018), pp. 8279–8296.

[14] Donald L Pavia et al. *Introduction to spectroscopy*. Cengage learning, 2014.

[15] E. Hecht. *Optics*. Always learning. Pearson, 2016. ISBN: 9781292096933. URL: `https://books.google.nl/books?id=Bv1RrgEACAAJ`.

[16] Hiroyuki Fujiwara. *Spectroscopic ellipsometry: principles and applications*. John Wiley & Sons, 2007.

[17] Serge Huard. *Polarization of light*. 1997.

[18] *Chiral Molecules*. URL: `https://people.eecs.berkeley.edu/~sequin/CS39/IMGS/Chiral-Molecules/`.

[19] ME Palumbo and GA Baratta. "Infrared spectra of CO2 in H2O: CH3OH: CO2 icy mixtures". In: *Astronomy and Astrophysics, v. 361, p. 298-302 (2000)* 361 (2000), pp. 298–302.

[20] Frans Snik et al. "An overview of polarimetric sensing techniques and technology with applications to different research fields". In: *Polarization: measurement, analysis, and remote sensing XI* 9099 (2014), pp. 48–67.

[21] Ranganath R Navalgund, V Jayaraman, and PS Roy. "Remote sensing applications: An overview". In: *current science* (2007), pp. 1747–1766.

[22] Stefano Bagnulo. "Stellar spectropolarimetry: basic principles, observing strategies, and diagnostics of magnetic fields". In: *Polarimetric Detection, Characterization and Remote Sensing*. Springer. 2011, pp. 1–30.

[23] Sandra Potin. "Spectrophotométrie de la matière extra-terrestre". PhD thesis. Université Grenoble Alpes, 2020.

[24] Débora Gonçalves and Eugene A Irene. "Fundamentals and applications of spectroscopic ellipsometry". In: *Química Nova* 25 (2002), pp. 794–800.

[25] S Bagnulo, Alberto Cellino, and MF Sterzik. "Linear spectropolarimetry: a new diagnostic tool for the classification and characterization of asteroids". In: *Monthly Notices of the Royal Astronomical Society: Letters* 446.1 (2015), pp. L11–L15.

[26] Ulrich Schade, Richard Wäsch, and Lyuba Moroz. "Near-infrared reflectance spectroscopy of Ca-rich clinopyroxenes and prospects for remote spectral characterization of planetary surfaces". In: *Icarus* 168.1 (2004), pp. 80–92.

[27] Victoria E Hamilton. "Thermal infrared (vibrational) spectroscopy of Mg–Fe olivines: A review and applications to determining the composition of planetary surfaces". In: *Geochemistry* 70.1 (2010), pp. 7–33.

[28] Hans Keppler and Joseph R Smyth. *Water in nominally anhydrous minerals*. Vol. 62. Walter de Gruyter GmbH & Co KG, 2018.

[29] Humberto Campins et al. "Water ice and organics on the surface of the asteroid 24 Themis". In: *Nature* 464.7293 (2010), pp. 1320–1321.

[30] F Scipioni et al. "Deciphering sub-micron ice particles on Enceladus surface". In: *Icarus* 290 (2017), pp. 183–200.

[31] AA De Almeida, Patan Deen Singh, and CM Burgoyne. "Haser model CN, C2 and C3 production rates in some comets". In: *Earth, Moon, and Planets* 47.1 (1989), pp. 15–31.

[32] DF Lupishko and Yu G Shkuratov. "On spectral dependence of polarization of asteroids". In: *Solar System Research* 50 (2016), pp. 329–336.

[33] Alberto Cellino et al. "A polarimetric study of asteroids: fitting phase–polarization curves". In: *Monthly Notices of the Royal Astronomical Society* 455.2 (2016), pp. 2091–2100.

[34] Michael J Gaffey, Thomas H Burbine, and Richard P Binzel. "Asteroid spectroscopy: Progress and perspectives". In: *Meteoritics* 28.2 (1993), pp. 161–187.

[35] Sandra Potin et al. "Style and intensity of hydration among C-complex asteroids: A comparison to desiccated carbonaceous chondrites". In: *Icarus* 348 (2020), p. 113826.

[36] Olivier Poch et al. "Ammonium salts are a reservoir of nitrogen on a cometary nucleus and possibly on some asteroids". In: *Science* 367.6483 (2020), eaaw7462.

[37] Carlé M Pieters and Lucy A McFadden. "Meteorite and asteroid reflectance spectroscopy: Clues to early solar system processes". In: *Annual Review of Earth and Planetary Sciences* 22.1 (1994), pp. 457–497.

[38] *Rosetta - Frequently Asked Questions*. URL: `https://www.esa.int/Science_Exploration/Space_Science/Rosetta/Frequently_asked_questions`.

[39] Roy V Myers and Kenneth H Nordsieck. "Spectropolarimetry of comets Austin and Churyumov-Gerasimenko". In: *Icarus* 58.3 (1984), pp. 431–439.

[40] Nikolai Kiselev and Vera Rosenbush. "Polarimetry of comets: progress and problems". In: *Photopolarimetry in remote sensing*. Springer, 2004, pp. 411–430.

[41] Martha S Hanner. "The silicate material in comets". In: *Space Science Reviews* 90.1-2 (1999), pp. 99–108.

[42] John K Davies et al. "The detection of water ice in comet Hale-Bopp". In: *Icarus* 127.1 (1997), pp. 238–245.

[43] Karen Magee-Sauer et al. "The organic composition of Comet C/2001 A2 (LINEAR): I. Evidence for an unusual organic chemistry". In: *Icarus* 194.1 (2008), pp. 347–356.

[44] Frans Snik et al. "SPEX: the spectropolarimeter for planetary exploration". In: *Space Telescopes and Instrumentation 2010: Optical, Infrared, and Millimeter Wave*. Vol. 7731. SPIE. 2010, pp. 383–394.

[45] John R Spencer et al. "Enceladus: An active cryovolcanic satellite". In: *Saturn from Cassini-Huygens* (2009), pp. 683–724.

[46] S Potin et al. "Some things special about NEAs: Geometric and environmental effects on the optical signatures of hydration". In: *Icarus* 333 (2019), pp. 415–428.

[47] Thomas Gehrels. "Photometric Studies of Asteroids. V. The Light-Curve and Phase Function of 20 Massalia." In: *Astrophysical Journal, vol. 123, p. 331* 123 (1956), p. 331.

[48] Robert M Nelson et al. "Low phase angle laboratory studies of the opposition effect: search for wavelength dependence". In: *Planetary and Space Science* 50.9 (2002), pp. 849–856.

[49] RM Nelson et al. “The opposition effect in simulated planetary regoliths. Reflectance and circular polarization ratio change at small phase angle”. In: *Icarus* 147.2 (2000), pp. 545–558.

[50] Begzsuren Tumendemberel. “Study of spectro-polarimetric bidirectional reflectance properties of leaves”. PhD thesis. 2019.

[51] Won Chegal et al. “Calibration method for rotating-analyser-type spectral imaging ellipsometers”. In: *Measurement Science and Technology* 16.3 (2005), p. 716.

[52] Stefano Spadaccia et al. “Experimental study of frost detectability on planetary surfaces using multicolor photometry and polarimetry”. In: *Icarus* 396 (2023), p. 115503.

[53] Sloane J Wiktorowicz and Larissa A Nofi. “Simultaneous linear and circular optical polarimetry of asteroid (4) vesta”. In: *The Astrophysical Journal Letters* 800.1 (2015), p. L1.

[54] Takahiro Iwata et al. “NIRS3: the near infrared spectrometer on Hayabusa2”. In: *Space Science Reviews* 208 (2017), pp. 317–337.

[55] AA Simon-Miller and DC Reuter. “OSIRIS-REx OVIRS: A scalable visible to near-IR spectrometer for planetary study”. In: *44th Annual Lunar and Planetary Science Conference*. 1719. 2013, p. 1100.

[56] Amy A Simon et al. “In-flight calibration and performance of the OSIRIS-REx Visible and IR Spectrometer (OVIRS)”. In: *Remote Sensing* 10.9 (2018), p. 1486.

[57] SENTECH Instruments GmbH. *Spectroscopic ellipsometer SENresearch 4.0*. URL: `https://www.sentech.com/en/SENresearch__219/`.

[58] *Sopra GES 5E*. URL: `https://www.epfl.ch/research/facilities/cmi/equipment/metrology/sopra-ges-5e/`.

[59] *VASE Ellipsometer*. URL: `https://www.jawoollam.com/download/pdfs/vase-brochure.pdf`.

[60] *UVISEL Plus Spectroscopic Ellipsometer*. URL: `https://static.horiba.com/fileadmin/Horiba/Products/Scientific/Emerging_Businesses/UVISEL_PLUS/UVISEL-Plus-Reference-Spectroscopic-Ellipsometer-Brochure-2020.pdf`.

[61] Martin P Lévesque. “The DRDC spectro-polarimetric goniometer”. In: (2017).

[62] *Bruker FilmTek 6000 PAR-SE*. URL: `https://www.bruker.com/en/products-and-solutions/test-and-measurement/ellipsometers-and-reflectometers/multi-angle-reflectometers/filmtek-6000-par-se.html`.

[63] Joungchel Lee et al. “Rotating-compensator multichannel ellipsometry: Applications for real time Stokes vector spectroscopy of thin film growth”. In: *Review of scientific instruments* 69.4 (1998), pp. 1800–1810.

[64] Y-T Kim, RW Collins, and K Vedam. “Fast scanning spectroelectrochemical ellipsometry: In-situ characterization of gold oxide”. In: *Surface Science* 233.3 (1990), pp. 341–350.

[65] RT Graf et al. “Polarization modulation Fourier transform infrared ellipsometry of thin polymer films”. In: *Applied spectroscopy* 40.4 (1986), pp. 498–503.

[66] DE Aspnes and AA Studna. “High precision scanning ellipsometer”. In: *Applied Optics* 14.1 (1975), pp. 220–228.

[67] Aaldert van Amerongen et al. “SPEXone: a compact multi-angle polarimeter”. In: *International Conference on Space Optics—ICSO 2018*. Vol. 11180. SPIE. 2019, pp. 223–236.

[68] P-Y Deschamps et al. “The POLDER mission: Instrument characteristics and scientific objectives”. In: *IEEE Transactions on geoscience and remote sensing* 32.3 (1994), pp. 598–615.

[69] *Wire-Grid Polarizers*. URL: `https://www.thorlabs.com/newgrouppage9.cfm?objectgroup_id=5510`.

[70] *Photoelastic Modulator*. URL: `https://www.hindsinstruments.com/wp-content/uploads/PEMCSC-Technical-Overview.pdf`.

[71] *Medium Power Xenon Research Light Source*. URL: `https://www.newport.com/f/medium-power-xenon-light-sources`.

[72] *66997-250Q-R085 QTH Light Source*. URL: `https://www.newport.com/p/66997-250Q-R085`.

[73] *Monochromator*. May 2023. URL: `https://www.lightsource.tech/en/glossary/monochromator/`.

[74] *Characteristics of Single and Double Monochromator UV-VIS Spectrophotometers.* URL: `https://www.shimadzu.com/an/service-support/technical-support/analysis-basics/fundamentals-uv/single_double.html#1`.

[75] Rongqing Hui and Maurice O'Sullivan. *Fiber-Optic Measurement Techniques.* Academic Press, 2022.

[76] *CS260B configured monochromator.* URL: `https://www.newport.com/f/cs260b-configured-monochromators`.

[77] *Invenio Fourier Transform Spectrometer.* URL: `https://www.bruker.com/en/products-and-solutions/infrared-and-raman/ft-ir-research-spectrometers/invenio-ft-ir-spectrometer.html`.

[78] *Rochon Polarizers.* URL: `https://www.edmundoptics.com/f/rochon-polarizers/14175/`.

[79] Jay N Damask. *Polarization optics in telecommunications.* Vol. 101. Springer Science & Business Media, 2004.

[80] *Mounted Superachromatic Waveplates.* URL: `https://www.thorlabs.com/newgrouppage9.cfm?objectgroup_id=2193`.

[81] *Fresnel Rhombs.* URL: `https://www.laser2000.com/en/polarizers/81109-fresnel-rhomb-waveplates.html`.

[82] *Fresnel Rhombs.* URL: `https://www.thorlabs.com/newgrouppage9.cfm?objectgroup_id=154`.

[83] *Fresnel Rhombs.* URL: `https://www.b-halle.de/products/retarders/fresnel_rhombs.html`.

[84] Subiao Bian, Changcai Cui, and Oriol Arteaga. "Mueller matrix ellipsometer based on discrete-angle rotating Fresnel rhomb compensators". In: *Applied Optics* 60.16 (2021), pp. 4964–4971.

[85] Subiao Bian et al. "Calibration of achromatic Fresnel rhombs with an elliptical retarder model in Mueller matrix ellipsometers". In: *Thin Solid Films* 763 (2022), p. 139581.

[86] *Two-color detectors.* URL: `https://www.hamamatsu.com/us/en/product/optical-sensors/infrared-detector/two-color-detector.html`.

[87] Hongtao Yuan et al. "Polarization-sensitive broadband photodetector using a black phosphorus vertical p–n junction". In: *Nature nanotechnology* 10.8 (2015), pp. 707–713.

[88] *1000W Lamp.* URL: `https://www.newport.com/p/66295-1KQ-R1`.

[89] *250W Lamp.* URL: `https://www.newport.com/p/66997-250Q-R085`.

[90] *100W IR Lamp.* URL: `https://www.newport.com/f/ir-light-source-kits`.

[91] *Getting Light into a Monochromator.* URL: `https://www.newport.com/t/getting-light-into-a-monochromator`.

[92] *66881 QTH Lamp Housing Drawing.* URL: `https://www.newport.com/medias/sys_master/images/images/h64/h27/8797306322974/XM-Data-Sheet.pdf`.

[93] *Calculating Output Power of Collimated Beams.* URL: `https://www.newport.com/t/calculating-output-power`.

[94] *CS260B Datasheet.* URL: `https://www.newport.com/medias/sys_master/images/images/h02/h8a/9699582443550/CS260B-Datasheet-121020.pdf`.

[95] *CS260B User Manual.* URL: `https://www.newport.com/mam/celum/celum_assets/np/resources/Cornerstone_CS260B_User_Manual.pdf?1`.

[96] *330R Specification Sheet.* URL: `http://www.gratinglab.com/Products/Product_Tables/Efficiency/Efficiency.aspx?catalog=53-*-330R`.

[97] *560R Specification Sheet.* URL: `http://www.gratinglab.com/Products/Product_Tables/Efficiency/Efficiency.aspx?catalog=53-*-560R`.

[98] *636R Specification Sheet.* URL: `http://www.gratinglab.com/Products/Product_Tables/Efficiency/Efficiency.aspx?catalog=53-*-636R`.

[99] *690R Specification Sheet.* URL: `http://www.gratinglab.com/Products/Product_Tables/Efficiency/Efficiency.aspx?catalog=53-*-690R`.

[100] *Micrometer Driven Slits.* URL: `https://www.newport.com/p/74001`.

[101] *USFW-100 Filter Wheel.* URL: `https://www.newport.com/p/USFW-100`.

[102] *10CGA-590 Cut-On Filter*. URL: https://www.newport.com/p/10CGA-590.

[103] *10CGA-1000 Cut-On Filter*. URL: https://www.newport.com/p/10CGA-1000.

[104] *1.65um CWL, 25mm Diameter, Infrared Longpass Filter*. URL: https://www.edmundoptics.com/p/165mum-25mm-diameter-infrared-longpass-filter/23270/.

[105] *2.40um CWL, 25mm Diameter, Infrared Longpass Filter*. URL: https://www.edmundoptics.com/p/240mum-25mm-diameter-infrared-longpass-filter/23271/.

[106] *Focus or Collimate Light with an Off-Axis Parabolic Mirror*. URL: https://www.thorlabs.com/newgrouppage9.cfm?objectgroup_id=14193.

[107] *Toroidal mirrors*. URL: https://www.shimadzu.com/opt/products/aspherical/o-k25cur0000007p3b.html.

[108] Weihai Huang, Kodai Nagayama, and Jiwang Yan. "Fabrication of microlens arrays on single-crystal CaF2 by ultraprecision diamond turning". In: *Journal of Materials Processing Technology* 321 (2023), p. 118133. ISSN: 0924-0136. DOI: https://doi.org/10.1016/j.jmatprotec.2023.118133. URL: https://www.sciencedirect.com/science/article/pii/S0924013623002789.

[109] *Standard ZFG Multimode Fibers*. URL: https://leverrefluore.com/wp-content/uploads/2024/01/LVF-standard-ZFG-MM-fibers-Datasheet-2024.pdf.

[110] *Standard IFG Multimode Fibers*. URL: https://leverrefluore.com/wp-content/uploads/2024/01/LVF-standard-IFG-MM-fibers-Datasheet-2024.pdf.

[111] *Terminated Fiber Adapters*. URL: https://www.thorlabs.com/newgrouppage9.cfm?objectgroup_id=69.

[112] Baoliang Wang and Jennifer List. "Basic optical properties of the photoelastic modulator part I: useful aperture and acceptance angle". In: *Polarization Science and Remote Sensing II*. Vol. 5888. SPIE. 2005, pp. 436–443.

[113] *K10CR1/M Motorized Rotation Mount*. URL: https://www.thorlabs.com/thorproduct.cfm?partnumber=K10CR1/M.

[114] *Tip, Tilt, and Rotation Stage*. URL: https://www.thorlabs.com/thorproduct.cfm?partnumber=TTR001/M.

[115] *Compact 9mm Travel Vertical Translation Stage*. URL: https://www.thorlabs.com/thorproduct.cfm?partnumber=XRNV1/M.

[116] *Hastings Triplet Achromatic Lenses*. URL: https://www.thorlabs.com/newgrouppage9.cfm?objectgroup_id=5368.

[117] Bob Mellish. *Eso Supernova*. URL: https://supernova.eso.org/exhibition/images/0802_chromatic-1080/.

[118] *Lens Design Guidelines*. URL: https://www.pencilofrays.com/lens-design-spreadsheet.

[119] *Optical Materials*. URL: https://www.crystran.co.uk/optical-materials.

[120] *Tips for Designing Manufacturable Lenses and Assemblies*. URL: https://www.edmundoptics.com/knowledge-center/application-notes/optics/tips-for-designing-manufacturable-lenses-and-assemblies/.

[121] *C4159 Series Amplifier for Infrared Detectors*. URL: https://www.hamamatsu.com/content/dam/hamamatsu-photonics/sites/documents/99_SALES_LIBRARY/ssd/c4159-01_etc_kird1011e.pdf.

[122] Claude Elwood Shannon. "Communication in the presence of noise". In: *Proceedings of the IRE* 37.1 (1949), pp. 10–21.

[123] *25mm Optical Construction Rails*. URL: https://www.thorlabs.com/thorproduct.cfm?partnumber=XE25L825/M.

[124] *Motorized Rotation Stage, 120 mm, High-Torque Mini-Step Drive*. URL: https://www.newport.com/p/RV120BPP.

[125] Robert D Fiete and Theodore Tantalo. "Comparison of SNR image quality metrics for remote sensing systems". In: *Optical Engineering* 40.4 (2001), pp. 574–585.

[126] Max Planck. "The theory of heat radiation". In: *Entropie* 144.190 (1900), p. 164.

[127] *Principles of Lock-in Detection.* URL: https://www.zhinst.com/sites/default/files/li_primer/zi_whitepaper_principles_of_lock-in_detection.pdf.

[128] *Signaloc - A Research Grade Lock-in Amplifier.* URL: https://www.hindsinstruments.com/products/components/lock-in-amplifiers/#product-info.

[129] *Calculating Psi and Delta Using a Photoelastic Modulator.* URL: https://www.hindsinstruments.com/wp-content/uploads/Calculating-Psi-and-Delta-Using-A-PEM-Technical-Note.pdf.

[130] Gerald E Jellison and Frank A Modine. "Polarization modulation ellipsometry". In: *Handbook of Ellipsometry.* Springer, 2005, pp. 433–480.

[131] SN Jasperson and SE Schnatterly. "An improved method for high reflectivity ellipsometry based on a new polarization modulation technique". In: *Review of Scientific Instruments* 40.6 (1969), pp. 761–767.

[132] *Understanding Optical Alignment.* URL: https://www.edmundoptics.com/knowledge-center/application-notes/optics/understanding-optical-specifications/.

[133] *Light Sources.* URL: https://www.newport.com/medias/sys%5C_master/images/images/hfb/hdf/8797196451870/Light-Sources.pdf.

[134] *Avalanche Photodiode Detector.* URL: https://www.hindsinstruments.com/products/components/photo-detectors/avalanche-photo-diode-detector#product-info.

[135] *CS165CU/M - Zelux® 1.6 MP Color CMOS Camera, M6 Taps.* URL: https://www.thorlabs.com/thorproduct.cfm?partnumber=CS165CU/M.

[136] Bogdan Vasilescu, Pierre Piron, and Jérôme Loicq. "Performance analysis of a spectropolarimeter employing a continuous phase variation". In: *Optics Express* 31.13 (2023), pp. 21078–21092.

[137] Linda Hirschy et al. "Basic optical properties of the photoelastic modulator. Part III: thermal properties". In: *Current Developments in Lens Design and Optical Engineering XIII.* Vol. 8486. SPIE. 2012, pp. 332–340.

[138] *XP Power 15 V Dual Power Supply.* URL: https://www.xppower.com/portals/0/pdfs/SF_ECL05-30.pdf.

[139] *436 nm Bandpass Filter.* URL: https://www.edmundoptics.com/p/436nm-cwl-25mm-dia-hard-coated-od-4-10nm-bandpass-filter/19789/.

[140] *656 nm Bandpass Filter.* URL: https://www.edmundoptics.com/p/656nm-cwl-25mm-dia-hard-coated-od-4-10nm-bandpass-filter/19820/.

[141] *1064 nm Bandpass Filter.* URL: https://www.edmundoptics.com/p/1064nm-cwl-25mm-dia-hard-coated-od-4-10nm-bandpass-filter/19835/.

[142] *1550 nm Bandpass Filter.* URL: https://www.edmundoptics.com/p/1550nm-cwl-25mm-dia-hard-coated-od-4-10nm-bandpass-filter/28578/.

[143] *2700 nm Bandpass Filter.* URL: https://www.edmundoptics.com/p/270m-cwl-250mm-diameter-011-fwhm-ir-bandpass-filter/27177/.

[144] *3600 nm Bandpass Filter.* URL: https://www.edmundoptics.com/p/360m-cwl-250mm-diameter-014-fwhm-ir-bandpass-filter/27180/.

[145] *Post Holders.* URL: https://www.thorlabs.com/newgrouppage9.cfm?objectgroup_id=1268.

A

Further Design Details

A.1. Instrument Budget

Table A.1: Budget for the spectroscopic ellipsometer instrument.

Component	Sub-component	Supplier	Unit Price	Quantity	Total Price (before tax)	Total Price (after 20% tax)
Light source	QTH source [89]	Newport	€ 5,923.79	1	€ 5,923.79	€ 7,108.55
	QTH spare lamps [72]	Newport	€ 57.00	5	€ 285.00	€ 342.00
	Monochromator [76]	Newport	€ 24,050.00	1	€ 24,050.00	€ 28,860.00
	Controller [76]	Newport	€ 1,576.00	1	€ 1,576.00	€ 1,891.20
	Filter wheel [76]	Newport	€ 1,893.00	1	€ 1,893.00	€ 2,271.60
	Filter adapters [76]	Newport	€ 19.40	5	€ 97.00	€ 116.40
	Longpass filters [104, 105]	Edmund Optics	€ 321.00	2	€ 642.00	€ 770.40
	Longpass filters [102, 103]	Newport	€ 49.00	2	€ 98.00	€ 117.60
Optical fibres	Fibres and bundle [109]	Le Verre Fluoré	€ 9,751.00	1	€ 9,751.00	€ 11,701.20
	Mount [111]	Thorlabs	€ 15.49	1	€ 15.49	€ 18.59
Sample stage	Tip/tilt + rotation [114]	Thorlabs	€ 940.08	1	€ 940.08	€ 1,128.10
	Single-axis translation [115]	Thorlabs	€ 660.36	1	€ 660.36	€ 792.43
Goniometric arms	Rotation stages [124]	Newport	€ 7,780.00	2	€ 15,560.00	€ 18,672.00
	Arms [123]	Thorlabs	€ 38.34	2	€ 76.68	€ 92.02
Polarimetry	Linear polarizer [69]	Thorlabs	€ 1,093.59	2	€ 2,187.18	€ 2,624.62
	Photoelastic modulator [70]	HINDS	€ 17,740.00	1	€ 17,740.00	€ 21,288.00
	PEM Lock-In Amplifier [128]	HINDS	€ 2,240.00	2	€ 4,480.00	€ 5,376.00
	Rotation mounts [113]	Thorlabs	€ 1,364.60	2	€ 2,729.20	€ 3,275.04
Detector	Detector [86]	Hamamatsu	€ 230.04	2	€ 460.08	€ 552.10
	Detector Amplifier [86]	Hamamatsu	€ 1,169.50	1	€ 1,169.50	€ 1,403.40
	Detector Power Supply [138]	Mouser	€ 49.02	1	€ 49.02	€ 58.82
Miscellaneous	Additional mounts	Thorlabs	€ 1,000.00	1	€ 1,000.00	€ 1,200.00
	Substitute filters [139–142]	Edmund Optics	€ 284.00	4	€ 1,136.00	€ 1,363.20
	IR Filters [143, 144]	Edmund Optics	€ 433.00	2	€ 866.00	€ 1,039.20
	Bandpass Filters	Thorlabs	€ 330.42	3	€ 991.26	€ 1,189.51
	Waveplate	Thorlabs	€ 461.09	1	€ 461.09	€ 553.31
	Lab rotation mounts	Thorlabs	€ 100.15	2	€ 200.30	€ 240.36
	Lab Computer	ICT Delft	€ 950.00	1	€ 950.00	€ 1,140.00
	USB Cables	Amazon	€ 10.50	1	€ 10.50	€ 12.60
	Condenser	Custom	€ 1,000.00	2	€ 2,000.00	€ 2400.00
Custom refocusing elements	Focusing and collimating mirrors	Custom	€ 1,000.00	2	€ 2,000.00	€ 2400.00
	Observation arm triplets	Custom	€ 1,000.00	2	€ 2,000.00	€ 2400.00
TOTAL						**€ 122,398.24**

Table A.1 shows the financial budget for the instrument, based on known components and prices in June 2024. A 20% increase was applied to all components in order to account for shipping and other taxes. Clearly, components such as the monochromator, PEM, and optical fibres cost significantly more than the rest of the system. The rotation stages from Newport are also quite an expensive component. If a higher torque level is required due to the weight of components, it is possible, but investigating lower mass options for components on the arms could be an effective way of saving costs. Overall, there is still a lot of room in the budget for further purchases that may be necessary for supporting equipment.

A.2. Optical Fibre Full Drawing

Figure A.1 shows the full mechanical drawing for the optical fibre provided by Le Verre Fluoré. This drawing was provided based on the design requirements given to them, and was confirmed for manufacturing.

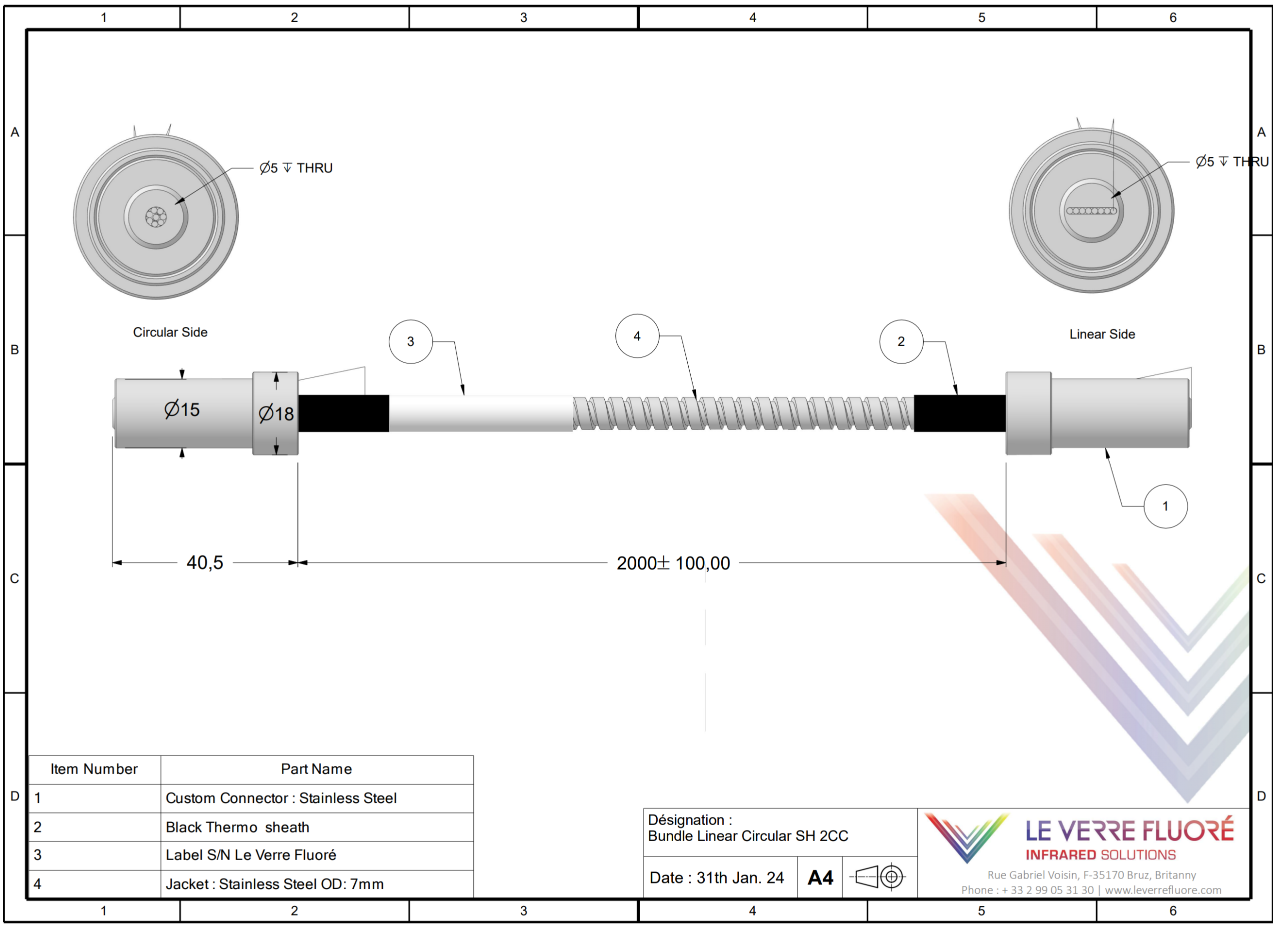

Item Number	Part Name
1	Custom Connector : Stainless Steel
2	Black Thermo sheath
3	Label S/N Le Verre Fluoré
4	Jacket : Stainless Steel OD: 7mm

Désignation :
Bundle Linear Circular SH 2CC

Date : 31th Jan. 24 A4

Rue Gabriel Voisin, F-35170 Bruz, Britanny
Phone : + 33 2 99 05 31 30 | www.leverrefluore.com

Figure A.1: Mechanical drawing of optical fibre provided by Le Verre Fluoré.

A.3. Lens Type Comparison

This section outlines the performance of a doublet and singlet design used for the observation arm collimator. Tables A.2 and A.3 show the specifications used for the singlet and doublet designs, respectively. Figures A.2 and A.3 show the performance of this singlet and doublet, with r_{beam} being the radius of the beam at the position of the analyzer. The larger the radius of the beam beyond 12.7 mm, the more light gets wasted as parts of the beam would simply hit the polarizer's rotation mount. It is therefore recommended to keep the collimated beam radius as close to 12.7 mm as possible.

Table A.2: Observation arm collimator singlet specifications. The diameter of all lenses in this doublet is 28.4 mm.

Lens	Material	Front Radius [mm]	Back Radius [mm]	Thickness [mm]	Air Gap After Lens [mm]
Front	MgF_2	136.048	−135.691	2.212	N/A

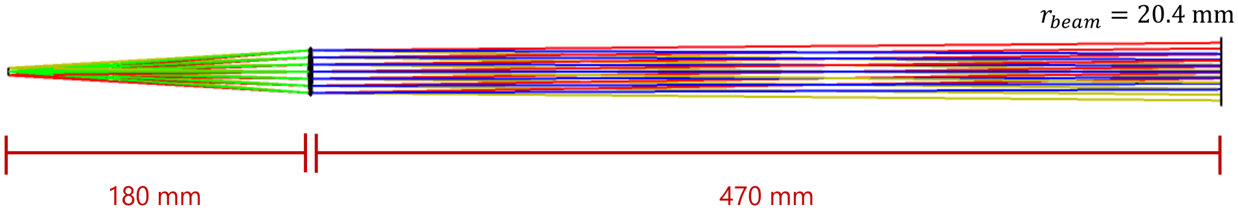

Figure A.2: Collimator singlet dimensions and layout.

Table A.3: Observation arm collimator doublet specifications. The diameter of all lenses in this doublet is 28.4 mm.

Lens	Material	Front Radius [mm]	Back Radius [mm]	Thickness [mm]	Air Gap After Lens [mm]
Front	MgF_2	224.440	−225.152	2.362	1.501
Back	CaF_2	457.673	−342.043	1.912	N/A

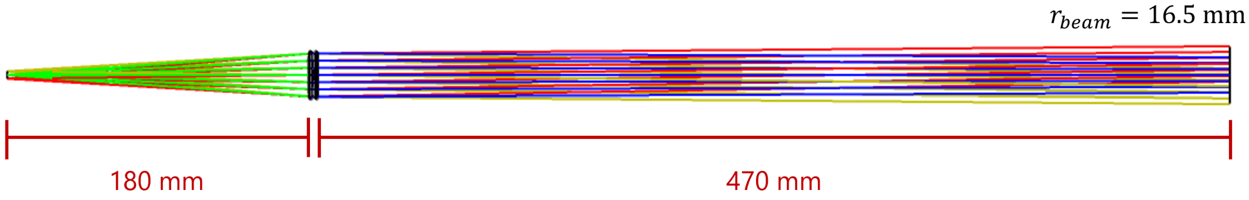

Figure A.3: Collimator doublet dimensions and layout.

Both the singlet and doublet lenses have beam radii of much larger than 12.7 mm. The triplet produces a beam with a 13.3 mm radius, while the doublet produces one with 16.5 mm radius and the singlet has a 20.6 collimated beam radius. These result in significant losses that make the triplet the far superior option for collimating the beam on the observation arm.

A.4. Lens Material Comparison

This section shows the performance of the remaining lens material combinations for the triplets used in this instrument. For brevity, only the transverse ray aberrations are shown as a comparison point to the aberrations for the CaF_2 and MgF_2 - CaF_2 - MgF_2 triplets shown in Figure 5.29. The triplets were first optimized in Zemax, though the manufacturability considerations were not taken into account at this stage. Their transverse ray aberrations were then investigated at 11 wavelengths between 300 nm and 4500 nm.

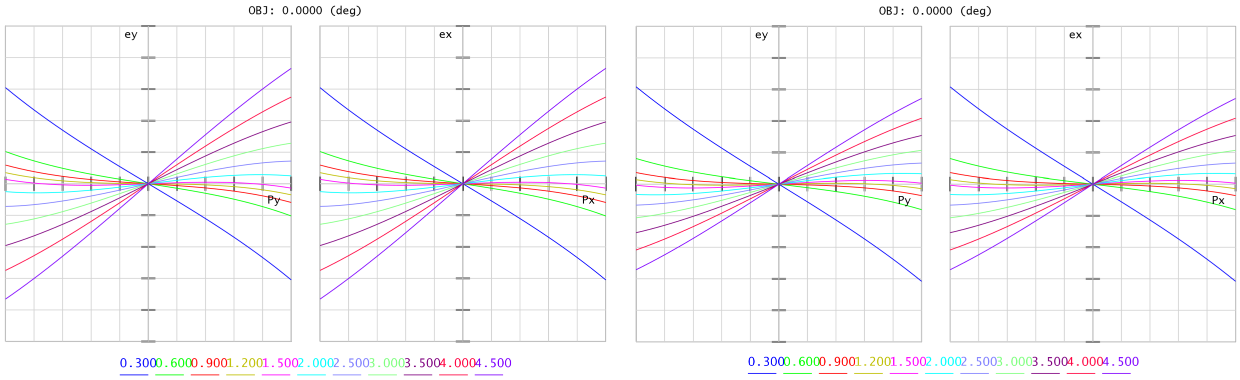

(a) MgF_2 triplet transverse ray aberration.

(b) CaF_2 - MgF_2 - CaF_2 triplet transverse ray aberration.

Figure A.4: Comparison of transverse ray aberrations. Curves with larger deviations from a horizontal line have a larger transverse aberration.

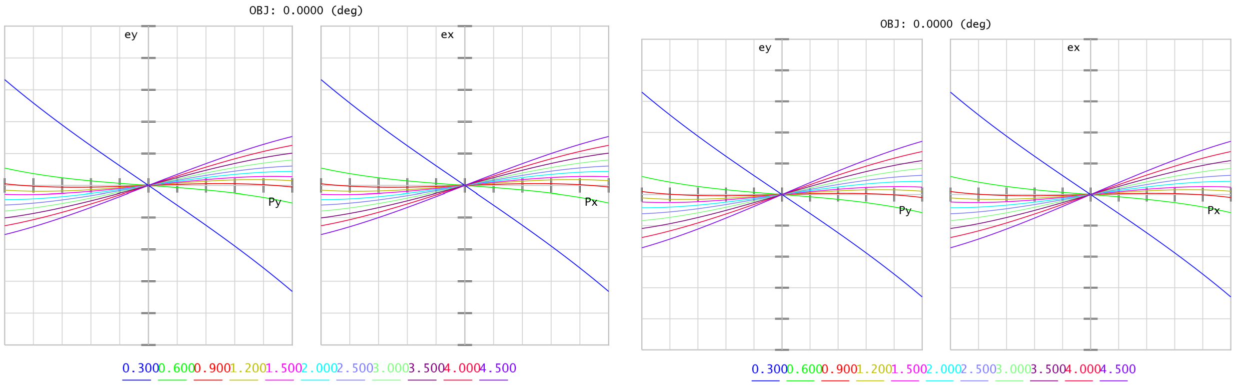

(a) BaF_2 triplet transverse ray aberration.

(b) BaF_2 - MgF_2 - BaF_2 triplet transverse ray aberration.

Figure A.5: Comparison of transverse ray aberrations. Curves with larger deviations from a horizontal line have a larger transverse aberration.

It is clear from these transverse ray aberration plots that the performance in the infrared is much worse for these material combinations than it is for the MgF_2 - CaF_2 - MgF_2 triplet shown in Figure 5.29b. The next closest performance is that of the MgF_2 - BaF_2 - MgF_2 triplet, however the aberrations are still larger. Another factor is that CaF_2 is easier to source than BaF_2, and has some heritage from the SHADOWS instrument [23]. The aberration curves corresponding to wavelengths in the infrared deviate much more from the x-axis in these plots, and thus these material combinations were not considered further.

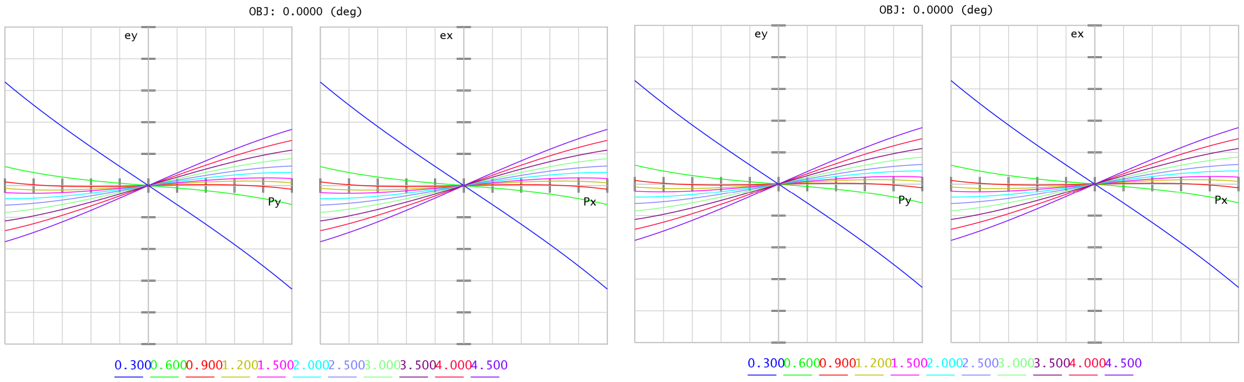

(a) BaF_2 - CaF_2 - BaF_2 triplet transverse ray aberration.

(b) CaF_2 - BaF_2 - CaF_2 triplet transverse ray aberration.

Figure A.6: Comparison of transverse ray aberrations. Curves with larger deviations from a horizontal line have a larger transverse aberration.

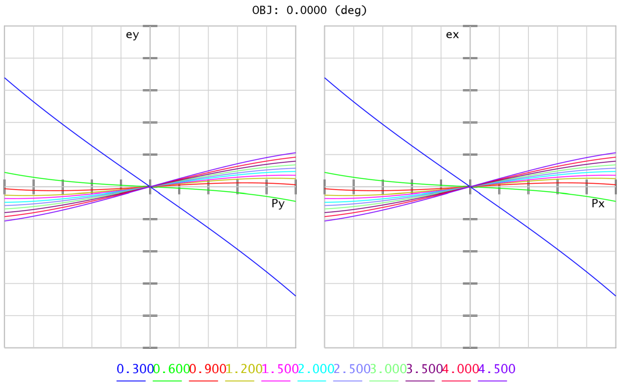

Figure A.7: MgF_2 - BaF_2 - MgF_2 triplet transverse ray aberration.

A.5. 3D Model Considerations

A 3D model of the instrument was developed, mostly for visualization and presentation purposes. Most dimensions are accurate, though some exact features such as the optical fibres are omitted as they are difficult to model accurately. This 3D model cannot be used as a 1-1 replica for the actual construction of the instrument, and should be improved prior to use in simulations. The diagrams and Zemax models are therefore more accurate to the dimensions and performance of the instrument, and are therefore included in the main body of the thesis. However, 3D modelling of the instrument did reveal some mechanical issues that will need to be considered during the assembly phase, and is thus added in this Appendix.

The 3D model was made mostly using CAD models provided from Thorlabs and Newport, while some custom components such as standoffs for matching component heights and the PEM optical head were designed in Solid Edge using approximate dimensions provided by mechanical drawings. Refocusing elements such as the toroidal mirror, off-axis parabolic mirror, and focuser triplet were exported to CAD models from Zemax and then mounted in standard Thorlabs mounts. In the actual assembly process, it is highly likely that mounts and standoffs will be replaced with adjustable versions, such that high precision alignment changes can be completed. However, these were left out of the 3D model due to complexity.

Figure A.8 shows the full model of the light source and goniometer instrument, both placed on a 900 mm x 1200 mm optical table. Everything fits on the table with the spacing calculated in Zemax, confirming the volume layout decided in Section 5.5.3. Most lens and mirror mounts require a standoff to match heights with components such as the lamp and the monochromator. These are shown as simple optical posts, but in practice would likely be the adjustable posts Thorlabs provides [145].

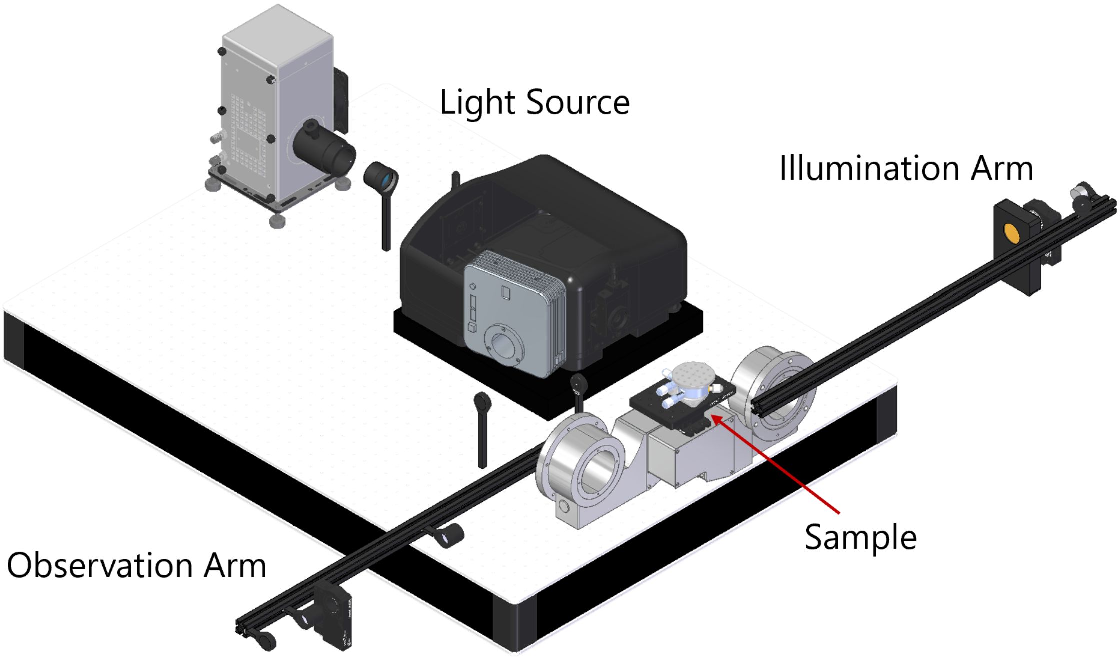

Figure A.8: Full 3D model of the instrument with major sections labelled.

Figure A.9a shows a side view of the model with sub-components labelled, while Figure A.9b shows a back view of the model. As is clear from the side view, the monochromator requires a custom platform with a height of 42.15 mm such that the slit is level with the lamp. This alignment is important, especially if a baffle is desired to maximize throughput.

Figure A.10 shows the observation arm connected to the rotation stage. The connection itself takes up to 145 mm of the observation arm, meaning the collimator distance needs to be adjusted to compensate. The distance needs to be measured from the sample, not from the end of the optical rail as initially measured. This will depend on the final placement and height of the sample. The small weight of the collimator will not affect the moment on the observation arm too much, and thus calculations for moving the collimator on the observation arm were not updated in the main body of the thesis at this time. However, precise placement of the observation arm collimator should be considered such that it is 180 mm from the sample surface.

Components can be attached to the optical railing using a solution Thorlabs provides called the T-nut, which contains a threaded hole that can be placed anywhere along the railing. The T-nut is shown in Figure A.11a. Measuring the position of the T-nut precisely will be important for this instrument design. It is also important to ensure that the weight of the component being attached to the T-nut is not too large, or else there could be some deflection upon repositioning of the arm that could cause misalignment. It is also likely that the standoff requires a fixture to the railing such that the T-nut does not move up and down after attachment. These factors will need to be considered when the final designs and masses are established. Figure A.11b shows the attachment of the T-nut to the railing and standoff for an optical mount.

Figure A.12 shows the design for the sample platform. The tip / tilt / rotation stage needs to be placed on top of the translation stage for accurate positioning of the sample relative to the arms. An interface plate was required between the two to make this connection. Modelling this in more detail has revealed that it is quite difficult to align the sample with the illumination and observation arms in all orientations. When the sample is on top of the rotation stages as shown in Figure A.8, the illumination arm and observation arm do not point at the sample when at 0° (nadir). The opposite is true when the sample is placed between the two rotation stages.

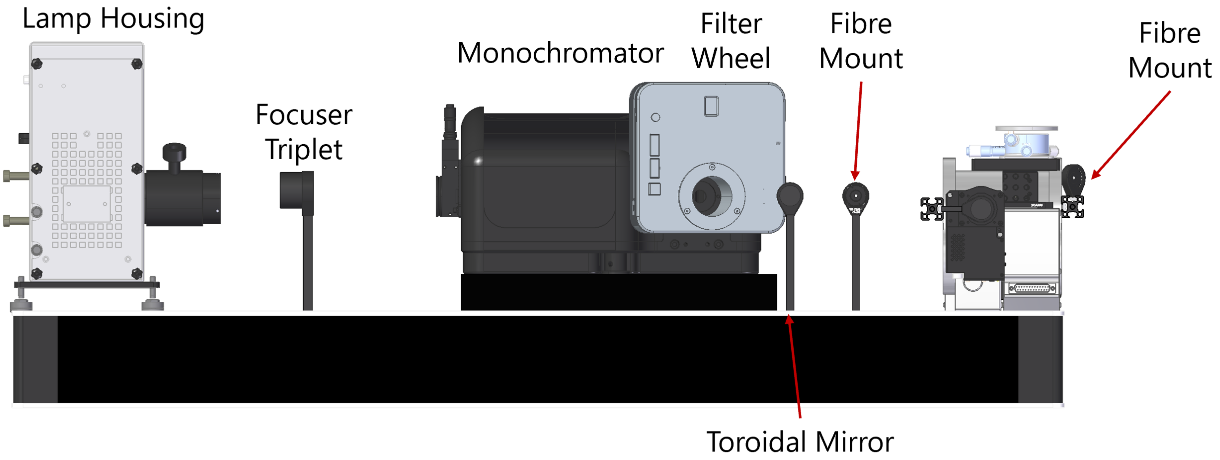

(a) Full 3D model side view.

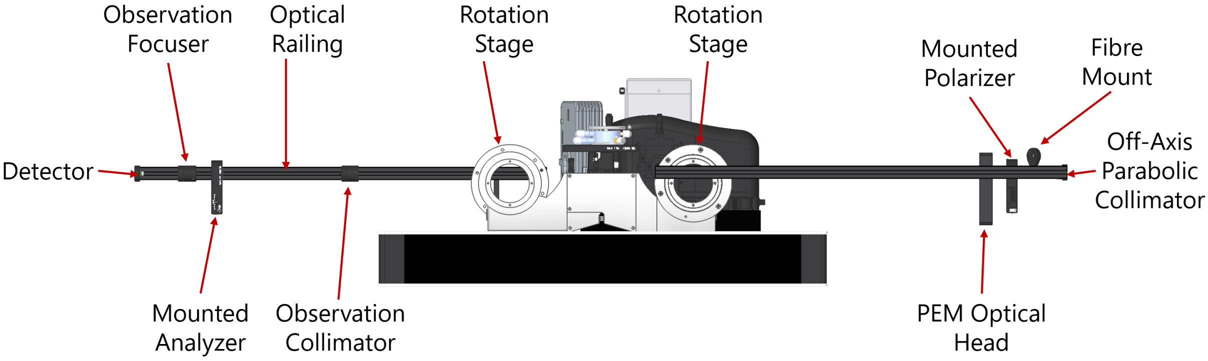

(b) Full 3D model back view.

Figure A.9: Labelled 3D model views.

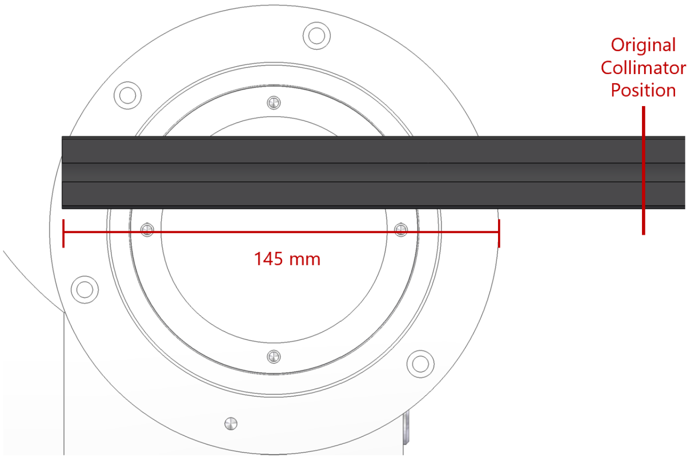

Figure A.10: 3D model showing connection of the observation arm with the rotation stage.

The sample will need a positioning solution to ensure it is aligned with the axis of rotation such that reflection is possible at any orientation. A fully motorized solution may be more useful for repositioning the sample

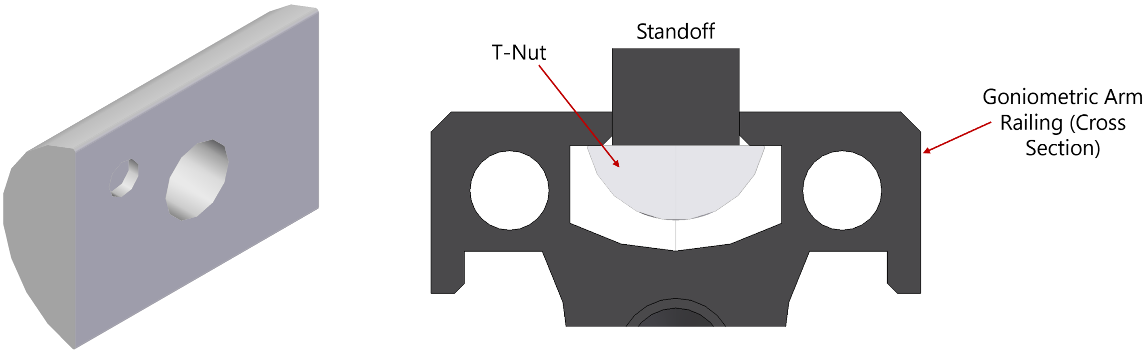

(a) T-nut used for securing optical components to goniometric arms.

(b) Attachment between T-nut and optical component.

Figure A.11: Goniometric arm attachment.

automatically between measurements. However, it is important to balance the efficiency of the experiment with the ability to appropriately cool icy samples to a steady temperature. If motorized sample platforms cannot withstand cold operating temperatures, a slower manual option may be preferred.

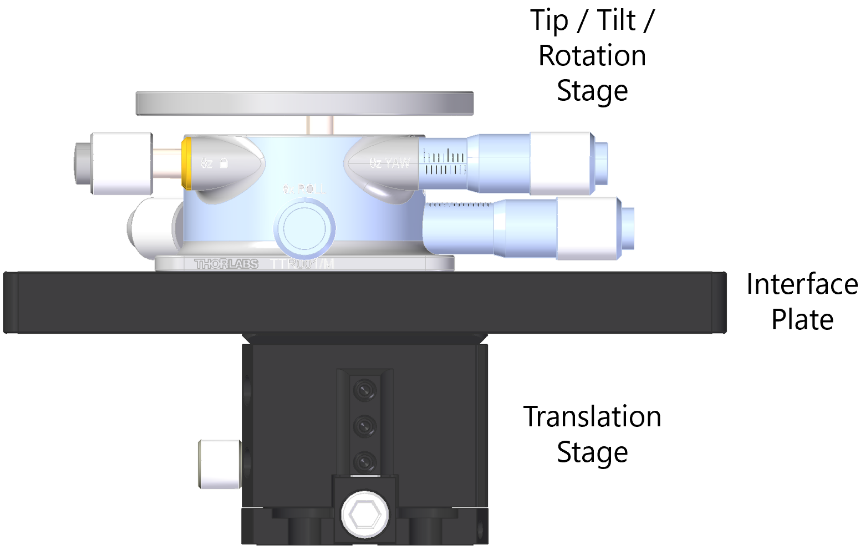

Figure A.12: 3D model showing the sample platform design.

The Hamamatsu detector was also designed in Solid Edge using dimensions given by Hamamatsu. Mounting the detector in place will be a challenge as it is quite small and the legs do not provide much stability. As a result, it may be necessary to attach the detector to a breadboard or circuit board to hold the detector in place, and attach it to a mount that can move to enable 3-axis control and mitigate any focusing difficulties. An example of detector mounting (without positioning control) is shown in Figure A.13.

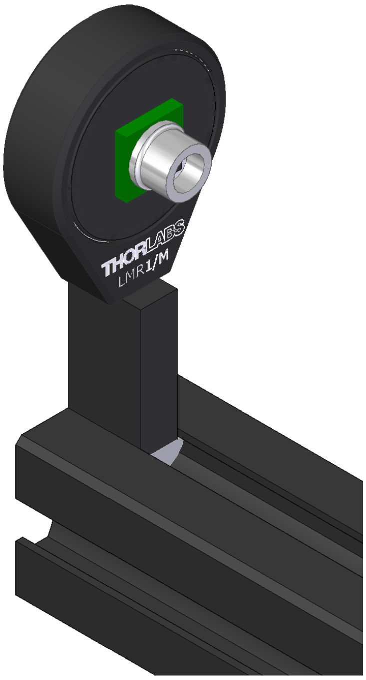

Figure A.13: 3D model showing the detector mounting design.

B

Further Simulation Details

This appendix outlines some simulation results and details that were omitted from the main body of this work for brevity. The full codebase and documentation for the end-to-end simulator can be found at `https://github.com/adynmiles/PoGo-simulation`

B.1. Illumination and Observation Spot Size

Figure B.1 shows how the diameter and area of the illumination and observation spots increase with an increasing goniometer angle. The diameter of the illumination spot quickly grows, meaning a smaller fraction of the input light can be gathered by the observation arm. This explains the maximum angle limitation for the goniometric arms. Further study on the SNR limits could identify whether the maximum goniometric angle should be further reduced.

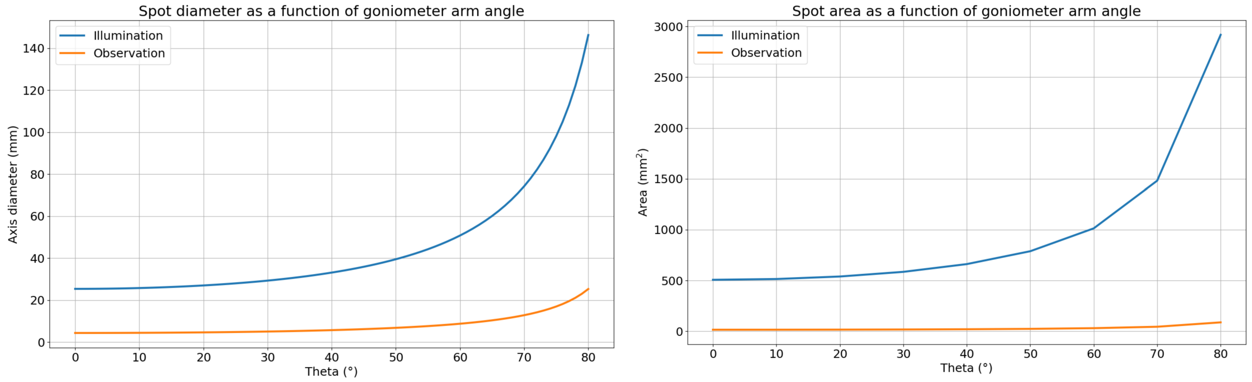

(a) Spot diameter for different goniometer angles.

(b) Spot area for different goniometer angles.

Figure B.1: Illumination and observation spot size diameter and area comparisons.

B.2. Polarimetric Accuracy Simulations

B.2.1. Notes on Derivation of Intensity Equation for PEM

For the PEM, the intensity equation takes a slightly different form due to the retardation modulation of the PEM. Intensity can be calculated through a sequential multiplication of the Jones matrices for each element in the optical track. The output polarization of light that is transmitted through the ellipsometer can be described as:

$$\boldsymbol{L_{out}} = \boldsymbol{A}\boldsymbol{R}(A)\boldsymbol{S}\boldsymbol{R}(-M)\boldsymbol{M}\boldsymbol{R}(M)\boldsymbol{R}(P)\boldsymbol{P}\boldsymbol{L_{in}} \tag{B.1}$$

Here, $\boldsymbol{L_{out}}$ is the output polarization, and $\boldsymbol{L_{in}}$ is the input polarization. $\boldsymbol{A}$ is the Jones matrix for the analyzer, while $\boldsymbol{R}(A)$ corresponds to the rotation matrix for the analyzer at the analyzer angle A. The same is true for the modulator $\boldsymbol{M}$ and the polarizer $\boldsymbol{P}$. Rotation matrices are necessary when the transmission axis does not align with the p-polarization axis. Before applying the rotation for the next component in the instrument, it is first necessary to rotate back to p- and s-coordinates, which explains the $\boldsymbol{R}(-P)$ and $\boldsymbol{R}(-M)$ terms.

The Jones matrices for each term are given below:

$$\boldsymbol{A} = \begin{bmatrix} 1 & 0 \\ 0 & 0 \end{bmatrix} \tag{B.2a}$$

$$\boldsymbol{R}(A) = \begin{bmatrix} \cos(A) & \sin(A) \\ -\sin(A) & \cos(A) \end{bmatrix} \tag{B.2b}$$

$$\boldsymbol{S} = \begin{bmatrix} \sin(\Psi)\exp(i\Delta) & 0 \\ 0 & \cos(\Psi) \end{bmatrix} \tag{B.2c}$$

$$\boldsymbol{R}(-M) = \begin{bmatrix} \cos(-M) & \sin(-M) \\ -\sin(-M) & \cos(-M) \end{bmatrix} \tag{B.2d}$$

$$\boldsymbol{M} = \begin{bmatrix} 1 & 0 \\ 0 & \exp(i\delta) \end{bmatrix} \tag{B.2e}$$

$$\boldsymbol{R}(M) = \begin{bmatrix} \cos(M) & \sin(M) \\ -\sin(M) & \cos(M) \end{bmatrix} \tag{B.2f}$$

$$\boldsymbol{R}(P) = \begin{bmatrix} \cos(P) & \sin(P) \\ -\sin(P) & \cos(P) \end{bmatrix} \tag{B.2g}$$

$$\boldsymbol{P} = \begin{bmatrix} 1 & 0 \\ 0 & 0 \end{bmatrix} \tag{B.2h}$$

Multiplying from right to left will result in an expression for the output polarization of light. The intensity can then be solved using the following:

$$\boldsymbol{L_{out}} = \begin{bmatrix} E_x \\ 0 \end{bmatrix} \tag{B.3a}$$

$$I = |E_x|^2 \tag{B.3b}$$

The term-by-term derivation of the intensity equation is very long and is thus omitted from this thesis for brevity. However, the following identities were central in deriving the expressions for α_0, α_1, and α_2 shown in Equation 6.15:

$$\cos(-M) = \cos(M) \tag{B.4a}$$

$$\sin(-M) = -\sin(M) \tag{B.4b}$$

$$\cos(P - M) = \cos(P)\cos(M) + \sin(P)\sin(M) \tag{B.4c}$$

$$\sin(P - M) = \sin(P)\cos(M) - \cos(P)\sin(M) \tag{B.4d}$$

$$\cos(2M) = \cos^2(M) - \sin^2(M) \tag{B.4e}$$

$$\sin(2M) = 2\sin(M)\cos(M) \tag{B.4f}$$

$$\exp(i\delta) = \cos(\delta) + i\sin(\delta) \tag{B.4g}$$

$$|i| = 1 \tag{B.4h}$$

Note that only the p-coordinate of the intensity is measured because the analyzer is only letting that orientation of light through to the detector.

B.2.2. Signal-to-Noise Ratio Wavelength Analysis

As the signal-to-noise ratio does change with wavelength, it is useful to understand the error that can be expected as a function of wavelength for the ellipsometer. For this, the inverse of the SNR was calculated at each wavelength, and applied to the intensity signal. The main difference between this simulation and the detector noise simulation addressed in Section 6.4.5 is that this noise is not randomized within a range bounded by the noise value at the wavelength, the upper bound of this noise is simply applied. If the noise were to be randomized, the effect of wavelength on the instrument error could not be properly analyzed.

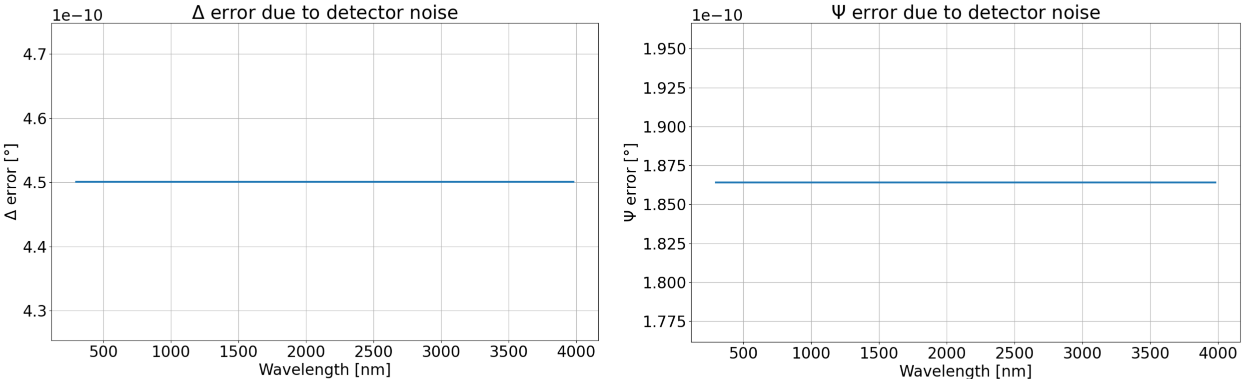

(a) Detector noise impacts on Δ error as a function of wavelength. **(b)** Extinction ratio impacts on Ψ error as a function of wavelength.

Figure B.2: Detector noise effects on Ψ and Δ error.

Figure B.2 shows the effect of detector noise on the Ψ and Δ error over the spectral range of the instrument. When not randomizing the SNR within a distinct range, the detector error has virtually no effect on Ψ and Δ. This error also shows virtually no change as a function of wavelength as well. This is similar to the extinction ratio behaviour seen in Section 6.4.4. According to these simulations, simply increasing or decreasing the amplitude of the intensity signal has virtually no effect on the instrument error due to the impact of the lock-in amplifier. Adding random behaviour makes it more difficult for the lock-in amplifier to track the signal, leading to slightly higher error as seen in Section 6.4.5. This will need to be verified during the characterization phase to ensure these errors are not significant.

B.2.3. Isolated Monte Carlo Cases

In Section 6.4.6, a Monte Carlo simulation is applied to investigate how different random errors in the system can stack to produce an expected performance metric for the instrument. However, that analysis mainly shows the spread in error between minimum and maximum, without much focus on the randomness of these measurements and the most likely conditions. This section addresses Monte Carlo simulations taken at individual values of Ψ and Δ to investigate any trends in performance over 100 Monte Carlo trials.

Figure B.3 shows the results of a Monte Carlo simulation taken at inputs $\Psi = 45°$ and $\Delta = 160°$, with a 1° analyzer error. Figure B.4 shows the results of a 1° polarizer error on the Δ outputs, with Figure B.4a showing $\Delta = 160°$, and Figure B.4b showing $\Delta = 20°$, the mirrored reflection of this angle.

For the analyzer error, the Ψ outputs are relatively evenly spread around the desired Ψ output, meaning the random position of the analyzer is consistently linked to the Ψ output. The polarizer error behaviour is quite interesting though, as regardless of whether the polarizer angle is greater than or less than the target angle, the Δ output is consistently an underestimate of the desired output. When re-examining this Monte Carlo simulation with Δ at 20° (a mirrored reflection of the 160° simulation), the Δ outputs are consistently overestimates of the desired output. The reason behind this behaviour is currently unknown, and should be

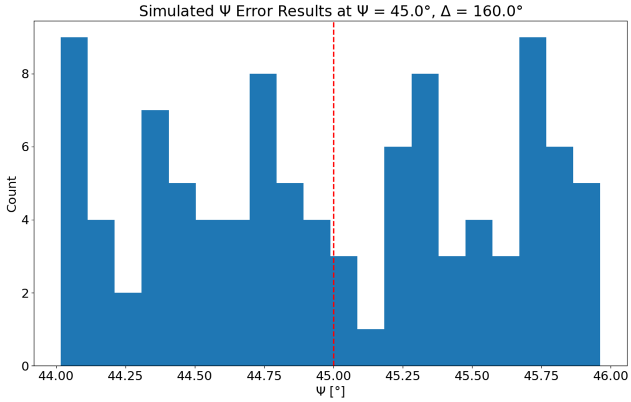

Figure B.3: Monte Carlo analysis of Ψ with 1° analyzer error. The desired output is shown with a dashed red line.

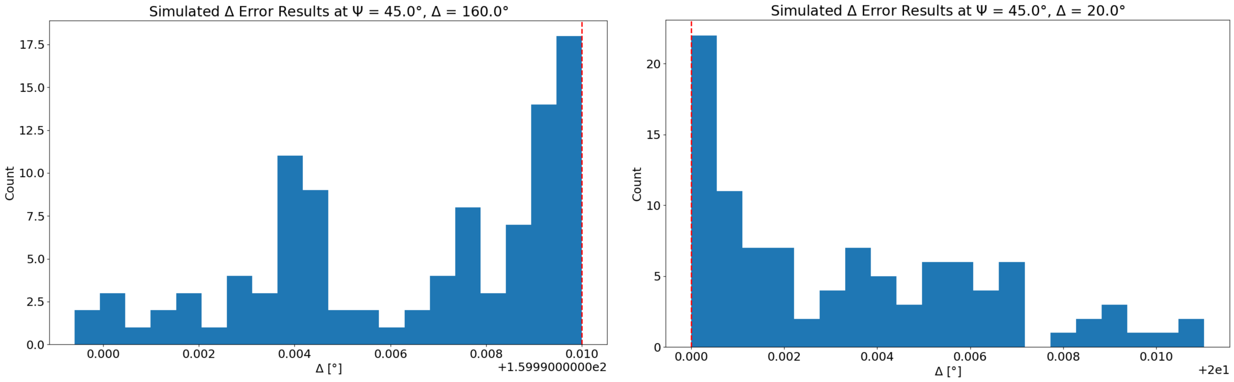

(a) Monte Carlo analysis with $\Delta = 160°$.

(b) Monte Carlo analysis with $\Delta = 20°$.

Figure B.4: Monte Carlo analysis of Δ with 1° polarizer error. The desired output is shown with a dashed red line.

investigated further to understand why the polarizer angle does not have a similar effect on the outputs as the analyzer angle.

Overall, while random errors are inputted for the angles of the polarizer and analyzer, the outputs are not always random and need to be investigated to determine if there are systematic behaviours of the ellipsometer that can be corrected, or at least understood.

B.2.4. Stokes Parameter Error Representations

As shown in Equation 6.22, the Stokes parameters are related to both Ψ and Δ. Therefore, the same errors that impact the values of Ψ and Δ should have an effect on the Stokes parameters.

Figure B.5 shows the error of each of the Stokes parameters with no angular or retardance error. Similar to Δ and Ψ, the error is extremely low, validating the simulation.

When a 1° analyzer error is introduced, the Stokes parameter error is shown in Figure B.6. The Stokes parameters follow a similar trend to the Ψ and Δ parameters. In Section 2.2.1, linear polarization intensities on planetary surfaces were found to be around 0.5%, while the circular intensities are around 0.05%. With errors peaking around 3% for linear Stokes parameters, and 0.6% for circular Stokes parameters, a 1° error is not sufficient for measurements of these planetary surfaces.

By using calibration techniques, the angular error can be adjusted to much lower than 1°. The Stokes error at 0.14°, the minimum angular error, is much closer to measuring intensities from planetary surfaces, as shown in Figure B.7. S_1 has maximum error around 0.05%, while the circular error is 0.075%. While significantly better

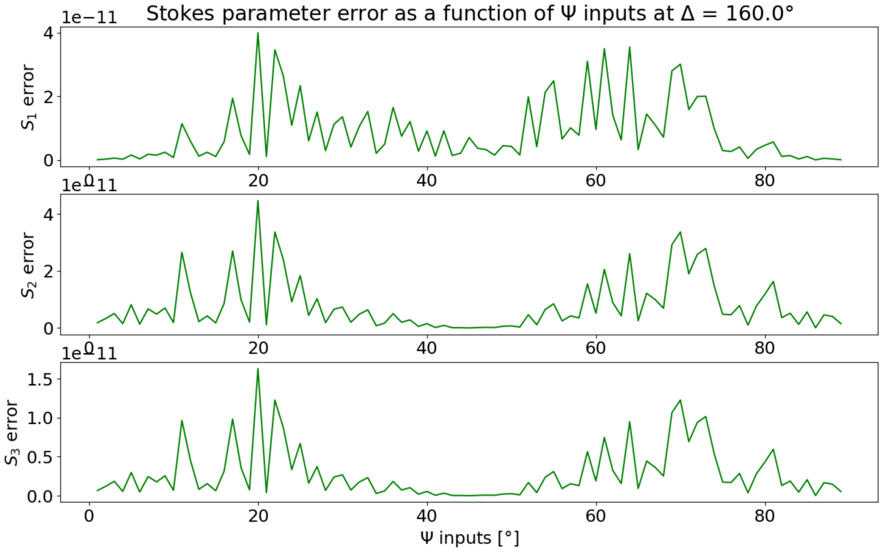

Figure B.5: Stokes parameters error with no input error in the simulation.

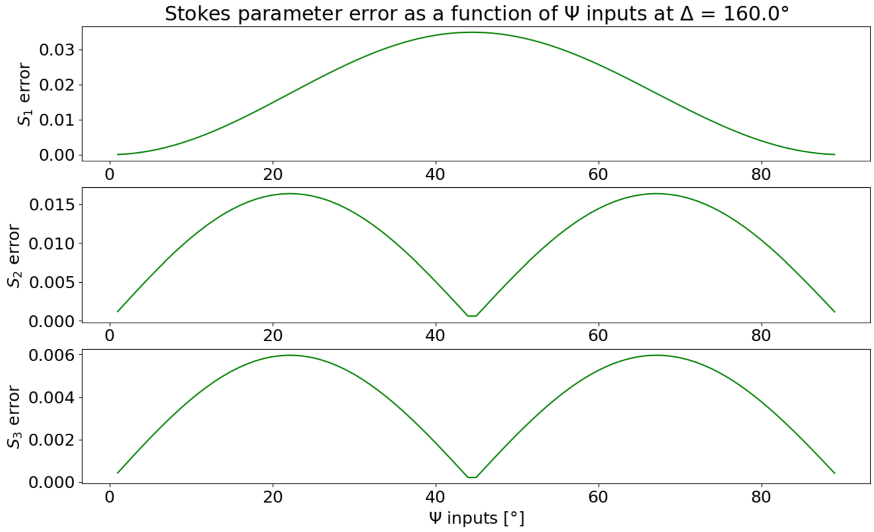

Figure B.6: Stokes parameters error with 1° analyzer error input.

than the error at 1°, there is still some room for improvement as stacking errors due to retardance and static birefringence will further increase these errors.

Overall, the accuracy of the Stokes parameters suggests that the angular error must be further reduced, either through better feedback control methods for the angular error, or through more accurate rotation mounts to hold the polarizers. It also shows that requirements derived from intensities on planetary surfaces are much more attainable and could be considered if relaxation of the requirements becomes necessary.

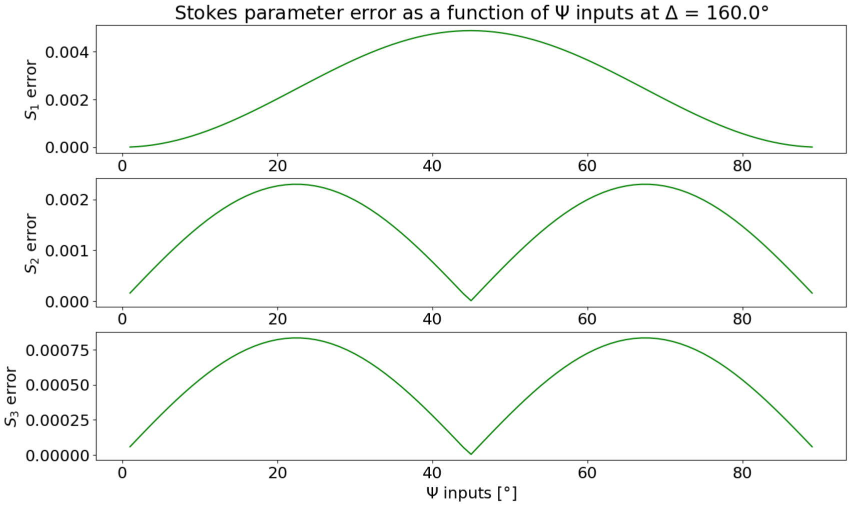

Figure B.7: Stokes parameters error with 0.14° analyzer error input.

B.2.5. Representations of Other Parameters

This section discusses the error involved with other parameters, such as Degree of Linear Polarization, Angle of Linear Polarization, and Degree of Circular Polarization.

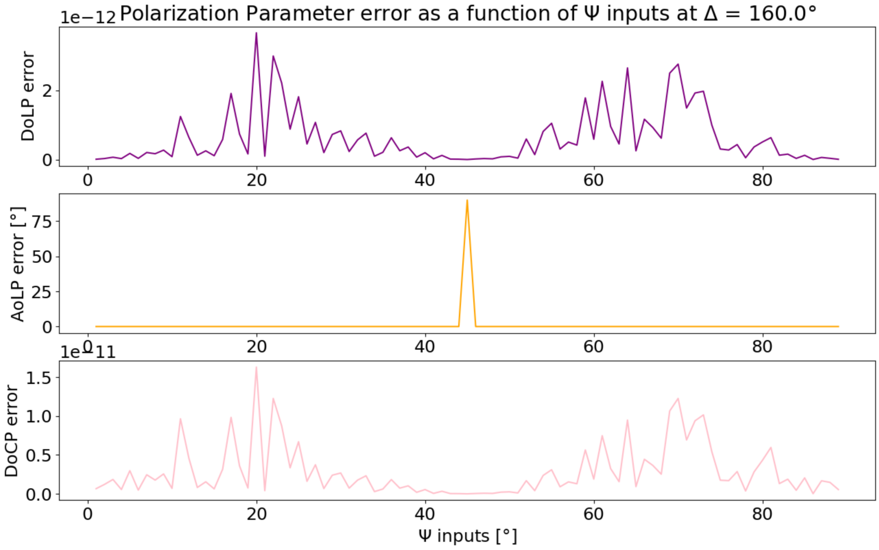

Figure B.8: Other parameters error with no input error in the simulation.

Figure B.8 shows the error associated with these parameters when the input error is zero. The degree of linear polarization and degree of circular polarization maintain a very low error, however the angle of linear polarization has a spike in error at $\Psi = 45°$. The issue with the angle of linear polarization as a parameter is that it has discrete positions at which the value changes by a multiple of $\pi/2$, which is a large change. These discrete positions do not leave a lot of room for error, and thus while the AoLP may be very close to the correct value, if it is on the wrong side of these discrete regions, the value will be incorrect. Changing the formula to accept some error could cause other problems in the results, and thus it is recommended to look at a few data points around the transition between discrete regions to determine trends and see if the error is simply an offset or if there is large measurement error. It does make the angle of linear polarization a somewhat unreliable parameter around $\Psi = 45°$.

Similar error behaviour is shown when input errors are included, with an example at 1° error shown in Figure

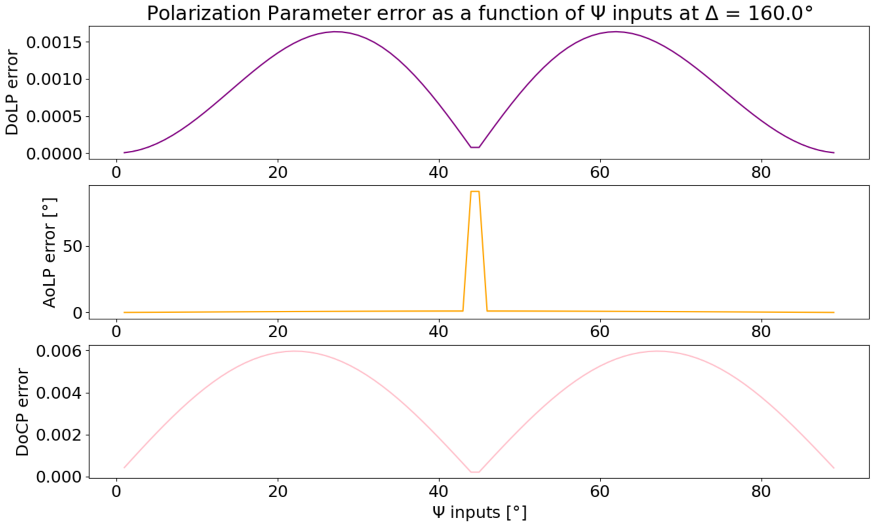

Figure B.9: Other parameters error with 1° analyzer error.

B.9. Physically, a $\Psi = 45°$ corresponds to equal polarization intensity in the *p* and *s*-polarization direction, so if there is any error in the Δ value, it will be unclear what angle this polarization is entering from.